Numerical Modeling of Thermal/Saline Discharges in Coastal Waters

By

Hossein Kheirkhah Gildeh

A thesis submitted under supervisions of
Dr. Majid Mohammadian and Dr. Ioan Nistor
in partial fulfilment of the requirements for the degree of

Masters of Applied Science in Civil Engineering

Department of Civil Engineering
University of Ottawa
Ottawa, Canada
April 2013

The M.A.S.c in Civil Engineering is a joint program
with Carleton University administrated
by Ottawa-Carleton Institute for Civil Engineering

To my parents...

برای پدر و مادر مهربان و فداکارم که به من زندگی آموختند...

Abstract

Liquid waste discharged from industrial outfalls is categorized into two major classes based on their density. One type is the effluent that has a higher density than that of the ambient water body. In this case, the discharged effluent has a tendency to sink as a negatively buoyant jet. The second type is the effluent that has a lower density than that of the ambient water body and is hence defined as a (positively) buoyant jet that causes the effluent to rise. Negatively/Positively buoyant jets are found in various civil and environmental engineering projects: discharges of desalination plants, discharges of cooling water from nuclear power plants turbines, mixing chambers, etc. This thesis investigated the mixing and dispersion characteristics of such jets numerically. In this thesis, mixing behavior of these jets is studied using a finite volume model (OpenFOAM). Various turbulence models have been applied in the numerical model to assess the accuracy of turbulence models in predicting the effluent discharges in submerged outfalls. Four Linear Eddy Viscosity Models (LEVMs) are used in the positively buoyant wall jet model for discharging of heated waste including: standard k-ε, RNG k-ε, realizable k-ε and SST k-ω turbulence models. It was found that RNG k-ε, and realizable k-ε turbulence models performed better among the four models chosen. Then, in the next step, numerical simulations of 30˚ and 45˚ inclined dense turbulent jets in stationary ambient water have been conducted. These two angles are examined in this study due to lower terminal rise height for 30˚ and 45˚, which is very important for discharges of effluent in shallow waters compared to higher angles. Five Reynolds-Averaged Navier-Stokes (RANS) turbulence models are applied to evaluate the accuracy of CFD predictions. These models include two LEVMs: RNG k-ε, and realizable k-ε; one Nonlinear Eddy Viscosity Model (NLEVM): Nonlinear k-ε; and two Reynolds Stress Models (RSMs): LRR and Launder-Gibson. It has been observed that the LRR turbulence model as well as the realizable k-ε model predict the flow more accurately among the various turbulence models studied herein.

Résumé

Les déchets liquides rejetés par les effluents industriels sont classés en deux grandes catégories en fonction de leur densité. Dans la première catégorie comprend l'effluent a une densité supérieure à celle du l'eau ambiante. Dans ce cas, le jet est dense et l'effluent a tendance à avoir une courbure en bas. Dans la deuxième catégorie la densité du jet est inférieure à celle de l'eau ambiante et l'effluent évolue vers le haut. Les deux cas sont présents dans la nature et dans divers projets industriels, en l'occurrence au niveau des systèmes de décharge, des usines de dessalement, des centrales nucléaires, etc. Cette thèse a pour objectif l'étude des caractéristiques de mélange et de dispersion de ces jets en utilisant le modèle numérique (OpenFOAM) basé sur la méthode des volumes finis. Plusieurs modèles de turbulence ont été appliqués aux différents cas des jets, afin d'évaluer les performances de ces modèles pour prédire l'évolution des rejets au fond du système. Quatre modèles de turbulence ont été appliqués aux équations de Navier-Stokes (RANS) avec une viscosité turbulente linéaire (LEVMs) pour l'étude du jet type horizontal avec une température relativement élevée à celle du système à savoir : le modèle standard k-ε, le modèle RNG k-ε, le modèle Réalisable k- ε, et le modèle SST k-ω. Il a été prouvé numériquement que les modèles RNG k-ε et Réalisable k-ε sont les plus performants pour ce type de jet. Ensuite, deux cas de jets denses avec des angles d'inclinaison 30˚ et 45˚ ont été étudiés. Les deux valeurs d'angle d'inclinaison ont été choisies parce que le maximum de la hauteur du jet reste au-dessous de la surface d'eau et c'est un bon choix pour le cas les écoulements peu profonds rencontrés dans la pratique. Cinq modèles (RANS) ont été appliqués pour ces cas pour déterminer les prédictions des jets à savoir: le modèle linaire RNG k-ε, le modèle linaire Réalisable k-ε, le modèle non linaire k-ε et les deux modèles type RSMs: LRR et Launder-Gibson. Il a été prouvé numériquement que les modèles LRR et Réalisable k-ε sont le bon choix pour le jet dense.

Acknowledgements

I would like to express my sincere gratitude to my supervisors, Dr. Majid Mohammadian and Dr. Ioan Nistor, for their continued guidance and support throughout all stages of this investigation.

I also want to thank Qatar Ministry of Environment for kindly providing funding for this project.

Furthermore, I would like to thank my brother Morteza for all his help and continuous support since childhood.

Table of Contents

List of Figures

List of Tables

List of Symbols

a,b	Constants in Eqn. 5.20;
b_c	Concentration spread width [m];
b_u	Velocity spread width [m];
B_0	Buoyancy flux [m^4/s^3];
C	Concentration on the numerical mesh;
C_0	Concentration at source;
C_a	Ambient water concentration;
C_{max}, C_m, C_c	Centerline maximum concentration;
D	Diameter of nozzle [m], and diffusion coefficient [m^2/s];
Dk_{eff}	Effective diffusivity for k [m^2/s];
$D\varepsilon_{eff}$	Effective diffusity for ε [m^2/s];
$D\omega_{eff}$	Effective diffusity for ω [m^2/s];
F_d	Densimetric Froude number;
G_k	Generation of turbulent kinetic energy;
g	Gravity acceleration [m/s^2];
g'	Modified gravity acceleration [m/s^2];
H_a	Ambient water depth [m];
k	Turbulent kinetic energy;
k_{eff}	Heat transfer coefficient [W/s°C];
L_M	Momentum length scale [m];
L_Q	Source length scale [m];
M_0	Kinematic momentum flux [m^4/s^2];
P	Pressure [N/m^2];
Pr	Prandtl number;
Pr_t	Turbulent Prandtl number;
Q_0	Jet discharge flux [m^3/s];

R	Renormalization term;
Re_0	Discharge Reynolds number;
r	Radial distance from jet centerline [m];
S	Salinity and dilution;
S_m	Dilution value of the jet centerline peak;
S_r	Dilution value of the return point;
S_{ij}	Strain rate tensor;
s	Curvilinear distance starting from the nozzle tap [m];
T	Temperature on the numerical mesh [°C];
T_0	Temperature at source [°C];
T_m	Temperature values along a section [°C];
T_{m0}	Centerline maximum temperature [°C];
t	Time [s];
u, v, w	Velocity in the x, y, z direction, respectively [m/s];
U_0	Velocity at source [m/s];
U_m	Velocity values along a section [m/s];
U_{m0}	Centerline maximum velocity [m/s];
U_{ms}	Maximum velocity at an offset section [m/s];
U_c	Centerline maximum velocity [m/s];
u_i', u_j'	Fluctuating part of velocity [m/s];
x, y, z	Coordinates;
x_0	Horizontal location of nozzle tap [m];
x_m	Horizontal location of the jet centerline peak [m];
x_r	Return point [m];
y_0	Vertical location of nozzle tap [m];
y_m	Vertical location of the jet centerline peak [m];
y_t	Maximum terminal rise height [m];
$y_{m/2}$	Velocity-half-height [m];
$y_{tm/2}$	Temperature-half-height [m];

$z_{m/2}$	Velocity-half-width [m];
$z_{tm/2}$	Temperature-half-width [m];
γ	Turbulent intermittency;
ε	Dissipation rate for k in k-ε;
Θ	Initial jet angle [°];
μ	Dynamic viscosity [N.s/m^2];
υ	Kinematic viscosity [m^2/s];
υ_t	Turbulent kinematic viscosity [m^2/s];
υ_{eff}	Effective kinematic viscosity [m^2/s];
ρ	Density on the computational mesh [kg/m^3];
ρ_0	Discharge density [kg/m^3];
ρ_a	Ambient water density [kg/m^3];
ρ_t	Water density as a function of temperature [kg/m^3];
$\bar{\Omega}_{ij}$	Mean rate of rotation tensor;
ω	Dissipation rate for k in k-ω;
ω_k	Angular velocity for rotating reference frame [m/s].

Chapter I

Introduction

1.1 Effluent Discharge and Impacts on the Environment

Discharges of domestic and industrial effluents into coastal and estuarine waters and the emission of incinerated urban waste into the atmosphere provide two examples of environmental flows in which water and air quality, respectively, are determined by the behavior and structure of the particle-laden, turbulent, dense/buoyant jets generated by discharges. Industrial power plants discharge these effluents into the seawater body (Lattemann and Hoepner, 2008) mostly as submerged jets due to their higher effectiveness.

Moreover, increase in population, shortages of clean and potable water, and advancements in desalination plant technology have increased rapidly in the last decades (GWI, 2004). In arid and semi-arid countries, desalination plants are considered as the best alternative to respond to the high demand for drinkable water. Desalination plants remove the dissolved minerals from coastal water bodies and produce effluents with a high salt concentration, called brines. These may also have an elevated temperature, especially for the Multi-Stage Flash (MSF) desalination plants. Disposal of these brines, which have higher density than the receiving water, causes many environmental impacts, especially in the near field of outfall systems, which is the natural habitat of marine species and fish (e.g. Einav and Lokiec, 2003; Hashim and Hajjaj, 2005; Lattemann and Hoepner, 2008; Sajwani, 1998). Some areas like Red Sea, Persian Gulf and generally low wave energy areas combined with the presence of shallow waters are particularly sensitive to effluent discharges.

Effluent discharge systems of the industrial power plants must be designed properly in order to minimize environmental impacts and associated remediation costs (Fig. 1.1). They also have to satisfy environmental criteria and standards (e.g. US-EPA and EU regulations). Nevertheless, ocean outfall systems are mostly not optimized regarding either environmental impacts or the practical needs. In some cases, the regulations also lack the clear guidelines for ambient or effluent standards (Jirka, 2004).

Fig. 1.1: Sewage discharge in Willamette River. From: www.hevanet.com

The density differences between the effluent and ambient water, represented by the buoyancy flux, induce various flow and mixing characteristics of the discharge. In the case of the dense jets, especially brine from Reverse Osmosis (RO) desalination plants, the flow has the tendency to fall as a negatively buoyant plume. On the other hand, the buoyant jets (e.g. effluents from MSF desalination plants) have lower density than ambient water which causes the plume to rise.

The mixing process is divided into two physical regions, where different physical mechanisms predominate. In the first region that is named *near-field*, the mixing is intense; it results mainly from turbulence generated by the initial buoyancy and momentum of the discharge and their interactions with the ambient flow. Beyond this region, the self-induced turbulence will be decayed and mixing just results from ambient oceanic turbulence. In this region which is named *far-field*, dilution increases at a much slower rate than in the near-field (Figs. 1.2, 1.3). The mixing characteristics of only the near-field are studied in this thesis.

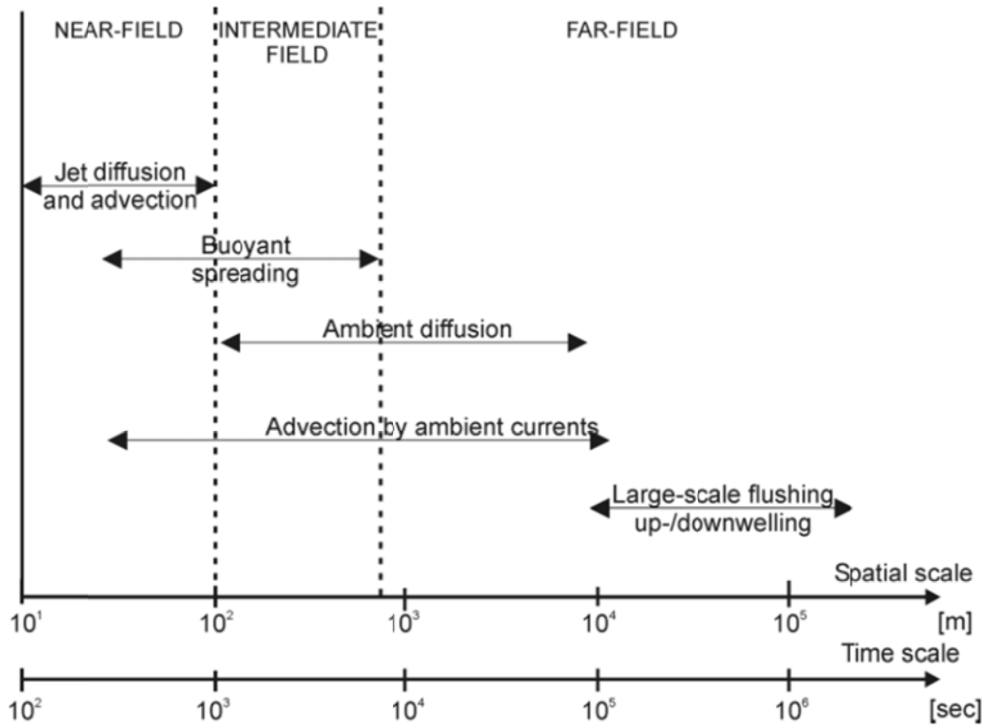

Fig. 1.2: Spatial and temporal scales in near-field and far-field mixing process. From: Jirka et al. (1976)

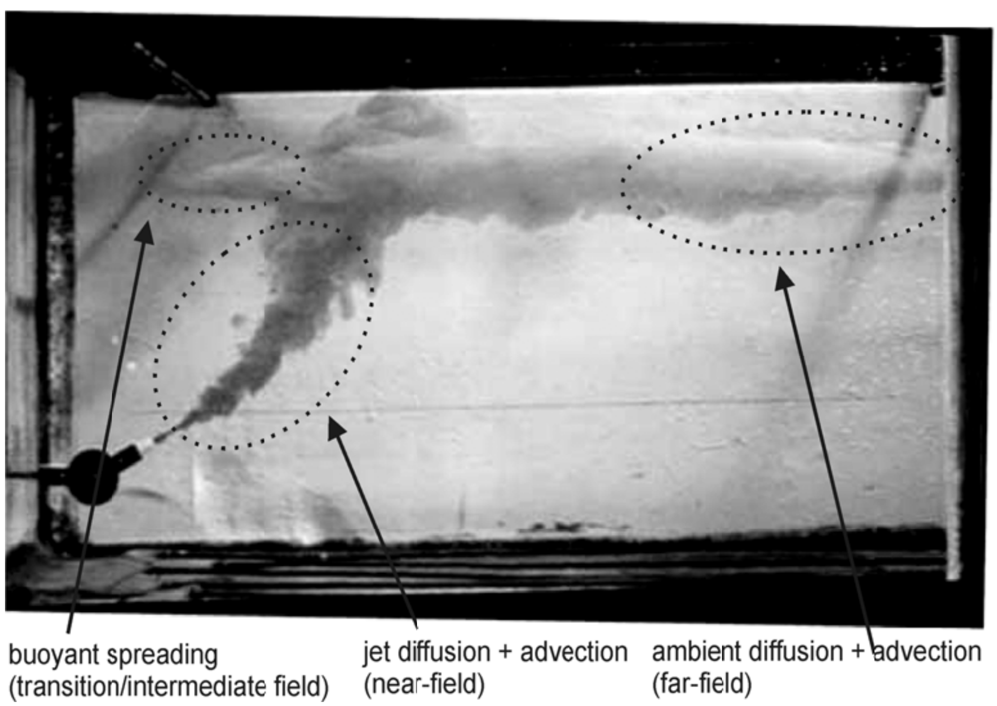

Fig. 1.3: Three major domains in positively buoyant jet of a submerged discharge. From: Jirka et al. (1976)

Effluent outfalls characteristics need to be investigated to minimize environmental impacts and associated costs while being in compliance with regulatory demands. A major principle of the effluent outfall design is to decrease the concentrations of the waste source by exact measures within the industrial plant (e.g. decreasing the additive usage, enhancing plant efficiency, etc.) or designing proper intake and pre-treatment technologies. A second principle is the application of improved mixing technologies such as submerged diffuser(s), situated in less sensitive regions (offshore, deep waters).

Ballinger et al. (2009) described the effluent discharge characteristics as follows:

1.1.1 Discharge Characteristics

a) *The discharge structure*: the type of the discharge structure (open channel, submerged/elevated pipe, etc.), the site of the discharge structure (at the bank, in the water body, in the bay, close to break waters or groynes, etc.), the dimensions of the discharge structure (channel cross-section, pipe diameter, multiport installation, etc.), the orientation of the discharge structure (discharge angles relative to prevalent currents or dominant geographical/bathymetrical features).

b) *The effluent*: the type (municipal/industrial wastewater, combined overflow, drainage water, cooling water, desalination plant effluent), the physical properties (temperature, salinity, viscosity, etc.), the fluxes (volume and momentum flux resulting from flow rate and discharge velocities), the chemical/biological properties (substance/bacteria concentrations, etc.) and the loads (yearly substance loads discharged).

1.1.2 Receiving Water Characteristics

a) *The local conditions near the discharge site*: the type of water body (river, lake, etc.), the physical properties (temperature, salinity, density, velocities, etc.), the meteorological/hydrological conditions (flow, velocity and water level variations, density variations, reversing/non-reversing flows, etc.) and the topography (meandering river, coastal, bay, etc.).

b) *The regional conditions for the whole water body or for a part of that*: the proximity to other influencing factors (other discharges, morphological changes, dams, etc.), the proximity to sensitive aquatic ecosystems (mangrove forests, salt marshes, coral reefs, or low energy intertidal areas and shallow coasts) and the general flushing characteristics (residence times, exchange times).

The main problem arises due to the strongly limited mixing behavior as effluent enters the receiving waters. The mixing mechanism is significantly influenced by the effluent density, which is dominated by the varying effluent salinity and temperature. One efficient measure is implementing discharge technologies capable of enhanced effluent dispersion in the receiving environment and providing an adequate discharge area to avoid pollutant accumulation, protect sensitive regions, and utilize natural purification processes. Submerged diffuser outfalls such as efficient mixing devices installed at locations with high transport and purification capacities are able to reduce environmental impacts significantly (a design procedure for an inclined submerged dense jet is discussed in Appendix A).

1.2 Objectives

The previous section explained the general mechanism which exists in effluent discharges of positively/negatively buoyant jets. Based on those considerations, the main objectives of this investigation are:

- To evaluate the performance of a numerical model in simulation of submerged plumes;
- To choose the appropriate numerical model to simulate both effluent discharge scenarios: positively and negatively buoyant jets;
- To analyze the governing equations of the mathematical model and implement the required terms in the model;
- To investigate and assess a wide range of turbulence models within the numerical model and finally recommend the most accurate ones;
- To find out the stable numerical schemes to solve the model equations;

- To verify the numerical model results, focusing on the velocity and concentration fields with comprehensive experimental and numerical data provided by other researchers.

In order to achieve the objectives of this thesis, numerical studies on buoyant and dense jets have been conducted. Tests were carried out using the OpenFOAM numerical model which is explained in detail in Chapter III.

1.3 Novelty of the Study

Different types of the jets (including buoyant and dense jets) have been extensively studied experimentally. However, numerical modeling in this field has been mostly started in the 21st century with availability of computational resources.

This study contributed to a numerical model that works for all three possible jets based on the variation of their density (positive, neutral, and negative). This is the first time (to the best knowledge of the author) that an open-source code is used to model an incompressible fluid with variation of density due to changes in temperature and salinity.

Moreover, various turbulence closure models have been examined in this project which is done for the first time to evaluate the accuracy of the numerical models in predicting the jet properties of the positively and negatively buoyant effluents discharging from industrial plants into the coastal waters.

Finally, evaluation of different numerical schemes for solving the required terms in governing equations has been concentrated widely in this study to improve the accuracy of calculations as much as possible.

1.4 Organization of Manuscript

The thesis is organized in the form of technical papers, and divided into six chapters. Chapter I is the Introduction. Chapter II provides the Literature Review: in this chapter a comprehensive literature review of the both scenarios (buoyant/dense jets) is presented. The literature review includes recent experimental and numerical studies on the subject. Chapter III provides the theoretical concepts of mathematical and numerical modeling and the process undertaken to develop the model using the OpenFOAM toolbox. The concept of turbulence modeling is also described in this section.

Chapter IV is the first technical paper. In this paper, the submerged buoyant wall jet was studied numerically. Four different turbulence models were applied in this paper: (i) standard k-ε; (ii) RNG (Re-Normalisation Group) k-ε; (iii) realizable k-ε; (iv) SST (Shear Stress Transport) k-ω. These turbulence models were explained in detail in the Appendix D.

Chapter V includes the second technical paper which studies the effluent discharges of inclined dense jets for two angles (30° and 45°). These two angles are very applicable for shallow water regions regarding the lower terminal rise height of these jets. In this paper, five turbulence models have been examined to compare the accuracy of various models. Two of these models are chosen from the first study due to their better accuracy in predicting the flow field. These five models are: (i) RNG k-ε; (ii) realizable k-ε; (iii) nonlinear k-ε; (iv) Launder-Gibson; (v) LRR. These turbulence models are explained in detail in the Appendix E.

Finally, Chapter VI presents the final conclusions and recommendations for future studies. It should be mentioned that since the main results of the thesis are presented as technical papers, the author tried to avoid repetition of material in the rest of document as much as possible.

Chapter II

Literature Review

2.1 Introduction

Effluents may be discharged either as surface or submerged jets. The surface discharging of negatively buoyant jets do not have enough mixing efficiency due to their reduced mixing within the ambient water in the near-field compared to the submerged discharges. This causes a density current that develops at the bottom of the receiving water body (Fig. 2.1). However, submerged discharges are nowadays increasingly applied since they obtain a higher mixing rate. This is because in the submerged jets (both positively and negatively buoyant jets) water entrainment towards the jet centerline occurs from all directions (Fig. 2.2). This increases the dilution rate for submerged jets. Dilution is one of the most important parameters for designing the ocean outfall systems.

(a)

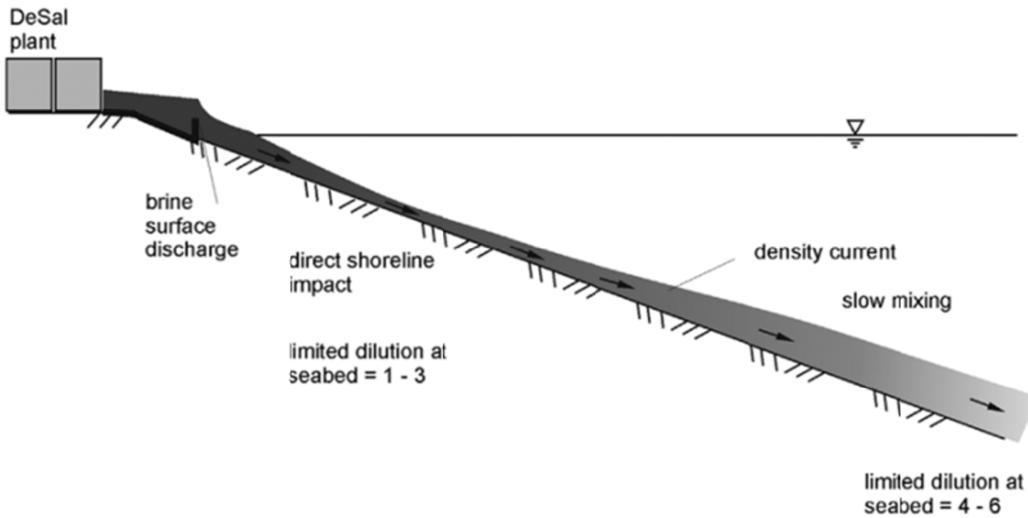

(b)

Fig. 2.1: Surface discharge strategy. (a) Effluent discharge in Hesham power station outfall, UK (b). An sketch of surface discharge of dense jets, from Bleninger and Jirka (2008)

(a)

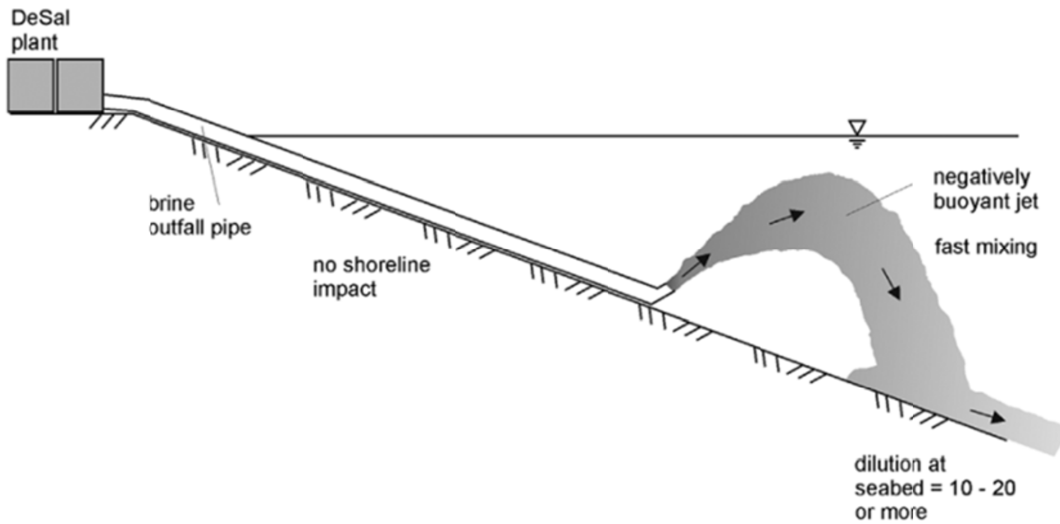

(b)

Fig. 2.2: Submerged discharge strategy. (a) effluent discharge of Hollywood outfall, USA (b). sketch of submerged discharge of dense jets, from Bleninger and Jirka (2008)

Distribution of the concentration depends on the location of the outfall and on the transport capacities of different currents. Moreover, high mixing efficiencies can be gained by introducing submerged high velocity discharges placed offshore which may generate both negatively and positively buoyant jets. Since submerged jets are more effective in effluents discharges, two types of such jets are modeled numerically in this study: positively buoyant wall jet, and negatively buoyant inclined jet. These two jets are shown in Fig. 2.3.

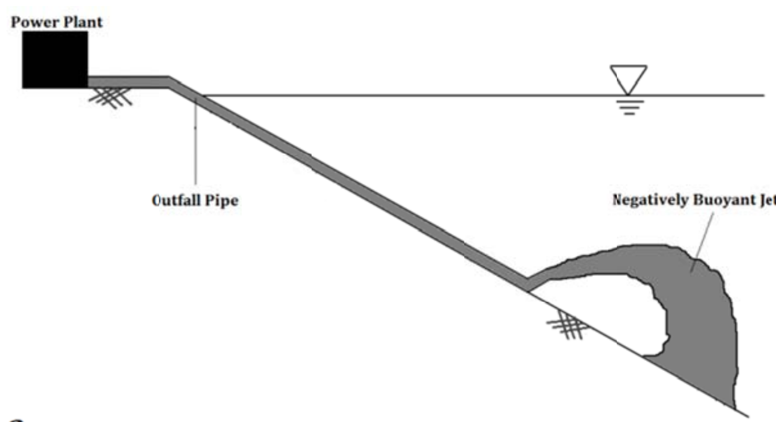

a

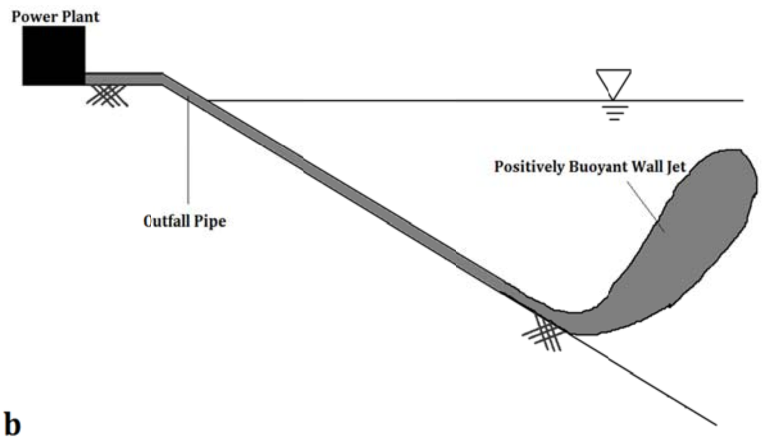

Fig. 2.3: Discharge strategies for power plant effluents. (a) Negatively buoyant discharge - higher density than ambient water. (b) Positively buoyant wall discharge - lower density than ambient water

A review of previous studies on both these jets is presented in this chapter. For each case, the experimental studies are discussed first and then the numerical investigations of other researchers are reviewed.

2.2 Positively Buoyant Wall Jet

2.2.1 Experimental Studies

Positively buoyant jets are mainly thermal jets resulting from cooling water systems of industrial plants (e.g. nuclear power plants). The density of these jets is lower than that of the ambient water.

Sharp (1975, 1977) is one of the pioneers who considered submerged outfall of thermal effluents as a buoyant wall jet. His study focused on the properties of a buoyant jet discharged immediately above a horizontal surface. The jet behaved as a wall jet in the initial part of its trajectory; nonetheless after rising from the surface to which it initially clung, the jet acted as a normal free jet (Fig. 2.4).

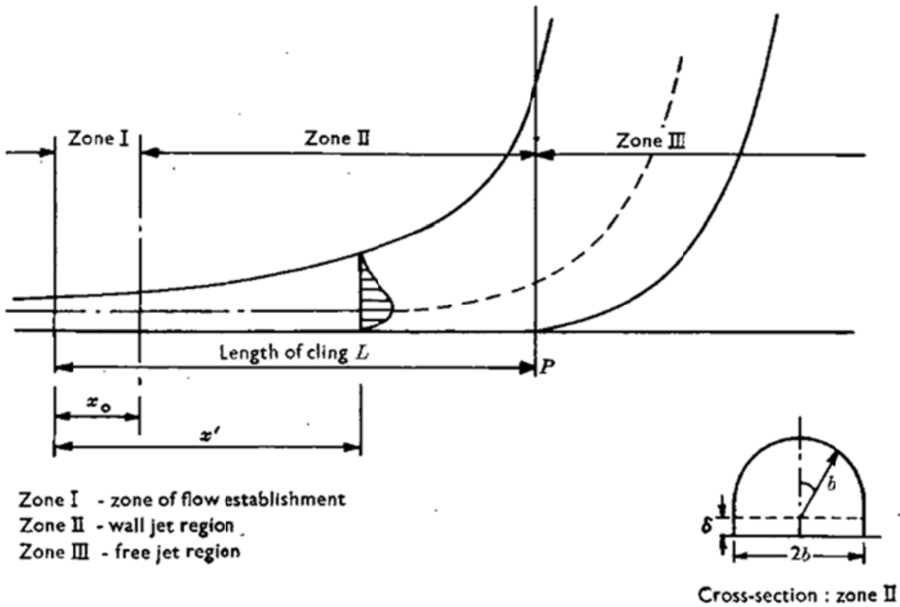

Fig. 2.4: Zones of flow. From Sharp and Vyas (1977)

Rajaratnam and Pani (1974) investigated three dimensional bluff wall jets originating from circular, elliptic, square, rectangular, and equilateral triangular nozzles experimentally. They showed that in the fully-developed flow, the distribution of the axial velocity in the central as well as transverse planes is similar. Balasubramanian and Jain (1978) studied a single round buoyant jet discharging into a shallow quiescent body of water with densimetric Froude number ranging from 5 to 20 and submergence ratios ranging from 2.5 to 7 experimentally. They measured the temperature distributions for the test basin. Sobey et al. (1988) studied buoyant discharge in its most elementary geometry, a round buoyant jet discharging horizontally from a vertical side wall into a stationary water body on a flat-bed. They also investigated the proximity of the bed and the free surface. They found out that for smaller values of the bed parameter ($Z_0/l_M<0.1$), Coanda attachment (Coanda effect is the tendency of a fluid jet to be attached to a nearby surface) to the bed has a major influence on the initial development. The jet path is initially deflected toward the neighboring bed and total mixing process is limited by the influence of momentum. Then the buoyancy eventually prevails and the jet path rises toward the free surface. The overall flow pattern which they sketched is shown in Fig. 2.5. They finally compared the jet path, centerline dilution and horizontal and vertical half widths with an integral model in an unconfined environment.

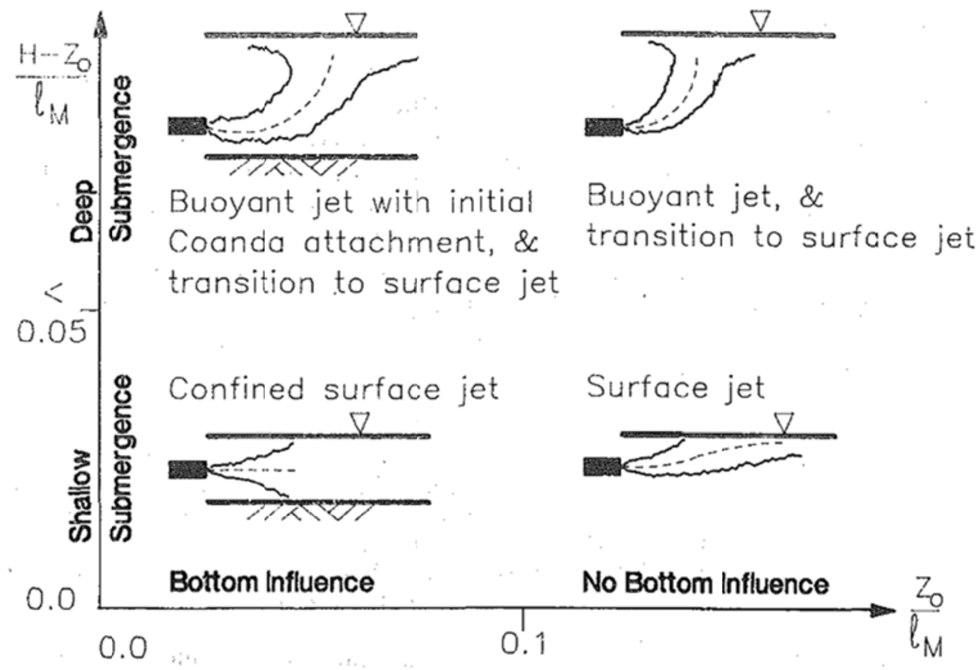

Fig. 2.5: Flow pattern regime. From Sobey et al. (1988)

Law and Herlina (2002) applied novel experimental equipment, a combination of Particle Image Velocimetry (PIV) and Plannar Laser Induced Fluorescence (PLIF) approach, in order to study a circular three-dimensional turbulent wall jet. Both velocity and concentration profiles exhibited similarity in the streamwise and spanwise directions after sufficient distance from the nozzle. They argued that, the existence of a secondary mean motion is responsible for the far greater lateral spread compared to the normal spread for both momentum and scalar mixing. Using curve fitting, the mean properties of the three-dimensional wall jet were approximated. The consistency of the relationships is further examined based on mass conservation and momentum balance. More recently, Michas and Papanicolaou (2008) investigated horizontal, round, turbulent buoyant jets that discharge in a homogeneous calm ambient fluid. In their experiments, the initial jet Richardson numbers (Richardson number is a dimensionless number that expresses the ratio of potential to kinetic energy) ranged from very small (jet-like) to around unity (plume-like), to include the full extent of applications. The mixing characteristics such as trajectories obtained with video imaging, turbulence properties measured with fast response thermistors, and dilution factors were evaluated. They understood that trajectories of buoyancy-conserving horizontal jets bend faster than those observed in heated jets. They argued that flow resembled a jet-like behavior in the horizontal regime, while the mean and turbulent temperature profiles become asymmetrical in the transition and the vertical regime. The maximum intensity of turbulence doubles in the vertical regime if compared to that in the horizontal part of the flow. Minimum dilutions obtained from experiments at the jet axis were compared to the results of a one-dimensional numerical model of a heated horizontal jet, where the loss of buoyancy flux was accounted for (Fig. 2.6).

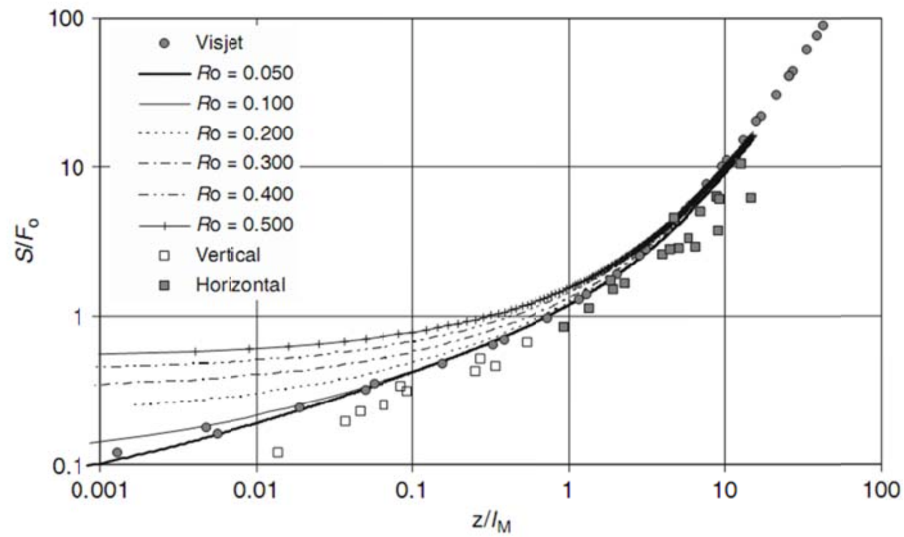

Fig. 2.6: Normalized centerline dilution. From Michas and Papanicolaou (2008)

2.2.2 Numerical Studies

The above-mentioned studies were all performed experimentally. However, a few researchers have recently investigated the buoyant horizontal jets numerically. Maele and Merci (2006) applied the standard and realizable *k-ε* models. Both the simple and the generalized gradient diffusion hypotheses were applied for the calculation of the buoyancy production of turbulent kinetic energy. They found that the buoyancy modification based on the simple gradient diffusion hypothesis has a negligible influence on the results for their test cases. They concluded that, the realizable *k-ε* model performed well for the test cases considered. Kim and Cho (2006) used a three-dimensional model to numerically study the buoyant flow, along with its mixing characteristics, of heated water discharged from the surface and submerged side outfalls in shallow and deep waters with a cross flow. The results of their numerical model agreed well with the experimental results, particularly, the jet trajectories, and the distribution of the dimensionless excess temperature. They argued that if the heated water is discharged into shallow water where the momentum flux ratio and the discharge densimetric Froude number are high, the submerged discharge method is better than the surface discharge method in terms of the scale of the recirculation zone and the minimum dilution (Fig. 2.7). In deep water, where the momentum flux ratio and discharge densimetric Froude number are low, however, the submerged discharge method had a few advantages. They used the FLOW-3D which is a commercial CFD package and RNG k-ε model was applied for turbulence closure.

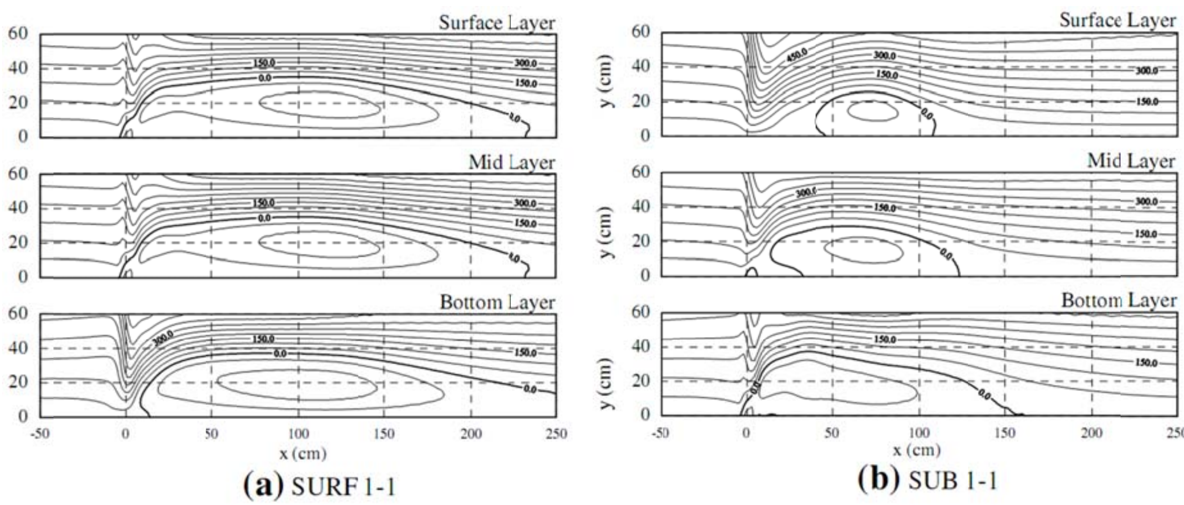

Fig. 2.7: The *x*-*y* streamline distribution. From Kim and Cho (2006)

Xiao et al. (2009) developed a fast non-Boussinesq integral model for the horizontal buoyant round jets. Verification of this model is established with available experimental data and comparisons over a large range of density variations with the CFD code named GASFLOW. The model has proved to be an efficient engineering tool for predicting horizontal strongly buoyant round jets. Huai et al. (2010) applied the realizable k-ε model to simulate the buoyant wall jet and gave the results of cling length, centerline trajectory and temperature dilutions at certain sections. The comparison between the numerical results and Sharp's experimental data indicated that their model was effective in estimating velocity distribution and temperature dilutions. The velocity profiles at the central plane and z-plane both showed a strong similarity at a certain distance from the nozzle, and the distributions of velocity and temperature dilutions also exhibited a similarity along the axial direction at centerline in the near-field (Fig. 2.8). Based on the results, they gave the corresponding relationships between the distance and the dilution of velocity and temperature.

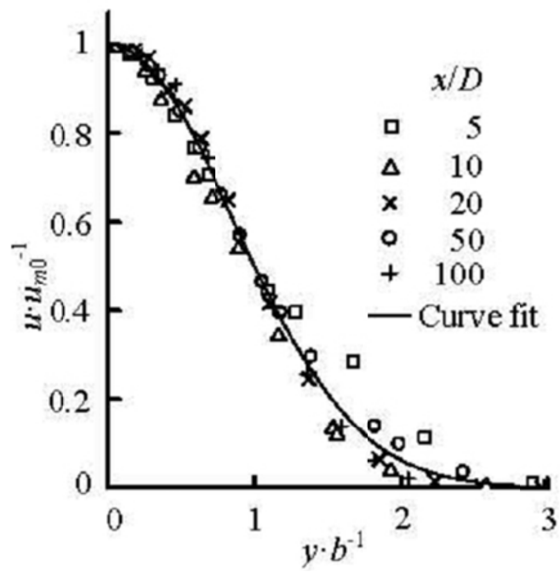

Fig. 2.8: Velocity profile in the z-plane. From Huai et al. (2010)

2.3 Inclined Dense Jet

2.3.1 Experimental Studies

The same as previous case (submerged buoyant wall jet), more experimental studies have been done in this field by researchers than numerical ones. Similar to the last section, previous experimental investigations are reviewed first and then previous numerical studies are discussed.

Zeitoun et al. (1970) investigated both experimental and numerical analyses of dense jets directed upward, and inclined at an angle to the horizontal. They concluded that for some densimetric Froude numbers, a jet directed at a 60° angle has the longest trajectory and therefore the maximum dilution (Fig. 2.9), compared to other angles. They also discussed on the design concepts of outfall systems for desalination plants of different sizes.

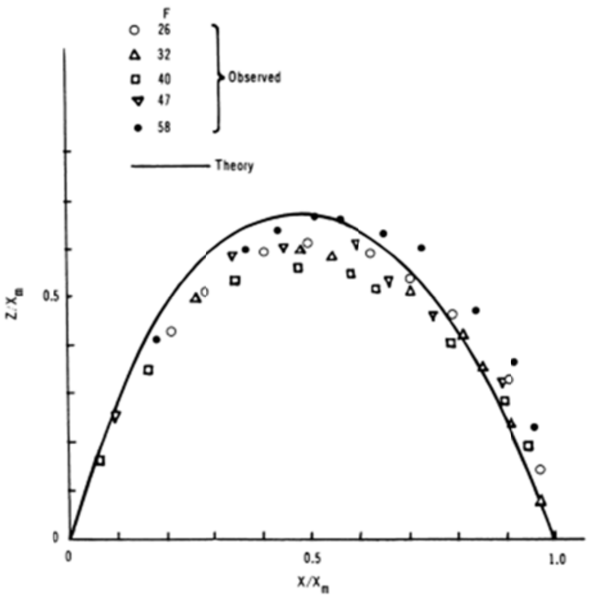

Fig. 2.9: Normalized profile of upper boundary of dense jet for ϴ=60°. From Zeitoun et al. (1970)

Roberts and Toms (1987) conducted an extensive series of experiments on the characteristics of inclined and vertical dense jets discharged into a uniform cross-flow of various speeds and directions (Fig. 2.10). The inclined jets were maintained at 60° to the horizontal and the results for terminal rise height, dilutions at the terminal rise height, and impact points were compared to those for vertical jets. For discharges into stagnant ambient, they found that the effect of source volume flux should not be neglected for jet Froude numbers less than about 25. Empirical equations to predict the dilution and rise height based on dimensional and length scale arguments were also presented in their work. The dilution of an inclined jet increases as the angle to the current increases. As they reported, dilutions for inclined jets discharging into the cross-flow are lower than for a vertical jet and dilutions for discharges with the cross-flow are generally higher. Applications to design were discussed, and it was found that inclined jets are generally preferable to vertical ones. This is because of the lower terminal rise height of the inclined jet, the much higher dilution under stagnant conditions, and the horizontal momentum given to the waste-field.

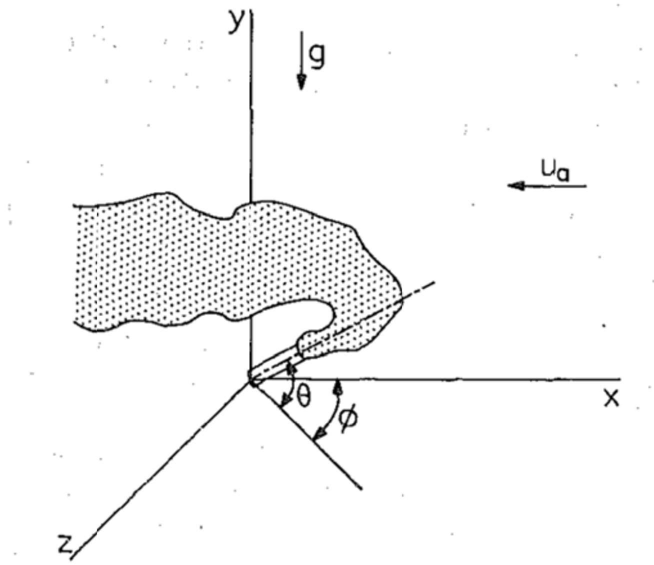

Fig. 2.10: Definition sketch. From Roberts and Toms (1987)

Roberts et al. (1997) performed experiments using laser-induced fluorescence (LIF) and a micro-conductivity probe on turbulent dense jets inclined upwards at an angle of 60° into stationary environments. Such jets are often used to discharge industrial wastewaters. Time-averaged LIF images showed concentration profiles vary smoothly in space but instantaneous images show considerable patchiness. They reported that dilution at the jet impact point was higher than previously reported data. Downstream of the impact point, the flow became predominantly horizontal with a complex additional mixing process that results in ultimate dilutions considerably higher than the impact dilution. The flow was reported to be highly turbulent in the vicinity of the falling jet with large concentration fluctuations. These fluctuations decay with distance due to turbulence collapse under the influence of density stratification. The end of the mixing zone is defined by them as the location where the intensity of the concentration fluctuations falls to 0.05 (i.e. 5%) of their mean value (Fig. 2.11). Normalized expressions for dilution, rise height, and other properties were derived and experimental coefficients, which are also used in this thesis to compare the numerical results with, were presented from which the flow properties could be predicted.

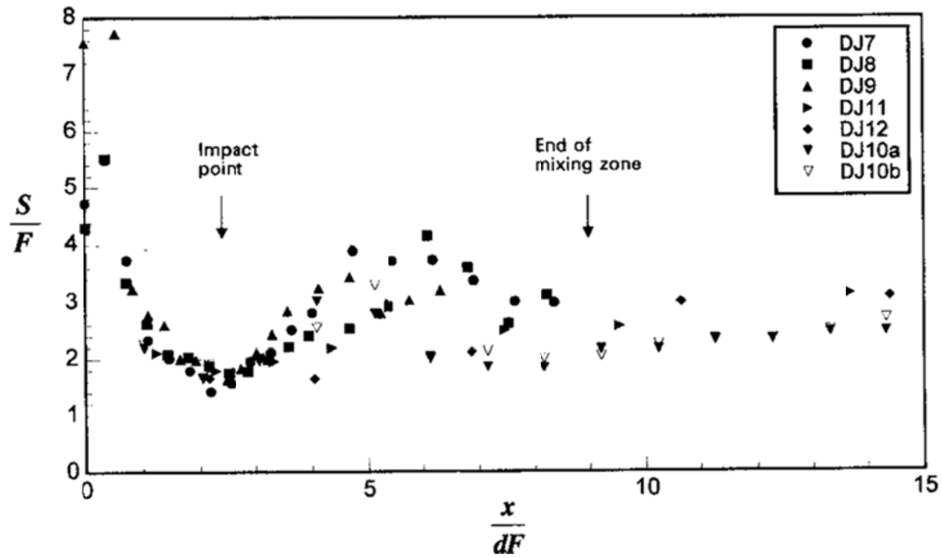

Fig. 2.11: Variation of lower boundary dilution with distance. From Roberts et al. (1997)

Cipolina et al. (2005) reported experimental data on the geometry of dense inclined jets issuing in a lab-scale glass rectangular tank. The surrounding fluid was always tap water at room temperature while the dense jets were water solutions of NaCl. Four parameters were changed in the experiments, namely nozzle diameter, inclination, jet density and flow rate. Jet trajectories were revealed by a colored tracer. Images of the jet were recorded by a digital camera and then further digitally processed, eventually resulting in a time-averaged tracer intensity field. All jet geometrical parameters, once normalized, were found to be very well correlated to the densimetric Froude number (Fig. 2.12). Moderate jet viscosity variations were found to not significantly affect jet behavior. The reported data allow a quick and easy estimation of maximum rise level, position of the trajectory maximum, and impact point distance of dense jets issued at different angles above the horizontal.

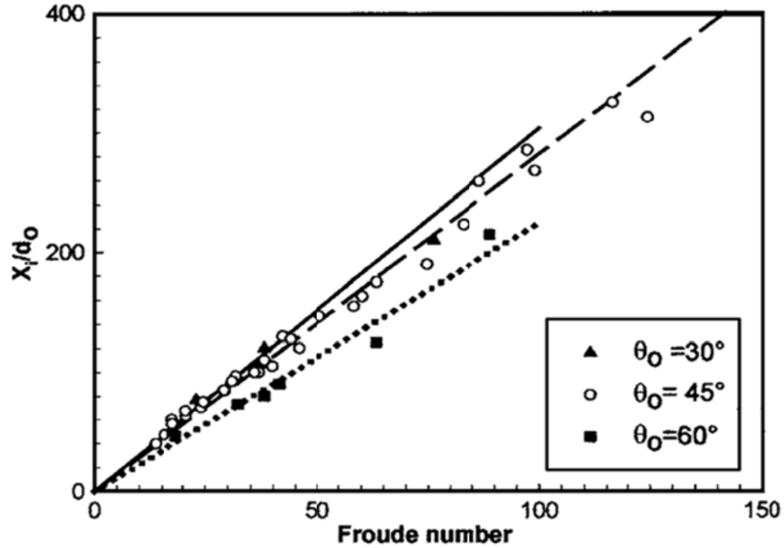

Fig. 2.12: Dimensionless impact point distance versus Froude number. From Cipolina et al. (2005)

Kikkert et al. (2007) developed analytical solutions to predict the behavior of inclined negatively buoyant discharges and these solutions were compared with data from previous studies and their own experiments, where Light Attenuation (LA) and Laser Induced Fluorescence (LIF) techniques were employed to study these flows (Fig. 2.13). Comparisons showed that the analytical solutions provide reasonable predictions of the flow path for initial discharge angles ranging from 25° to 90° and initial Froude numbers ranging from 14 to 99. The solutions also predicted the maximum height of the outer edge of the jet with reasonable accuracy, and thus the outer spread of the jet was well predicted. However, the inner spread was underestimated and minimum dilution predictions were shown to be conservative by approximately 18% at the centerline maximum height and 34% at the return or impact point. Predictions from the CorJet and VisJet numerical models were also shown to be conservative.

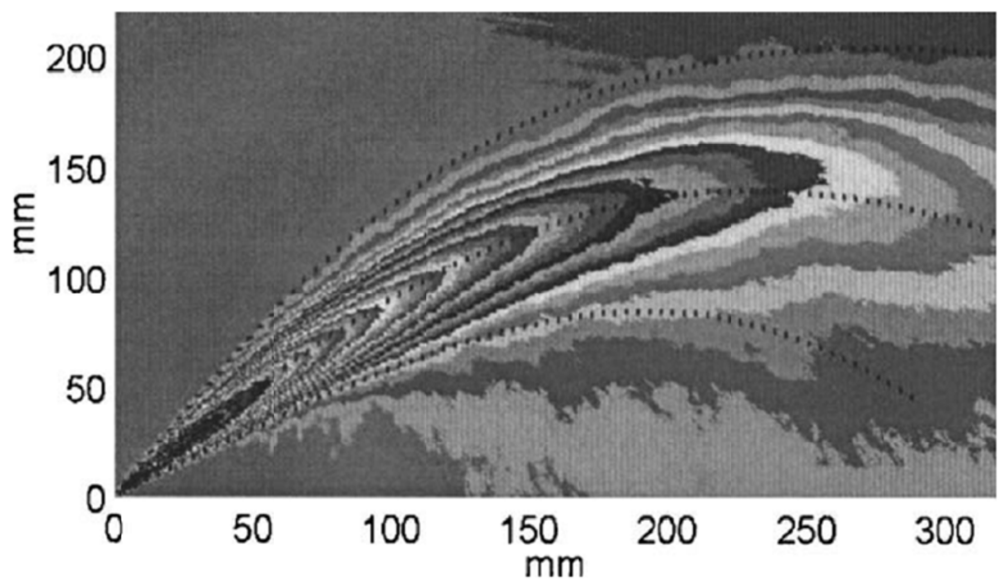

Fig. 2.13: Averaged LIF image showing the path and additional mixing associated with a negatively buoyant discharge. The dashed lines represent model predictions of the flow's path and spread. From Kikkert et al. (2007)

Modern, large capacity plants require submerged discharges, in the form of a negatively buoyant jet, that ensure a high dilution in order to minimize harmful impacts on the marine environment. Therefore, several researchers have focused on the inclined dense jets. Jirka's (2008) examination of laboratory data and the parametric application of a jet integral model suggested that flatter discharge angles of about 30° to 45° above horizontal may have considerable design advantages. These relate to better dilution levels at the impingement location, especially if the bottom slope and port height are taken into account, there is better offshore transport of the mixed effluent during weak ambient current conditions, and there is the ability to locate in more shallow water near shore.

Shao and Law (2010) performed a very comprehensive investigation on the mixing and trajectory characteristics of 30º and 45º inclined dense jets which is relevant for many coastal cities with shallow waters (10-20 m). 60° inclined dense jets had been recommended for brine discharges from desalination plants to achieve a maximum mixing efficiency. However, the terminal rise associated with 60° is relatively high and thus the angle may be too large for disposal in shallow coastal waters. Therefore, they investigated the mixing behavior of dense jets discharging at smaller angles of 30° and 45° in a stationary ambient (Fig. 2.14). Combined Particle Image Velocimetry (PIV) and Planar Laser Induced Fluorescence (PLIF) were used as the measurement approaches that captured the velocity and concentration fields, respectively. Based on the experimental results, the characteristic geometrical features of the inclined dense jets, including the location of the centerline peak and the return point where the dense jet returns to the source level, etc., were quantified. The mixing and diluting behaviors are also revealed through the analysis of the axial and cross-sectional velocity and concentration profiles. In addition to the free inclined discharges, their study also examined the effect of the proximity to the bed. Through the comparison of the results between two experimental series with distinct z_0/D but overlapping z_0/L_M, the latter was identified as the deciding factor for the boundary influence.

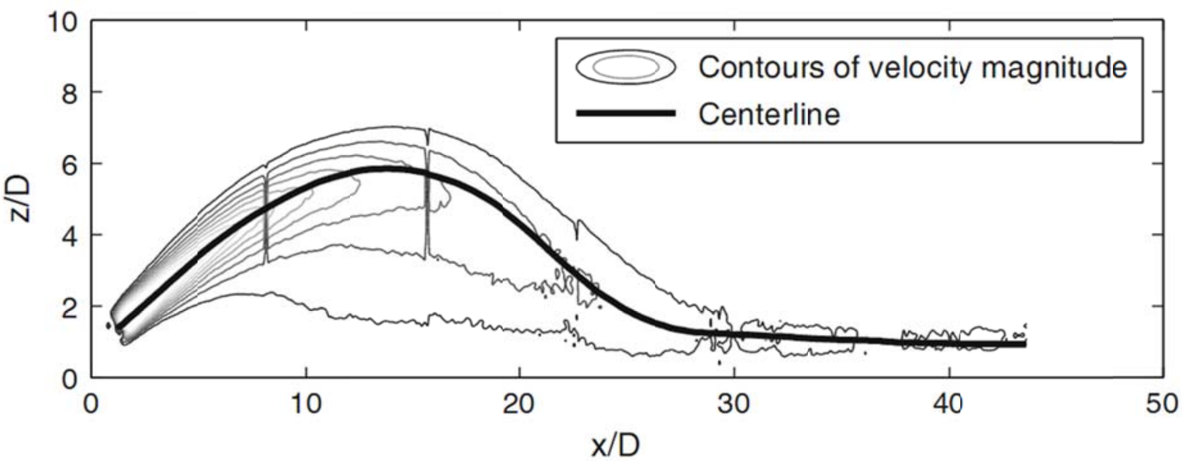

Fig. 2.14: Jet centerline trajectory. From Shao and Law (2010)

Papakostantis et al. (2011a, 2011b) presented experimental results on inclined turbulent round jets with negative buoyancy discharging in a calm homogeneous fluid. Six different discharge angles from 45° to 90° to the horizontal were studied, and the jet evolution was recorded by means of a video camera. Results concerned the main geometrical characteristics of the jet trajectory, i.e. the initial terminal height of rise reached by the jet at flow initiation, the final terminal height of rise observed at steady state (Fig. 2.15), the horizontal distance from the source at which the terminal height is observed and the horizontal distance to the point where the jet returns at the source elevation. The densimetric Froude number at the source ranged between 7 and 60, whereas the Reynolds number was generally higher than 6000. Results were given in dimensionless form and confirmed theoretical considerations obtained by dimensional analysis. Detailed measurements using a micro-scale conductivity probe were carried out at the horizontal location of the terminal rise height, mostly along the vertical direction of the axial jet plane and in the transverse direction. The dimensionless vertical distribution of the mean concentration was found to be asymmetric, whereas the transverse distribution was approximately Gaussian. They found that, at the same horizontal location, the vertical distribution of the concentration turbulent intensity has a maximum at a point systematically higher than the jet axis. The width of the mean concentration distribution, the heights to the location of the maximum mean concentration and to the maximum turbulent intensity as well as the minimum dilution were also determined in their study. From measurements in the region where the jet returns to the source elevation, the minimum dilution and the horizontal distance to the return point were estimated.

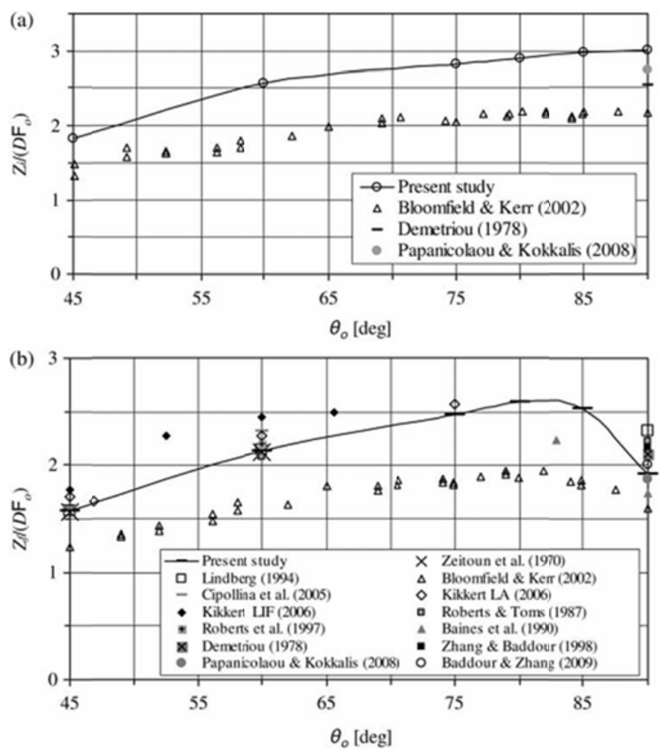

Fig. 2.15: Dimensionless (a) initial and (b) final terminal rise heights versus discharge angle Θ_0. From Papakostantis et al. (2011a)

Lai and Lee (2012) reported results of a comprehensive experimental investigation of inclined dense jets in an otherwise stagnant fluid. The tracer concentration field was measured for six jet discharge angles: θ = (15°, 30°, 38°, 45°, 52°, & 60°) and jet densimetric Froude number of $Fr = 10–40$ using the PLIF technique; selected jet velocity measurements were made using PIV. The detailed jet mixing characteristics and turbulence properties were presented. The direct velocity measurement revealed that the mixing is jet-like until the maximum rise. Empirical correlations for the maximum jet rise height, jet dilution at maximum rise, and impact dilution were also presented in their study. Both the time-mean concentration (Fig. 2.16) and intermittency showed that the upper jet edge spreading is similar to a positively buoyant jet; at the lower edge the buoyant instability induces significant detrainment and mass outflux for $\theta > 15°$. The dimensionless maximum rise height $Z_{max}/(FrD)$ was found to be independent of source conditions for $Fr \geq 25$, and varied from 0.44 for $\theta = 15°$ to 2.08 for $\theta = 60°$. Dilution measurements at terminal rise showed the difference in dilution is small for $\theta = 38°–60°$ and the asymptotic dilution constant is $S_t/Fr = 0.45$. The impact dilution S_i was also found not to be sensitive to jet angle for $\theta = 38°–60°$ and can be expressed as $S_i/Fr = 1.06$ for $Fr \geq 20$.

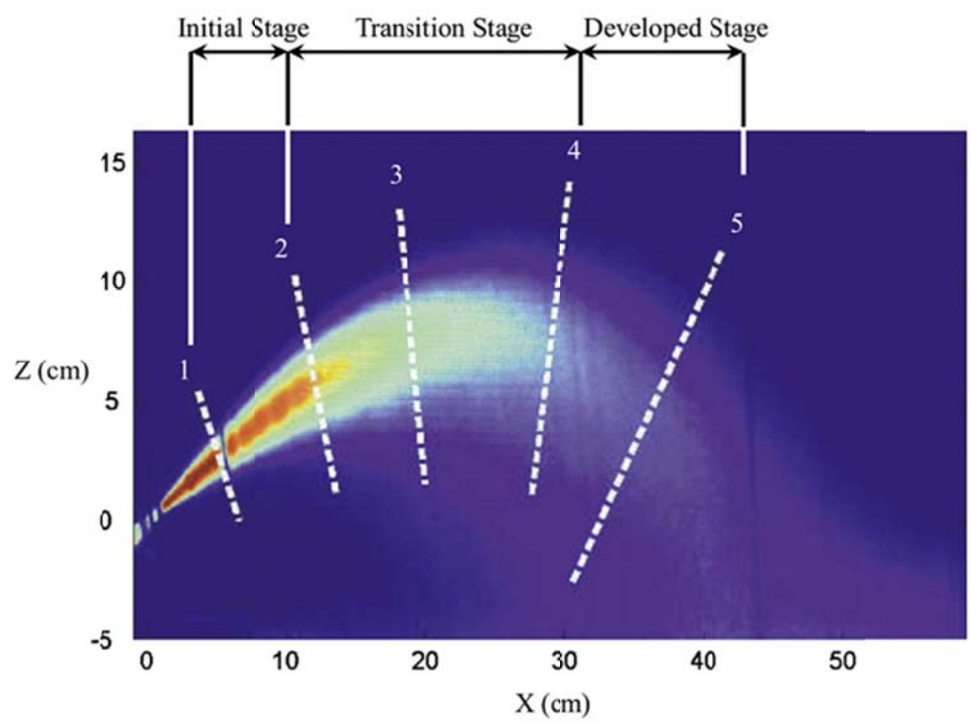

Fig. 2.16: Measured tracer concentration field of a 30° dense jet (Fr=21.8). From Lai and Lee (2012)

The Lagrangian jet model VISJET was also used in that study to interpret the experimental results. A detailed derivation for a general formulation of the entrainment coefficient was presented as well. Despite the observed detrainment, the trajectory and dilution were reasonably predicted; the maximum jet rise was under-predicted by 10–15% and associated dilution by 30% approximately. However, the predicted variation of jet behavior with discharge angle was in good agreement with measurements.

2.3.2 Numerical Studies

Experimental studies have been actively followed in this field, while numerical studies have very rarely been done for the dense inclined jets, and hence are still being pursued and need further investigation. Experimental research on the subject is limited with respect to the parameters and flow details studied. Vafeiadou et al. (2005) presented the results of numerical simulations of negatively buoyant jets issuing upwards at various angles. A 3-D numerical model, named CFX-5 (e.g. see ANSYS CFX-5, 2004), was employed to simulate the hydrodynamic and mixing characteristics of selected laboratory experiments (Vafeiadou, 2005). In particular, three experiments by Roberts et al. (1997) for an inclination angle of 30° to the vertical were reproduced using grid refinement near the nozzle and the bottom of the tank and a shear stress transport turbulence closure scheme. Further, the experiments were repeated for other angles of inclination, and the results were compared to those of Bloomfield and Kerr (2002). The numerical results were mostly found to be in agreement with the laboratory experiments. The initial terminal height of rise was seen to be larger than the final one by about 20% and both increase with increasing Froude number. The maximum final height of rise was found to occur at an inclination angle of about 10° to the vertical and in quantitative agreement with the experiments of Bloomfield and Kerr (2002). The computed initial height of rise did not change appreciably in the range of angles 0° to 20° and was close to the experimental results, although the latter showed a decrease with the angle of inclination. Their numerical model seems to underestimate slightly the height of rise and considerably the distance to the impact point observed by Roberts et al. (1997). The vertical distribution of velocity and concentration within the density current which forms on the bottom after the impact were obtained and presented. Overall, the numerical model was found to be a valuable tool for studying flow details and the behavior of dense jets beyond the range of available experimental data.

Elhaggag et al. (2011) conducted experimental and numerical investigations of the dense brine jets for disposal areas of limited extent. First, a new experimental model representing a section of sea floor with a single port brine outfall was built to study different characteristics of dense jets. Second, a number of numerical experiments have been conducted via Fluent CFD package to compare the numerical results with its corresponding physical observations and measurements. Experimental observations were made for both the terminal height of rise of dense jets discharged vertically from circular outlets into calm and homogeneous environment and for concentration profiles along the dense jet trajectory. Various combinations of port diameters and concentration of effluent salinities were investigated to cover a wide range of conditions. The experimental observations of concentrations along the dense jet trajectory were analyzed to quantify the mixing patterns for a given operating condition from the source point to the terminal rise height . The numerical model has been used to identify the penetration depth (Fig. 2.17) and also to get the temporal variation of the brine breakthrough curves at different locations above the disposal port. The numerical model has shown the existence of multi-peak breakthrough curves for the farthest points from the port (but the closest to the water free surface).

Fig. 2.17: Vertical jet penetration height. From Elhaggag et al. (2011)

Chapter III

Mathematical and Numerical Model

3.1 Introduction

Prediction of concentration/temperature transfer and fluid flow processes can be achieved by two main methods: experimental investigations and theoretical (analytical and/or numerical) modeling.

Even if reliable information about physical processes could only be obtained by measurements, experimental investigations involving full scale equipment are often very expensive. The alternative is therefore to use scaled models and conditions, and extrapolate their results to full scale. This scaling, however, is not completely free from errors: general rules for correct scaling are often unavailable, phenomena may not be scalable (i.e. turbulence, etc), measuring instruments errors may weight more.

Such problems can be avoided with the help of a mathematical model that would suitably represent the actual physical process. For fluid dynamics problems, the mathematical model often consists of a set of *Partial Differential Equations (PDEs)*. If classical mathematical techniques were to be used to solve such equations, there would be little hope of predicting many cases of practical interest with closed form solution. With the development of numerical methods and the availability of computers, closure can be found almost for most practical problems.

Furthermore, computer analysis offers several advantages compared to experimental investigations: low cost, high speed, complete and detailed information, and capability to simulate both real and ideal conditions. At the same time, numerical calculations have several disadvantages: a suitable mathematical model for describing the physical conditions may not be available, or numerical solution of the complex problems may sometimes be comparable in cost to experiments, model problems involving complex geometries, and strong non linearity may be more expensive to solve (Mangani 2010).

The starting point of a numerical method is the *Mathematical Model*, i.e. the set of PDEs and boundary conditions. Fluid dynamic science explains that exact conservation laws describe the behavior of all flows: no matter the type of flow, it will respect the general governing equations. General purpose methods however are often impractical, if not impossible, to solve. Therefore, it is more convenient to include simplifications in the mathematical model and develop a solution method designed for that particular set of equations. Then a suitable *Discretization Method*, approximating the set of differential equations by a system of algebraic equations for the variables at a number of discrete points in space and time, is necessary. The most important discretization methods are: *Finite Difference Method* (*FDM*), *Finite Volume Method* (*FVM*) and *Finite Element Method* (*FEM*). The discrete locations where the variables are to be calculated are defined by the *Numerical Grid*. The numerical grid is a discrete representation of the flow domain (both in space and time) through the use of a finite number of sub-domains such as elements, control volumes, etc.

Then a *Finite Approximation* technique has to be selected taking in consideration the choice for the discretization method and the numerical grid. This choice influences a lot the accuracy of the solution as well as the development, coding, debugging and the speed of the solution method. More accurate approximations involve, in fact, more nodes and give usually a fuller coefficient matrix. A compromise between accuracy and efficiency is always necessary. Once this large system of non-linear algebraic equations has been built by discretization techniques, it must be solved using a *Solution Method*. Such methods use successive linearization of the equations and the resulting linear systems are almost always solved by iterative techniques. Usually there are two levels of iterations: inner iterations, within which the linear equations are solved, and the outer iterations, that deal with the non linearity and coupling of the equations. As last point, it is important to determine suitable *Convergence Criteria*. It is fundamental to properly set stopping conditions for both the inner and the outer cycles in order to obtain accurate solution in an efficient way.

Once defined, numerical methods must be checked to posses certain properties in order to establish whether a method is appropriate or not. The most important properties are:

• *Consistency*: discretization should become exact as the grid spacing tends to zero. In other words truncation error, i.e. the difference between exact and discretized equation, must go to zero as $\Delta t \rightarrow 0$ and $\Delta x \rightarrow 0$.

• *Stability*: errors appearing in the course of numerical solution process do not magnify. For iterative methods, stable methods are the ones that do not diverge.

• *Convergence*: the solution of the discretized equation tends towards the exact solution as the grid spacing tends to zero. It is a difficult property to demonstrate, it is usually acceptable to test grid-independency for a solution.

• *Conservation*: solution must respect conservation of physical quantities both on local and global scale. It is a very important property because it limits solution error. Even if on fine grids non-conservative schemes can also lead to correct solutions, conservative ones are usually preferred.

• *Accuracy*: is the property of well approximating the exact solution, in other words limiting modeling, discretization and iteration errors.

3.2 Mathematical Model

In this section conservation equations of concentration, momentum and temperature for incompressible flows, are described.

Firstly, equations are derived in the most general form. The same approach has been used to obtain all the basic equations for fluid motion: apply the appropriate fundamental physical principle to a suitable model of the flow and then extract the mathematical equations which embody such physical principles. The fluid flow has been modeled with an infinitesimal control volume fixed in space with the fluid moving through it. As a consequence, equations are proposed in the differential conservation form. To switch from one form to another one must remember the concept of the substantial derivative:

$$\frac{d}{dt} = \frac{\partial}{\partial t} + \left(\vec{U}.\nabla\right) \tag{3.1}$$

meaning that the rate of increase of a scalar of fluid particle, on the left hand side of Eqn. (3.1), is equal to the rate of increase of fluid element plus the net rate of flow of the scalar out of fluid element, on the right hand side of the same equation (Anderson, 1995).

3.2.1 The Continuity Equation

The fundamental physical concept standing behind the continuity equation is that mass is conserved. In other words the rate of increase of mass in fluid element must equal the net rate of flow of mass into fluid element (Fig. 3.1) or the rate of change of mass in particle is equal to zero (Malalasekera and Versteeg, 1995):

$$\frac{dm}{dt} = 0 \tag{3.2}$$

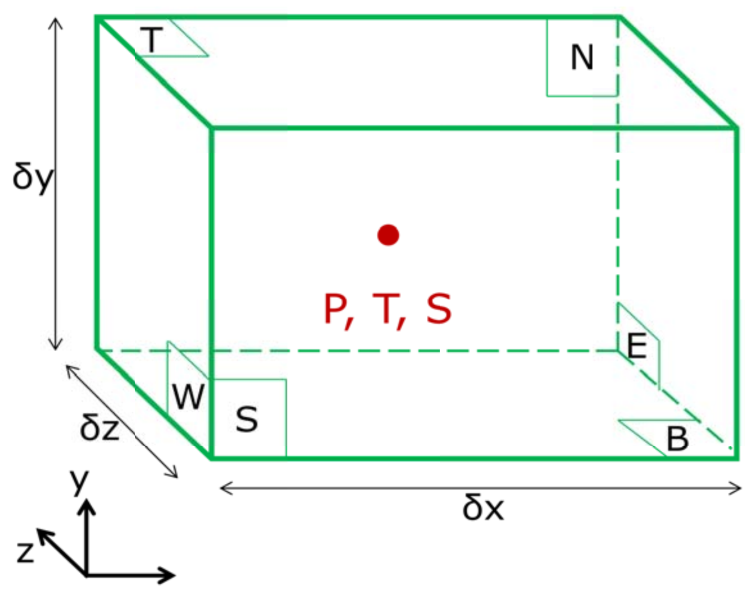

Fig. 3.1: Fluid element for conservation law. Reproduced from Malalasekera and Versteeg (1995)

Then, the well-known differential continuity equation is written as:

$$\nabla.\left(\rho\vec{U}\right) = 0 \tag{3.3}$$

which means:

$$\frac{\partial}{\partial x}(\rho u)+\frac{\partial}{\partial y}(\rho v)+\frac{\partial}{\partial z}(\rho w)=0 \tag{3.4}$$

The Navier-Stokes equations describe conservation of mass and momentum. For the purpose of this thesis, we limited the attention to incompressible fluids. This does not automatically mean that the fluid density is constant, but rather than it is independent of pressure *P*. The density may still vary due to other reasons, such as variation of temperature (T) and/or salinity (S):

$$\rho = f(S,T) \tag{3.5}$$

In this thesis, the density is calculated for both the jet and the ambient water according to the equation of state of seawater proposed by Millero and Poisson (1981):

$$\rho = \rho_t + AS + BS^{3/2} + CS \tag{3.6}$$

where

$$\begin{aligned} A &= 8.24493\times10^{-1} - 4.0899\times10^{-3}T + 7.6438\times10^{-5}T^2 - 8.2467\times10^{-7}T^3 + 5.3875\times10^{-9}T^4 \\ B &= -5.72466\times10^{-3} + 1.0227\times10^{-4}T - 1.6546\times10^{-6}T^2 \\ C &= 4.8314\times10^{-4} \end{aligned} \tag{3.7}$$

and ρ_t is the density of water that varies with the temperature as follows:

$$\begin{aligned} \rho_t &= 999.842594 + 6.793952\times10^{-2}T - 9.095290\times10^{-3}T^2 + \\ &1.001685\times10^{-4}T^3 - 1.120083\times10^{-6}T^4 + 6.536336\times10^{-9}T^5 \end{aligned} \tag{3.8}$$

3.2.2 The Momentum Equation

From Newton's second law, the momentum equation is defined as: the rate of increase of momentum of a fluid particle equals the sum of forces on the fluid particle. The equation for a three-dimensional system may be written as following:

$$\frac{\partial u}{\partial t}+u\frac{\partial u}{\partial x}+v\frac{\partial u}{\partial y}+w\frac{\partial u}{\partial z}=-\frac{1}{\rho}\frac{\partial P}{\partial x}+\frac{\partial}{\partial x}\left(\upsilon_{eff}\left(\frac{\partial u}{\partial x}\right)\right)+\frac{\partial}{\partial y}\left(\upsilon_{eff}\left(\frac{\partial u}{\partial y}\right)\right)+\frac{\partial}{\partial z}\left(\upsilon_{eff}\left(\frac{\partial u}{\partial z}\right)\right) \tag{3.9}$$

$$\frac{\partial v}{\partial t}+u\frac{\partial v}{\partial x}+v\frac{\partial v}{\partial y}+w\frac{\partial v}{\partial z}=-\frac{1}{\rho}\frac{\partial P}{\partial y}+\frac{\partial}{\partial x}\left(\upsilon_{eff}\left(\frac{\partial v}{\partial x}\right)\right)+\frac{\partial}{\partial y}\left(\upsilon_{eff}\left(\frac{\partial v}{\partial y}\right)\right)+\frac{\partial}{\partial z}\left(\upsilon_{eff}\left(\frac{\partial v}{\partial z}\right)\right)-g\frac{\rho-\rho_0}{\rho} \tag{3.10}$$

$$\frac{\partial w}{\partial t}+u\frac{\partial w}{\partial x}+v\frac{\partial w}{\partial y}+w\frac{\partial w}{\partial z}=-\frac{1}{\rho}\frac{\partial P}{\partial z}+\frac{\partial}{\partial x}\left(\upsilon_{eff}\left(\frac{\partial w}{\partial x}\right)\right)+\frac{\partial}{\partial y}\left(\upsilon_{eff}\left(\frac{\partial w}{\partial y}\right)\right)+\frac{\partial}{\partial z}\left(\upsilon_{eff}\left(\frac{\partial w}{\partial z}\right)\right) \tag{3.11}$$

where *u, v, w* are the mean velocity components in the *x, y, z* direction, respectively, *t* is the time, *P* is the fluid pressure, υ_{eff} represents the effective kinematic viscosity ($\upsilon_{eff}=\upsilon_t+\upsilon$), υ_t is the turbulent kinematic viscosity, *g* is the gravity acceleration, ρ is the fluid density, and ρ_0 is the reference fluid density.

One should note that the equations are divided by density (ρ) and the buoyancy term is added to the momentum equation in vertical direction (*y*-coordinate) to account for variable density effects.

3.2.3 The Concentration/Temperature Equation

Advection-Diffusion equation is solved for transport of concentration/temperature in the system.

Temperature evolution is modeled using the advection-diffusion equation as:

$$\frac{\partial T}{\partial t}+u\frac{\partial T}{\partial x}+v\frac{\partial T}{\partial y}+w\frac{\partial T}{\partial z}=k_{eff}\left(\frac{\partial^2 T}{\partial x^2}+\frac{\partial^2 T}{\partial y^2}+\frac{\partial^2 T}{\partial z^2}\right) \tag{3.12}$$

with

$$k_{eff}=\frac{\upsilon_t}{\mathrm{Pr}_t}+\frac{\upsilon}{\mathrm{Pr}} \tag{3.13}$$

where *T* is the fluid temperature, k_{eff} is the heat transfer coefficient, *Pr* is the Prandtl number, and Pr_t is the turbulent Prandtl number. In the present study, it was numerically found that the results are not significantly sensitive to Pr_t and *Pr* within the range of (0.6-1). Thus, both coefficients were set to 1.0.

Concentration transport equation is like the temperature and is written as:

$$\frac{\partial C}{\partial t}+u\frac{\partial C}{\partial x}+v\frac{\partial C}{\partial y}+w\frac{\partial C}{\partial z}=D\left(\frac{\partial^2 C}{\partial x^2}+\frac{\partial^2 C}{\partial y^2}+\frac{\partial^2 C}{\partial z^2}\right) \tag{3.14}$$

where C is the fluid concentration (salinity, S), and D is the isotropic diffusion coefficient.

3.3 Discretization Approaches

After the physical mathematical model has been derived, the goal is to manipulate it in a form suitable for computer calculations. First step on this path regards the discretization of the equations. The main task of a discretization approach is to convert a partial differential equation, valid on the entire domain, into a set of discrete algebraic equation, one for every node considered. The value at the node is, of course, put in relation with neighbor nodes. The simultaneous satisfaction of all the equations in the set then give the numerical solution. The most popular discretization techniques are presented and discussed as follows (Anderson, 1995).

• **Finite Difference Method (FDM)** approximates conservation equations in differential form substituting partial derivatives via truncated Taylor series expansions or polynomial fitting. Even if, in principle, it can be applied to all types of grids, actual applications are limited to structured grids where grid lines are used as local coordinate lines. In such a way in fact, it is easy to obtain higher-order schemes. The biggest drawback of FDM is that it does not necessarily enforce conservation, consequently it is hard to get reliable simulations of complex geometries and the use is restricted to the simple ones.

• **Finite Volume Method (FVM)** works with the integral form of the conservation equations. Usually, the domain is divided into finite volumes whose centroid represent the calculation node. The grid just defines boundaries in between different volumes and need not to be related to any metrics. Interpolation is used to express variable values at the surface in terms of nodal values. This method is conservative by construction as long as surface integrals for volumes sharing the same face are equal for both of them. The disadvantage of

FVM in comparison with FDM is that building higher than second order schemes for 3D simulation is much more difficult due to the three levels of approximation introduced: interpolation, differentiation and integration. Because of its very physical approach, ease to be understood and implemented, FVM is the most widely used approach in fluid mechanics.

• **Finite Element Method (FEM)** may appear similar to FVM, the distinguishing feature is the weight function: conservation equations are multiplied by a weight function before being integrated. Solution is supposed to adhere within each volume to a shape function constructed from values at the corners of the elements. Such a hypothesis is substituted into the conservation equations whose derivative with respect to nodal value is set to zero to minimize the residual. The main advantage in using FEM is the ability in dealing with arbitrary geometries, while the main drawback, common to all integral methods, is that the resulting matrix may result not well structured meaning that efficient solving methods are difficult to implement.

3.3.1 Finite Volume Method

OpneFOAM which is used in this study is based on the FVM. As mentioned above, FVM is based on conservation equations in the integral form. To obtain such equations, integration over a finite volume must be performed. To better fix ideas, the generic conservation equation for a transported scalar *Φ* is written as following:

$$\int_S \overrightarrow{J_\Phi}.\vec{n}dS = \underbrace{\int_S \rho\Phi\left(\vec{U}.\vec{n}\right)dS}_{Convection} - \underbrace{\int_S \Gamma_\Phi\left(\nabla\Phi.\vec{n}\right)dS}_{Diffusion} + \underbrace{\int_\Omega q_\Phi d\Omega}_{Source} \tag{3.15}$$

Such an equation applies over each control volume and the entire domain as well, underlying once again the main feature of FVM: global conservation. To obtain an algebraic equation the three integrals must be approximated by quadrature formulae. A Typical bi-dimensional quadrilateral control volume is shown in Fig. 3.2.

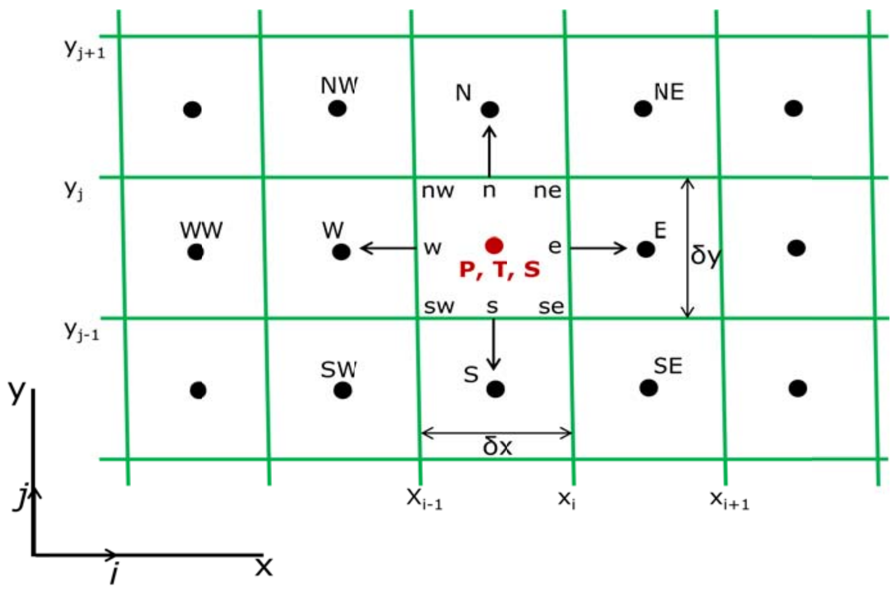

Fig. 3.2: Typical bi-dimensional quadrilateral control volume. Reproduced from Mangani (2010)

3.4 OpenFOAM

The OpenFOAM (**OPEN** **F**ield **O**peration **A**nd **M**anipulation) code is an object-oriented numerical simulation toolbox for continuum mechanics, written in C++ language, released by OpenCFD Ltd (http://www.openfoam.com) (OpenCFD, 2011). It is capable of supporting all typical features of C++ programming: it enables the construction of new types of data specific for the problem to be solved (i.e. a virtual class for turbulence model with virtual functions such as ε, k, μ_t, and etc.), the bundling of data and operations into hierarchical classes preventing accidental corruptions (i.e. a base class for storing mesh data and a derived class for acceding them), a natural syntax for user defined classes (i.e. operator overloading) and it easily permits the code re-use for equivalent operations on different types (i.e. templating) (Jasak, 1996; Jasak et al., 2004; Juretic, 2004).

The most important feature of OpenFOAM in assisting CFD programmers is that the toolbox implements operator-based implicit and explicit second and fourth-order Finite Volume (FV) discretization in three dimensional space and on curved surface.

Differential operators can be treated like finite volume calculus (fvc) or finite volume method (fvm) operators.

The first approach performs explicit derivatives returning a field while the second method is an implicit derivation converting the expression into matrix coefficients. The idea behind this is to think about partial differential equations in terms of a sum of single differential operators that can be discretized separately with different discretization schemes. Differential operators within OpenFOAM are defined as follows:

- $fvm::ddt = \frac{\partial}{\partial t}$,
- $fvm::d2dt2 = \frac{\partial^2}{\partial t^2}$,
- $fvm::div = \sum_i \frac{\partial}{\partial x_i}$,
- $fvm::laplacian = \sum_i \frac{\partial^2}{\partial x_i^2}$

In addition, implicit treatment of source terms is done by: *fvm:Sp* and *fvm:SuSp*. Explicit equivalent for the previous operators are defined and furthermore other common operators such as *curl*, *gradient*, etc, have been implemented.

Building different types of PDEs is now only a matter of combining the same set of basic differential operators in a different way. To give an example of the capability of such a top-level code, consider a standard equation like momentum conservation:

$$\frac{\partial \rho \vec{U}}{\partial t} + \nabla.\left(\rho \vec{U}\vec{U}\right) - \nabla.\left(\mu \nabla \vec{U}\right) = -\nabla p \tag{3.16}$$

It can be implemented in an astonishingly almost natural language which is ready to compile C++ source code:

```
  solve
(
    fvm::ddt(rho, U)
  + fvm::div(phi, U)
  -  fvm::laplacian(mu, U)
     ==
  -  fvc::grad(p)
 );
```

letting programmers concentrate their efforts more on the physics than on programming.

The above example clearly shows that OpenFOAM programmers do not think in terms of cells or faces but in terms of objects (*U*, *rho*, *phi*, etc) defined as a field of values, no matter what dimension, rank or size, over mesh elements such as points, edges, faces, etc. Just to fix the idea, for example the velocity field is defined at every cell centroid and boundary-face centers, with its given dimensions and the calculated values for each direction, and represented by just a single object *U* of the class *GeometricField*.

Important feature allowed by object programming is the dimensional check. Physical quantities objects are in fact constructed with a reference to their dimensions and thus only valid dimensional operations can be performed. Avoiding errors and permitting an easier understanding, come directly as a consequence of an easier debug.

OpenFOAM is flexible in defining new models and solvers in the simplest way, but it is not really a ready to use code. Its strength in fact stands in being open not only in terms of source code but, in its inner structure and hierarchical design, giving the user the opportunity to fully extend its capability. Moreover, the possibility of using top-level libraries containing a set of models for the same purpose which refer to the same interface, guarantees programmers for smooth and efficient integration with the built-in functionality.

Most of the selections necessary to set up calculations are done at runtime, meaning that options can change while the code is running. For further information about how to use and how to program OpenFOAM see (OpenFOAM programmers guide, 2011).

OpenFOAM consists of a library of efficient CFD related C++ modules. These features can be combined together to create “*Solvers*” and “*Utilities*”. The available features in OpenFOAM are listed in Appendix B.

3.5 Model Preparation

In the OpenFOAM tool-chain, it is possible to use an entirely Open Source Software (OSS) tool-chain, or a combination of OSS and commercial tools. Figs. 3.3 and 3.4 show the simulation process priority and the whole tool-chain of OpenFOAM, respectively.

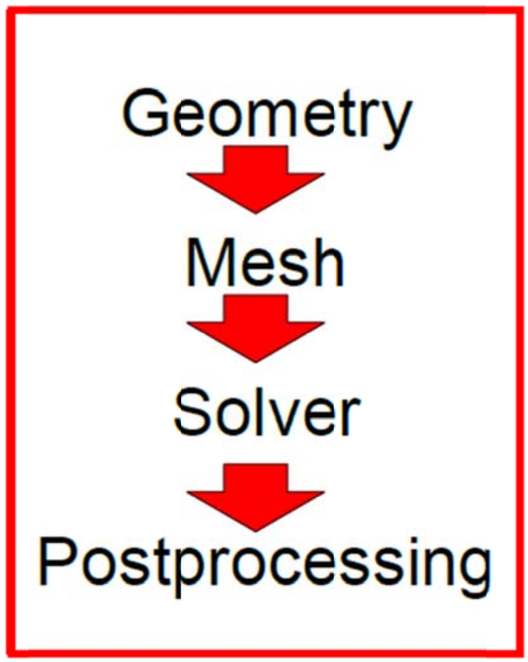

Fig. 3.3: Simulation process priority in OpenFOAM. From OpenFOAM (2011)

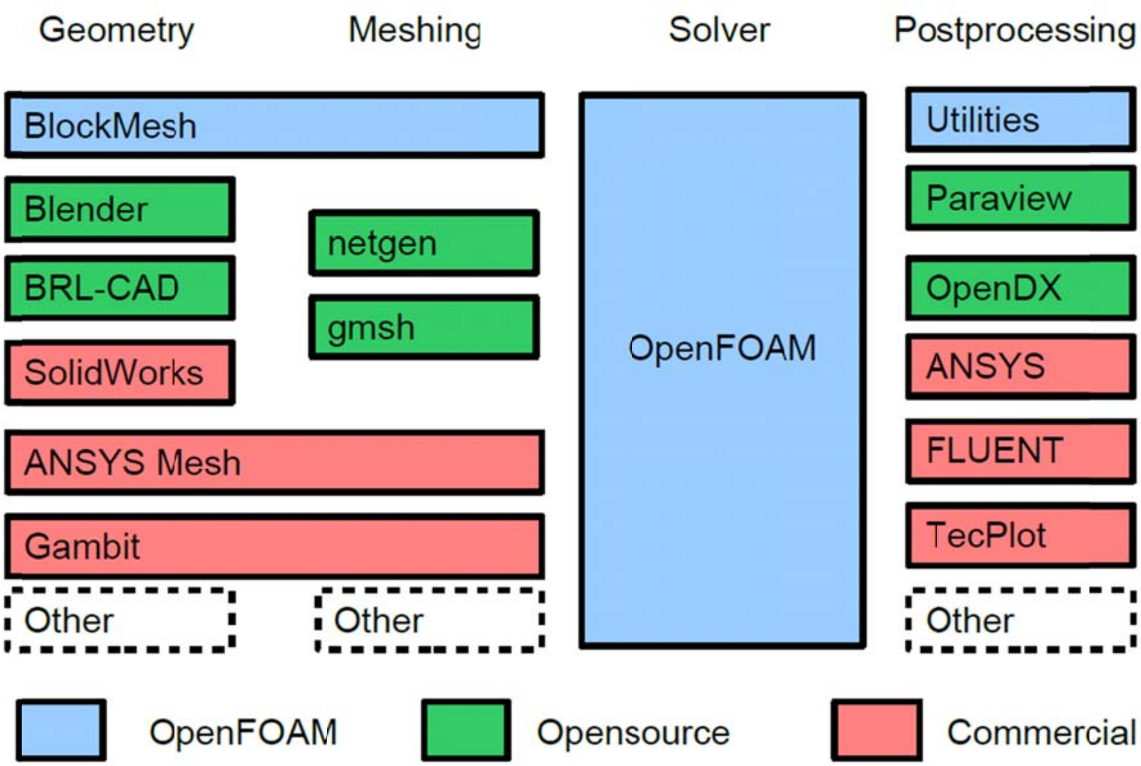

Fig. 3.4: OpenFOAM tool-chain. From OpenFOAM (2011)

The aim of this section is to explain how OpenFOAM existing applications are used in order to simulate the desired positively/negatively buoyant jets.

The preparation of the model is divided into two steps. The first step is to implement the required equations in the basic solver, which is explained in the next section . The second step is how to set up the case file and the input file, described in Appendix C.

3.5.1 Implementation of the Solver (*mypisoFoam*)

The governing equations are solved numerically using the finite volume method. The solver which is used within OpenFOAM is the modified *pisoFoam*. This solver is a transient solver for incompressible flow. The code first predicts the velocity field by solving the velocity equation (momentum equations). Although the continuity equation is presented, *pisoFoam* does not actually solve it; instead, it solves a pressure Poisson equation in PISO (Pressure-Implicit with Splitting of Operators). Rather than solve all of the coupled equations in a coupled or iterative sequential fashion, PISO splits the operators into an implicit predictor and multiple explicit corrector steps. At each time step, velocity, concentration and temperature are predicted, and then pressure and velocity are corrected. The velocity is predicted implicitly because of the greater stability of implicit methods, which means that a set of coupled linear equations, expressed in matrix-vector form as $Ax=b$, are solved. It then solves the concentration and temperature equations (Eqns. 3.12, 3.14). As in the velocity predictor, the concentration and temperature are predicted implicitly from Eqns. (3.12, 3.14).

In order to solve the equations, a new solver, called *mypisoFoam*, was developed and added to OpenFOAM. Here, the implementation of the momentum equation is shown in *mypisoFoam* solver as an example.

As explained before, each term in a PDE is represented in OpenFOAM code using the classes of static functions *finiteVolumeMethod* and *finiteVolumeCalculus*, shortened as *fvm* and *fvc*, respectively. *fvm* and *fvc* contain static functions, representing deferential operators that discretize the terms in the PDE.

Equations, and terms of equations are declared as *tmp<Type>* where *<Type>* is either *<fvVectorMatrix>* if the equation is a vector equation, like the momentum equation, or *<fvScalarMatrix>* if the equation is a scalar equation, like the ε-equation. The names indicate that the resulting discretized equations are stored as matrices.

The first part of the code for momentum equations (Eqns. 3.9-3.11) is to introduce a new definition of density that is a function of both temperature and salinity. The density calculation is based on Millero and Poisson (1981) as written in Eqns. (3.6-3.8).

```
rho==1000;
rho==(rho/1000*(999.842594+6.793952e-2*T-(9.095290e-3*pow(T,2))+
(1.001685e-4*pow(T,3))-(1.120083e-6*pow(T,4))+(6.536336e-9*pow(T,5))+
S*(8.24493e-1-4.0899e-3*T+(7.6438e-5*pow(T,2))-(8.2467e-7*pow(T,3))+
(5.3875e-9*pow(T,4)))+(pow(S,1.5))*(-5.72466e-3+1.0227e-4*T-1.6546e-6*pow(T,2))+S*(4.8314e-4)));
```

The second part of the *UEqn.H* implements the LHS of the momentum equations (Eqns. 3.9-3.11).

```
///
    fvVectorMatrix UEqn
    (
        fvm::ddt(U)
      + fvm::div(phi, U)
      + turbulence->divDevReff(U)
     - g*(rho-1000)/1000

    );
///
            UEqn.relax();
```

And finally the last part of the algorithm adds the RHS (which is equal to the pressure gradient) and solves the momentum equations.

```
if (momentumPredictor)
{
    solve(UEqn == -fvc::grad(p));
}
```

The PISO algorithm which is used in the *mypisoFoam* solver can be understood, for simplicity, by considering a one dimensional, inviscid flow along the *x*-direction. So the momentum equation is simplified to:

$$\frac{\partial u}{\partial t} + u\frac{\partial u}{\partial x} = -\frac{1}{\rho}\frac{\partial P}{\partial x} \tag{3.17}$$

By using the Euler implicit time stepping with linear interpolation of values to the cell faces and linearization of the convective term by taking the convective velocity from the old time step *n*, the discretized implicit velocity predictor forms the following equation:

$$[\frac{1}{\Delta t} + (\frac{u^n_{i+\frac{1}{2}} - u^n_{i-\frac{1}{2}}}{2\Delta x})]\Delta V u^*_i + (\frac{u^n_{i+\frac{1}{2}}}{2\Delta x})\Delta V u^*_{i+1} - (\frac{u^n_{i-\frac{1}{2}}}{2\Delta x})\Delta V u^*_{i-1} = \frac{u^n_i}{\Delta t}\Delta V - (\frac{1}{\rho}\frac{\partial P}{\partial x})^n_i \Delta V \tag{3.18}$$

where the predicted values are denoted by *. Notice that pressure is taken from the old time level *n* since it is yet unknown. Now, the cell volume ΔV can be divided out as follows to get the correct coefficient matrices and vectors that are used in the corrector step:

$$[\frac{1}{\Delta t}+(\frac{u^n_{i+\frac{1}{2}}-u^n_{i-\frac{1}{2}}}{2\Delta x})]u_i^* +(\frac{u^n_{i+\frac{1}{2}}}{2\Delta x})u_{i+1}^* -(\frac{u^n_{i-\frac{1}{2}}}{2\Delta x})u_{i-1}^* = \frac{u_i^n}{\Delta t}-(\frac{1}{\rho}\frac{\partial P}{\partial x})_i^n \qquad (3.19)$$

In vector form, this becomes:

$$Cu^* = r - \nabla P^n \qquad (3.20)$$

where C is the coefficient array multiplying the solution u^* vector and r is the right-hand side explicit terms. If the viscous and turbulent stress terms are included, they would modify the coefficient matrix C and would not change the general form of the matrix-vector equation. This equation can be changed to:

$$Au^* + H'u^* = r - \nabla P^n \qquad (3.21)$$

where A is diagonal matrix of C and H' is the off-diagonal matrix as A (i.e. $A+H'=C$). Using a matrix solver, the above equation is solved for the predicted velocity u^*.

Moreover, the discretized explicit velocity corrector is written as:

$$[\frac{1}{\Delta t}+(\frac{u^n_{i+\frac{1}{2}}-u^n_{i-\frac{1}{2}}}{2\Delta x})]u_i^{**} +(\frac{u^n_{i+\frac{1}{2}}}{2\Delta x})u_{i+1}^* -(\frac{u^n_{i-\frac{1}{2}}}{2\Delta x})u_{i-1}^* = \frac{u_i^n}{\Delta t}-(\frac{1}{\rho}\frac{\partial P}{\partial x})_i^* \qquad (3.22)$$

The first corrected velocity u^{**} is being solved from the predicted velocity u^*, old velocity u^n, and the first corrected pressure P^*. The problem is that the corrected pressure is still unknown. This equation can be expressed in matrix-vector form like in Eqn. (3.21):

$$Au^{**} + H'u^* = r - \nabla P^* \qquad (3.23)$$

Introducing $H=r-H'u^*$ and inverting A (which is easy since it is diagonal), Eqn. (3.23) becomes:

$$u^{**} = A^{-1}H - A^{-1}\nabla P^* \qquad (3.24)$$

The point of the corrector step is to make the corrected velocity field divergence free so that it adheres to the continuity equation. By applying the divergence to the above equation and recognizing that $\nabla u^{**} = 0$ due to the continuity equation yields a Poisson equation for the first corrected pressure:

$$\nabla^2 (A^{-1} p^*) = \nabla.(A^{-1} H) \qquad (3.25)$$

When the first corrected pressure p^* has been calculated, Eqn. (3.25) can be solved for the first corrected velocity u^{**}.

The higher correction steps might be applied using the same A matrix and H vector. The second correction step is also shown below:

$$\nabla^2 (A^{-1} p^{**}) = \nabla.(A^{-1} H) \qquad (3.26)$$

$$u^{***} = A^{-1} H - A^{-1} \nabla P^{**} \qquad (3.27)$$

where p^{**} and u^{***} are the second corrected pressure and velocity, respectively. This method works for the other implicit time stepping schemes, for instance Crank-Nicholson or second-order backward. Issa (1985) states that if a second order accurate time stepping scheme is used, then three corrector steps should be used to reduce the discretization error due to PISO algorithm to second-order (Issa, 1985).

The *mypisoFoam* solver just solves continuity and momentum equations, hence we added the advection-diffusion equation for concentration and temperature to this solver and compiled it to use for our case, as explained in the Appendix C.

3.6 Turbulence Modeling

A turbulent flow field is characterized by velocity fluctuations in all directions and has an in finite number of scales (degrees of freedom). Solving Navier-Stokes equations for a turbulent flow is usually impossible, because the equations are elliptic, nonlinear and coupled (pressure-velocity, temperature-velocity) thus require huge computing facilities.

When the flow is turbulent, the instantaneous variables may be decomposed as below:

$$U_i = \overline{U_i} + u_i \tag{3.28}$$

$$P = \overline{P} + p \tag{3.29}$$

The reader is reminded that the continuity and NS equations may be written as:

$$\frac{\partial \rho}{\partial t} + (\rho U_i)_{,i} = 0 \tag{3.30}$$

$$\frac{\partial \rho U_i}{\partial t} + \left(\rho U_i U_j\right)_{,j} = -P_{,i} + \left[\mu\left(U_{i,j} + U_{j,i} - \frac{2}{3}\delta_{i,j} U_{k,k}\right)\right]_{,j} \tag{3.31}$$

where *(.)*$_{,j}$ refers to derivation with respect to x_j. Since we are dealing with incompressible flows, the last term on the right hand side of above equation is neglected. Now, taking the average of the above equations leads to:

$$\frac{\partial \rho}{\partial t} + \left(\rho \overline{U_i}\right)_{,i} = 0 \tag{3.32}$$

$$\frac{\partial \rho \overline{U_i}}{\partial t} + \left(\rho \overline{U_i U_j}\right)_{,j} = -\overline{P}_{,i} + \left[\mu\left(\overline{U}_{i,j} + \overline{U}_{j,i}\right) - \rho \overline{u_i u_j}\right]_{,j} \tag{3.33}$$

where $\overline{u_i u_j}$ is the Reynolds stress tensor. The above equations are called Reynods-Averaged Navier Stokes (RANS) equations. The estimation of the Reynolds stress tensor may be performed using various turbulence models as explained below.

3.6.1. Different Turbulence Models

Turbulence models may be categorized into the following groups:

- *Algebraic models (Zero-equation models)*: An algebraic equation is used to compute a turbulent viscosity, often called eddy viscosity. The Reynolds stress tensor is then computed using an assumption which relates the Reynolds stress tensor to the velocity gradients and the turbulent viscosity. This assumption is called the Boussinesq assumption. Models which are based on a turbulent (eddy) viscosity are called eddy viscosity models.

- *One-equation models*: In these models a transport equation is solved for a turbulent quantity (usually the turbulent kinetic energy) and a second turbulent quantity (usually a turbulent length scale) is obtained from an algebraic expression. The turbulent viscosity is calculated from Boussinesq assumption.

- *Two-equation models*: These models fall into the class of eddy viscosity models. Two transport equations are derived which describe transport of two scalars, for example the turbulent kinetic energy *k* and its dissipation *ε*. The Reynolds stress tensor is then computed using an assumption which relates the Reynolds stress tensor to the velocity gradients and an eddy viscosity. The latter is obtained from the two transported scalars.

- *Reynolds stress models*: In these models, a transport equation is derived for the Reynolds tensor $\overline{u_i u_j}$. One transport equation has to be added for determining the length scale of the turbulence.

3.6.1.1 Boussinesq Assumption

The relationship between the Reynolds stresses and velocity gradients via the turbulent viscosity is named Boussinesq assumption which is written as

$$\left[\mu\left(\overline{U}_{i,j}+\overline{U}_{j,i}\right)-\left(\rho\overline{u_i u_j}\right)\right]_{,j}=\left[(\mu+\mu_t)\left(\overline{U}_{i,j}+\overline{U}_{j,i}\right)\right]_{,j} \tag{3.34}$$

or

$$\rho\overline{u_i u_j}=-(\mu_t)\left(\overline{U}_{i,j}+\overline{U}_{j,i}\right)+\tfrac{2}{3}\,\delta_{i,j}\rho_k \tag{3.35}$$

where the last term is equal to zero in incompressible flows.

3.6.1.2 Algebraic Models

In zero equation models an expression for the turbulent viscosity is needed. The dimension of ν_t is [m²/s]. A turbulent velocity scale U multiplied by a turbulent length scale l gives the correct dimension: $\nu_t \propto Ul$. This is reasonable, because these scales are responsible for most of the transport by turbulent diffusion. In an algebraic turbulence model, the velocity gradient is used as a velocity scale and a physical length is used as the length scale. In boundary layer-type of flow:

$$\nu_t = l_{mix}^2 \left| \frac{\partial U}{\partial y} \right| \tag{3.36}$$

where y is the coordinate normal to the wall, and l_{mix} is the mixing length, and the model is called the mixing length model. It is an old model and is rarely used in simulations. One problem with the model is that l_{mix} is unknown and must be determined. More modern algebraic models are the Baldwin-Lomax model (Baldwin and Lomax, 1978) and the Cebeci-Smith model (Cebeci and Smith, 1974) which are frequently used in aerodynamics.

3.6.1.3 One-Equation Models

A transport equation is usually solved for the turbulent kinetic energy in one-equation models. The unknown turbulent length scale is required which is usually obtained from an algebraic expression. This length scale is proportional to the thickness of the boundary layer or the width of a jet or a wake. Since it is not possible to find a general expression for an algebraic length scale, this model is not applicable to general flows. Two-equation models are used more frequently than zero and one-equation models as explained in the following.

3.6.1.4 Two-Equation Models

Several two-equation models have been proposed for turbulent flows. The most popular yet efficient model is the standard k- ε model which is briefly reviewed here.

3.6.1.4.1 The *k* Equation

When the Eqns. (3.28) and (3.29) are plugged in the NS equations, some terms are unknown, namely the production term, the turbulent diffusion term, and the dissipation term.

Using NS equations, after some algebraic manipulations, the following equation is obtained for the turbulent energy

$$\left(\rho\overline{U_j}k\right)_{,j} = -\rho\overline{u_i u_j}\overline{U_{i,j}} - \left[\overline{u_j p} + 0.5\overline{\rho u_j u_i u_i} - \mu k_j\right]_{,j} - \mu\overline{u_{i,j}u_{i,j}} \tag{3.37}$$

$$P_k = -\rho\overline{u_i u_j}\overline{U_{i,j}} = \mu_t\left(\overline{U_{i,j}} + \overline{U_{j,i}}\right)\overline{U_{i,j}} - \frac{2}{3}\rho k\overline{U_{i,i}} \tag{3.38}$$

It is commonly assumed that that k is diffused down the gradient, i.e from region of high k to regions of small k (Fourier's law for heat flux: heat is diffused from hot to cold regions). Therefore, the third term in Eqn. (3.37) may be written as:

$$0.5\,\overline{\rho u_j u_i u_i} = -\frac{\mu_t}{\sigma_k}k_{,j} \tag{3.39}$$

where σ_k is the turbulent Prandtl number for k.

The fifth term on the RHS of Eqn. (3.37) is the dissipation term:

$$\varepsilon \equiv v\overline{u_{i,j}u_{i,j}} \tag{3.40}$$

Therefore, the k equation is written as

$$\left(\rho\overline{U_j}k\right)_{,j} = \left[\left(\mu + \frac{\mu_t}{\sigma_k}\right)k,j\right]_{,j} + P_k - \rho\varepsilon \tag{3.41}$$

3.6.1.4.2 The Modeled *ε* Equation

An exact equation for the dissipation can be derived from the NS equation (Wilcox, 1993). However, the number of unknown terms is very large and they involve double correlations of fluctuating velocities, and gradients of fluctuating velocities and pressure. It is better to derive an ε equation based on physical reasoning. In the exact equation for ε, the production term includes, as in the k equation, turbulent quantities and velocity gradients. The production and dissipation of ε are assumed to be proportional to those of k as $c_{\varepsilon 1}\frac{\varepsilon}{k}P_k$ and $-c_{\varepsilon 2}\rho\frac{\varepsilon^2}{k}$, respectively. Thus the transport equation for the dissipation is written as

$$\left(\rho\overline{U_j\varepsilon}\right),j = \left[\left(\mu + \frac{\mu_t}{\sigma_\varepsilon}\right)\varepsilon,j\right],j + \frac{\varepsilon}{k}(c_{\varepsilon 1}P_k - c_{\varepsilon 2}\rho\varepsilon) \tag{3.42}$$

Several other two-equation turbulence models as well as Reynolds Stress Models (RSMs) are available in OpenFOAM, which are explained in the following chapters.

Chapter IV

Technical Paper I

Numerical Modeling of Turbulent Buoyant Wall Jets in Stationary Ambient Water

Abstract

The main focus of this study is on the near field flow and mixing characteristics of thermal wall jets. A numerical study of buoyant wall jets discharged from submerged outfalls (e.g., from desalination plants) has been conducted. The performance of different RANS (Reynolds-Averaged Navier-Stokes) turbulence models has been investigated and the standard k-ε, RNG k-ε, realizable k-ε and SST k-ω turbulence models have been studied using OpenFOAM model. The results of cling length, plume trajectory, temperature dilutions, and temperature and velocity profiles are compared to both available experimental and numerical data. It was found that the realizable k-ε model performs best among the four models chosen herein. According to the results from different simulations, the paper proposes corresponding relationships and comparative graphs which are helpful for a better understanding of buoyant wall jets.

Keywords: Outfall, Wall Jet, OpenFOAM, Cling Length, Temperature, Dilution, Velocity.

4.1 Introduction

Liquid wastes discharged from industrial outfalls are categorized in two major classes based on their density. One type is the effluent that has a higher density than the ambient water body. In this case the outfall jet has a tendency to sink as a negatively buoyant plume, shown in Fig. 4.1a. The second type is the effluent that has a lower density than the ambient water body and which is hence defined as a buoyant jet that causes the plume to rise as shown in Fig. 4.1b (e.g. Bleninger et al., 2009). This is, for instance, liquid waste discharged from

MSF (Multi Stage Flash) desalination plants that is high temperature water which is generated by the cooling systems of the plant. The latter is the type of jet studied in this paper.

When a buoyant jet is discharged into a marine environment, at a point remote from any boundary of the domain considered, it rises and mixes with the ambient fluid because of the turbulent flow generated by the presence of shear stresses that develop around the jet-ambient liquid interface. Nevertheless, if the effluent is discharged in touch with a solid horizontal boundary, it is subjected to the Coanda effect and clings to the floor for a while before the effect of buoyancy forces, which cause the jet to lift and rise away from this horizontal boundary (e.g. Foster and Parker, 1970) as

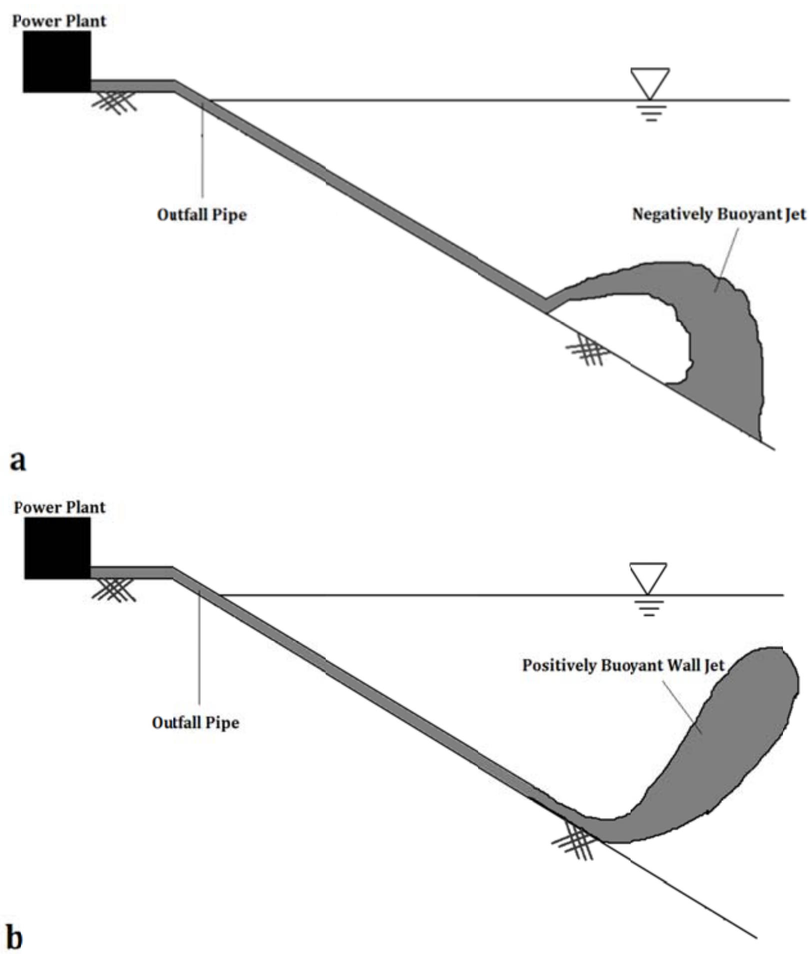

Fig. 4.1: Discharge strategies for power plant effluents. (a) Negatively buoyant discharge; higher density than ambient water. (b) Positively buoyant wall discharge; lower density than ambient water

shown in Fig. 4.2. Such a buoyant wall jet, is widely used in practice due to the ease of outfall construction, and has been extensively studied in the literature (e.g. Anwar, 1969).

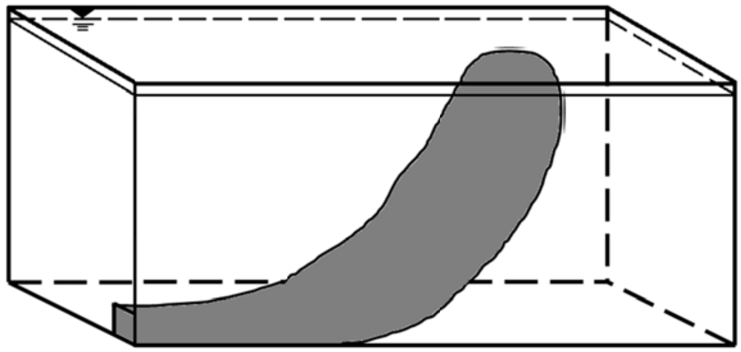

Fig. 4.2: A buoyant wall jet discharge

A large number of studies have been performed on buoyant jets (e.g. Sforza and Herbst, 1970; Rajaratnam and Pani, 1974; Balasubramanian and Jain, 1978 and Kuang and Lee, 2002). Sharp (1975, 1977) is one of the pioneers who considered submerged outfall of thermal effluents as a buoyant wall jet. His study focused on the properties of a buoyant jet discharged immediately above a horizontal surface. The jet behaved as a wall jet in the initial part of its trajectory; nonetheless after rising from the surface to which it initially clung, the jet acted as a normal free jet. Sobey et al. (1988) studied buoyant discharge in perhaps its most elementary geometry - a round buoyant jet discharging horizontally from a vertical side wall into a stationary water body on a flat-bed. Law and Herlina (2002) applied novel experimental equipment, a combination of Particle Image Velocimetry (PIV) and Plannar Laser Induced Fluorescence (PLIF) approach, in order to study a circular three-dimensional turbulent wall jet. More recently, Michas and Papanicolaou (2008) investigated horizontal, round turbulent buoyant jets that discharge into a homogeneous, calm ambient fluid.

All of the above-mentioned studies were conducted experimentally. However, numerical simulations on buoyant wall jets are still being studied and require further investigation. Maele and Merci (2006) applied standard and realizable k-ε turbulence models and examined different types of buoyant plumes. They found that the realizable k-ε model performs better for the cases considered. Kim and Cho (2006) investigated buoyant flow of heated water discharged from surface and submerged side outfalls in shallow and deep water with a cross flow. They used FLOW-3D which is a commercial CFD package and RNG k-ε model was applied for turbulence closure. Xiao et al. (2009) developed a fast non-Boussinesq integral model for the horizontal turbulent buoyant jets by using a CFD (Computational Fluid Dynamics) code named GASFLOW. Based on Sharps' experimental data (1975, 1977), recently, Huai et al. (2010) investigated horizontal buoyant wall jet numerically. They only applied one turbulence model, realizable k-ε, for their study. They presented results mainly for the near field and proposed some relationships between the distance and the dilution of velocity and temperature based on the numerical results.

It is now understood that the jet velocity distribution in the vertical cross section includes two different flow regions. The region between the wall and the level of the maximum velocity is defined as the boundary layer, while the region above that level is the free mixing area. The velocity scale for the streamwise (x-y) and spanwise (x-z) profiles is represented by the maximum streamwise velocity, U_{m0}. As shown in Fig. 4.3, the vertical length scale is taken as $y_{m/2}$ which is the point along the y-coordinate where the velocity has a value $U_{m0}/2$. The lateral length scale is also represented by $z_{m/2}$ which is defined similarly.

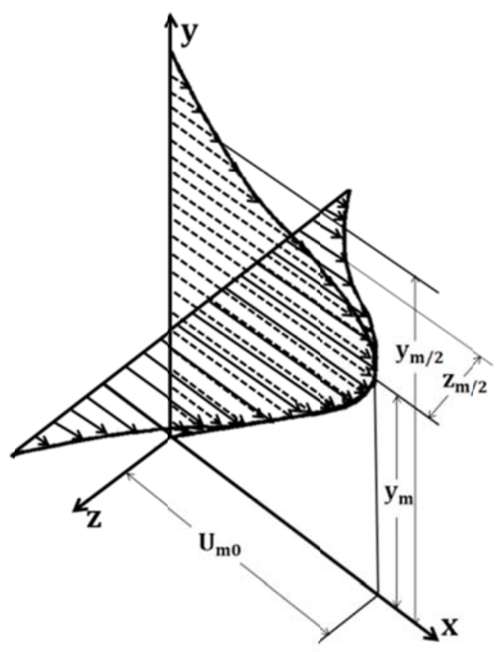

Fig. 4.3: A sketch of velocity structure

Existing studies on turbulent wall jets mainly focused on the flow kinematic behavior while mixing characteristics were rarely investigated. However, understanding of how a wall jet disperses is fundamental for buoyant wall jets. Hence, it would also be of interest to evaluate pollutant discharges in the form of jets moving close to a boundary. For instance, a simple way of effluent disposal is the direct release through a submerged pipe, with the pipe laid on the bottom for ease of construction as previously shown in Fig. 4.1.

4.2 Mathematical Formulation

4.2.1 Governing Equations

The governing equations are the well-known Navier-Stokes equations for three-dimensional, incompressible fluids as follows:

Continuity Equation:

$$\frac{\partial u}{\partial x}+\frac{\partial v}{\partial y}+\frac{\partial w}{\partial z}=0 \tag{4.1}$$

Momentum Equations:

$$\frac{\partial u}{\partial t}+u\frac{\partial u}{\partial x}+v\frac{\partial u}{\partial y}+w\frac{\partial u}{\partial z}=-\frac{1}{\rho}\frac{\partial P}{\partial x}+\frac{\partial}{\partial x}\left(\upsilon_{eff}\left(\frac{\partial u}{\partial x}\right)\right)+\frac{\partial}{\partial y}\left(\upsilon_{eff}\left(\frac{\partial u}{\partial y}\right)\right)+\frac{\partial}{\partial z}\left(\upsilon_{eff}\left(\frac{\partial u}{\partial z}\right)\right) \tag{4.2}$$

$$\frac{\partial v}{\partial t}+u\frac{\partial v}{\partial x}+v\frac{\partial v}{\partial y}+w\frac{\partial v}{\partial z}=-\frac{1}{\rho}\frac{\partial P}{\partial y}+\frac{\partial}{\partial x}\left(\upsilon_{eff}\left(\frac{\partial v}{\partial x}\right)\right)+\frac{\partial}{\partial y}\left(\upsilon_{eff}\left(\frac{\partial v}{\partial y}\right)\right)+\frac{\partial}{\partial z}\left(\upsilon_{eff}\left(\frac{\partial v}{\partial z}\right)\right)-g\frac{\rho-\rho_0}{\rho} \tag{4.3}$$

$$\frac{\partial w}{\partial t}+u\frac{\partial w}{\partial x}+v\frac{\partial w}{\partial y}+w\frac{\partial w}{\partial z}=-\frac{1}{\rho}\frac{\partial P}{\partial z}+\frac{\partial}{\partial x}\left(\upsilon_{eff}\left(\frac{\partial w}{\partial x}\right)\right)+\frac{\partial}{\partial y}\left(\upsilon_{eff}\left(\frac{\partial w}{\partial y}\right)\right)+\frac{\partial}{\partial z}\left(\upsilon_{eff}\left(\frac{\partial w}{\partial z}\right)\right) \tag{4.4}$$

where *u, v, w* are the mean velocity components in the *x, y, z* direction, respectively, *t* is the time, *P* is the fluid pressure, υ_{eff} represents the effective kinematic viscosity ($\upsilon_{eff}=\upsilon_t+\upsilon$), υ_t is the turbulent kinematic viscosity, *g* is the gravity acceleration, ρ is the fluid density, and ρ_0 is the reference fluid density.

One should note that the equations are divided by density (ρ) and the buoyancy term is added to the momentum equation in vertical direction (y-coordinate) to account for variable density effects.

Temperature evolution is modeled using the advection-diffusion equation as:

$$\frac{\partial T}{\partial t}+u\frac{\partial T}{\partial x}+v\frac{\partial T}{\partial y}+w\frac{\partial T}{\partial z}=k_{eff}\left(\frac{\partial^2 T}{\partial x^2}+\frac{\partial^2 T}{\partial y^2}+\frac{\partial^2 T}{\partial z^2}\right) \tag{4.5}$$

with

$$k_{eff}=\frac{\upsilon_t}{\mathrm{Pr}_t}+\frac{\upsilon}{\mathrm{Pr}} \tag{4.6}$$

where T is the fluid temperature, k_{eff} is the heat transfer coefficient, Pr is the Prandtl number, and Pr_t is the turbulent Prandtl number. In the present study, it was numerically found that the results are not significantly sensitive to Pr_t and Pr within the range of (0.6-1). Thus, both coefficients were set to 1.0.

4.2.2 Density Calculation

In the case of the buoyant wall jet released from submerged outfalls of industrial plants, the flow is characterized by several important parameters. The outfall diameter D, jet initial velocity U_0, jet initial density ρ_0, jet initial temperature T_0, and the densimetric Froude number F_d are the most important parameters of discharge. The densimetric Froude number is calculated as:

$$F_d=\frac{U_0}{\sqrt{g'D}}$$

(4.7)

$$g'=g\frac{\rho_a-\rho_0}{\rho_0} \tag{4.8}$$

The ambient water is assumed to have a temperature T_a which is less than that of the jet ($T_a<T_0$), while its density ρ_a is higher than that of the jet ($\rho_a>\rho_0$). In this paper, the density is calculated for both the jet and the ambient water according to the equation of state of seawater proposed by Millero and Poisson (1981):

$$\rho = \rho_t + AS + BS^{3/2} + CS \tag{4.9}$$

where

$$\begin{aligned} A &= 8.24493\times10^{-1} - 4.0899\times10^{-3}T + 7.6438\times10^{-5}T^2 - 8.2467\times10^{-7}T^3 + 5.3875\times10^{-9}T^4 \\ B &= -5.72466\times10^{-3} + 1.0227\times10^{-4}T - 1.6546\times10^{-6}T^2 \\ C &= 4.8314\times10^{-4} \end{aligned} \tag{4.10}$$

and ρ_t is the density of water that varies with the temperature as follows:

$$\begin{aligned} \rho_t &= 999.842594 + 6.793952\times10^{-2}T - 9.095290\times10^{-3}T^2 + \\ &1.001685\times10^{-4}T^3 - 1.120083\times10^{-6}T^4 + 6.536336\times10^{-9}T^5 \end{aligned} \tag{4.11}$$

Note that salinity (S) is not applicable for most thermal buoyant jets and temperature is the only factor that changes the density and is hence considered in this paper.

4.2.3 Computational Domain and Boundary Conditions

The sketch of the numerical model is shown in Fig. 4.4 with its coordinate system.

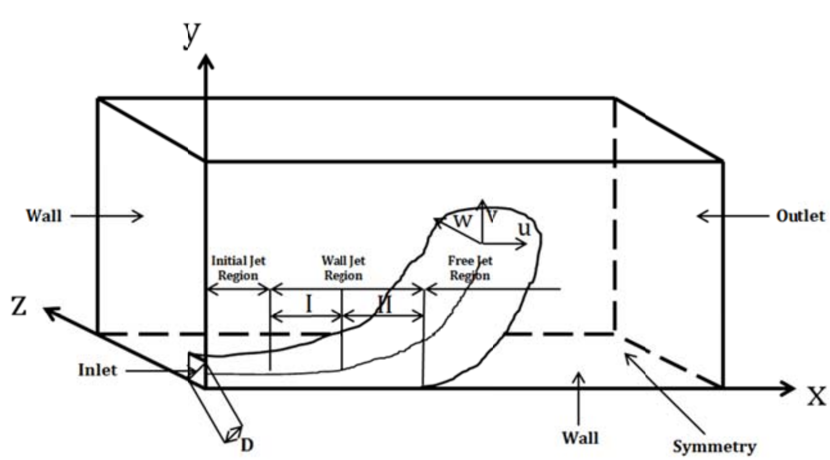

Fig. 4.4: Schematic view of the model and coordinate system

Only half of the wall jet domain is considered in this study due to the symmetry of the problem. The dimensions of the computational domain are chosen based on the available experimental setups. The numerical simulations were performed in a tank with dimensions of *2 m* length, *0.4 m* width, and *1.2 m* depth (Fig. 4.5a). A refined mesh is used for all simulations to better capture velocity and temperature characteristics in the near field zone (Fig. 4.5b). It is also noteworthy that the mesh independency tests are performed to get the best density for the mesh grid in more than five levels.

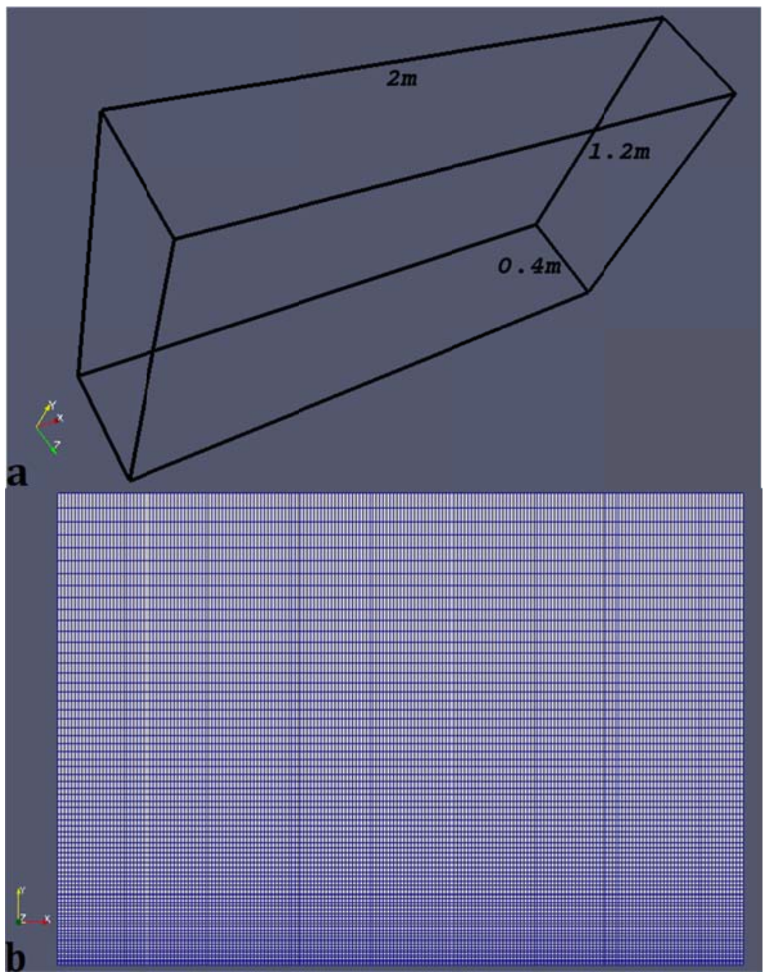

Fig. 4.5: Computational domain. (a) Domain dimensions of numerical model. (b) A refined mesh system (*x*-*y*)

For the inlet, as shown in Fig. 4.4, the boundary conditions are: $u=U_0$, $v=w=0$, $T=T_0$, $k=0.06u^2$, $\varepsilon=0.06u^3/D$, $\omega=\varepsilon/k$. The inlet values for k and ε are chosen based on Huai et al. (2010). Regarding the flow at the outlet section, a zero gradient boundary condition perpendicular to the outlet plane is defined for *u, v, w, k, ε, ω* and *T*. Moreover, for the wall boundaries, the standard wall functions are used for *k, ε* and *ω* and the no-slip condition is considered. Finally, the symmetry boundary was modeled using zero gradient conditions.

4.3 Turbulence Models

It is widely accepted among researchers in the field that no single turbulence model can be universally applied to all situations. Some considerations must be taken into account when choosing a turbulence model including: the physics encompassed in the flow, the level of accuracy and the computational resources available. In order to evaluate the performance of different turbulence models for buoyant jet discharges, four turbulence models are considered in this paper including (i) standard k-ε model, (ii) RNG (Renormalization Group) k-ε model, (iii) Realizable k-ε model and (iv) Shear Stress Transport (SST) k-ω model (see Appendix D).

The OpenFOAM CFD model (OPEN Field Operation And Manipulation) which is a free, open source software package produced by OpenCFD Ltd (2011), was used in simulations.

4.4 Numerical Algorithm

The governing equations are numerically solved using the finite volume method. The solver which is used within OpenFOAM is the modified *pisoFoam* (see OpenFOAM user and programmer guides, 2011). This solver is a transient solver for incompressible flow. The code first predicts the velocity field by solving the momentum equations. Pressure is then found by solving the Poisson equation in the Issa's PISO (Pressure-Implicit with Splitting of Operators) algorithm via an iterative process. Rather than solving all of the coupled equations in a coupled or iterative sequential fashion, PISO splits the operators into an implicit predictor and multiple explicit corrector steps. At each time step, velocity and temperature are predicted, and then pressure and velocity are corrected. The velocity is predicted implicitly because of the greater stability of implicit methods, which means that a set of coupled linear equations, expressed in matrix-vector form as $Ax=b$, are solved. More information about Issa's PISO algorithm can be found in references (e.g. Issa, 1985; Issa et al., 1986; Oliveira and Issa, 2001; Ferziger and Peric, 2002). The temperature equation (Eqn. 4.5) is then solved using the finite volume method.

The temporal term has been discretized by first order, implicit Euler scheme. The advection and diffusion terms are discretized by the standard finite volume method using Gaussian integration with a linear interpolation scheme for calculating values at face centers from cell centers.

For the pressure field, the PCG (Preconditioned Conjugate Gradient) method is used to solve the linear system. The PBiCG (Preconditioned Bi-Conjugate Gradient) method has been used for other fields, U, T, k, ε, and ω. In order to enhance the rate of convergence for iterative solvers, the DIC (Diagonal Incomplete Cholesky) pre-conditioner is used to calculate the pressure field. This is a simplified diagonal based pre-conditioner for symmetric matrices. The DILU (Diagonal Incomplete LU) pre-conditioner is used for the other fields, U, T, k, ε, and ω, which mostly include asymmetric matrices to be solved.

4.5 Results and Discussions

Three different cases have been numerically simulated. All four turbulence models have been applied to each case and the comparative results are presented. The characteristics of three cases are summarized in Table 4.1.

Table 4.1: Characteristics of the different simulated cases

Case	$D(mm)$	$U_0(m/s)$	$T_0(^oC)$	$\rho_0(kg/m^3)$	$T_a(^oC)$	$\rho_a(kg/m^3)$	F_d	Re_0
1	10.65	1.50	70	978.48	20	998.20	42.33	26101
2	12.58	0.55	90	970.41	4	999.97	11.61	11306
3	15.73	1.00	80	973.89	20	998.20	20.86	25705

4.5.1 Cling Length and Trajectory

As the fluid leaves the inlet which is attached to the horizontal wall, water entrainment occurs from all directions to the jet except for the wall region. This causes a lower pressure on the wall than at the top of the jet. This keeps the jet on the wall up to a point where the top suction pressure decreases and the buoyancy force becomes larger than the pressure difference. Therefore, the wall buoyant jets can be divided in three regions: (i) Initial Jet Region, (ii) Wall Jet Region and (iii) Free Jet Region. The Initial Jet Region is the distance from the inlet to the point where the velocity profile is almost uniform and equal to the maximum initial velocity. The Wall Jet Region itself is divided into two regions as explained in the following. The first region is the Wall Jet Region I which spans from the end of Initial Jet Region to the point where the jet centerline leaves the horizontal level and starts rising. Wall jet region II spans from the latter point to the point where the outer layer of jet leaves the floor. The Free Jet Region starts after the Wall Jet Region. These regions are shown in Fig. 4.4.

Cling length is often defined as the distance between the inlet and the position where the floor (wall) temperature has the condition of $(T-T_a)/(T_0-T_a)=3\%$ (e.g. Huai et al., 2010). The numerical results obtained for the cling length are presented in Fig. 4.6 and are compared with experimental and other numerical results. The axes are dimensionless and x axis represents the densimetric Froude number.

The results show good agreement with both the experimental and other researchers' numerical data. However, results show that for higher densimetric Froude numbers, the experimental cling length values obtained by Sharp (1977) are smaller than the numerical results published by Huai et al. (2010), and are more consistent with the numerical results obtained in the present study. The relationship between L/D and F_d for each turbulence model is given in Table 4.2. Sharp (1977) suggested the same relationship, $L/D=3.2F_d$.

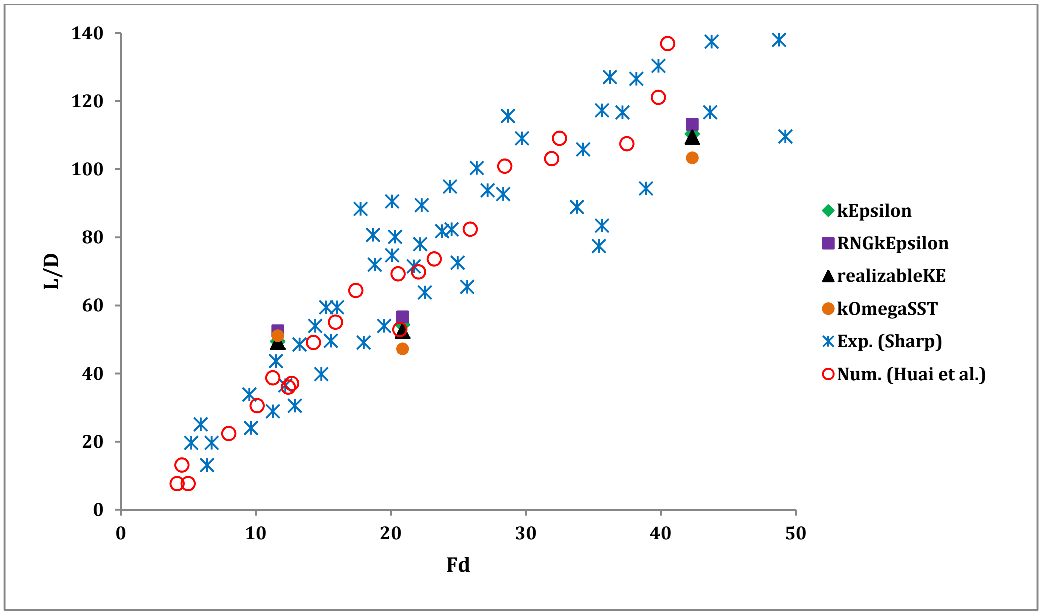

Fig. 4.6 : Comparison of experimental and numerical values of the cling length

Table 4.2: Cling length relationship according to the turbulence model used.

Turbulence Model	kEpsilon	RNGkEpsilon	realizableKE	kOmegaSST	Exp.
Cling Length	$L/D=2.70F_d$	$L/D=2.79F_d$	$L/D=2.71F_d$	$L/D=2.52F_d$	$L/D=3.20F_d$

As shown in Table 4.2, all the turbulence models have a smaller value for *L/D* than the experimental data. These values have been obtained from the trend line of each turbulence model. The cling length value for SST k-ω is the smallest one while the other models are close to each other. RNG k-ε is the closest one to experimental results.

Predicting the trajectory of jets is one of the key objectives in jet studies. This is also important in the design procedures for disposal outfalls since it provides the distance from the nozzle to where the jet reaches the water surface. This is critical, especially in regions with shallow water depths where depth is not enough to completely dilute the effluent. The trajectory of the two cases, as well as the results of several other studies are shown in the Fig. 4.7. The trajectory results obtained using the k-ε turbulence model category are much more accurate than the SST k-ω model. Except for the SST k-ω model, the results of this study are in better agreement with experimental data than the numerical results of Huai et al. (2010).

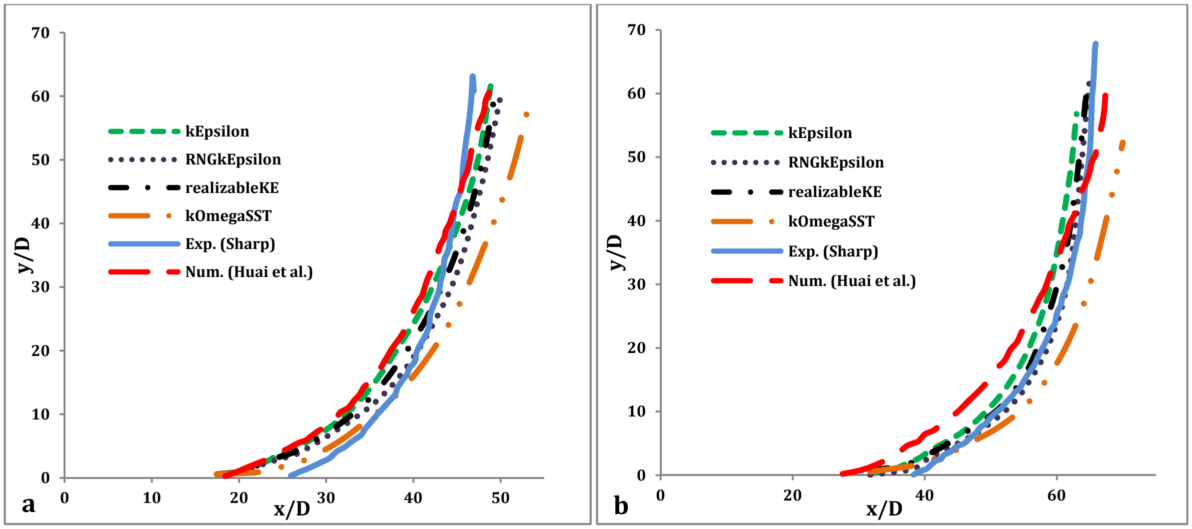

Fig. 4.7: Centerline trajectory. (a) Froude number about 12. (b) Froude number about 20.

4.5.2 Velocity Characteristics

4.5.2.1 Streamwise Velocity Profiles

The streamwise (*x*-*y*) velocity profiles along the centerline of the buoyant wall jet were extracted from different simulations. Since each case has four different sub-models itself (four turbulence models for each case), only the results for one case are presented in the following in most figures for brevity. The results of velocity field have been obtained along different jet sections in *x*-direction (different values of *x/D*) at the plane of symmetry. In Fig. 4.8, U_m is the velocity component in the x direction (along y at central plane), U_{m0} is the maximum of U_m values and its ordinate is y. Moreover, $y_{m/2}$ is the velocity-half-height which is the height of $U_m=U_{m0}/2$. On the abscissa and ordinate, U_{m0} and $y_{m/2}$ are taken as the velocity and length scales, respectively. All streamwise velocity profiles show self-similarity and are in good agreement with experimental results by Law and Herlina (2002) as seen in Fig. 4.8. Other previous studies such as Rajaratnam and Pani (1974), Padmanabham and Gowda (1991), and Abrahamsson et al. (1997) are also in agreement with the results showed in the Fig. 4.8. Verhoff's (1963) empirical equation, which is proposed for two-dimensional wall jet, is also in good agreement with the results obtained in the current study. The following equation was suggested by Verhoff:

$$\frac{U_m}{U_{m0}} = 1.48\left(\frac{y}{y_{m/2}}\right)^{1/7}\left[1 - erf\left(0.68\frac{y}{y_{m/2}}\right)\right] \tag{4.12}$$

From the existing agreement between Verhoff's formula, experimental and present study results, it can be concluded that there is no significant difference in velocity profiles between two-dimensional and three-dimensional wall jets at the symmetry plane (central plane).

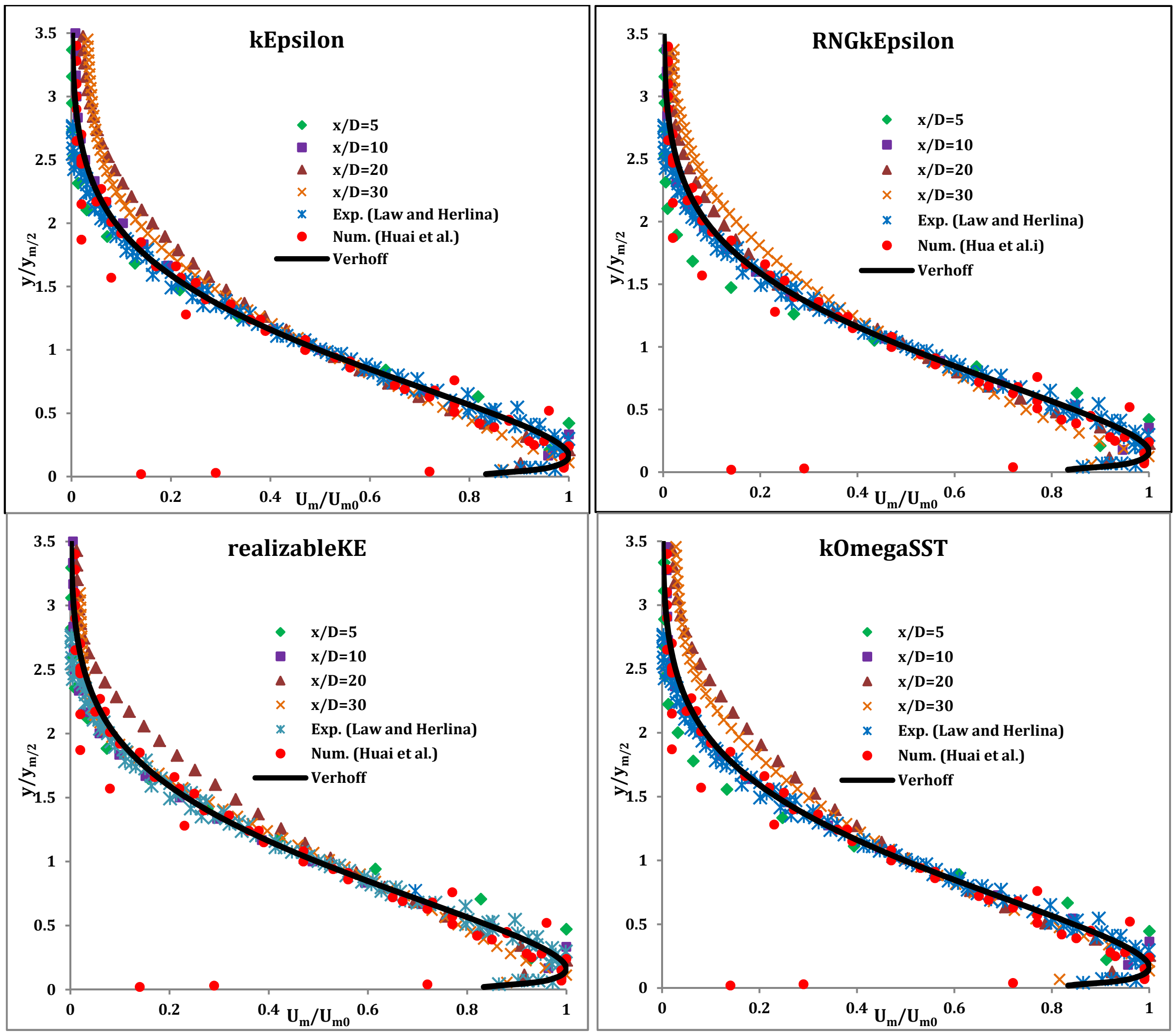

Fig. 4.8: Self similarity of streamwise velocity profiles for different turbulence models

Among different turbulence models' result shown in Fig. 4.8, the results of the SST k-ω model are not as accurate as those of the k-ε category models. On the other hand, RNG and realizable k-ε models' results are in better agreement with the experimental data and theory than the results of the standard k-ε model.

Fig. 4.9 also shows that the velocity profiles are independent of the Froude number. The results of the realizable k-ε model for all three cases show that the similarity profiles are consistent at the symmetry plane even though they have different trajectories.

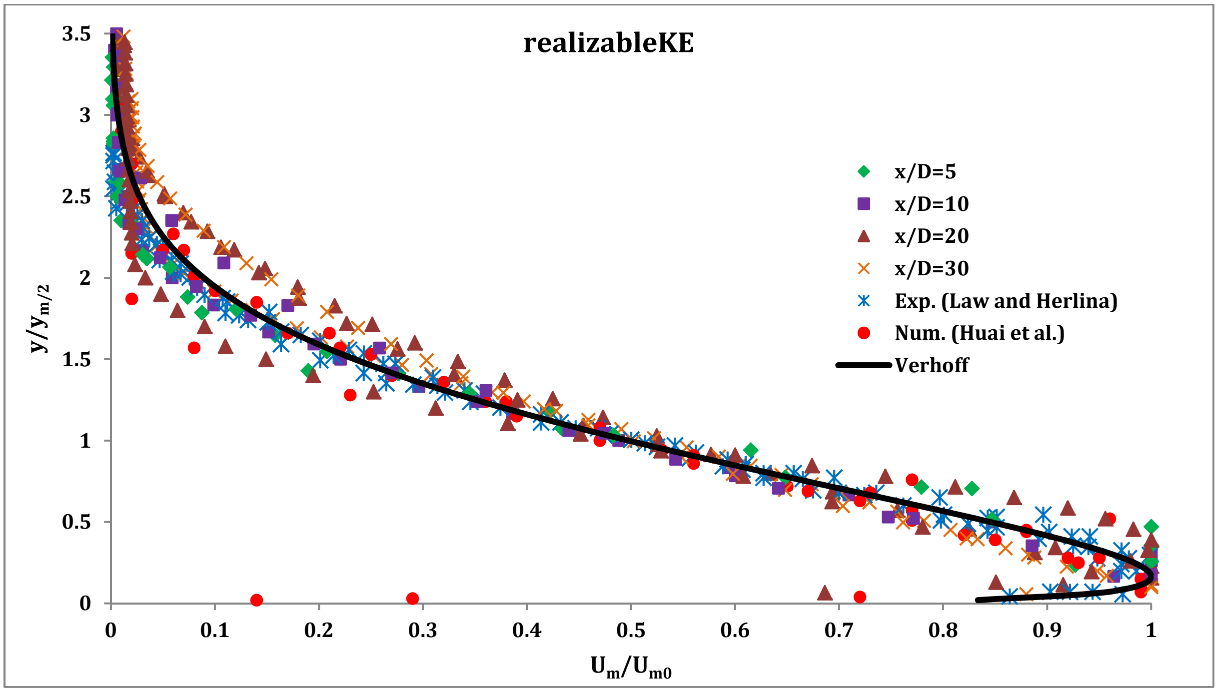

Fig. 4.9: Self similarity of streamwise velocity profiles for different cases

As seen in Figures 4.8 and 4.9, despite the slight scatter, the profiles exhibit a good similarity in different values of *x/D*. The deviation for larger values of *x/D* may be due to the buoyancy-induced distortion since these deviations mostly occur at higher elevations (i.e. $y/y_{m/2}>1$) where buoyancy dominates the flow.

The self-similarity of the velocity profiles at the central plane was extensively reported in the literature for both experimental and numerical studies. Nonetheless, results for offset measurement from the centerline were rarely presented. Law and Herlina (2002) reported experimental data for offset velocity profiles for the first time. They carried out measurements for two offset sections, *z/D=1.818* and *z/D=3.636*. The numerical results of this study as well as their experimental data are illustrated in Fig. 4.10 for the two above-mentioned sections. In this figure, $y_{m/2}$ and U_{ms} are the local length scale and maximum velocity for the offset section, respectively. As it is seen in this figure, the results for *z/D=3.636* in the area close to the inlet (*x/D=5* and *x/D=10*), are not in good agreement with Verhoff's curve and the scatters for the area after *x/D=10*. This is mainly because of the jet development in the width of the tank as shown in Fig. 4.11. When *z/D* is increased, the jet might not be developed yet at those *z* values and therefore the scatters get far away from the self-similarity profiles. It is also noteworthy that the results show some discrepancy in height, particularly for $y/y_{m/2}$ less than 1. However, these non-dimensional profiles obtained in this study are in reasonable agreement with both the experimental and Verhoff's results.

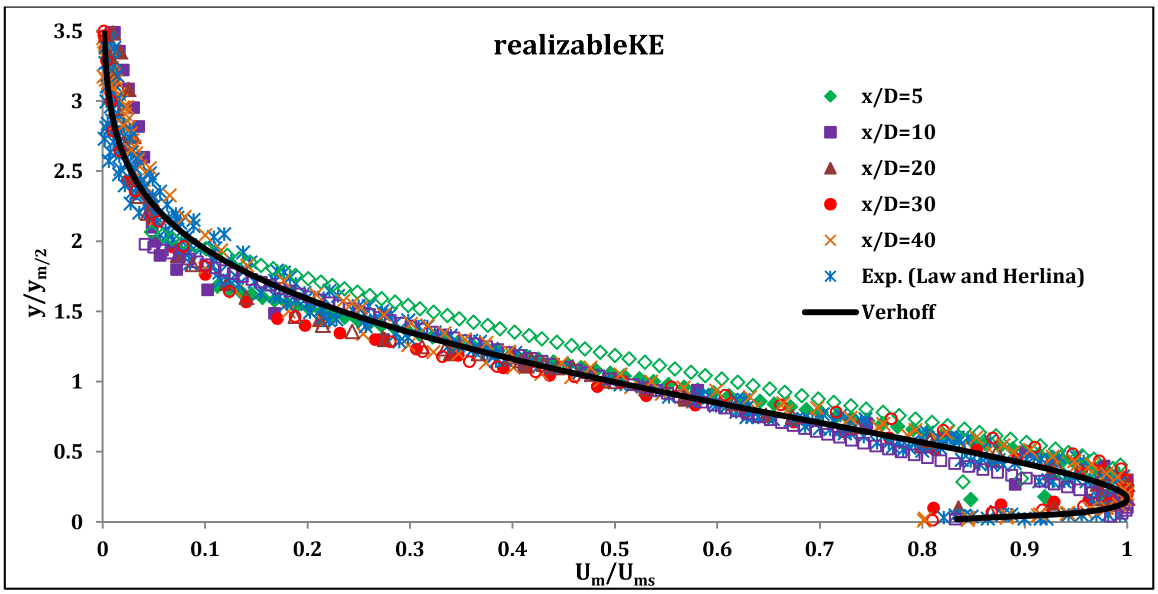

Fig. 4.10: Comparison of non-dimensional profiles for U at offset sections *z/D=1.818* and *3.636*. The solid fill scatters represent the cross section *z/D=1.818* and the no fill scatters show *z/D=3.636* at the same *x/D* values specified in the figure

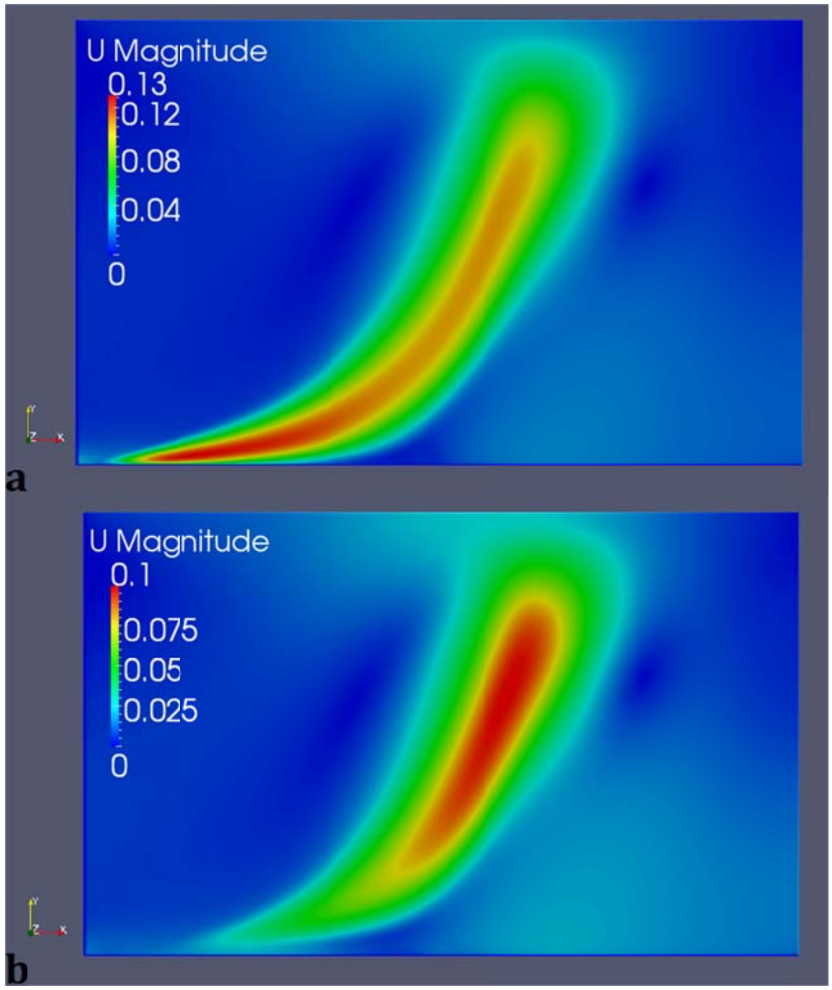

Fig. 4.11: Velocity contours at two offset sections. (a) $z/D=1.818$, (b) $z/D=3.636$

4.5.2.2 Spanwise Velocity Profiles

The spanwise velocity profiles were obtained at the height where the inlet centerline is located. This is the height at which the maximum values of the velocity and temperature are expected. The results for different turbulence models are shown in Fig. 12 where $z_{m/2}$ is the velocity-half-width corresponding to $U_m=U_{m0}/2$. The profiles at further downstream become more Gaussian with the maximum value at the centerline. They are also in better agreement with experimental data compared to the profiles from areas closer to the inlet. All turbulence models show better results than the results of the numerical model of Huai et al. (2010).

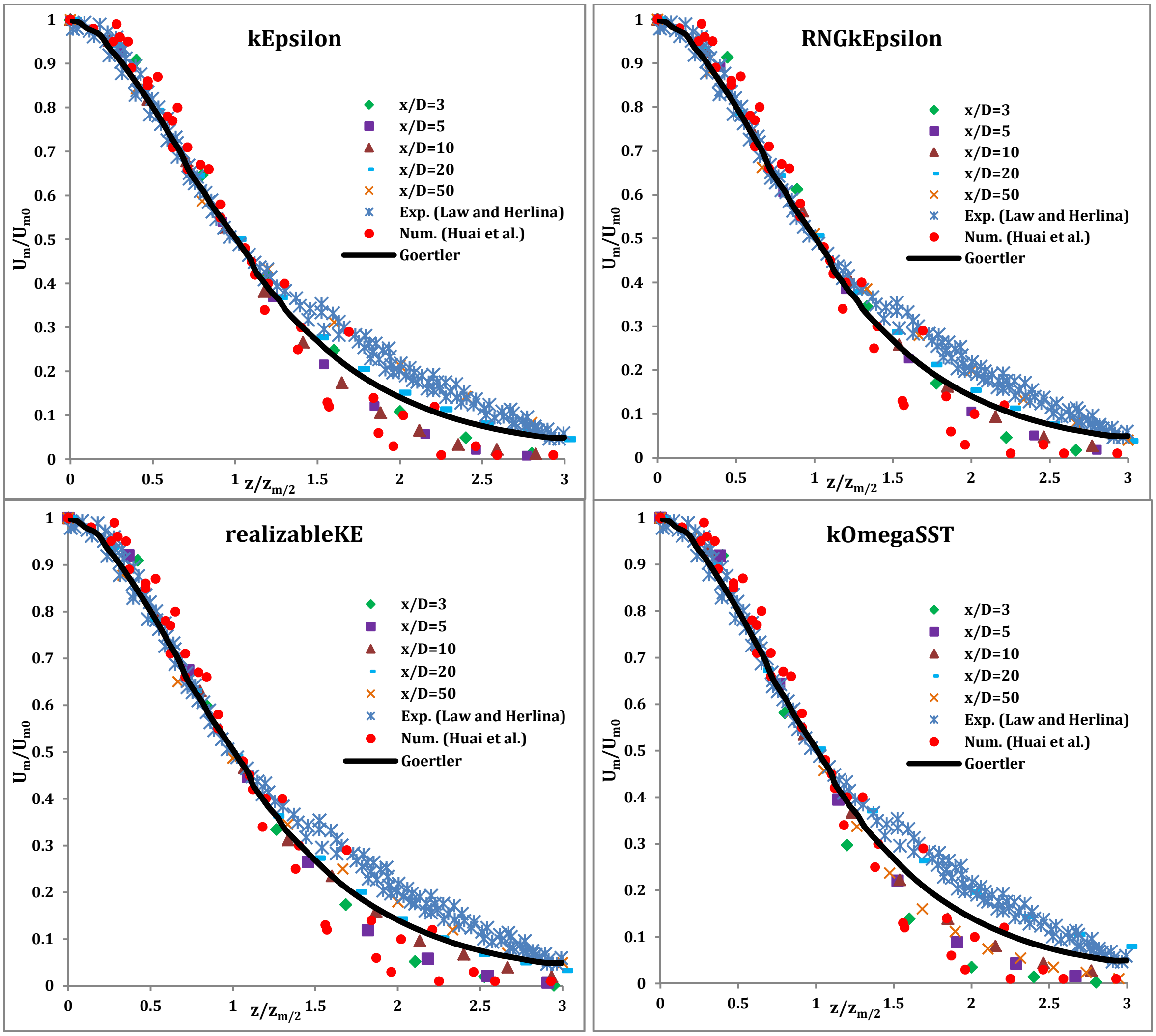

Fig. 4.12: Comparison of spanwise self-similarity of U profile at $y=y_m$ for different turbulence models

The Goertler solution for the free jet adapted from Schlichting (1979) is also shown in Fig. 12 with solid line. The Goertler solution is in a better agreement with the present study than the experimental data published by Law and Herlina (2002). Moreover, the other experimental measurements obtained by Rajaratnam and Pani (1974) and Padmanabham and Gowda (1991) showed very good agreement with the analytical solution proposed by Goertler and the results of this study. Similar to previous results presented herein, the SST k-ω model does not accurately predict and underestimates the velocity field. The results of k-ε category of turbulence models are close to each other and more accurate. It could be said that the RNG and the realizable models are slightly better than standard k-ε model especially for $z/z_{m/2}>1$. It was also observed that as streamwise profiles, the spanwise profiles are independent of the Froude number (not shown herein).

Fig. 4.13 shows the *w*-velocity distribution for one of the cases (case 3). The *w*-velocity distribution profiles also appear to be independent of Froude number. As shown in Fig. 4.13, the maximum value of the *w*-velocity component occurs near the plane of symmetry.

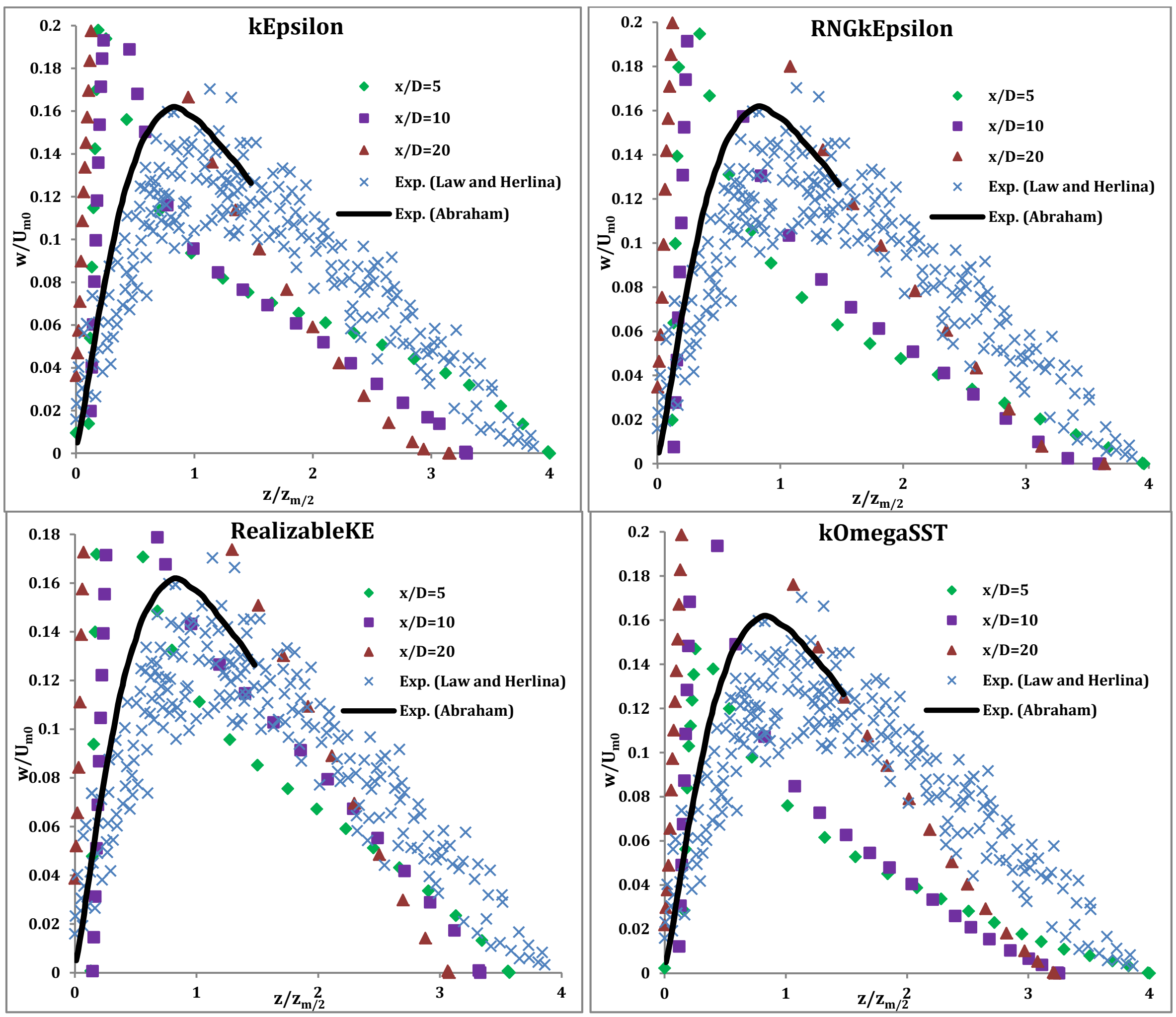

Fig. 4.13: Comparison of span wise *w*-velocity (velocity in *z* direction) profile at $y=y_m$

Villafruela et al. (2008) reported that *w*-velocity values increase from the plane of symmetry ($z=0$) to a maximum value approximately at $z=0.8z_{m/2}$. This is similar to the experimental results published by Abrahamsson et al. (1999). The maximum value for experimental results by Law and Herlina (2002) was reported to have occurred at the half-width of the wall jet. However, as shown in Fig. 4.13, the results of the current study are in a better agreement with those of Abrahamsson et al. (1999) rather than to those of Law and Herlina (2002). It should be noted that the present study results are similar to the experimental data for larger values of *x/D*. Again, the realizable k-ε model provides the most accurate results for the *w*-velocity distribution. Based on experimental data, Law and Herlina (2002), and Launder and Rodi (1981) inferred on the possibility of the formation of a secondary vortex, where the flow is directed away from the symmetry plane further away from the centerline.

4.5.2.3 Decay of Maximum Velocity

According to Sforza and Herbst (1970), longitudinal spreading of wall jet is divided into three regions based on the maximum velocity decay rate. These regions include: the potential core region, the characteristic decay region, and the radial-type decay region. Fig. 4.14 focuses on the third region which is farther away from the inlet. The velocity decay is almost linear in this region. The rate of decay along the plane of symmetry, between *20D* and *50D* is shown for four turbulence models.

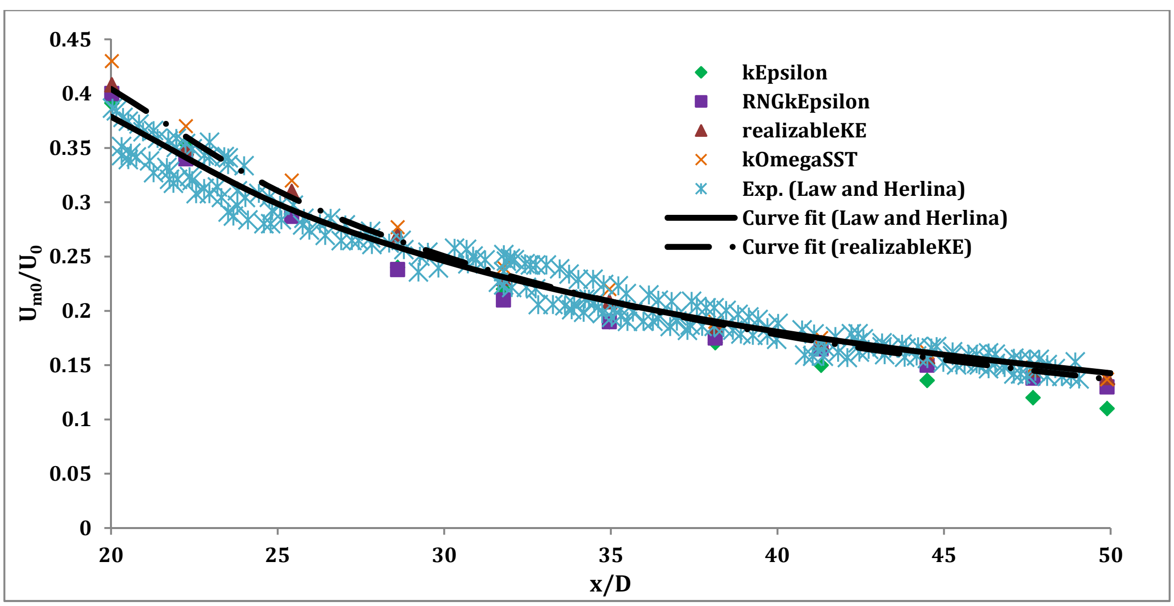

Fig. 4.14: Comparison of the maximum velocity decay: U_0 is the velocity at the inlet

The results of this study are in good agreement with the experimental results, especially for realizable k-ε turbulence model. The best curve fit for this model is shown in Fig. 4.14 which is close to the curve fit of experimental data and is formulated as follows:

$$\frac{U_{m0}}{U_0} = 13.99(\frac{x}{D})^{-1.183} \tag{4.13}$$

The best-fit curves for different studies and all the different turbulence models used are presented in Table 4.3. As shown, the results of numerical models are in good agreement with the results of almost all experimental studies, especially with those of Davis and Winarto (1980) and of Padmanabham and Gowda (1991).

Table 4.3: Summary of the present as well as previous investigations results for maximum velocity decay

Study	Stand. k-ε	RNG k-ε	realizable k-ε	SST k-ω	Law and Herlina (2002)	Sforza and Herbst (1970)	Newman et al. (1972)	Rajaratnam and Pani (1974)	Davis and winarto (1980)	Padm. and Gowda (1991)	Abrahamsson et al. (1997)
n	1.38	1.19	1.18	1.23	1.07	1.10	1.00	1.00	1.15	1.15	1.29
($U_{m0}=ax^{-n}$)										1.12	
										1.15	
										1.16	

4.5.3 Dilution and Temperature Characteristics

4.5.3.1 Dilution Characteristics

Dilution is related to the amount of water entrainment achieved by the jet. Dilution is defined as (e.g. Abessi et al., 2010; Huai et al., 2010)

$$S = \frac{T_0 - T_a}{T - T_a} \tag{4.14}$$

where T_0 is the initial jet temperature, T_a is the ambient water temperature, and T is the temperature at the computational mesh. Achieving higher dilution is the main purpose of outfall facilities.

Generally, when the jet is discharged, it behaves like a pure jet (called jet-like flow) for a while and, after passing a transient condition, which is named jet-to-plume-like flow, due to buoyancy forces, it behaves like a pure plume (called plume-like flow). Because of the high momentum force, the dilution in the jet-like region is less than in the other two regions. Water entrainment reaches the jet centerline at the end of the transient region and a higher dilution rate will subsequently occur.

Fig. 4.15 shows the temperature dilution values along the centerline at the plane of symmetry and at the cross section *y/D=35*. The results are in good agreement with the experimental data of Sharp (1975) for the lower Froude numbers that the experimental data is available for.

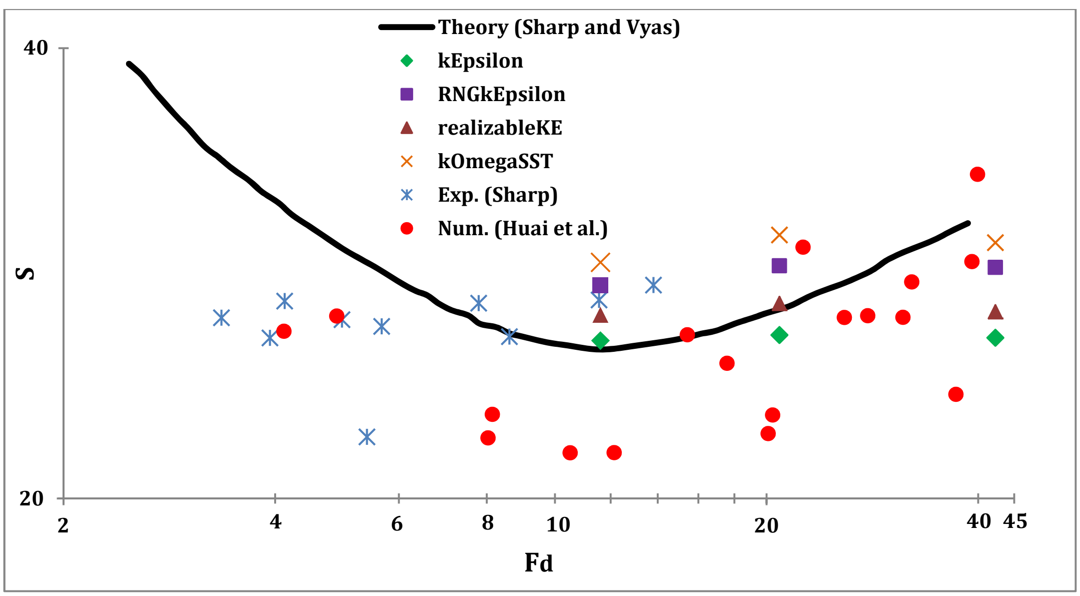

Fig. 4.15: Comparison of temperature dilution at the symmetry plane for different F_d numbers, *y/D=35*

At lower Froude numbers, the results of realizable k-ε are in good agreement with the theoretical solution proposed by Sharp and Vyas (1977). However, the results of current study underpredict the dilution rate for higher Froude numbers when compared to the results of the theoretical solution. Since experimental data are not available for higher Froude numbers, the numerical results of Huai et al. (2010) are used for comparison in that range. As shown in Fig. 4.15, the numerical results of Huai et al. (2010) are in good agreement with the present study for a Froude number of approximately 40.

Contours of temperature dilutions at the symmetry plane (*z=0*) are plotted in Fig. 4.16 for dilution values of *12, 15, 20, 30,* and *60*. The most inner layer represents *S=12* and the most outer layer corresponds to *S=60*. Fig. 4.16 shows that the dilution increases with the distance from the source and it depends on both the source (such as the inlet diameter *D,* densimetric Froude number F_d, etc), and the ambient water (such as the ambient water depth H_a, etc) characteristics. It can be inferred from Figs. 4.15 and 4.16 that the distance from the discharge source is more important in achieving higher dilution than Froude number.

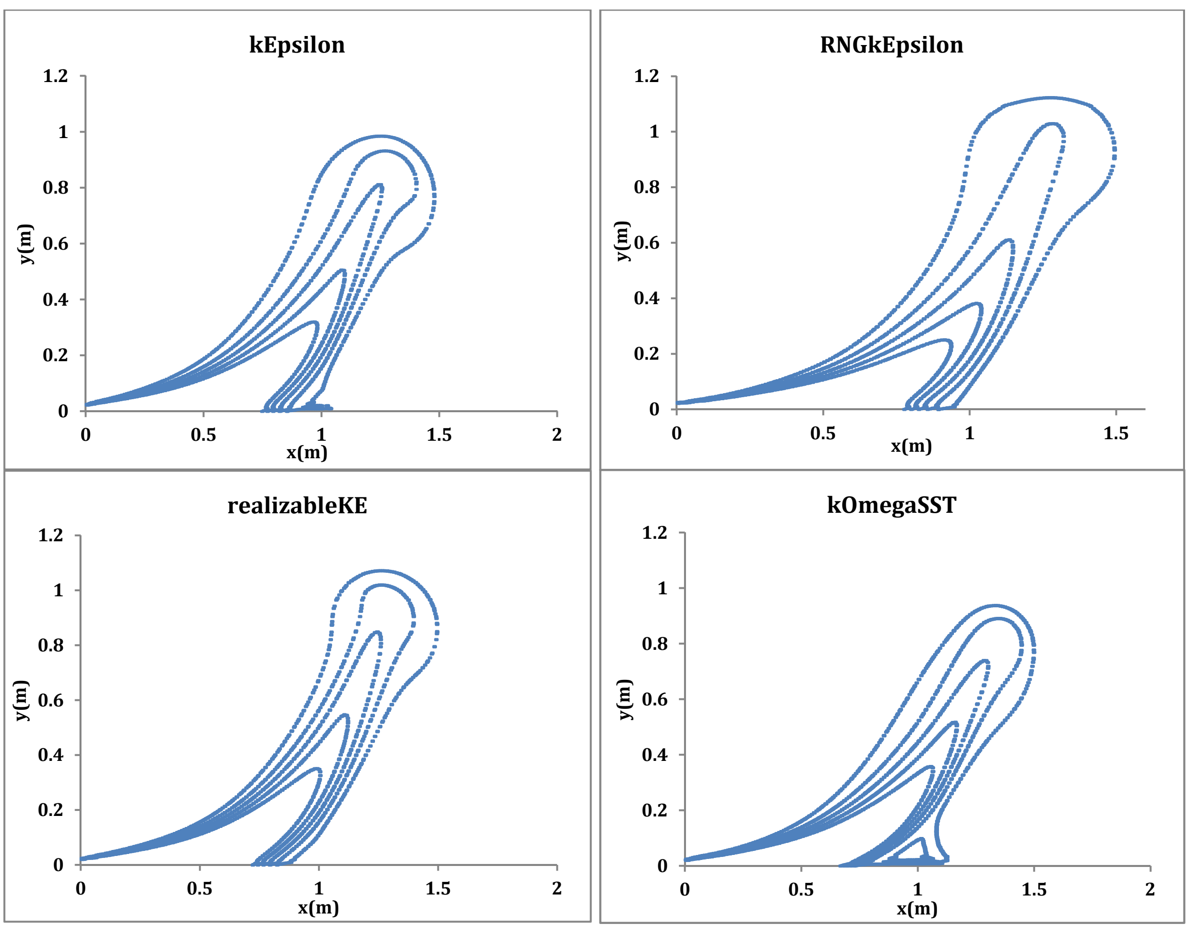

Fig. 4.16: Contours of temperature dilution at the symmetry plane for case 3. Dilution values are 12, 15, 20, 30, and 60 for each turbulence model

4.5.3.2 Streamwise Temperature Profiles

Dimensionless results for temperature profiles are presented in this section. The self-similarity temperature profiles along the centerline at the symmetry plane are shown in Fig. 4.17. As can be seen in this figure, the temperature decays exponentially from a maximum value T_m/T_{m0} at the floor to zero at a higher height. The results are normalized in both axes. T_m is the temperature along y section at the symmetry plane, T_{m0} the maximum temperature at the centerline along y, and $y_{tm/2}$ the temperature-half-height.

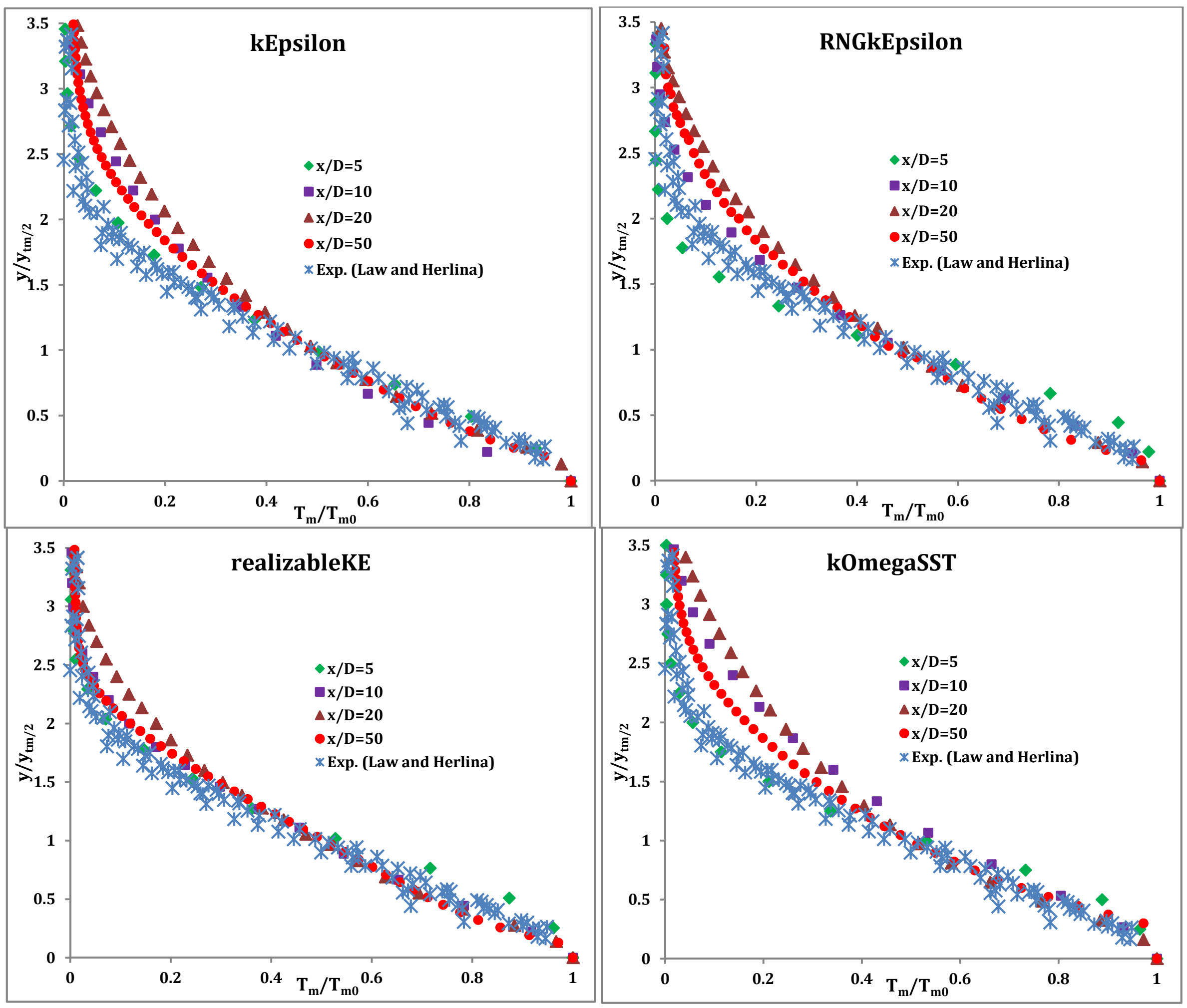

Fig. 4.17: Comparison of self similarity streamwise temperature profiles for different turbulence models

Generally, a Gaussian profile is assumed (e.g. Shao and Law, 2010) for the temperature distribution along the cross section at the central plane when the jet has entered the Zone of Established Flow (ZEF). As shown in Fig. 4.8, the general trend of all four turbulence models results follows the trend of the experimental data. Similar to the velocity field, for $1.5 \leq y/y_{tm/2} \leq 2.5$ and larger values of x/D, the temperature results of the present numerical study are higher than experimental results. One should note that, Law and Herlina (2002) measured concentration of a conservative tracer (rhodamine) to define their jet which likely contributed the discrepancies between model and experimental results in higher elevations. However, it is numerically found that the final jet density is important when jet properties are correlated to the densimetric Froude number regardless of the quota of temperature or/and concentration. Similar to the velocity profiles, the deviations for larger values of x/D are assumed reasonable due to the buoyancy forces that become more significant compared to momentum effects when the jet advances and starts rising up from the wall surface. However, the realizable k-ε model can be considered to have performed best among the selected turbulence models while the SST k-ω performed the worst.

As expected, the Gaussian shape of the temperature self-similarity profiles are the same for all three cases employing different Froude numbers. The results of the realizable k-ε model for three cases are shown in the Fig. 4.18. As shown in this figure, similar to the velocity profiles, temperature profiles appear to be independent of the Froude number.

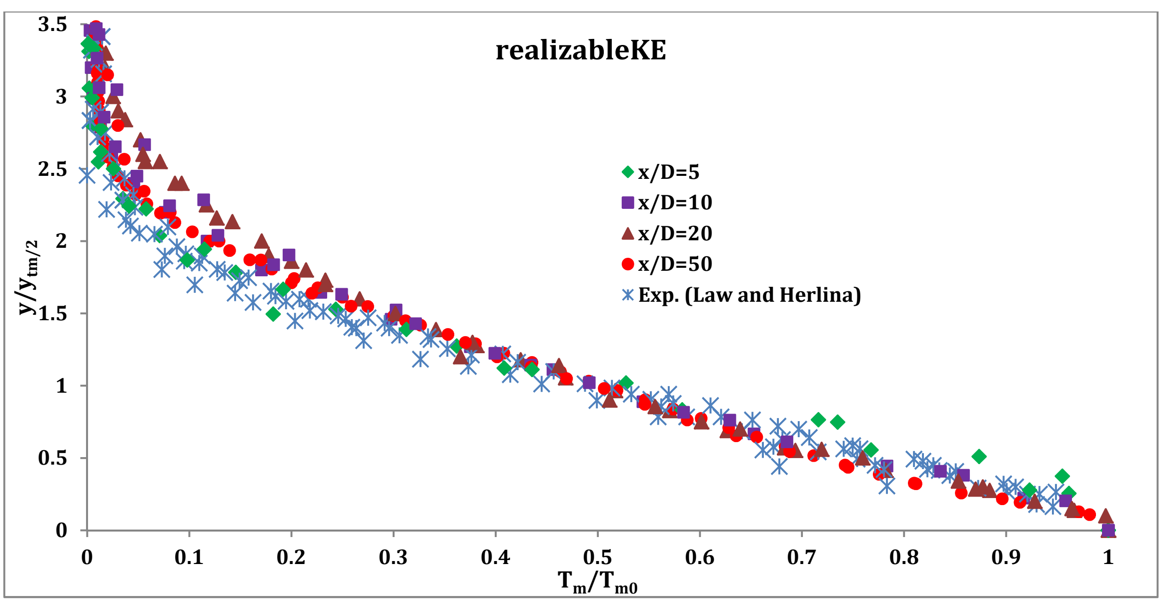

Fig. 4.18: Comparison of self similarity streamwise temperature profiles for different cases

4.5.3.3 Spanwise Temperature Profiles

Spanwise temperature profiles were extracted from the horizontal plane at the height of the inlet centerline ($y=y_m$). The spanwise self-similarity profiles are presented in Fig. 4.19 which shows that in the range of $3 \leq x/D \leq 50$ the profiles exhibit a shape similar to a top hat. RNG and realizable k-ε models provide better results than the other two turbulence models used and are in a better agreement with experimental data. Similar to the streamwise temperature profiles, it was found that the spanwise profiles are also independent of Froude number.

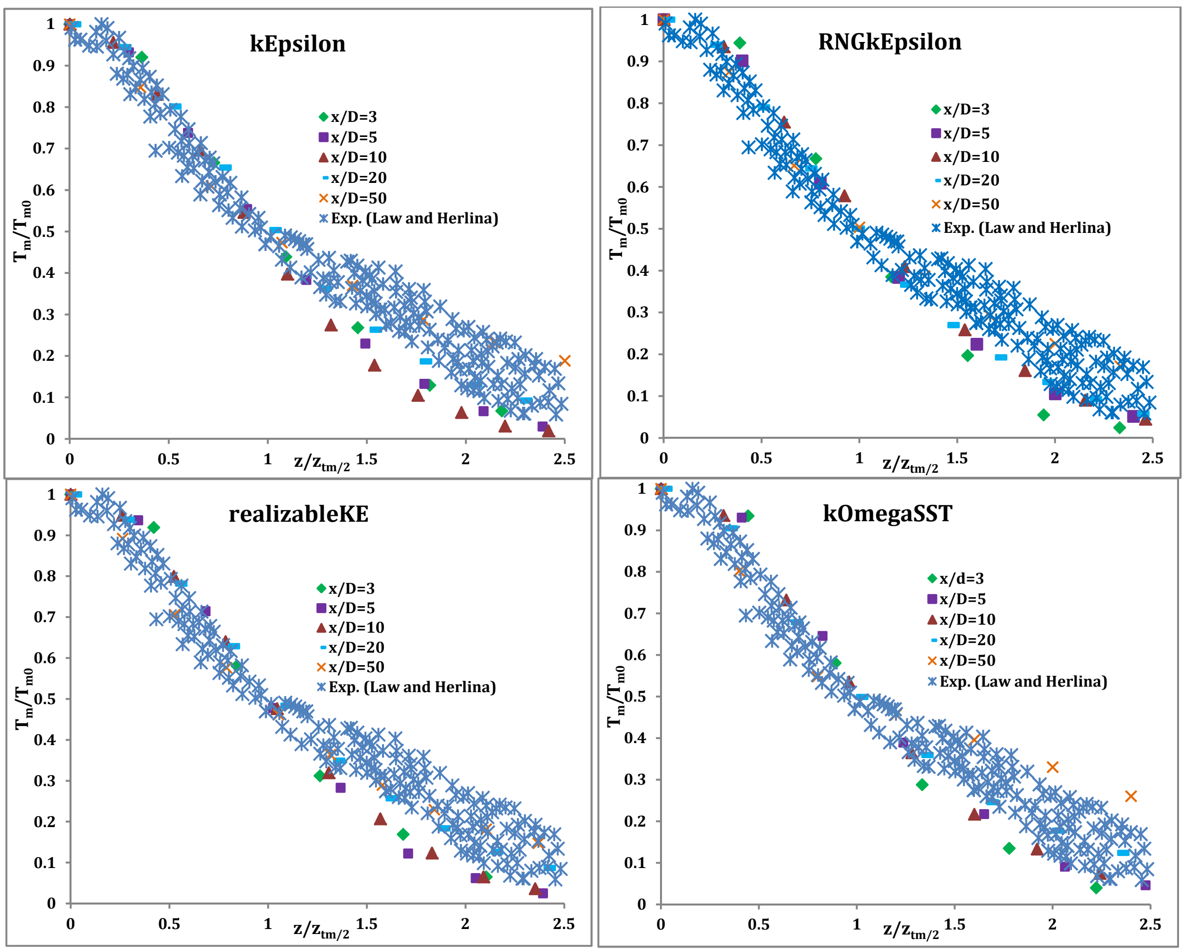

Fig. 4.19: Comparison of self similarity spanwise temperature profile at $y=y_m$ for different turbulence models

4.5.3.4 Maximum Temperature Decay

The temperature decay along the centerline for different turbulence models are compared to the experimental results by Law and Herlina (2002) in Fig. 4.20. Reasonable agreement is between the numerical and experimental results, except for the SST k-ω model which overpredicts the temperature values at the centerline for the interval *10≤x/D≤30*. The best-fit curve for all turbulence models results, as well as experimental results are presented in Table 4.4. The best turbulence model for this case is, again, the realizable k-ε as expected based on previous comparisons.

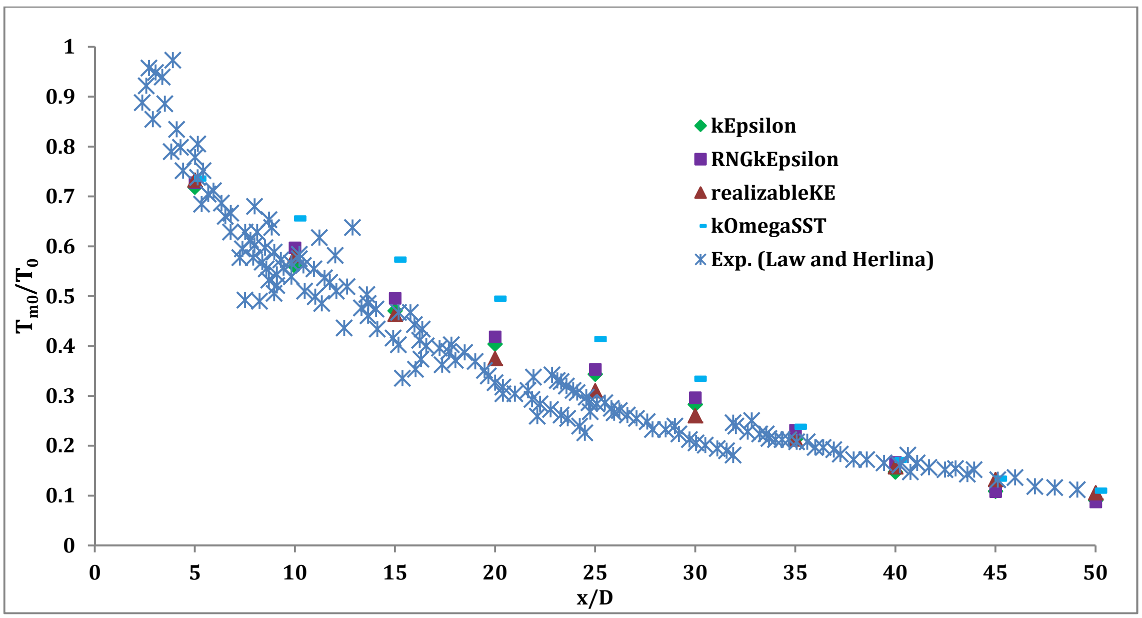

Fig. 4.20: Comparison of the maximum temperature decay along the jet centerline

Table 4.4: The best-fit curves for centerline temperature decay

Study	kEpsilon	RNGkEpsilon	realizableKE	kOmegaSST	Exp. (Law)
Best curve fit	$T_{m0}/T_0=4.25(x/D)^{-0.88}$	$T_{m0}/T_0=4.44(x/D)^{-0.88}$	$T_{m0}/T_0=3.76(x/D)^{-0.83}$	$T_{m0}/T_0=4.30(x/D)^{-0.83}$	$T_{m0}/T_0=2.51(x/D)^{-0.70}$

4.6 Conclusions

A detailed numerical study was conducted to investigate both the velocity and temperature fields of a three dimensional thermal wall jet. Heated water resulted from cooling systems of MSF desalination and power plants is an example of thermal wall jet. A finite volume method was applied to solve the equations numerically. Four different turbulence models were employed in order to evaluate the accuracy of RANS models when simulating the discharge of thermal fluid disposals. The numerical results were compared to previous experimental and numerical data. The results showed good agreement with the recent experimental data for velocity and temperature fields. Dilution rates for temperature and maximum temperature decay were highly accurate when compared to experimental data. Efficient design for discharge systems may hence be possible based on the results of the jet trajectory. Jet trajectory differs from case to case and is related to discharge and ambient water characteristics. It was confirmed that increasing discharge Froude number has a positive effect on dilution by inducing a more turbulent flow. However, through numerical experiments, it was found that the trajectory and the distance at which the jet passes could be more effective in obtaining higher dilution rates. Velocity profiles at the offset planes showed self-similarity along the sections in the zone of developed flow. The numerical results of maximum velocity decay were found to be in good agreement with results of several experimental studies. Streamwise and spanwise profiles for velocity and temperature showed self-similarity after an initial distance from discharge point. The general shape of these profiles was also found to be independent of the Froude number. The streamwise temperature profiles followed a general Gaussian form in various values of x/D. In the case of spanwise profiles, temperature exhibited the same characteristics as the velocity. However, some discrepancies were observed in the spanwise velocity profiles which could be due to the presence of secondary flows or buoyancy-induced instabilities which are not well captured by the turbulence models considered in this study. More advanced turbulence models are expected to improve the accuracy of the simulations for spanwise velocity which is currently investigated by the authors. Finally, among the four models examined in this study, the realizable k-ε turbulence model was found to be the most accurate and capable to accurately model thermal wall jets discharged into stationary ambient water.

Chapter V

Technical Paper II

Numerical Modeling of 30° and 45° Inclined Dense Turbulent Jets in Stationary Ambient

Abstract

Dispersion of turbulent jets in shallow coastal waters has numerous engineering applications. The accurate forecasting of the complex interaction of these jets with the ambient fluid presents significant challenge and has yet to be fully elucidated. In this paper, numerical simulations of 30° and 45° inclined dense turbulent jets in stationary water have been conducted. These two angles are examined in this study due to lower terminal rise heights for 30° and 45°, which is critically important for discharges of effluent in shallow waters compared to higher angles. Mixing behavior of dense jets is studied using a finite volume model (OpenFOAM). Five Reynolds-Averaged Navier-Stokes turbulence models are applied to evaluate the accuracy of CFD predictions. These models include two Linear Eddy Viscosity Models: RNG *k-ε*, and realizable *k-ε*; one Nonlinear Eddy Viscosity Model: Nonlinear *k-ε*; and two Reynolds Stress Models: LRR and Launder-Gibson. Based on the numerical results, the geometrical characteristics of the dense jets, such as the terminal rise height, the location of centerline peak, and the return point are investigated. The mixing and dilution characteristics have also been studied through the analysis of cross-sectional concentration and velocity profiles. The results of this study are compared to various advanced experimental and analytical investigations, and comparative figures and tables are discussed. It has been observed that the LRR turbulence model as well as the realizable k-ε model predict the flow more accurately among the various turbulence models studied herein.

Keywords: Desalination, Inclined dense jets, Mixing, Turbulence models, RSM, OpenFOAM.

5.1 Introduction

Rising populations, shortages of clean and potable water, and advancements in desalination plant technology have increased rapidly in the last decades (GWI, 2004). In arid and semi-arid countries, desalination plants are actively considered as the best solution to respond to the high demand for drinkable water. Desalination plants remove the dissolved minerals from coastal water bodies and produce effluents with a high salt concentration, called brines. Disposal of these brines, which have higher density than the receiving water, causes many environmental impacts, especially in the near field of outfall systems, which is the natural habitat of marine species and fish cultures (Sajwani, 1998; Einav and Lokiec, 2003; Hashim and Hajjaj, 2005; Lattemann and Hoepner, 2008).

Dense effluents are typically discharged to coastal waters in the form of submerged negatively buoyant jets from diffuser(s) located on the seabed (Fig. 5.1). The dense jet will eventually fall back onto the seabed, since the brine discharge is denser than the surrounding water. After it impacts the bed, a density current occurs, which continues spreading horizontally. Therefore, it is necessary to achieve rapid mixing and dispersion of concentrated brine discharge in order to minimize the marine environmental impacts. The prediction of mixing of dense jets is unavoidable for outfall design and environmental impact assessment. In vertical dense jets in stagnant water, the effluent tends to fall back on the diffuser(s), which has a negative impact on the jet dilution. This could be prevented by inclining the jet at an angle from the vertical direction (Fischer et al., 1979). However, optimum inclination is not only based on the maximum dilution at the key points of the dense jets, but also depends on the ambient water characteristics. For instance, as reported in the literature (Zeitoun et al., 1970; Roberts and Toms, 1987), 60° inclined jets have the maximum dilution since they produce the longest trajectory and therefore the highest dilution, but the associated terminal rise height is relatively high and the angle may be very large for shallow coastal waters, as is the case in the Persian Gulf area where many desalination plants are located.

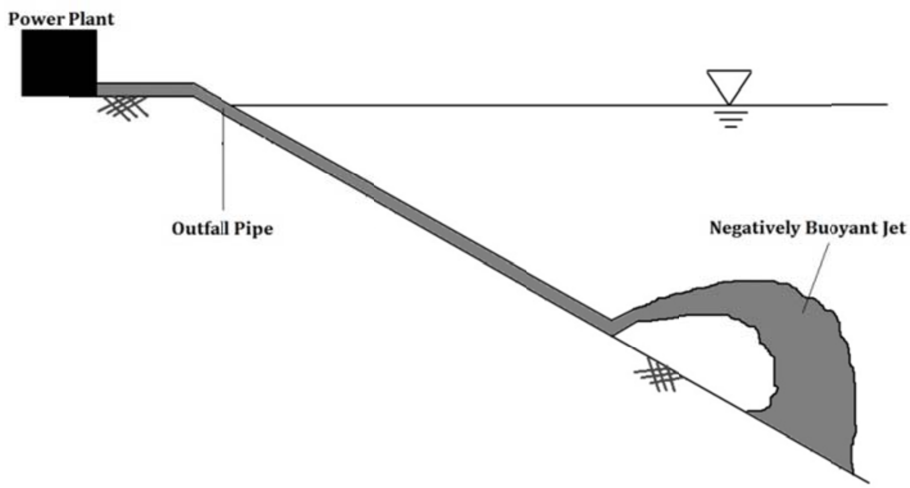

Fig. 5.1: Negatively buoyant (dense) jet resulted from a power (desalination) plant

Many experimental studies have been performed on inclined negatively-buoyant jets. Zeitoun et al. (1970) conducted several experiments on various discharge angles using a point-based conductivity meter technique to measure the trajectory and the minimum dilution. They observed that a 60° inclined jet produced the longest trajectory for entrainment. Roberts and Toms (1987) then performed experimental studies based on the latter suggestion, as well as for vertical dense jets. They used the same experimental technique and reported empirical correlations of dilution at jet terminal rise and jet impact point to the sea bed. They concluded that 60° jets have twice the dilution of vertical jets at both the terminal rise and impact points. Pincince and List (1973) carried out experiments to investigate the dilution of brine disposed into a flowing stream. They compared the results with integral model predictions and concluded that the model was able to predict the flow trajectory with reasonable accuracy; however, the dilution was significantly underestimated. Roberts et al. (1997) used a combination of Laser Induced Fluorescence (LIF) and micro-conductivity probes for the data acquisition close to the boundary for 60° inclination of a single port diffuser.

Later, Cipolina et al. (2005), conducted various experiments in order to obtain the visual trajectory measurements for 30°, 45°, and 60° jets with high densimetric Froude numbers ranging from 30 to 120. However, no dilution data were obtained. More recently, Kikkert et al. (2007) reported integrated concentration measurements for 15°, 30°, 45°, and 60° jets in stagnant water using both Light Attenuation (LA) and LIF techniques. They also developed an analytical model to interpret the experimental results which divides the jet flow into either a pure jet or plume regime. Their model results are in good agreement with previous data, especially in term of jet trajectory, and suggest that dense jets are jet-like before the terminal rise height. The integrated dilution measurements showed that the normalized dilution at terminal rise height is about the same as for 30° - 60° inclinations. This is different than earlier observations by Zeitoun et al. (1970), but is supported by CORJET model calculations, as Jirka (2004, 2008) reported. The CORJET model shows that the dilution at the terminal rise height of the 30° - 60° inclinations are close to each other, and that the 45° jet has a slightly higher value.

A very comprehensive investigation on the mixing and trajectory characteristics of 30º and 45º inclined dense jets which is relevant for many coastal cities with shallow waters (10-20 m) was performed by Shao and Law (2010). They used a combination of Particle Image Velocimetry (PIV) and Planar Laser Induced Fluorescence (PLIF) technique to resolve the velocity and concentration distribution profiles. They divided the experiments into two series: series F, in which the nozzle is placed far from the boundary (seabed), and series N, for cases close to the bottom boundary. The Coanda effect (see e.g. Shao and Law, 2010) was investigated in this study as well. Visual measurements of 45° to 90° inclined dense jets as well as turbulent concentration fluctuation of these jets have been recorded by Papakostantis et al. (2011a, 2011b). Lai and Lee (2012) also reported a comprehensive investigation of the tracer concentration field of inclined dense jets for jet densimetric Froude numbers of Fr = 10 - 40 and a broad range of jet angles Θ = 15°, 30°, 38°, 45°, 52°, and 60°. They used PIV and LIF systems to run their experiments. The experimental results have then been compared to the VISJET model (2003) as well as other experimental data from previous studies.

Experimental studies have been actively followed in this field, while numerical studies have very rarely been done for the dense inclined jets, and hence are still being pursued and need further investigation. Vafeiadou et al. (2005) studied inclined negatively buoyant jets numerically using a three-dimensional model named CFX-5. For turbulence closure, the SST (Shear Stress Transport) model was employed, which is based on a blending between the k-ε and the k-ω models. They used an unstructured grid with refinement near the bottom, where the boundary layer develops, and around the inflow nozzle. They concluded that the model underestimated slightly the terminal rise height and considerably the return point compared to experimental data by Roberts et al. (1997). Kim and Cho (2006) investigated numerically the buoyant flow of heated water discharged from surface and submerged side outfalls in shallow and deep water with a cross flow. They used the FLOW-3D model, which is a commercial CFD package, and the RNG k-ε model was applied for turbulence closure. Elhaggag et al. (2011) studied dense brine jets both experimentally and numerically. However, they focused only on the vertical dense jets, and no inclination is reported in their investigation. The numerical simulations were conducted via a FLUENT CFD package and were compared to those from their experimental study.

This paper presents the results of numerical modelling of inclined dense jets. Two angles, 30° and 45°, have been studied using an open source CFD code named OpenFOAM (OPEN Field Operation And Manipulation) (OpenFOAM user and programmer guides, 2011). Numerical equations are solved using a finite volume method. Mixing and dispersion characteristics of the jets are studied, as well as geometrical characteristics such as terminal rise height, return point, and centerline trajectory. A broad range of turbulence models, including Linear Eddy Viscosity Models (LEVMs), Non-Linear Eddy Viscosity Model (NLEVM), and Reynolds Stress Models (RSMs), have been tested and the results are compared with thorough experimental data.

5.2 Dimensional Analysis

The schematic view of an inclined negatively buoyant jet is seen in Fig. 5.2. The jet is discharged with an initial angle Θ to the horizontal with jet diameter D, jet velocity U_0, jet density ρ_0, and ambient water density ρ_a ($\rho_0 > \rho_a$). The jet mixes with ambient water as it is discharged and reaches a maximum rise height (also called terminal rise height y_t), and then falls because of negative buoyancy. It finally impacts the seabed at x_i (not shown in Fig. 5.2) and spreads as a density current which disperses horizontally. The concentration dispersion depends on both jet and ambient characteristics, such as jet discharge concentration C_0, the initial density difference $\Delta\rho_0 = \rho_0 - \rho_a$, U_0, D, Θ, and ambient water depth H. One of the key parameters in dense jet analysis is the jet densimetric Froude number, which is the ratio of inertia to buoyancy and is calculated as follows:

$$Fr = \frac{U_0}{\sqrt{g_0^{'} D}} \tag{5.1}$$

$$g_0^{'} = \left(\frac{\Delta\rho_0}{\rho_a}\right) g \tag{5.2}$$

where g is gravitational acceleration and $g_0^{'}$ is reduced gravitational acceleration. The jet mixing characteristics of interest are the maximum terminal rise height y_t, jet centerline peak horizontal and vertical locations (x_m, y_m), jet centerline peak dilution value S_m, the return point x_r where the plume returns to the source level, and its dilution S_r.

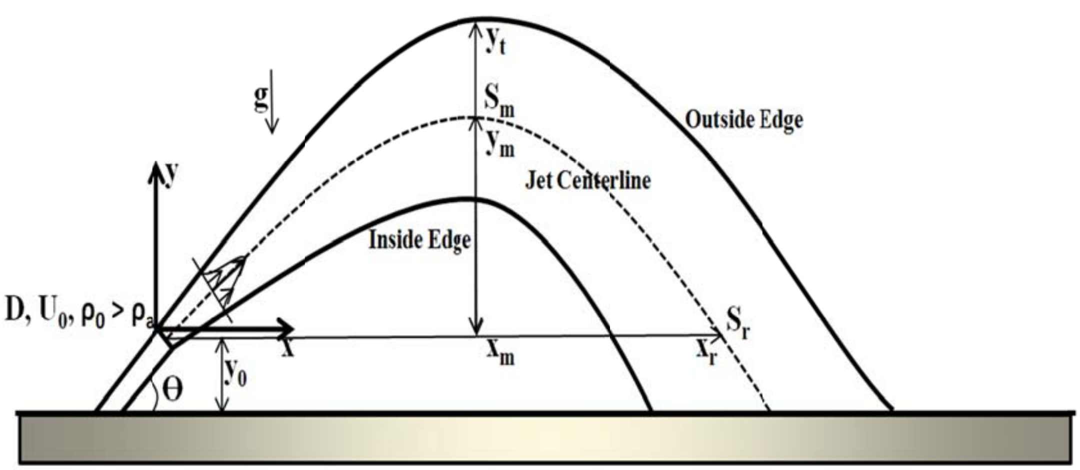

Fig. 5.2: Schematic diagram of the inclined dense jet in stagnant ambient water

The inclined negatively-buoyant jets are characterised by the jet discharge volume flux (Q_0), kinematic momentum flux (M_0), and the buoyancy flux (B_0) (Lai and Lee, 2012), which are given in the following equations:

$$Q_0 = U_0 \pi \frac{D^2}{4} \tag{5.3}$$

$$M_0 = U_0^2 \pi \frac{D^2}{4} \tag{5.4}$$

$$B_0 = Q_0 g_0^{'} \tag{5.5}$$

In dimensional analysis, it is shown (Lai and Lee, 2012) that a characteristic length (e.g., maximum terminal rise height) for the jet may be written as:

$$\frac{y_t}{L_M} = f\left(\frac{L_M}{L_Q}, \theta_0\right) \tag{5.6}$$

Or, it can be written as:

$$\frac{y_t}{FrD} = f(Fr, \theta_0) \tag{5.7}$$

where L_M and L_Q are the momentum and source length scales, respectively, and are calculated as:

$$L_M = \frac{M_0^{3/4}}{B_0^{1/2}} \tag{5.8}$$

$$L_Q = \frac{Q_0}{M_0^{1/2}} \tag{5.9}$$

L_M is a measure of the distance within which the jet momentum is more important than buoyancy, and L_Q represents the length over which source discharge is important. Similarly, the centerline peak dilution S_m (as well as return point dilution S_r) can also be expressed as:

$$\frac{S_m}{Fr} = f(Fr, \theta_0) \tag{5.10}$$

5.3 Numerical Model

5.3.1 Governing Equations

The governing equations are the well-known Navier-Stokes equations for three-dimensional, incompressible fluids, as follows:

Continuity equation:

$$\frac{\partial u}{\partial x}+\frac{\partial v}{\partial y}+\frac{\partial w}{\partial z}=0 \tag{5.11}$$

Momentum equations:

$$\frac{\partial u}{\partial t}+u\frac{\partial u}{\partial x}+v\frac{\partial u}{\partial y}+w\frac{\partial u}{\partial z}=-\frac{1}{\rho}\frac{\partial P}{\partial x}+\frac{\partial}{\partial x}\left(\upsilon_{eff}\left(\frac{\partial u}{\partial x}\right)\right)+\frac{\partial}{\partial y}\left(\upsilon_{eff}\left(\frac{\partial u}{\partial y}\right)\right)+\frac{\partial}{\partial z}\left(\upsilon_{eff}\left(\frac{\partial u}{\partial z}\right)\right) \tag{5.12}$$

$$\frac{\partial v}{\partial t}+u\frac{\partial v}{\partial x}+v\frac{\partial v}{\partial y}+w\frac{\partial v}{\partial z}=-\frac{1}{\rho}\frac{\partial P}{\partial y}+\frac{\partial}{\partial x}\left(\upsilon_{eff}\left(\frac{\partial v}{\partial x}\right)\right)+\frac{\partial}{\partial y}\left(\upsilon_{eff}\left(\frac{\partial v}{\partial y}\right)\right)+\frac{\partial}{\partial z}\left(\upsilon_{eff}\left(\frac{\partial v}{\partial z}\right)\right)-g\frac{\rho-\rho_0}{\rho} \tag{5.13}$$

$$\frac{\partial w}{\partial t}+u\frac{\partial w}{\partial x}+v\frac{\partial w}{\partial y}+w\frac{\partial w}{\partial z}=-\frac{1}{\rho}\frac{\partial P}{\partial z}+\frac{\partial}{\partial x}\left(\upsilon_{eff}\left(\frac{\partial w}{\partial x}\right)\right)+\frac{\partial}{\partial y}\left(\upsilon_{eff}\left(\frac{\partial w}{\partial y}\right)\right)+\frac{\partial}{\partial z}\left(\upsilon_{eff}\left(\frac{\partial w}{\partial z}\right)\right) \tag{5.14}$$

where u, v, and w are the mean velocity components in the x, y, and z directions, respectively, t is the time, P is the fluid pressure, υ_{eff} represents the effective kinematic viscosity ($\upsilon_{eff}=\upsilon_t+\upsilon$), υ_t is the turbulent kinematic viscosity, g is the gravity acceleration, ρ is the fluid density, and ρ_0 is the reference fluid density.

One should note that the equations are divided by density (ρ), and the buoyancy term is added to the momentum equation in the vertical direction (y-coordinate) to account for variable density effects.

Concentration evolution is modeled using the advection-diffusion equation, as:

$$\frac{\partial C}{\partial t}+u\frac{\partial C}{\partial x}+v\frac{\partial C}{\partial y}+w\frac{\partial C}{\partial z}=D\left(\frac{\partial^2 C}{\partial x^2}+\frac{\partial^2 C}{\partial y^2}+\frac{\partial^2 C}{\partial z^2}\right) \tag{5.15}$$

where C is the fluid concentration (salinity, S), and D is the diffusion coefficient. It was numerically found that the results are not significantly sensitive to Pr_t (turbulent Prandtl number) and Pr (Prandtl number) within the range 0.6-1.0. Thus, both coefficients were set to 1.0.

5.3.2 Density Calculation

In this study, the density is calculated for both the jet and the ambient water according to the equation for the state of seawater proposed by Millero and Poisson (1981):

$$\rho = \rho_t + AS + BS^{3/2} + CS \tag{5.16}$$

where

$$\begin{aligned} A &= 8.24493\times10^{-1} - 4.0899\times10^{-3}T + 7.6438\times10^{-5}T^2 - 8.2467\times10^{-7}T^3 + 5.3875\times10^{-9}T^4 \\ B &= -5.72466\times10^{-3} + 1.0227\times10^{-4}T - 1.6546\times10^{-6}T^2 \\ C &= 4.8314\times10^{-4} \end{aligned} \tag{5.17}$$

and ρ_t is the density of water that varies with the temperature (T), as follows:

$$\begin{aligned} \rho_t = {} & 999.842594 + 6.793952\times10^{-2}T - 9.095290\times10^{-3}T^2 + \\ & 1.001685\times10^{-4}T^3 - 1.120083\times10^{-6}T^4 + 6.536336\times10^{-9}T^5 \end{aligned} \tag{5.18}$$

S in Eqn. (5.16) denotes the salinity of water, and as shown in this equation, the dense jet density is a function of salinity and temperature. However, the temperature difference between the jet and ambient is negligible.

5.3.3 Computational Domain and Boundary Conditions

Only half of the dense jet domain is considered in this study since the problem is symmetrical. The dimensions of the computational domain are chosen based on the available experimental setups. The numerical simulations were performed in a tank with dimensions of 1.2 m length, 0.2 m width, and 0.5 m depth (Fig. 5.3a). A refined mesh is used for simulations to better capture velocity and concentration characteristics in the near-field zone, especially close to the nozzle and to the bottom boundary (Fig. 5.3b). It is also noteworthy that the mesh independency tests are performed to get the best density for the mesh grid in more than five levels.

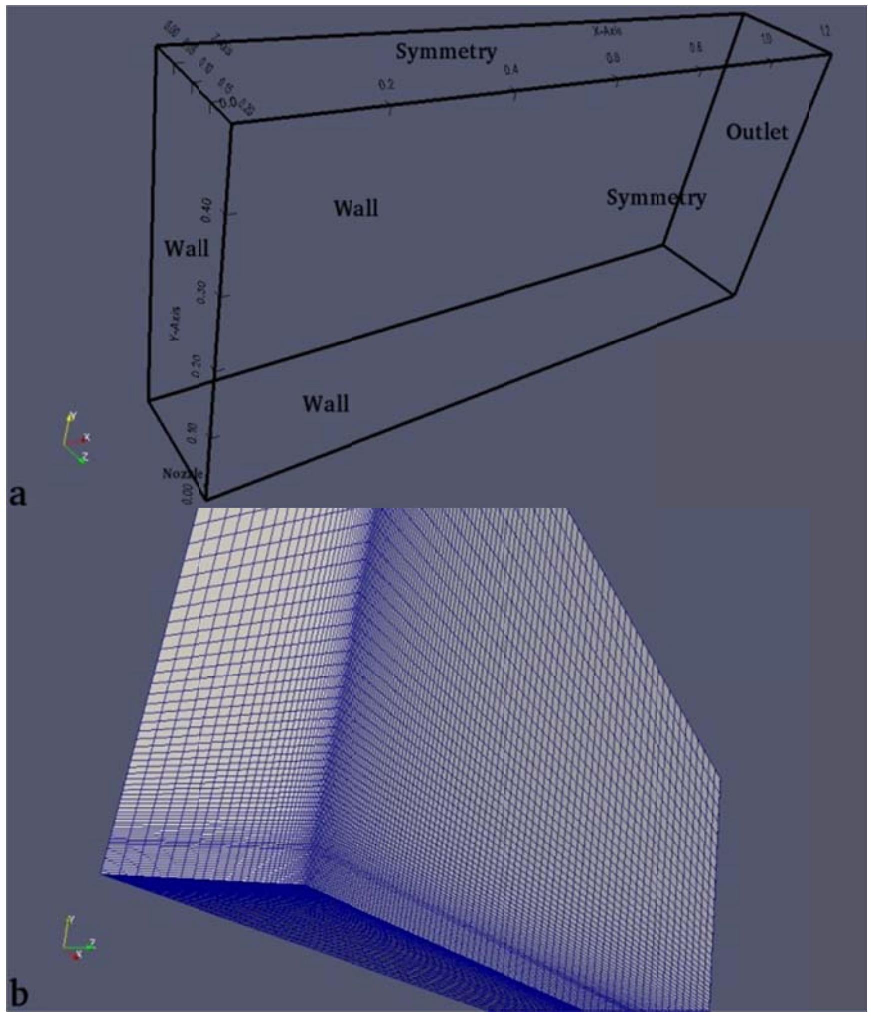

Fig. 5.3: Computational domain. (a) Domain dimensions and boundary conditions of the numerical model (b) A refined mesh system

For the inlet (nozzle), the boundary conditions are: $u=U_0\times Cos(\Theta)$, $v= U_0\times Sin(\Theta)$, $w=0$, $C=C_0$, $T=T_0$, $k=0.06u^2$, and $\varepsilon=0.06u^3/D$. The inlet values for k and ε are chosen based on Huai et al. (2010). Regarding the flow at the outlet section, a zero-gradient boundary condition perpendicular to the outlet plane is defined for u, v, w, k, ε, C, and T. Moreover, for the wall boundaries, the standard wall functions are used for k, and ε, and the no-slip condition is considered. Finally, the symmetry boundary was modeled using zero-gradient conditions.

5.3.4 Turbulence Models

It is widely accepted among researchers in the field that no single turbulence model can be universally applied to all situations. Some considerations must be taken into account when choosing a turbulence model, including the physics encompassed in the flow, the level of accuracy, and the computational resources available. In order to evaluate the performance of different turbulence models for dense jet discharges, five turbulence models are considered in this paper, including (i) RNG k-ε model, (ii) realizable k-ε model, (iii) Nonlinear k-ε model, (iv) LaunderGibsonRSTM model (RSM), and (v) LRR model (RSM) (see Appendix E for more details).

5.3.5 Numerical Algorithm

The governing equations are numerically solved using the finite volume method. The solver which is used within OpenFOAM is the modified *pisoFoam* (OpenFOAM user and programmer guides, 2011). This solver is a transient solver for incompressible flows. The code first predicts the velocity field by solving the momentum equations. Pressure is then found by solving the Poisson equation in Issa's PISO (Pressure-Implicit with Splitting of Operators) algorithm via an iterative process. Rather than solving all of the coupled equations in a coupled or iterative sequential fashion, PISO splits the operators into an implicit predictor and multiple explicit corrector steps. At each time step, velocity and concentration are predicted, and then pressure and velocity are corrected. The velocity is predicted implicitly because of the greater stability of implicit methods, which means that a set of coupled linear equations, expressed in matrix-vector form as $Ax=b$, are solved. More information about Issa's PISO algorithm can be found in (Ferziger and Peric, 2002; Issa, 1985; Issa et al., 1986; Oliveira and Issa, 2001). The concentration equation (Eqn. 5.15) is then solved using the finite volume method.

The temporal term has been discretized by the second-order implicit Crank-Nicolson scheme (OpenFOAM user guide, 2011). The advection and diffusion terms are discretized by the standard finite volume method using Gaussian integration with a first-order upwind interpolation scheme for advection and a fourth-order cubic scheme for diffusion in order to calculate values at the face centers rather than the cell centers. It is numerically found that advection terms are very sensitive to the higher-order schemes, especially in RSMs. On the other hand, diffusion terms are very stable when using higher-order schemes.

For the pressure field, the PCG (Preconditioned Conjugate Gradient) method is used to solve the linear system. The PBiCG (Preconditioned Bio Conjugate Gradient) method has been used for the other fields, U, C, T, k, and ε. In order to enhance the rate of convergence for iterative solvers, the DIC (Diagonal Incomplete Cholesky) pre-conditioner is used to calculate the pressure field. This is a simplified diagonal based pre-conditioner for symmetric matrices. The DILU (Diagonal Incomplete LU) pre-conditioner is used for the other fields, U, C, T, k, and ε, which mostly include asymmetric matrices.

5.4 Results and Discussions

Two different cases, 30° and 45°, have been numerically simulated. All five turbulence models have been applied to each case (totalling 10 simulations: 2 cases × 5 turbulence models), and the comparative results are presented. The characteristics of the two cases are summarized in Table 5.1.

Table 5.1: Numerical cases characteristics

Test #	Inclined Angle Θ	Inlet Diameter (*mm*)	Initial Inlet Height y_0 (*mm*)	$\Delta\rho/\rho_a$ (%)	Discharge Velocity U_0 (*m/s*)	Densimetric Froude # Fr_d	Jet to Plume Characteristic Length Scale L_m (*mm*)	Bed Proximity Parameter y_0/L_m
1	30	6.5	11.17	1.984	1	28.10	172.00	0.065
2	45	6	12.92	1.984	1.173	34.30	193.00	0.070

5.4.1 Jet Trajectory and General Characteristics

Fig. 5.4 shows the concentration contour maps for all ten numerical cases. The color bars indicate the concentration scale. As shown, the nonlinear *k-ε* model generates a longer trajectory compared to the other turbulence models. However, the other models are more or less close to each other. The jet trajectory (or jet centerline) is basically the first concept which characterises the general jet flow. The jet centerline is often derived from the maximum velocity or concentration location at different cross-sections perpendicular to the jet. According to these cross-sections, the best way to extract the centerline is by a velocity vector map starting from the nozzle. Although the concentration and velocity axes almost coincide, as argued in (Shao, 2009), the concentration axis often descends faster than the velocity axis.

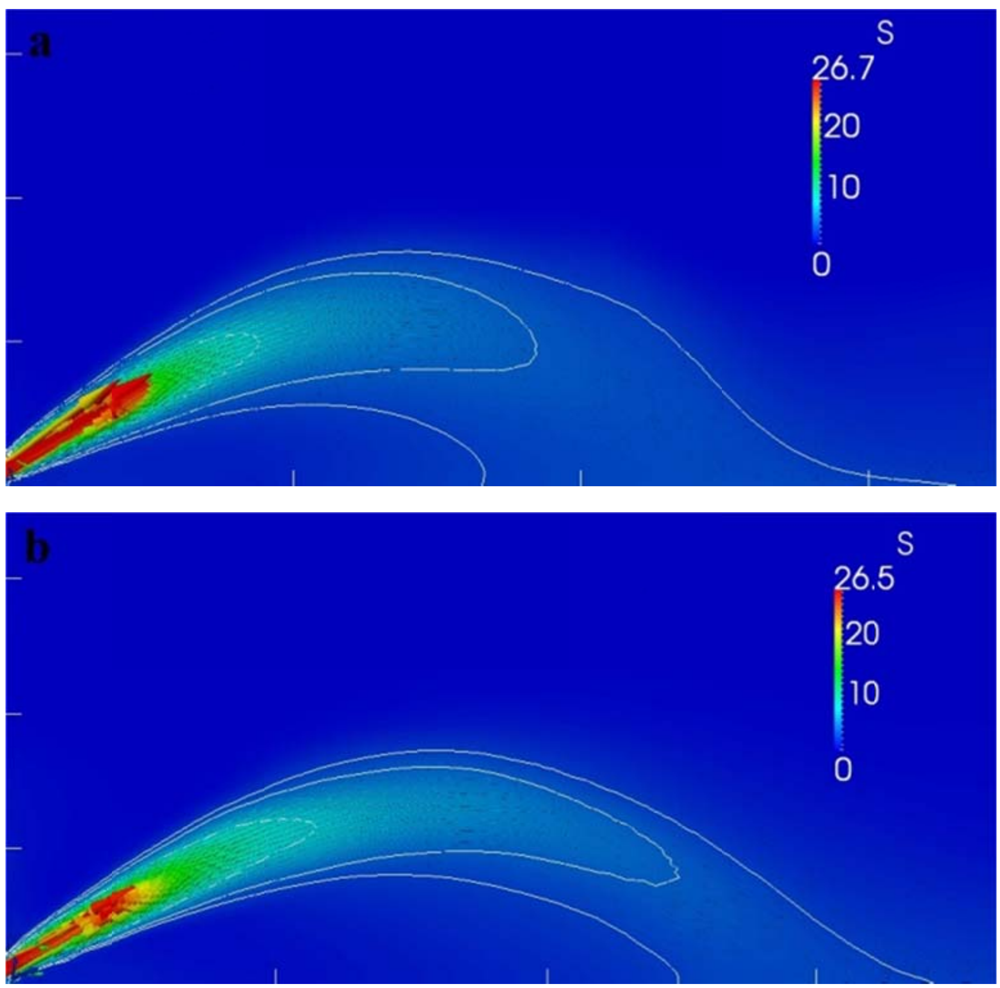

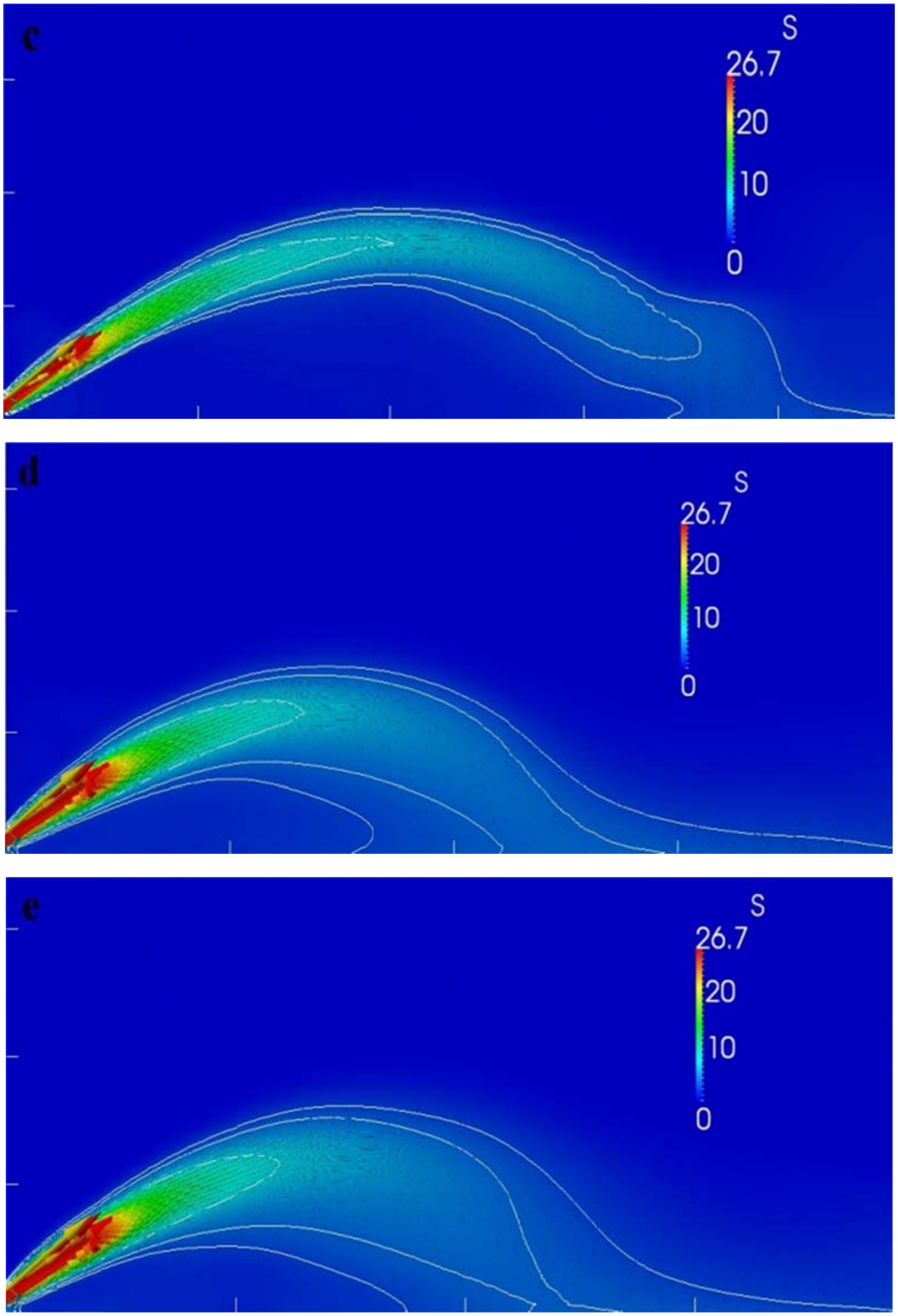
c
S
26.7
20
10
0
d
S
26.7
20
10
0
e
S
26.7
20
10
0

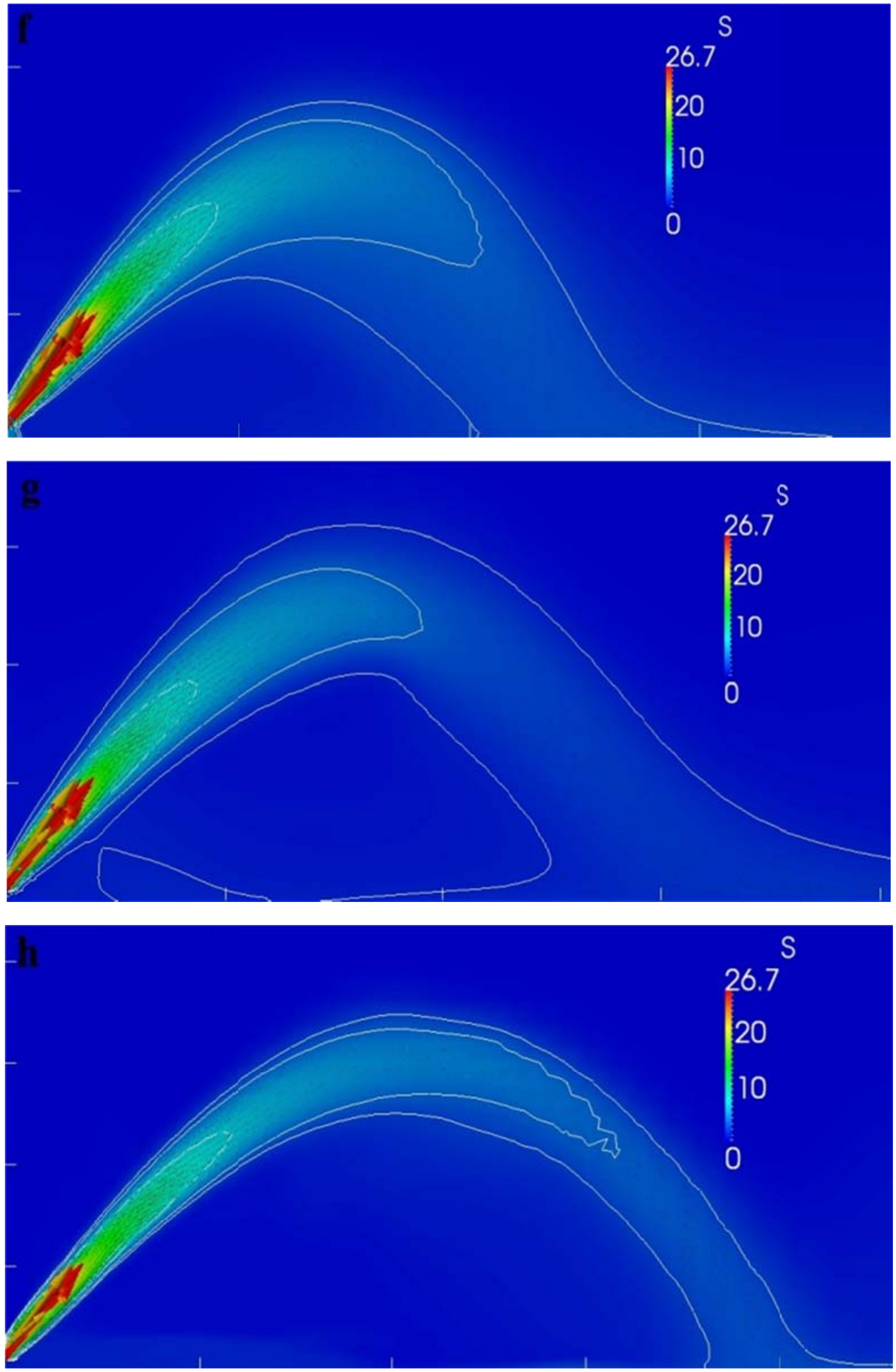
f
S
26.7
20
10
0
g
S
26.7
20
10
0
h
S
26.7
20
10
0

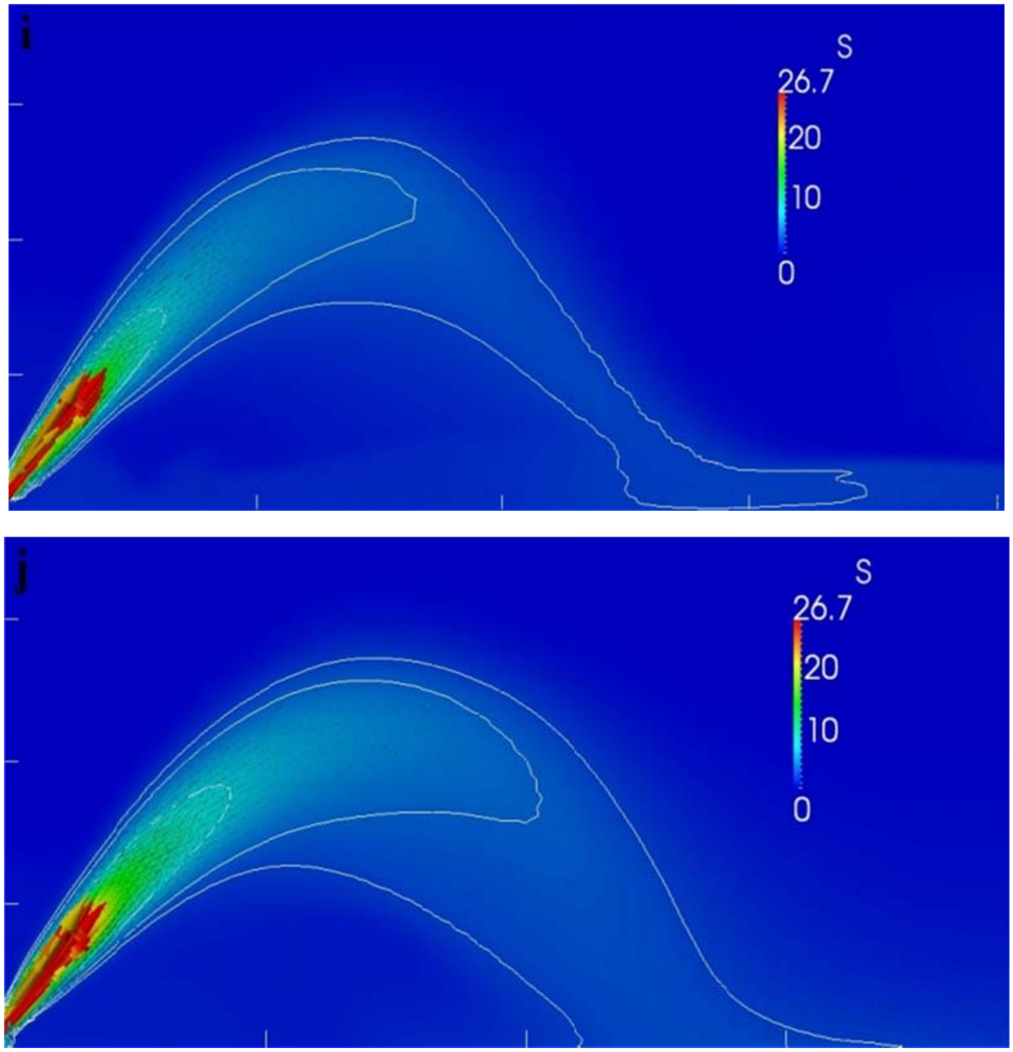

Fig. 5.4: Velocity vector and concentration contour maps for 30° (a-e: *Fr*=28.10) and 45° (f-j: *Fr*=34.30) inclined jets. a, f: RNGkEpsilon; b, g: realizableKE; c, h: NonlinearKE; d, i: LRR; e, j: LaunderGibsonRSTM

The jet trajectories for different angles and different densimetric Froude numbers are given in Fig. 5.5. As was expected, for the same angle the trajectory of a higher Froude number is longer, and thus the return point distance is longer. Similar to Fig. 5.4, the nonlinear *k-ε* model is farther away from the nozzle compared to the other turbulence models. x_0 and y_0 are the x and y location of the nozzle tap. For both angles, the jet trajectories are almost symmetrical for the ascending and descending portions in the figures, which is in agreement with the experiments done by Shao and Law (2010) and different than Ferrari and Querzoli (2004), who reported asymmetrical in the centerline trajectory for dense jets.

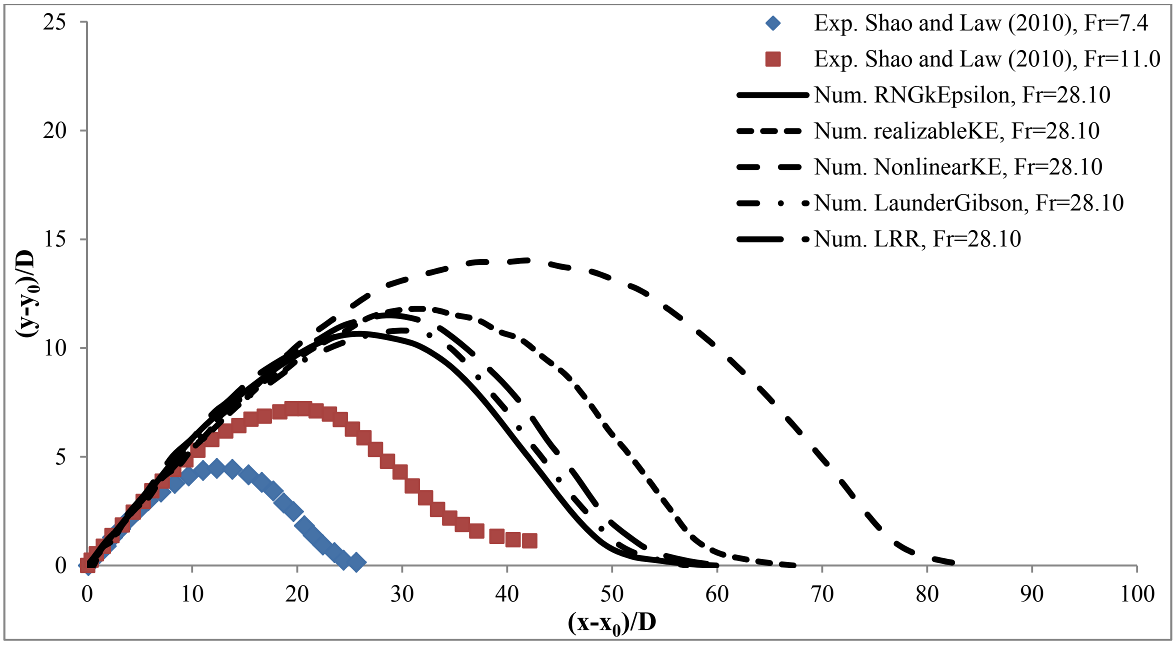

(a)

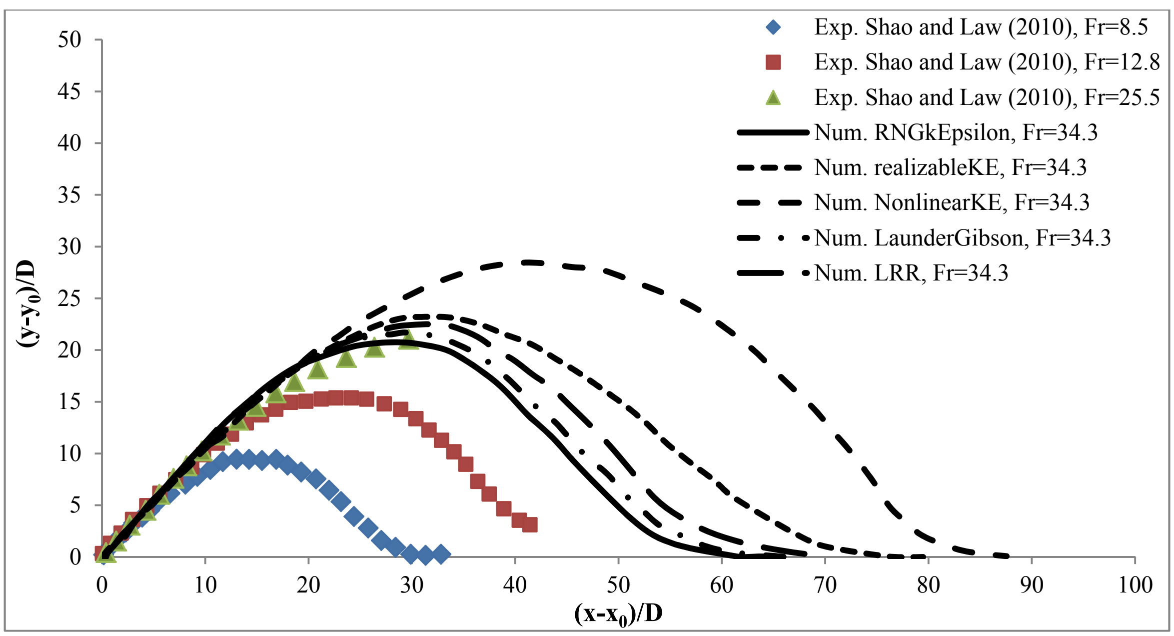

(b)

Fig. 5.5: Comparison of centerline trajectories with different Froude numbers. a. 30°, b. 45°

The numerical results shown in Fig. 5.5 are non-dimensionalized for a better comparison with the experimental data. Hence, the trajectories are normalized by L_M which is a factor of

Fr. Fig. 5.6 shows the results for the 30° and 45° angles and the comparison with previous studies.

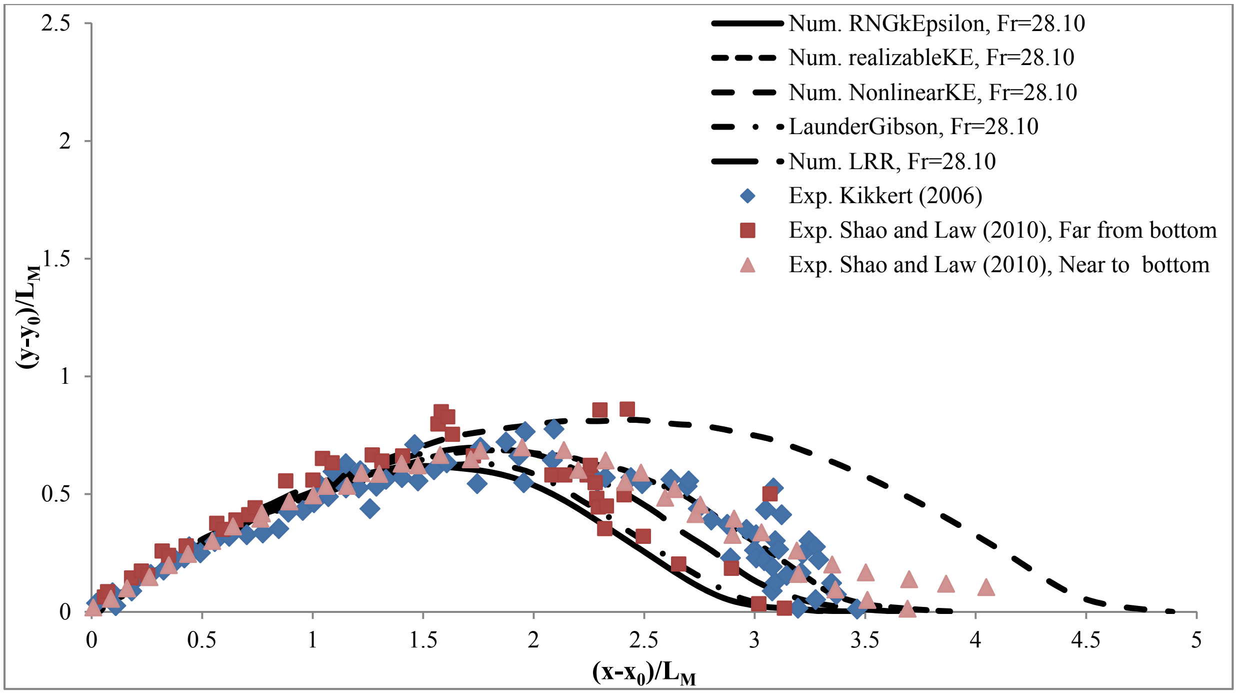

(a)

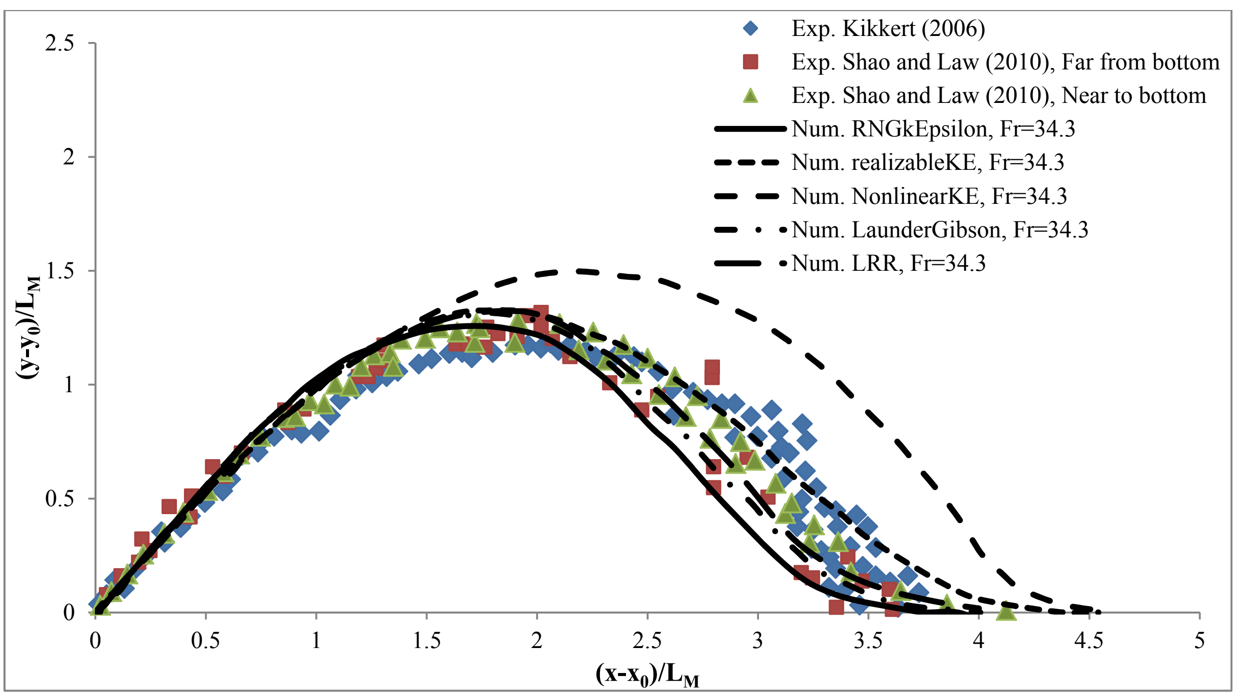

(b)

Fig. 5.6: Normalized centerline trajectories. a. 30°, b. 45°

In the study by Shao and Law (2004), the cases were divided into two series: (i) near to boundary; (ii) far from boundary. They investigated the boundary interactions in the dense jet discharges. It is noteworthy that for both inclined jets and for all five turbulence models, the trajectories are in good agreement with the experimental data and close to each other up to about the maximum terminal rise height. This is where the momentum forces are dominant up to that point. After that, in the descending part of the jet flow, the discrepancies are clear in the both experimental and numerical results. As shown in Fig. 5.6, the previous patterns of different turbulence models are repeated here. In both cases, the RNG k-ε model slightly under-predicts the trajectory in the descending part of the jet. On the other hand, the nonlinear k-ε model over-predicts after the maximum terminal rise height of the jet flow. The results of the realizable k-ε model are in better agreement with the experimental data as well as the RSMs (LRR and Launder-Gibson models).

5.4.2 Geometrical Properties and Mixing Characteristics

There are several key geometrical parameters in effluent discharges from desalination plants which should be well-studied for a comprehensive design of outfall systems. These parameters include the terminal rise height, the horizontal location of the return point, and the dilution values at these locations. Hence, it is important to determine which numerical model provides the most accurate results.

As discussed previously, dimensional analysis is utilized to correlate the geometrical and mixing quantities to the jet densimetric Froude number, *Fr*, or jet-to-plume length scale, L_M, as well as the nozzle diameter, *D*, in some cases (Roberts et al., 1997). Proportionality coefficients are also defined in order to compare the numerical results with the previous studies. These coefficients are calculated for all turbulence models. Many previous studies derived these coefficients empirically by experimental investigation. A summary of these experimental data is given in Tables 5.2 and 5.3, as well as the results for the present study. The coefficients from this study show that the results are generally in an acceptable range of accuracy compared to the various experimental data. Among different turbulence models, the nonlinear k-ε model coefficients for trajectory are higher than in other models, at about

15-25%. On the other hand, however, the dilution-related coefficients for this model are lower than in previous studies as well as in other turbulence models. Moreover, as shown in Tables 2 and 3 and the previous figures, the LRR turbulence model (a RSM) coefficients are close to those of the realizable *k-ε* model in terms of both trajectory and dilution, whereas the Launder-Gibson turbulence model, which is another RSM, as is LRR, predicts very similarly to the RNG *k-ε* model.

The comparative results for important trajectory locations and mixing features at these locations are presented in the following sections.

5.4.2.1 Jet Terminal Rise Height

Terminal rise height is defined as where the initial momentum vertical component decreases dramatically and equals zero in the dense jet trajectory. The jet rises up to this height and then falls towards the bed. This height is also named with different terminologies in the literature, such as maximum rise height (Madni and Ahmed, 1989), final fountain height (Bloomfield and Kerr, 2002), maximum height of the top boundary (Zeitoun et al., 1970), maximum height of the outer jet (Kikkert et al., 2007), and terminal rise height (Roberts and Toms, 1987; Roberts et al., 1997; Shao and Law, 2010). The latter is adopted in this paper and is denoted as y_t. This is the most critical parameter in brine discharge system design in order to ensure that all dispersion and mixing is done below the free water surface (Shao and Law, 2010).

Table 5.2: Comparison of numerical and experimental coefficients for 30° inclined jets

Parameter	Proportionality Coefficient	Present Study					Shao and Law (2010)		Kikkert et al. (2007)			Nemlioglu and Roberts (2006)	Cipolina et al. (2005)	Zeitoun et al. (1970)
		RNG	real	Nonlinear	Launder	LRR	$0.10 \le y_0/L_m \le 0.15$	$y_0/L_m > 0.15$	LA data	LIF data	Theory			
Terminal rise height	$C_1 = \frac{y_t}{D} Fr$	0.96	1.03	1.05	0.97	1.00	1.05	–	1.00	1.19	1.02	1.40	1.08	1.15
Horizontal location of return point	$C_2 = \frac{x_r}{D} Fr$	2.63	3.02	4.14	2.75	2.85	2.88	3.00	3.14	3.44	2.95	3.30	3.03	3.48
Return point dilution	$C_3 = \frac{S_r}{Fr}$	0.97	1.17	0.86	1.06	1.09	1.18	1.45	–	–	–	1.90	–	–
Vertical location of centerline peak	$C_4 = \frac{y_m}{D} Fr$	0.57	0.68	0.79	0.60	0.65	0.66	–	0.56	0.66	0.62	–	0.79	–
Horizontal location of centerline peak	$C_5 = \frac{x_m}{D} Fr$	1.56	1.87	2.19	1.62	1.79	1.70	1.54	1.75	1.85	1.70	–	1.95	–
Centerline peak dilution	$C_6 = \frac{S_m}{Fr}$	0.56	0.62	0.55	0.58	0.60	0.62	0.66	–	–	–	–	–	0.36

Table 5.3: Comparison of numerical and experimental coefficients for 45° inclined jets

Parameter	Proportionality Coefficient	Present Study					Shao and Law (2010)	Kikkert et al. (2007)			Nemlioglu and Roberts (2006)	Cipolina et al. (2005)	Zeitoun et al. (1970)
		RNG	real	Nonlinear	Launder	LRR	$y_0/L_m>0.15$	LA data	LIF data	Theory			
Terminal rise height	$C_1 = \frac{y_t}{D} Fr$	1.44	1.54	1.75	1.46	1.52	1.47	1.60	–	1.61	2.00	1.61	1.43
Horizontal location of return point	$C_2 = \frac{x_r}{D} Fr$	2.80	3.32	3.79	2.96	3.18	2.83	3.26	–	3.04	3.20	2.82	3.33
Return point dilution	$C_3 = \frac{S_r}{Fr}$	0.86	1.20	0.82	1.04	1.11	1.26	–	–	–	1.70	–	–
Vertical location of centerline peak	$C_4 = \frac{y_m}{D} Fr$	1.05	1.19	1.39	1.10	1.13	1.14	1.06	–	1.13	–	1.17	–
Horizontal location of centerline peak	$C_5 = \frac{x_m}{D} Fr$	1.57	1.75	2.04	1.65	1.72	1.69	1.84	–	1.88	–	1.80	–
Centerline peak dilution	$C_6 = \frac{S_m}{Fr}$	0.39	0.45	0.37	0.42	0.44	0.46	–	–	–	–	–	0.42

Aside from a lack of consensus in the terminal rise height terminology, there is also a lack of consensus on the determination of terminal rise height among researchers, especially in experimental investigations. Jirka (2008) reported that the terminal rise height is usually determined as the visual boundary of the captured flow images, which involves many uncertainties due to the amounts and types of dye used, recording instrument sensitivities, and other parameters. Lai and Lee (2012) reported that for a positively-buoyant jet in stationary fluid, the visual boundary can be defined as the $0.25C_{max}$ concentration contour, which corresponds to the radial position where the turbulent intermittency γ is 0.5. It also corresponds to the jet boundary defined by Chu et al. (1999) and Lee and Chu (2003). Their interpretations were that since the concentration distribution in the outer (upper) half is Gaussian and that the outer jet width grows at the same rate as a positively buoyant jet (inner half), the $0.25C_{max}$ visual boundary definition can be used to determine the y_t value. The commonly-used integral model CORJET uses two cut-off levels for the visual boundary: 3% and 25% (2004). In this study, the 3% level is used to derive the terminal rise height, similar to the study done by Shao and Law (2010).

The terminal rise height, y_t, for the concentration is normalized by the nozzle diameter and is plotted versus Fr for 30° and 45° in Fig. 5.7. The initial nozzle height y_0 is subtracted in the given y_t. The numerical results are compared with various previous experimental data as well as the analytical solution developed by Kikkert (2006). The results are very close to each other for different turbulence models and are consistent with the experimental data trend line. However, as shown in Fig. 5.7, for 45° the nonlinear k-ε slightly over-predicts the terminal rise height when compared to other models. The experimental data of Zeitoun et al. (1970) for a 45° inclined dense jet have an apparent deviation from Kikkert's theoretical solution for low Froude numbers.

The linear relationship between y_t/D and Fr may be better seen if y_t is normalized by L_M. Fig. 5.8 shows the numerical results compared to various previous results. As shown in Fig. 5.8, the normalized terminal rise height increases due to increases in the value of Θ, as expected. This study results for 30° and 45° fall within the predicted range of Kikkert's analytical solution. The results of analytical model of Lane-Serf et al. (1993), as well as their experimental results, are lower compared to other data for the terminal rise height. On the other hand, recent experimental results by Nemlioglu and Roberts (2006) are higher than in other studies.

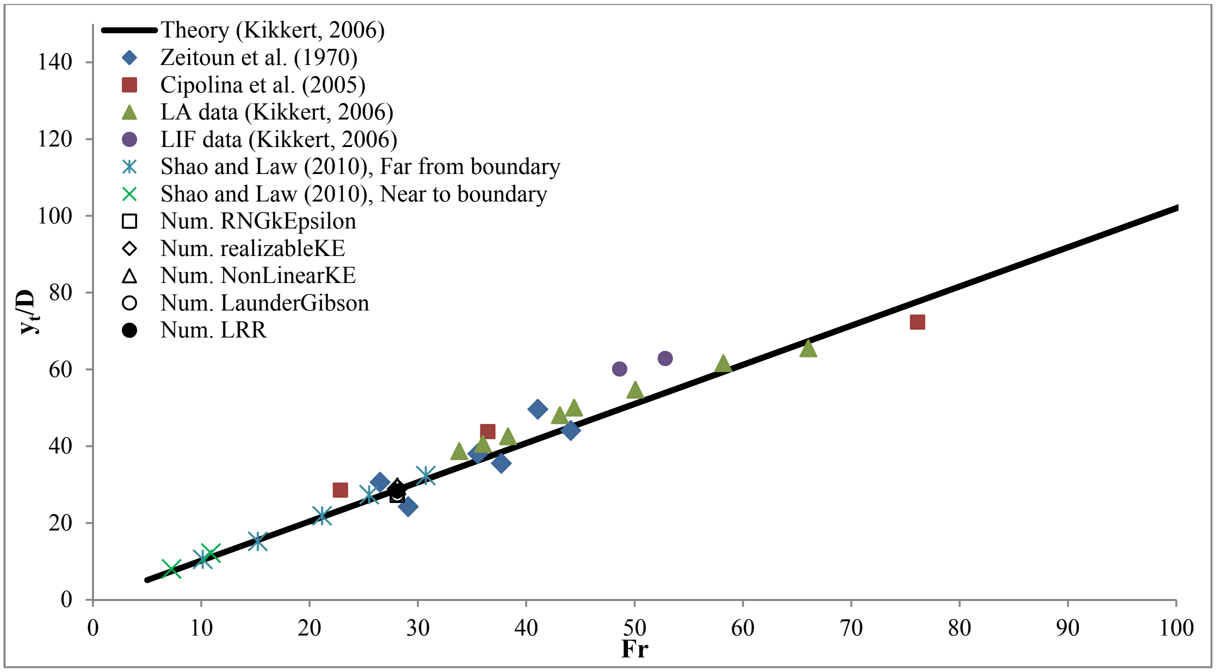

(a)

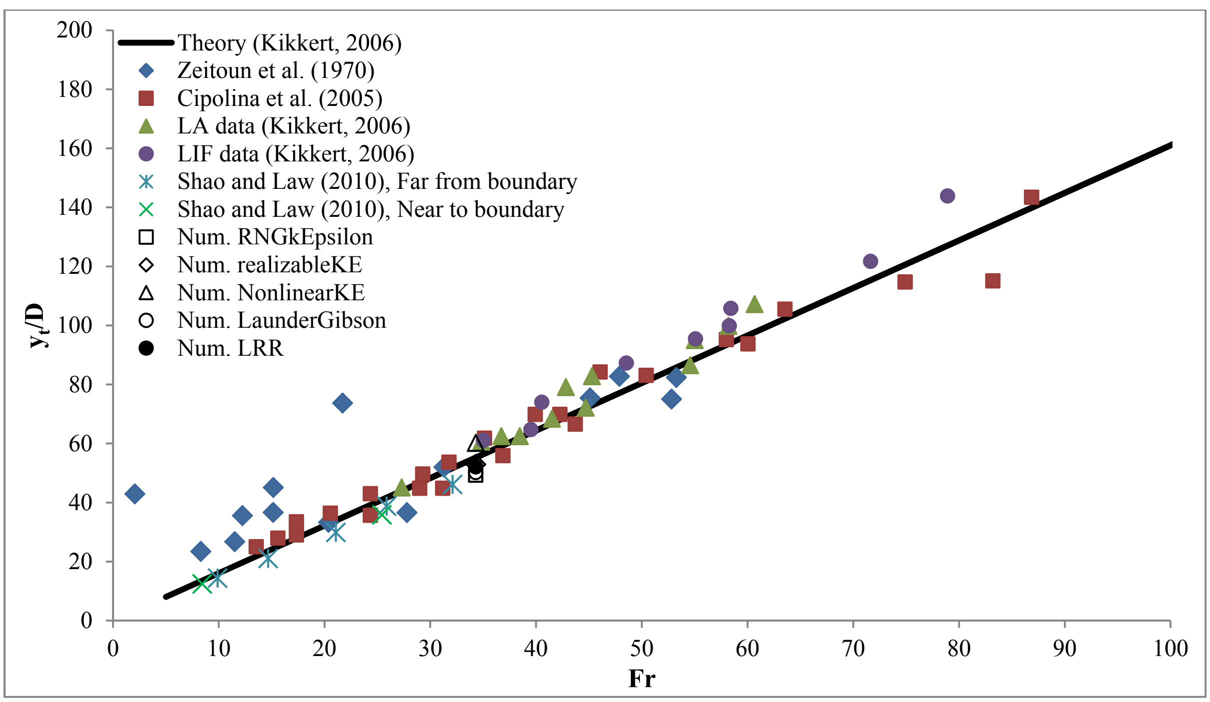

(b)

Fig. 5.7: Normalized terminal rise height vs. *Fr*. a. 30°, b. 45°

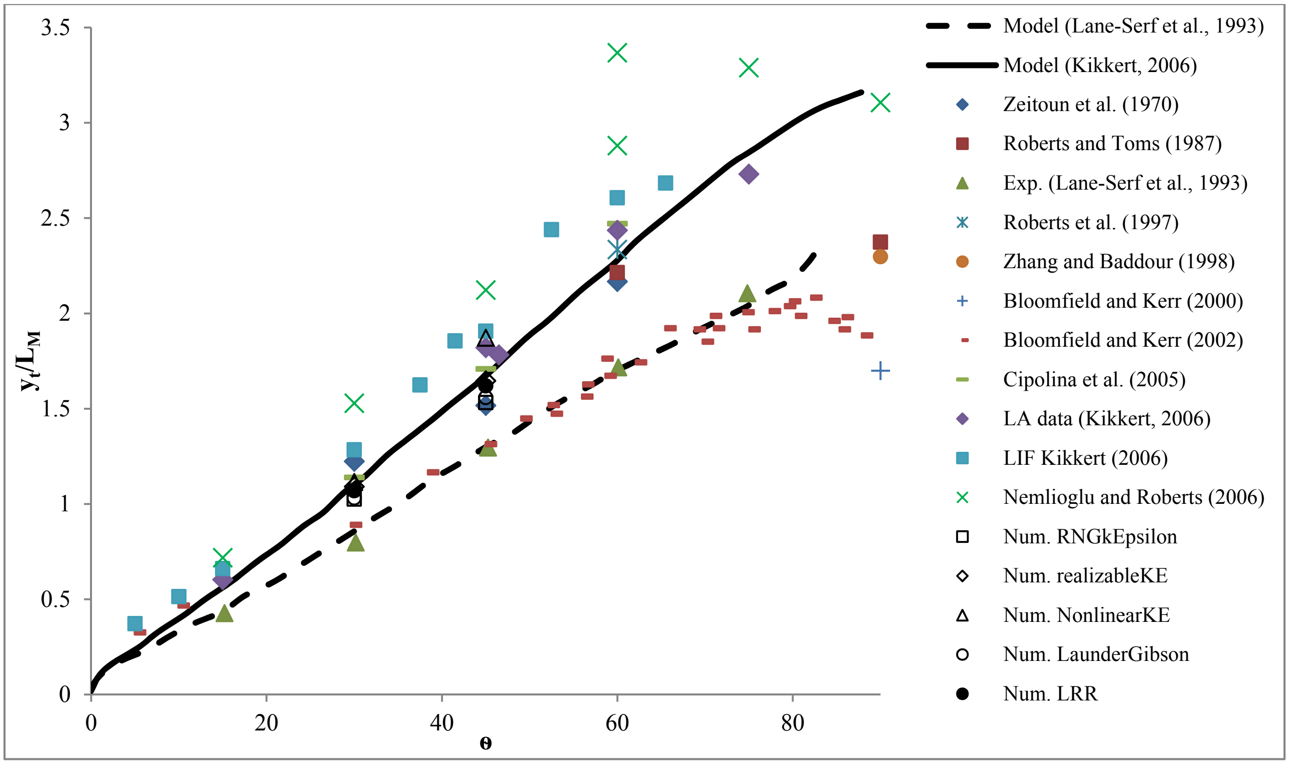

Fig. 5.8: Normalized terminal rise height as a function of initial discharge angle

5.4.2.2 Jet Centerline Peak

The jet centerline peak is defined from the centerline trajectory, which is previously determined and plotted. The horizontal and vertical locations (x_m, y_m) of the centerline peak are normalized by the nozzle diameter and are plotted versus *Fr* in Figs. 5.9 and 5.10, respectively. Similar to previous results, the different turbulence models are close to each other and the results are consistent with the experimental data. The results of the turbulence models confirm previous trajectory prediction results. It seems that the analytical model of Kikkert (2006) slightly underestimates the horizontal location of the jet centerline for a 30° inclined dense jet. As was expected from previous trends, the LRR turbulence model as well as the realizable *k-ε* model predicts x_m very well. The RNG *k-ε* turbulence model slightly under-predicts both the horizontal and vertical locations of the centerline peak, while the nonlinear *k-ε* model over-estimates the locations of these points.

Comparison of results of terminal rise height and centerline peak vertical location shows that the vertical density gradient tends to dampen turbulence at the outer (upper) boundary where its value is negative, whereas it promotes turbulence at the inner (lower) boundary where its value is positive (Shao and Law, 2010). This is the same behaviour as for positively buoyant jets for reverse boundaries. As a result, in dense jets, the outer (upper) edge becomes sharper and slightly closer to the jet centerline as compared to the inner (lower) edge.

Figs. 5.11 and 5.12 show the horizontal and vertical locations of the centerline peak when they are normalized by L_M. Previous investigations have been looked at for comparison. The numerical results of x_m for a 45° inclined dense jet are lower than both previous experimental data and the theoretical results from Kikkert (2006).

Fig. 5.12 includes the empirical linear formula from Ferrari and Querzoli (2004) for the vertical location of the centerline peak, which is written as the following:

$$\frac{y_m}{L_M} = (0.0321 \pm 0.0059)\theta \tag{5.19}$$

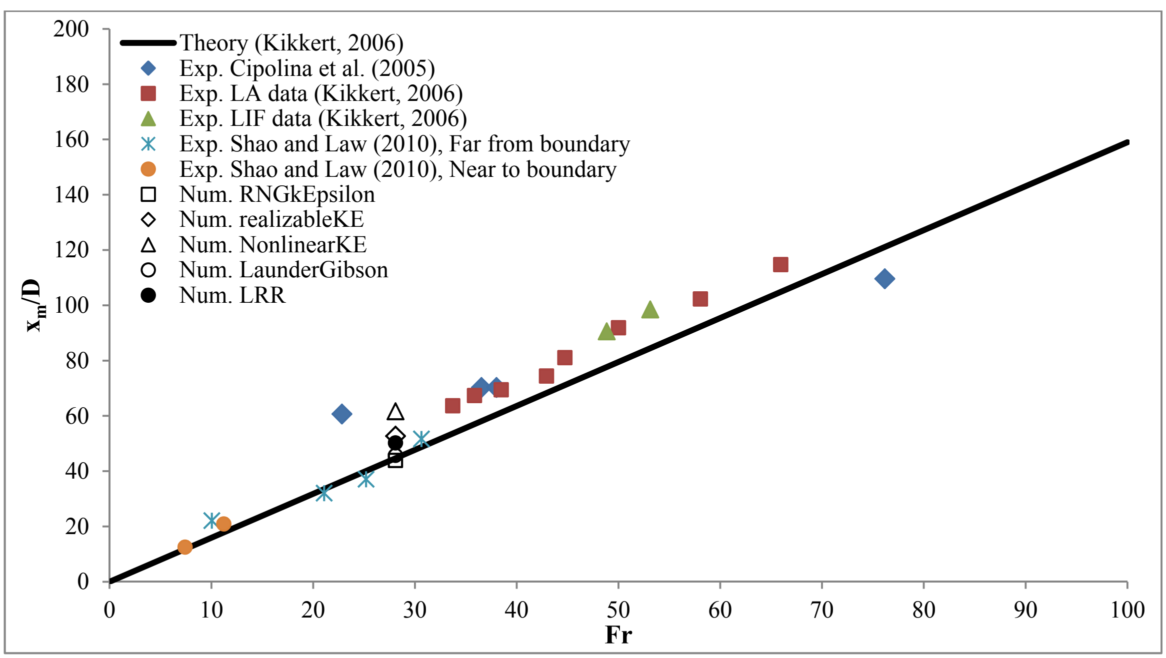

(a)

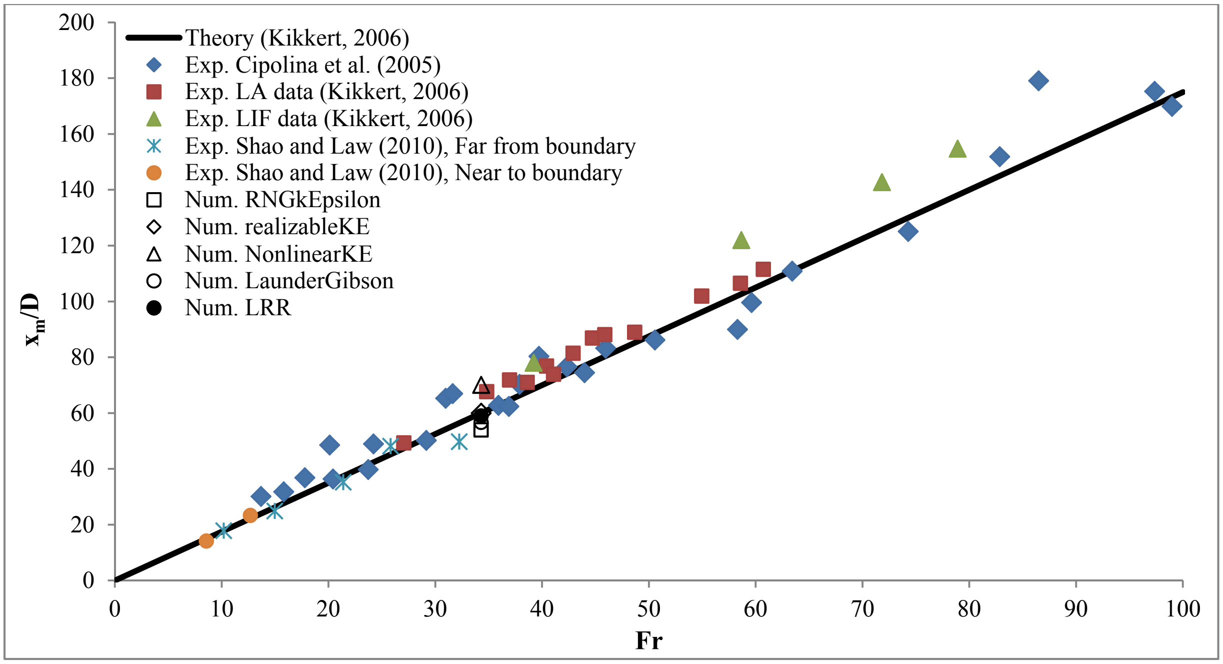

(b)

Fig. 5.9: Normalized horizontal location of centerline peak vs. *Fr*. a. 30°, b. 45°

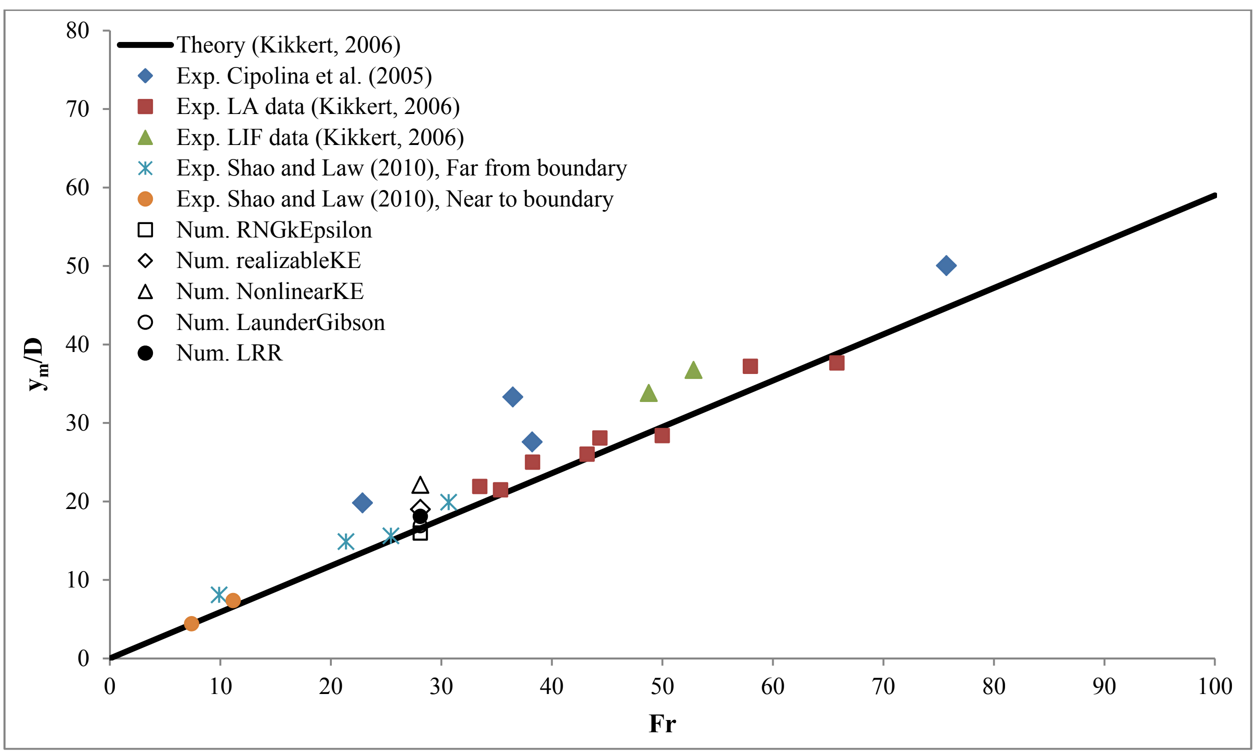

(a)

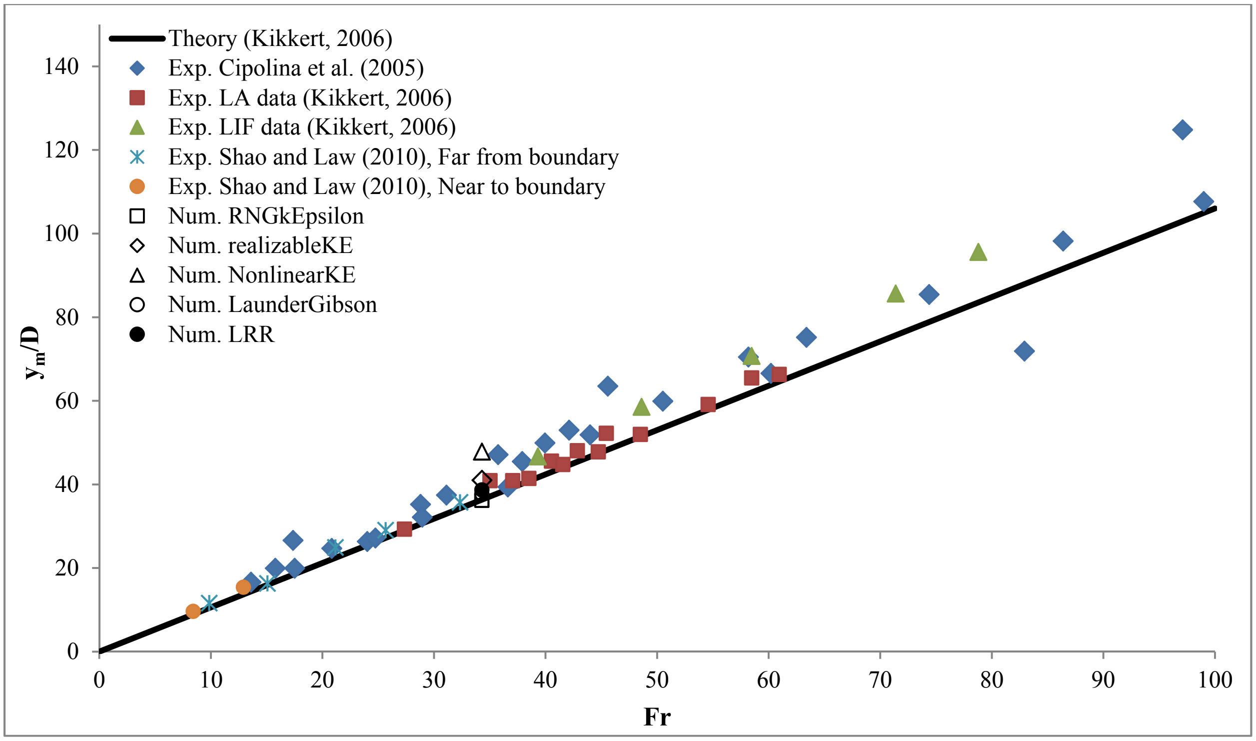

(b)

Fig. 5.10: Normalized vertical location of centerline peak vs. *Fr*. a. 30°, b. 45°

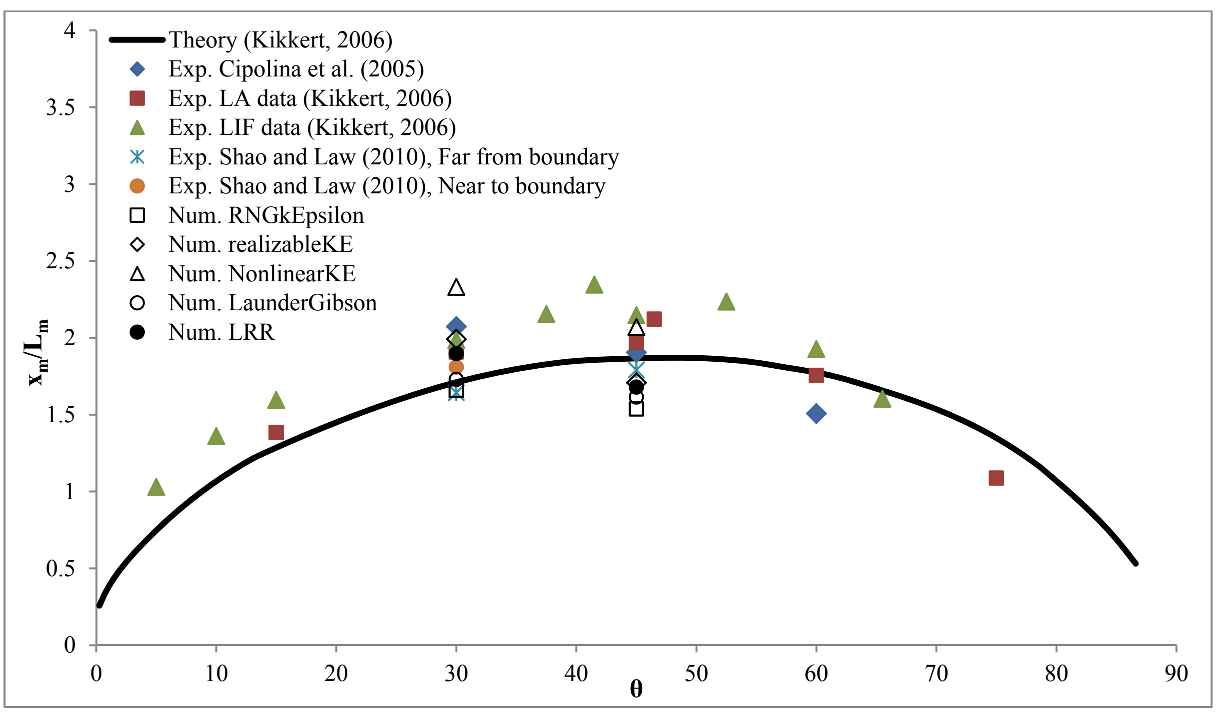

Fig. 5.11: Normalized horizontal location of centerline peak as a function of initial discharge angle

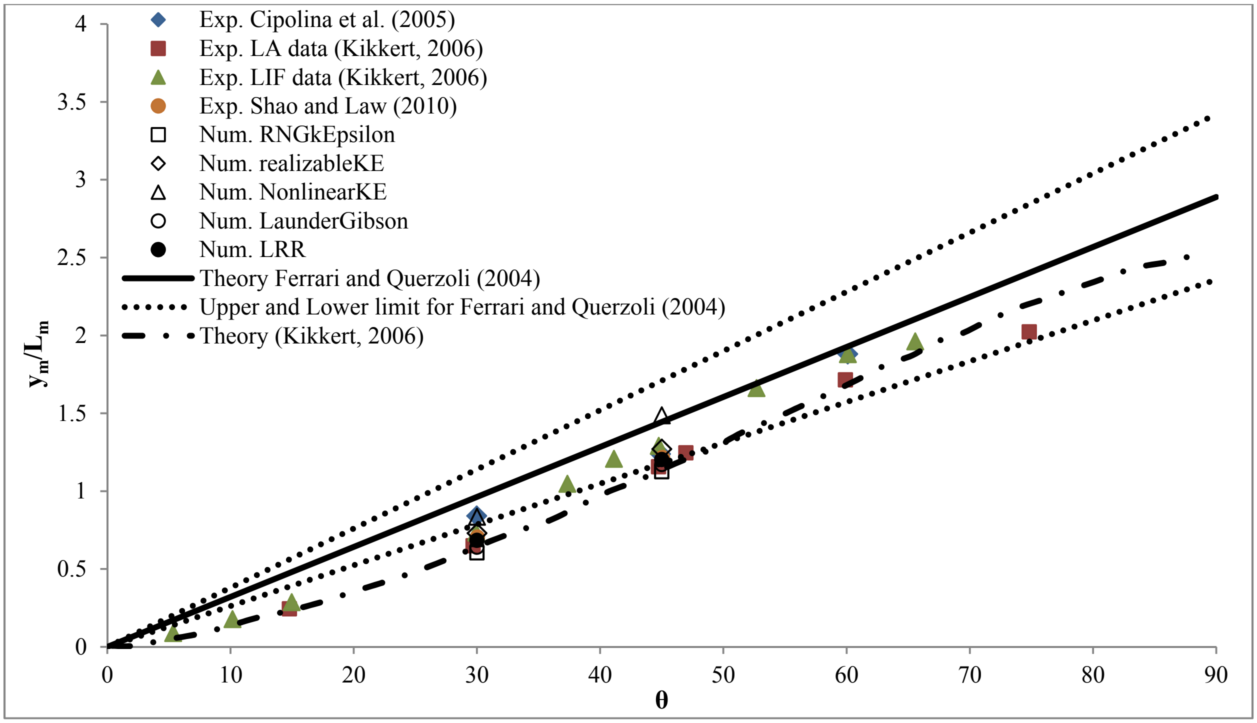

Fig. 5.12: Normalized vertical location of centerline peak as a function of initial discharge angle

The solid line is for the predicted value, and the dotted lines are the error bounds. However, most of the turbulence models as well as the previous experimental data and the analytical solution of Kikkert (2006) are consistent with the range between the predicted solution and the lower boundary (lower error boundary). The analytical solution of Kikkert is more realistic due to better consistency with the experimental data, but the model proposed by Ferrari and Querzoli (2004) could be used as a quick estimation of y_m, especially for angles larger than 30°.

5.4.2.3 Horizontal Location of Jet Return Point

The return point is defined as the point at which the dense jet passes the nozzle tap elevation when it is falling in the descending part of the jet. It is different from the impact point if the nozzle tap is placed above the bottom surface (as is the case in this study) or if the bottom is sloped. The impact point is very important and has been broadly investigated in previous studies (Roberts et al., 1997; Cipolina et al., 2005; Jirka, 2008; Ferrari and Querzoli, 2004;

Nemlioglu and Roberts, 2006; Kikkert, 2006), since it is the point that mixing and water entrainment is significantly reduced and the effluent remains attached to the bed afterwards. After this point, the plume is dispersed as a bottom dense current. However, the location of the impact point is dependent on the source height and bed slope, and therefore is very site-specific. Hence, the return point, which is independent of the source elevation and bed slope, is discussed in this paper for more generality. Since the practical nozzle height and the bed slope are typically small relative to the entire mixing zone that the jet passes through before reaching the return point, and therefore the distance between the return point and the impact point is not significant, so the return point can be used as a substitute for the impact point for practical purposes.

The return point can be determined from the centerline trajectories, as discussed earlier. As explained by Roberts et al. (1997), the impact point can be distinguished from the variation of the dilution (or concentration) along the bottom of the tank. This point (or the area around it) would have a rapid change in the dilution value due to a higher concentration around this area. After a short distance and because of more entrainment, the concentration drops again and dilution increases. The same pattern applies more significantly for the area close to the source, as is seen in Fig. 5.13 where the normalized dilution *S/Fr* is plotted versus the normalized distance from the nozzle $(x-x_0)/L_M$. The dilution value increases after effluent discharge and reaches a maximum level, then falls with a milder slope up to the return point. After this point, the dilution value increases slightly and will keep this value for a while. This might be considered as near-field mixing in the effluent discharge studies. For instance, Roberts et al. (1997) proposed that the active mixing zone starts from the nozzle up to the location where the effluent is diluted to about 95%. The remained 5% would mostly be dispersed as a dense current on the sea bottom, and the dilution rate would be very small compared to the near field. The numerical results for dilution along the x direction are close to each other and in better agreement with the experimental data from Shao and Law (2010) than from Nemlioglu and Roberts (2006) for 30°. The latter seems to over-predict in the same way as the nonlinear k-ε turbulence model compared to previous experimental data. The minimum values for all turbulence models except for the nonlinear k-ε model are very close to each other. After this point, the dilution value increases very little and remains constant afterwards. However, the results for the 45° inclined jet show more discrepancies between turbulence models, which may be due to higher Froude number for this case.

Shao and Law (2010) concluded that, since dilution values beyond the return point are similar for different Froude numbers (*Fr*=7.4 and 11.0 for 30°, and *Fr*=8.5 and 12.8 for 45°), it may not be a good solution to increase only the Froude number in order to get a higher dilution rate. Moreover, very small values for Froude numbers would result in a low dilution rate; therefore, it is very important to find an optimum range for Froude numbers that can produce the required dilution more efficiently.

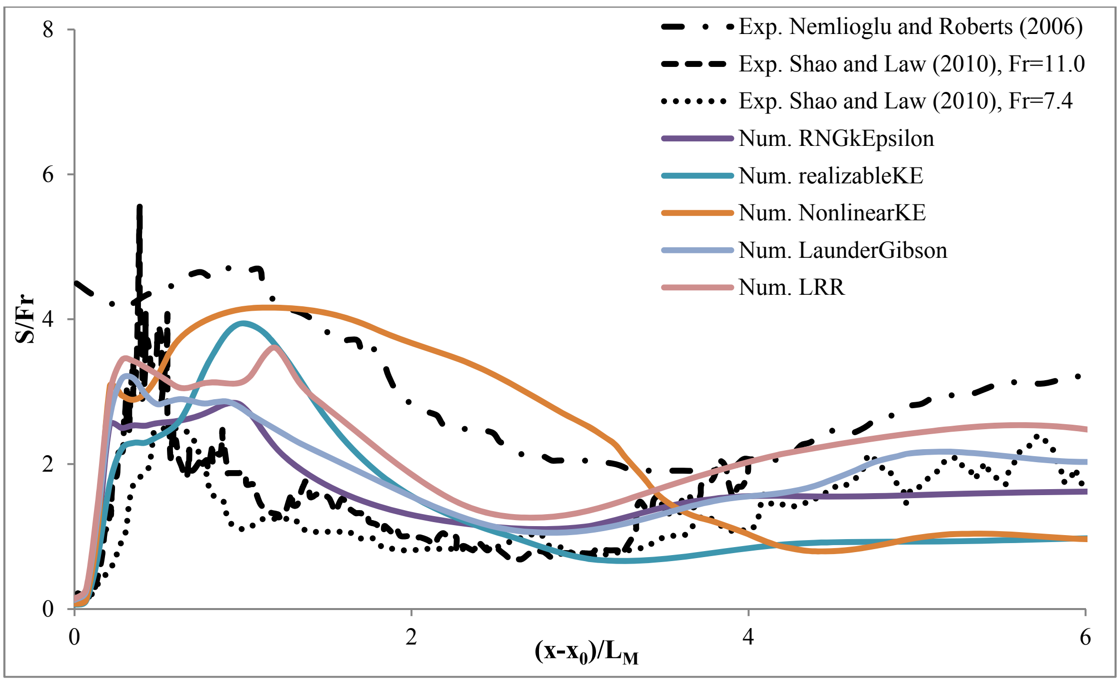

(a)

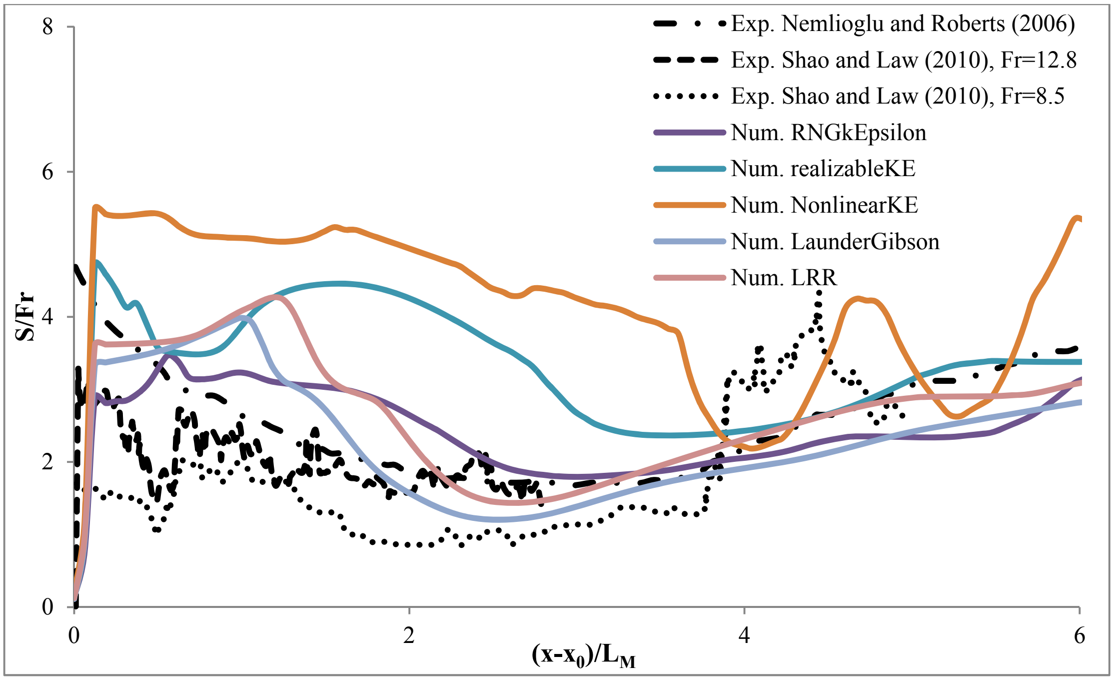

(b)

Fig. 5.13: Normalized variation of dilution along the inlet height level. a. 30°, b. 45°

Fig. 5.14 shows the horizontal location of the return point, which is normalized by the nozzle diameter and is plotted versus *Fr*. The numerical results are more consistent with the experimental data for 45° inclined dense jets rather than for 30°. The previous experimental results for 30° inclined jets are higher than the numerical predictions. Variation of the numerical results is more notable in the 45° case, and are in good agreement with Kikkert's (2006) analytical solution in both cases. The experimental data by Shao and Law (2010) are lower compared to other experimental data. The realizable *k-ε* and LRR models, which are in better agreement with the experimental data, are confirmed as the most accurate turbulence models in these figures as well.

The horizontal location of the return point is then normalized by L_M and plotted against the jet initial angle Θ in Fig. 5.15. The present study is compared to numerous previous experimental and analytical results. The analytical solution results by Ferrari and Querzoli (2004) are significantly higher than in the model by Kikkert (2006). Kikkert's analytical model divides the flow into two regimes: (i) jet-like regime; and (ii) plume-like regime. As seen from Fig. 5.15, for the jet-like regime, the return point increases with a larger slope than in the plume-like regime. The numerical results also verify this interpretation, that there is no large difference between the two angles, 30° and 45°, as seen in Fig. 5.15.

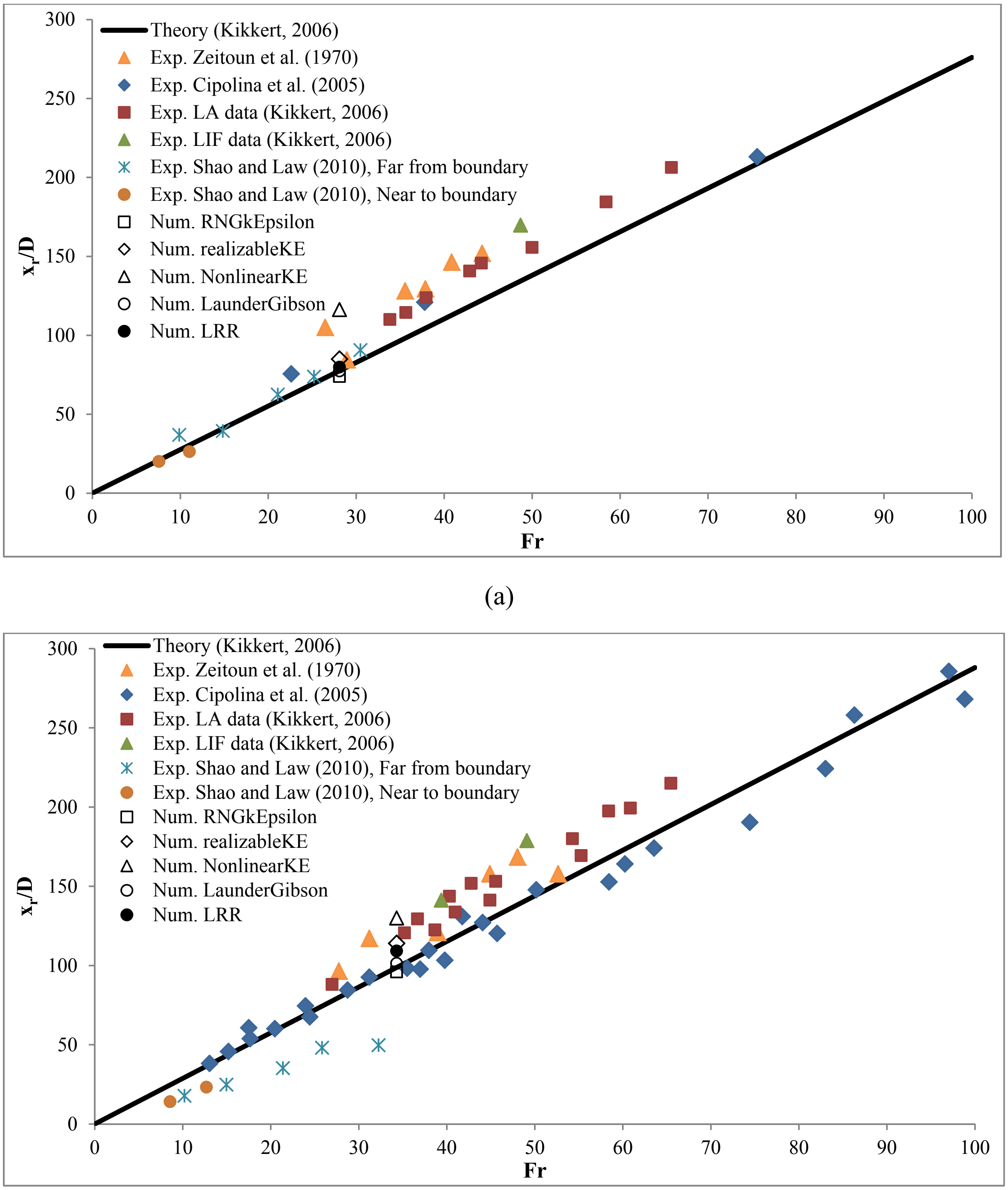

(a)

(b)

Fig. 5.14: Normalized horizontal location of return point vs. *Fr*. a. 30°, b. 45°

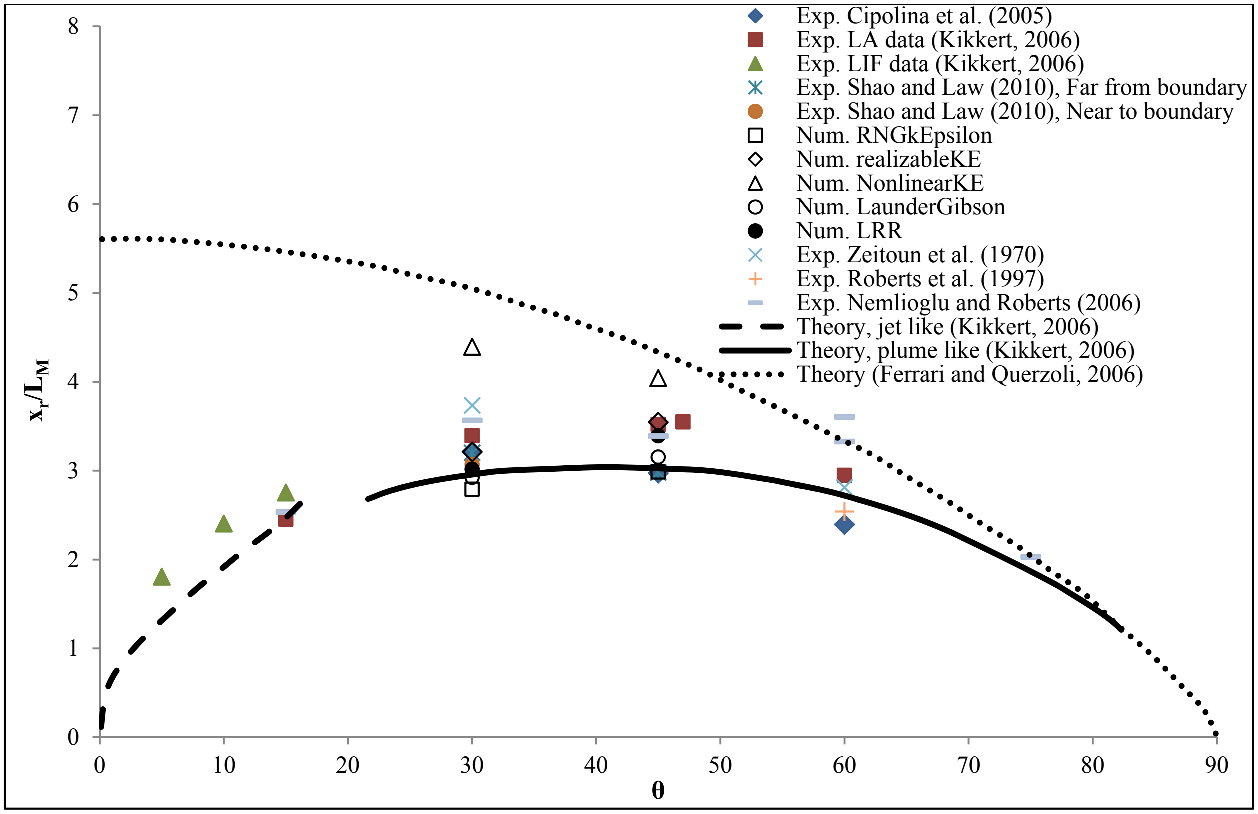

Fig. 5.15: Normalized horizontal location of return point as a function of initial discharge angle

5.4.2.4 Minimum Dilution at Centerline Peak and Return Point

The dilution values at several points of interest are of primary concern in the environmental impact assessment. Thus, the minimum dilutions achieved at these locations, such as dilution at the centerline peak and the return point, are very important to investigate. Normalized dilution at the jet centerline peak and return point by *Fr* is plotted versus the discharge angle Θ in Figs. 5.16 and 5.17, respectively.

As seen in Fig. 5.16, the numerical models slightly underestimate the dilution value at the jet centerline peak compared to the limited available experimental data. However, as Shao and Law (2010) discussed, the S_m value for the cases which are close to the boundary (the so-called boundary-affected tests) are slightly lower than the S_m value for the free jets. This may be the reason for the lower values for the numerical models as well, since they have also small values for the bed proximity parameter (y_0/L_m=0.065 for 30° and y_0/L_m=0.070 for 45°). It is also noteworthy that as expected, the realizable k-ε and LRR turbulence models are in better agreement with the experimental data than other turbulence models. The nonlinear *k-ε* turbulence model dilution value at centerline peak S_m is lower than in other models, which may be due to the smaller jet concentration spread and consequently larger water entrainment towards the jet centerline at this point.

As discussed before, the minimum dilution at the impact point, S_i, is more significant from the environmental point of view and has been studied more previously compared to the minimum dilution at the return point, S_r. However, the impact point is dependent on the specific nozzle height, and hence the dilution value at the return point has more generality and is also independent of the nozzle height.

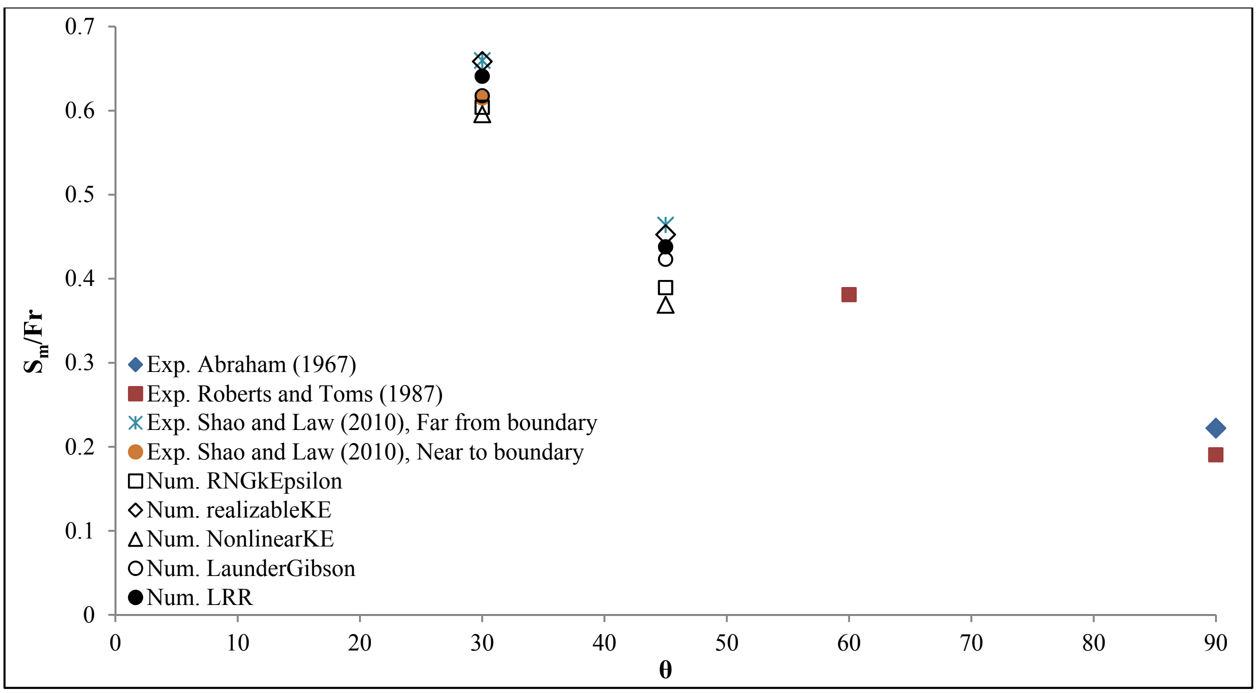

Fig. 5.16: Minimum dilution at centerline peak as a function of initial discharge angle

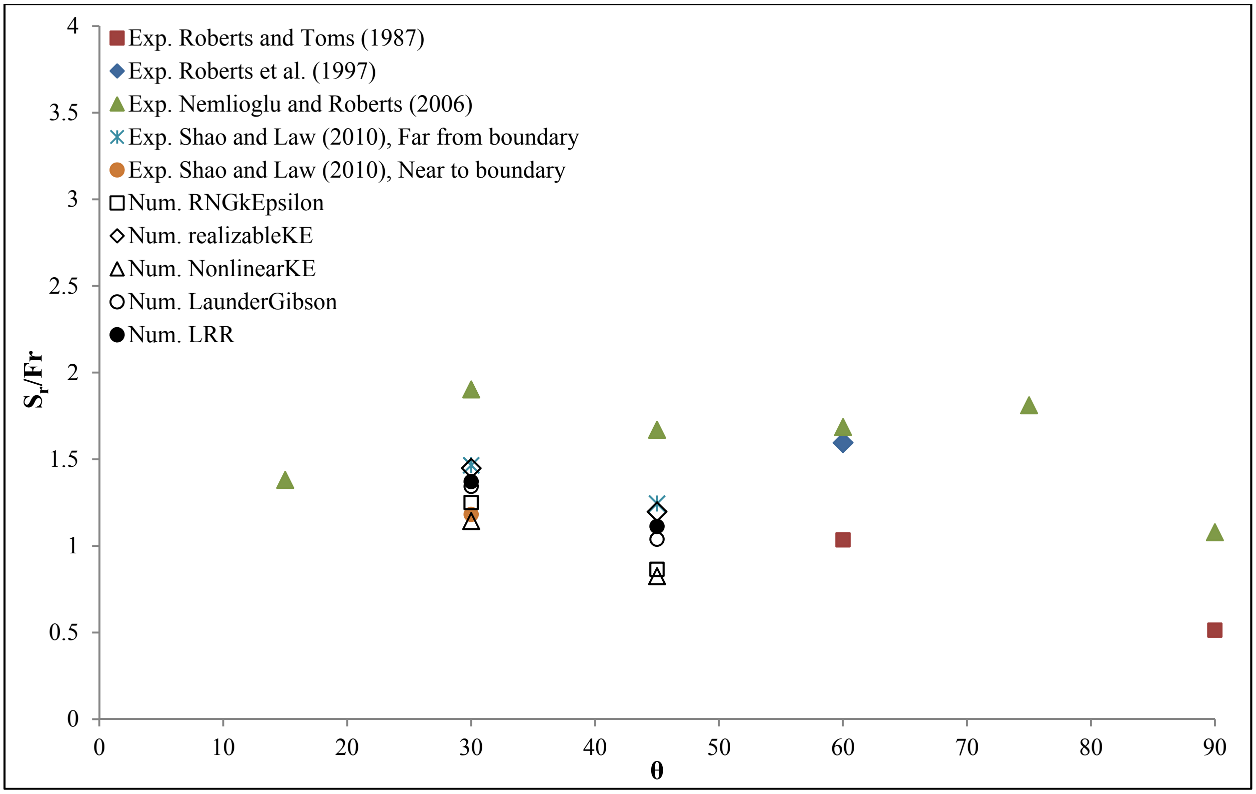

Fig. 5.17: Minimum dilution at the return point as a function of initial discharge angle

Fig. 5.17 includes the previous experimental data for S_i in order to compare with the current study (experimental data by Shao and Law (2010) are for return point, not impact point). One should note that obviously the dilution value at the impact point is higher than at the return point, and that is why the experimental data are highly scattered.

As in the case of the dilution value at the jet centerline peak, the numerical models underpredict the dilution value at the return point. However, similar to previous studies and as Nemlioglou and Roberts (2006) suggested, the numerical models confirm that discharge angle has little effect on the impact/return point dilution. More recently, Lai and Lee (2012) reported that S_i/Fr is not sensitive to jet angle when $\Theta \geq 38$, although the dilution of 45° jets is somewhat higher. They also suggested $S_i/Fr=1.06$ is a constant when $Fr \geq 20$. The impact point dilution reported in Kikkert (2006) was based on the integral concentration and measured by a Light Attenuation (LA) technique perpendicular to the jet center plane, and so they are not included in the comparison.

5.4.3 Centerline Maximum Velocity Decay

When the jet centerline is identified, the maximum velocity variation can be obtained along the centerline. Chen and Rodi (1980) suggested a power law relationship between the non-dimensionalized centerline dilution, $Fr.C_m/C_0$ and the non-dimensionalized vertical elevation, $y/D/Fr$, which is written as follows:

$$FrC_m / C_0 = a(y / D / Fr)^b \tag{5.20}$$

where a and b are the constants dependent on whether the flow is in the jet, transition, or plume regime. The different regimes are also divided according to the respective $y/D/Fr$ threshold values given by Chen and Rodi (1980). Shao and Law (2010) then concluded that there should be a similar relationship between FrU_m/U_0 and $s/D/Fr$ for the inclined dense jet. The variation of the normalized maximum centerline velocity versus the normalized downstream distance is presented in Fig. 5.18, where the axes are in a logarithmic scale. Five different cross-sections are presented for each turbulence model, and the results are compared with the experimental data from Shao and Law (2010). The curvilinear distance from the nozzle (s) is calculated in a discretized manner for each turbulence model.

As seen from Fig. 5.18, the numerical results follow the experimental data fairly well, and the RSMs are in very good agreement with the experimental data for both angles. However, the nonlinear k-ε turbulence model overestimates the result for the velocity field as well. The different turbulence models also capture the collapse of the decay processes fairly well. For both inclinations, a clear linearity is seen for the transition regime ($\sim 0.6 < s/D/Fr < \sim 6$).

5.4.4 Cross Sectional Concentration Profile

In the study of buoyant jets, a Gaussian profile is often assumed for the concentration distribution at the different cross sections when the jet is in the Zone of Established Flow (ZEF) (Shao and Law, 2010). In the present study the concentration and velocity profiles are extracted along several cross-sections as seen in Fig. 5.19. This figure shows a general inclined jet (30°) with the cross-sections perpendicular to the jet centerline. The profiles in this figure show the concentration (salinity, *S*) distribution along the cross-sections, which follows a Gaussian distribution trend. The profiles show a well-developed axisymmetric Gaussian pattern from *s/D*=3 to about *s/D*=15. After that point, the inner (lower) half spreads wider than the outer (upper) half. Shao and Law (2010) also discussed that there is a point after *s/D*=15 (about *s/D*=21) where the concentration centerline shifts a little bit below the jet velocity centerline.

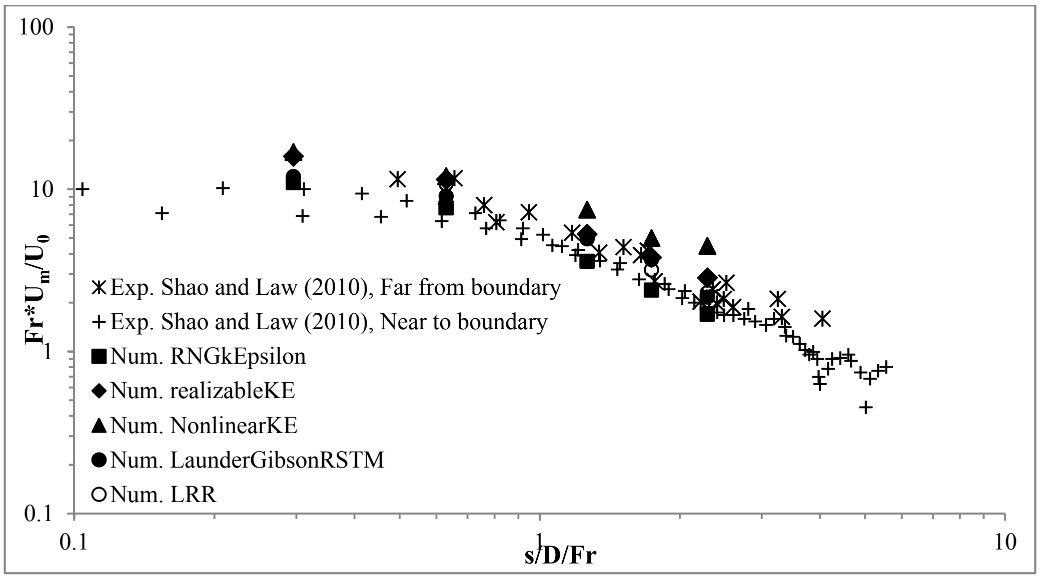

(a)

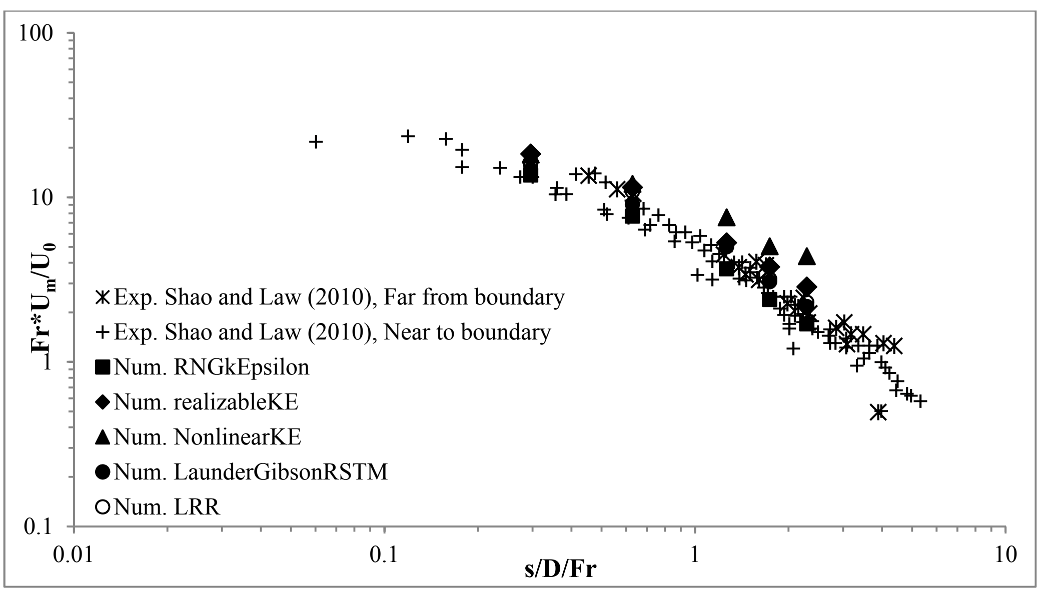

(b)

Fig. 5.18: Comparison of non-dimensionalized centerline maximum velocity decay. a. 30°, b. 45°

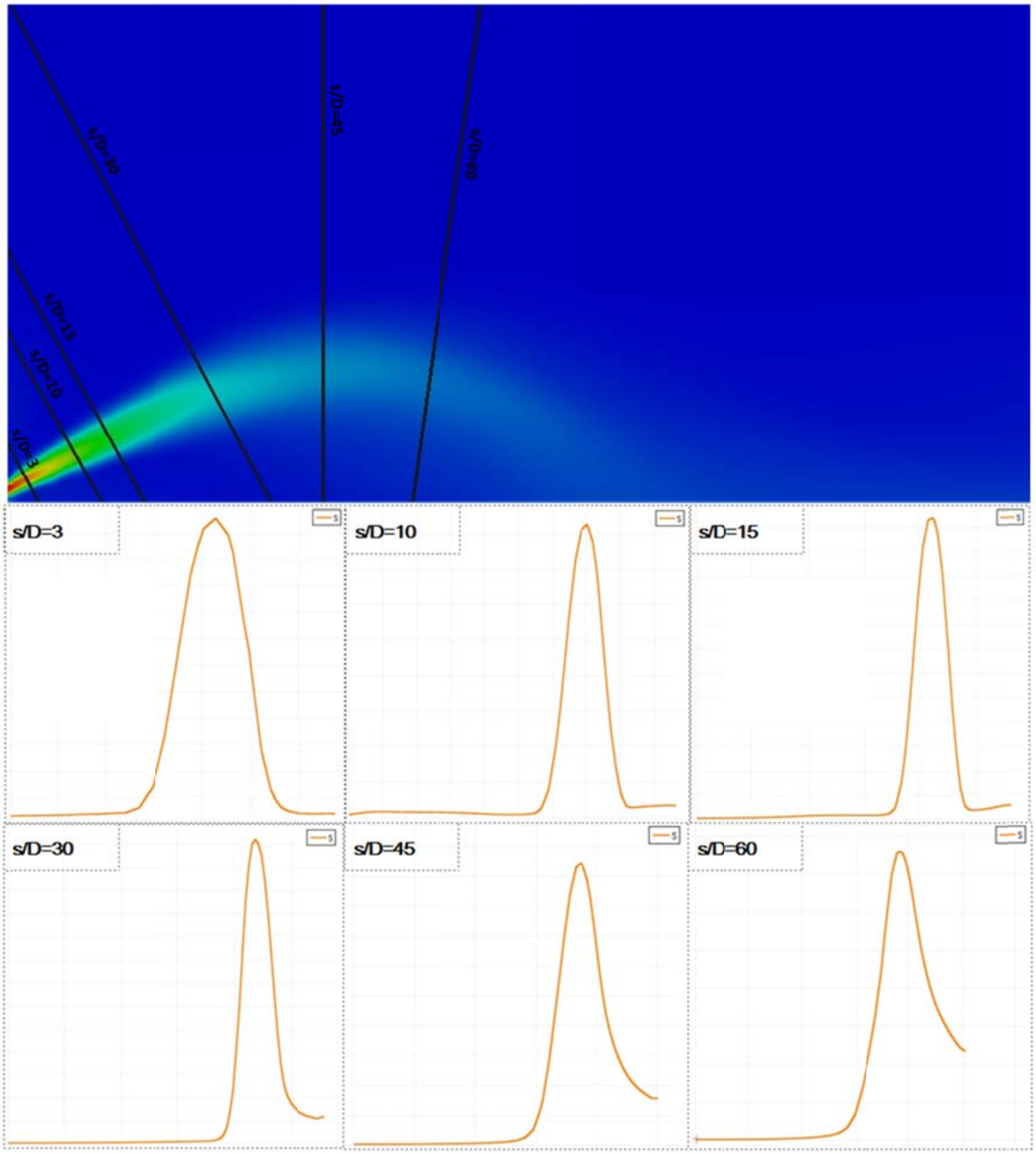

Fig. 5.19: Cross-sectional concentration (salinity, *S*) distributions at various downstream locations

For the cross-sections close to the impact point (not shown here), the concentration distribution falls into the general wall jet pattern. This suggests that the jet undergoes a transition from plume to wall jet. The concentration profiles for each turbulence model are extracted along different cross-sections and are compared to the recent experimental data by Shao and Law (2010) in Fig. 5.20.

Normalized cross-sectional profiles of C/C_c are plotted versus different values of r/b_c for all different turbulence models for 30° and 45° inclinations, where C is concentration along the cross section, C_c is the maximum concentration along the cross section, r is the radial distance, and b_c is the concentration spread width (using the e^{-1} notation).

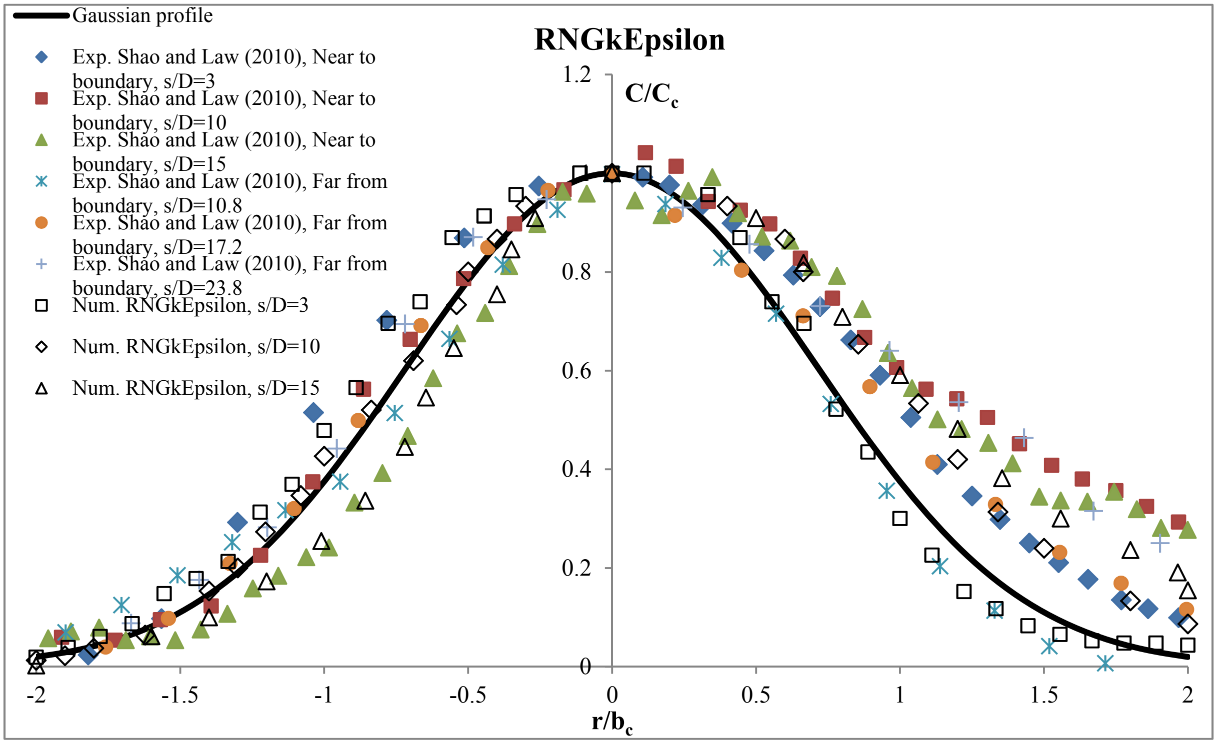

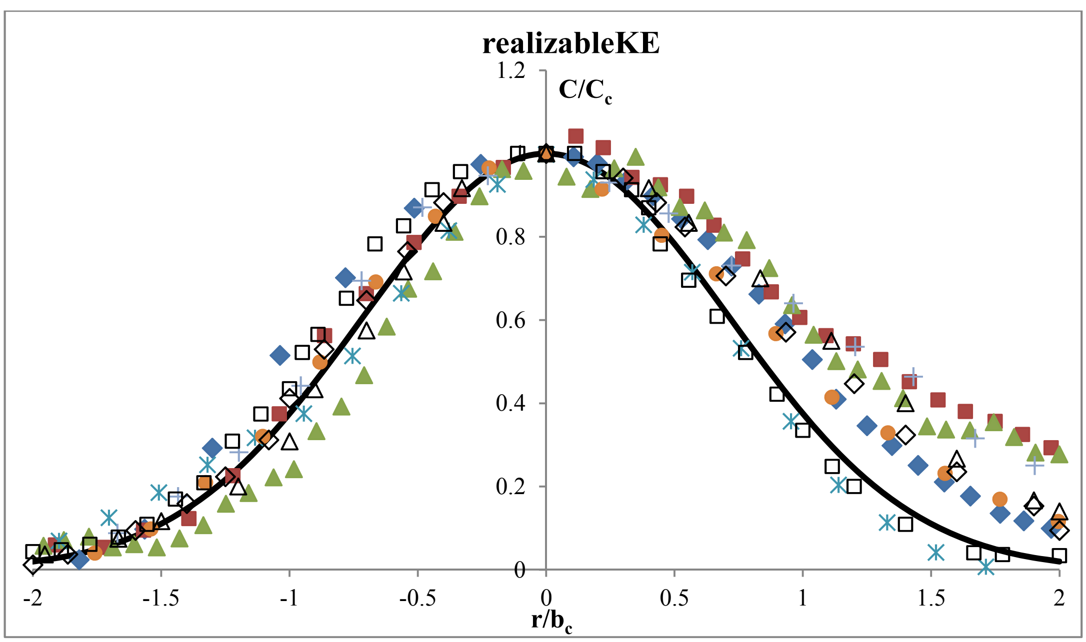

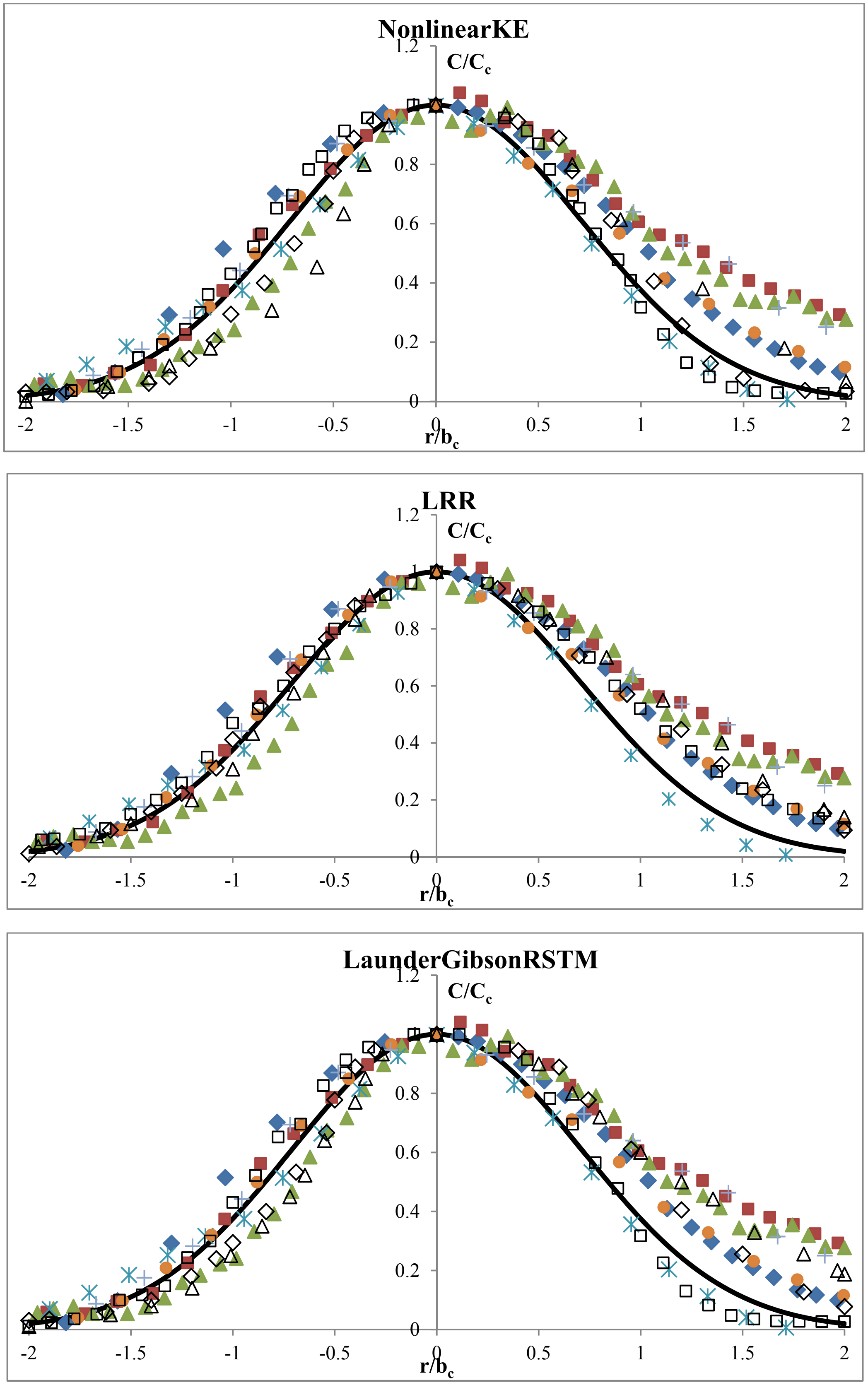

(a)

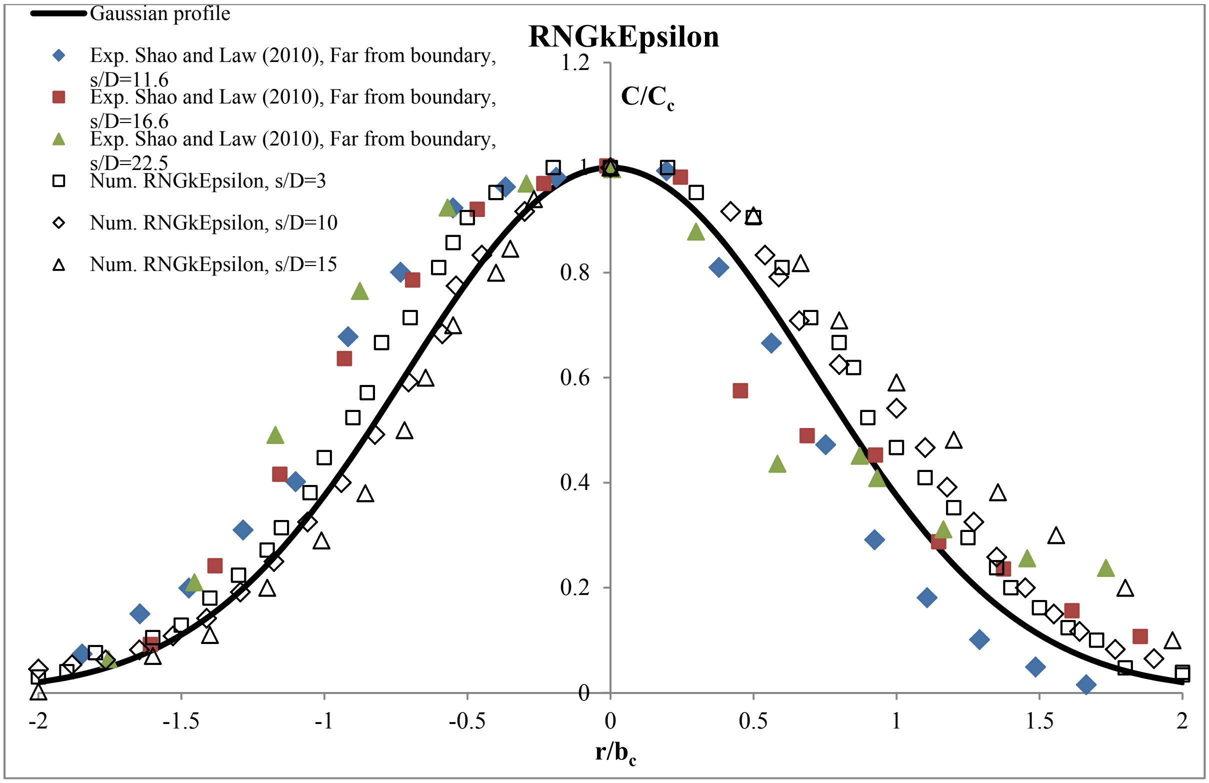
Gaussian profile
Exp. Shao and Law (2010), Far from boundary, s/D=11.6
Exp. Shao and Law (2010), Far from boundary, s/D=16.6
Exp. Shao and Law (2010), Far from boundary, s/D=22.5
Num. RNGkEpsilon, s/D=3
Num. RNGkEpsilon, s/D=10
Num. RNGkEpsilon, s/D=15
RNGkEpsilon
C/C$_c$
r/b$_c$

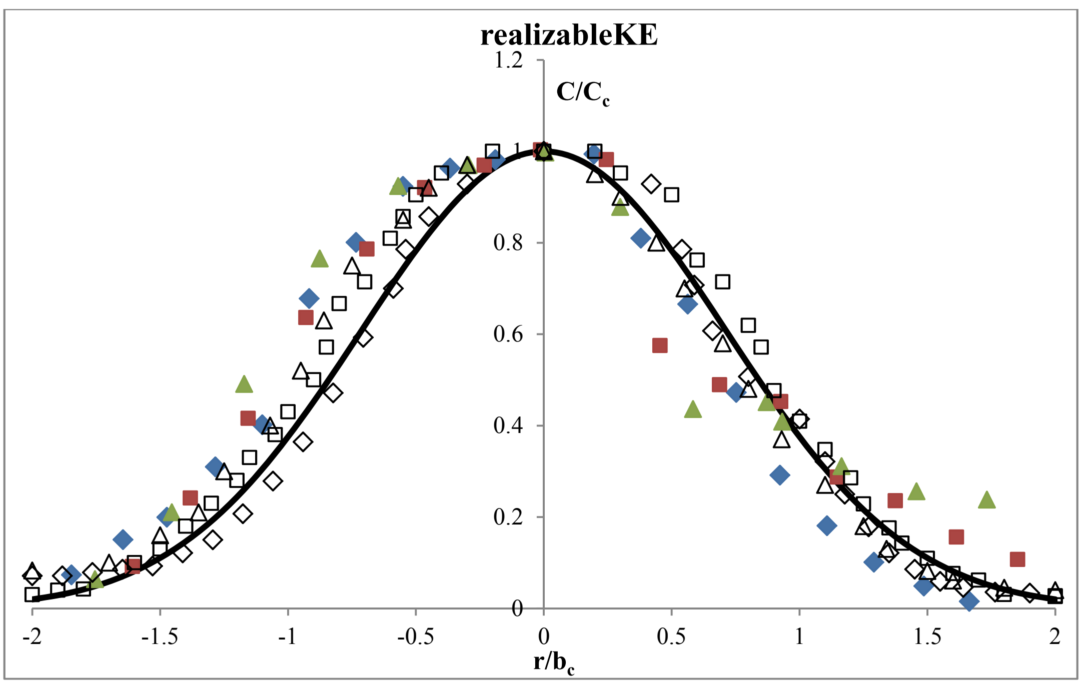
realizableKE
C/C$_c$
r/b$_c$

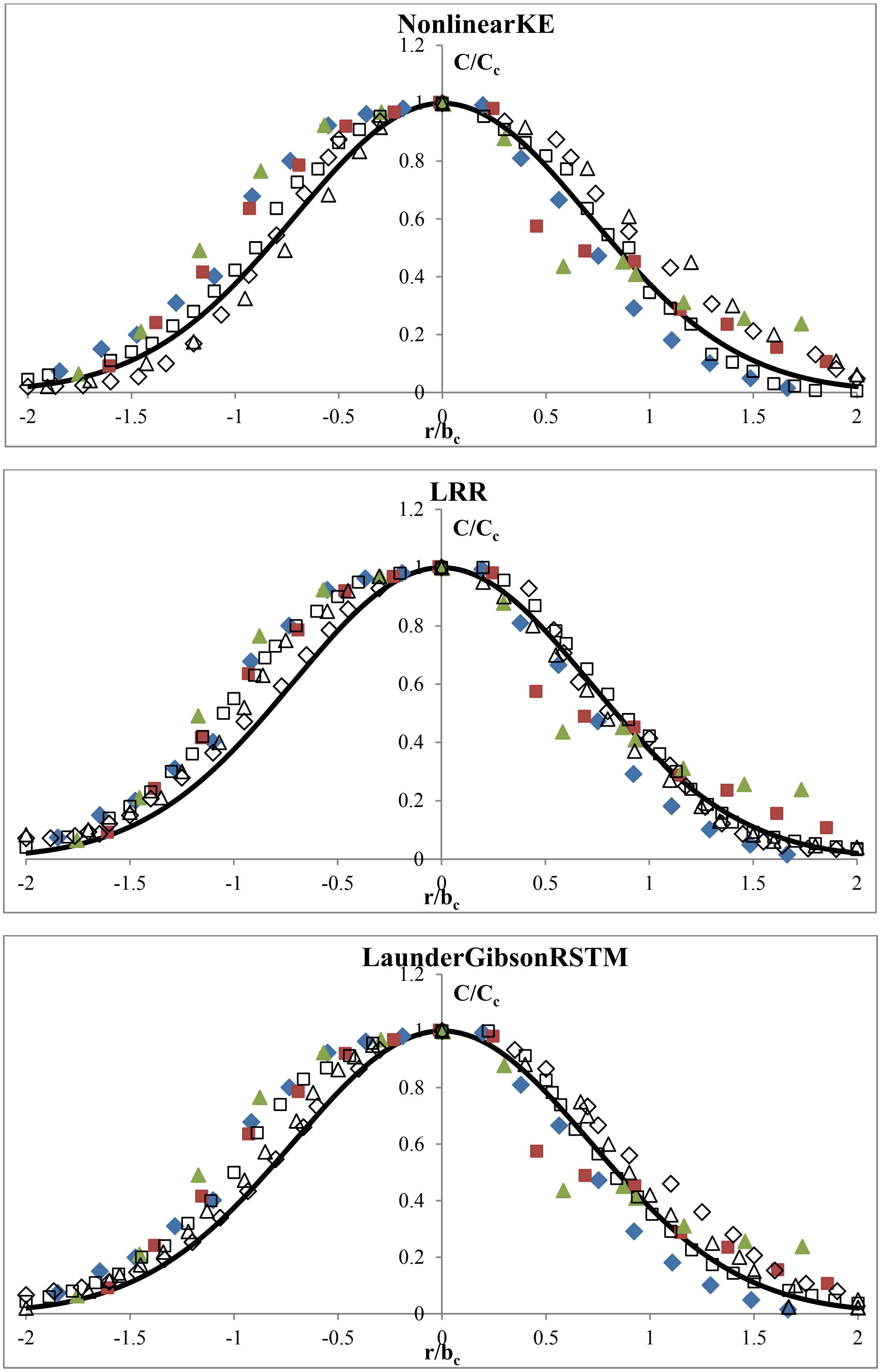

(b)

Fig. 5.20: Normalized concentration profiles at various downstream cross-sections. a. 30°, b. 45°

For both inclinations, a Gaussian pattern is seen for the outer (upper) half of the various cross-sections for different turbulence models, which is in good agreement with experimental data. On the other hand, the inner (lower) half widens considerably more compared to the outer half. This is mainly due to buoyancy-induced distortions. For the inner (lower) half, the distortion appears to increase with distance up to the maximum terminal rise point. After this maximum height, the distorted profiles appear to almost collapse. Compared to the experimental data, the realizable k-ε and RSM turbulence models are in slightly better agreement among the turbulence models tested herein. However, as seen from the figures, for the cross-sections closer to the source, the inner (lower) half deviates from the Gaussian profile less than the cross-sections further from the source. This is due to larger momentum forces in the area closer to the nozzle tap. As the jet goes farther, the momentum forces decrease and buoyancy forces dominate the flow, and consequently cause distortion mainly for the lower half of the jet. This overall process is consistent with the observations in Kikkert et al. (2007).

5.4.5 Cross-sectional Velocity Profile

Although the concentration field has been studied in mixing and dispersion investigations in more detail by previous researchers, velocity field characteristics give a good insight into jet velocity profiles as well as the jet velocity spread for inclined dense jets. Normalized cross-sectional profiles of U/U_c are plotted versus r/b_u in Fig. 5.21 for the same cross-sections as the concentration field, where U is the velocity along the cross-section, U_c is the maximum velocity along the cross-section, r is the radial distance, and b_u is the velocity spread width, again using the e^{-1} notation. The numerical results are compared to the experimental data from Shao and Law (2007), and the standard Gaussian profile.

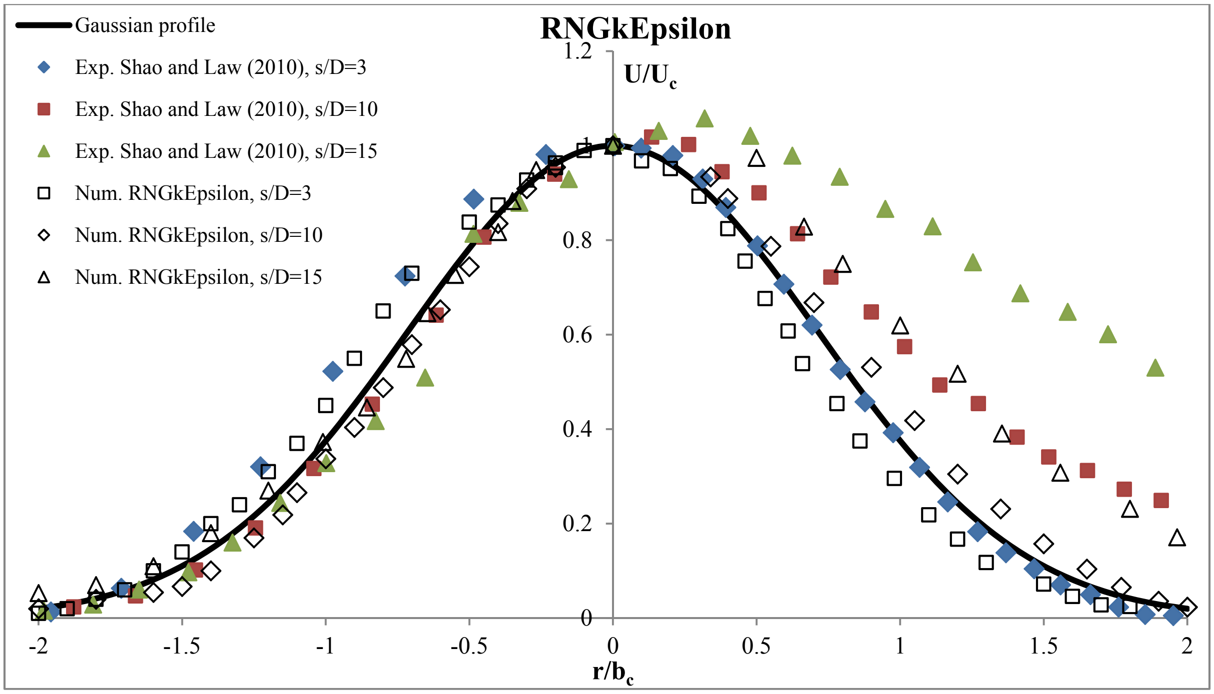
RNGkEpsilon
Gaussian profile
Exp. Shao and Law (2010), s/D=3
Exp. Shao and Law (2010), s/D=10
Exp. Shao and Law (2010), s/D=15
Num. RNGkEpsilon, s/D=3
Num. RNGkEpsilon, s/D=10
Num. RNGkEpsilon, s/D=15
U/U_c
r/b_c
1.2
0.8
0.6
0.4
0.2
0
-2
-1.5
-1
-0.5
0
0.5
1
1.5
2

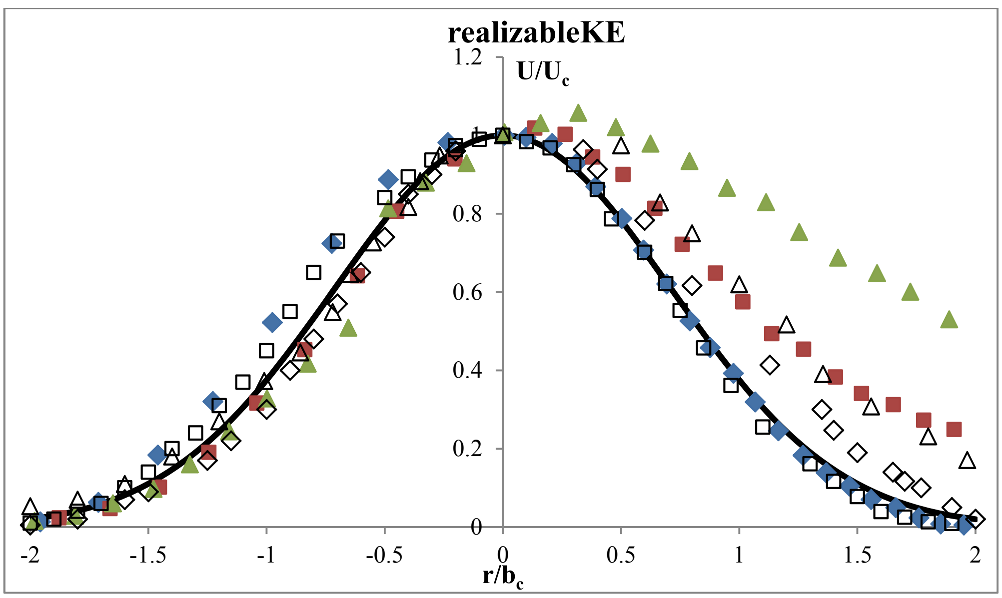
realizableKE
U/U_c
r/b_c
1.2
0.8
0.6
0.4
0.2
0
-2
-1.5
-1
-0.5
0
0.5
1
1.5
2

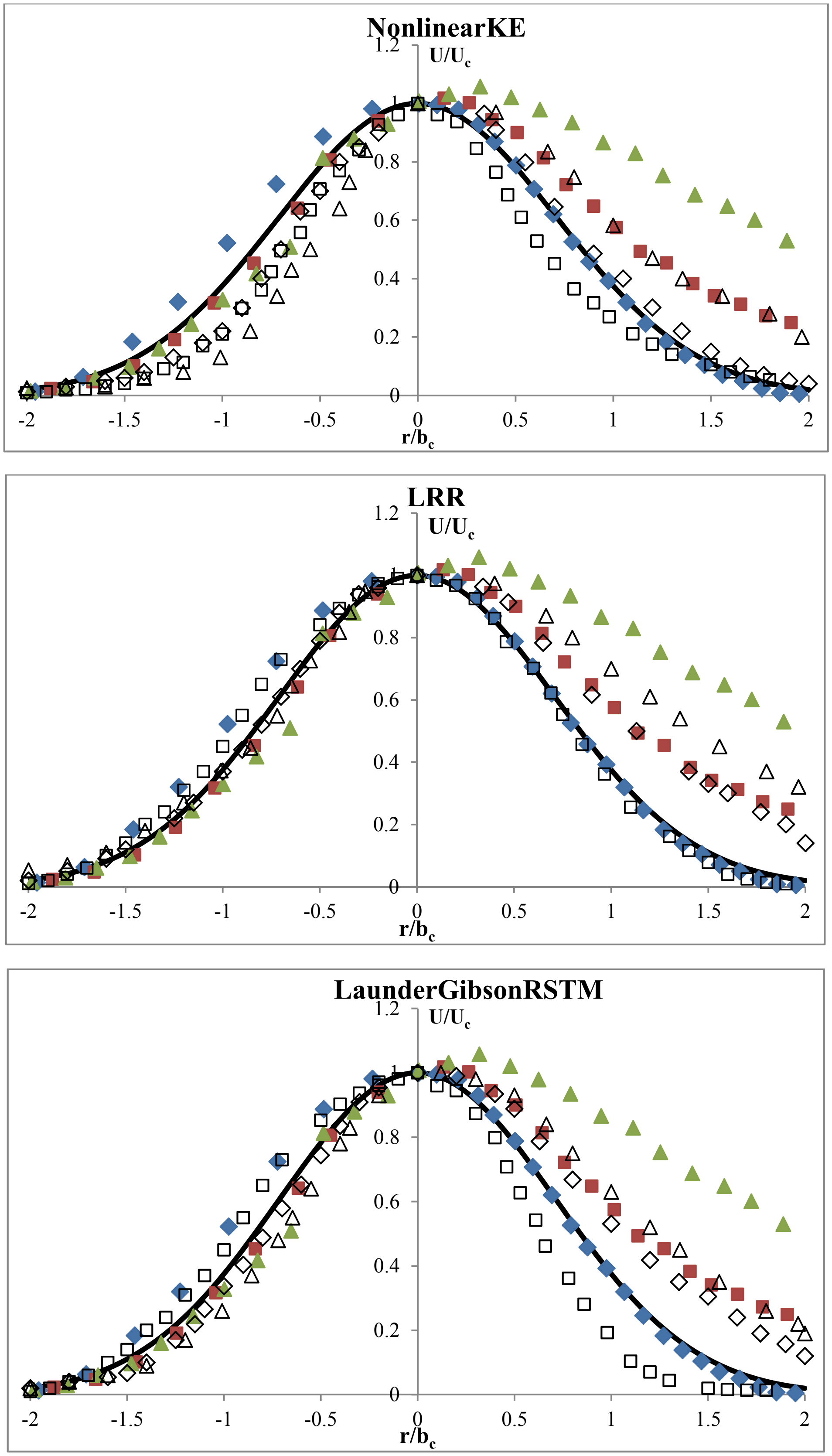

Fig. 5.21: Normalized velocity profiles at various downstream cross-sections for 30°

As in the case of the concentration profiles, symmetric Gaussian distribution is clearly revealed for different turbulence models. However, it seems that except for the nonlinear *k-ε* model, other models are in better agreement with the experimental data for the outer (upper) half of the jet compared to the inner (lower) half. As seen in Fig. 5.21, the turbulence models under-estimate the velocity values for the inner half of the jet, especially for the last two cross-sections (s/D=10 and s/D=15), where the instability is larger.

5.4.6 Jet Spread

Jet spread study is a means to characterize the jet growth, and it is done for both the concentration and velocity fields. It is based on the Gaussian distribution of concentration and velocity and then applying the e^{-1} ratio to the centerline maximum value. The spread width profiles for the various turbulence models are shown in Fig. 5.22 after normalization by respective Fr. Since the results for both angles were close to each other for the different cross-sections, each point represents the value for both 30° and 45°. Experimental data from Shao and Law (2005) is shown for a better comparison. As seen from Fig. 5.22, due to greater stability at the outer (upper) edge of the jet, the concentration and velocity spread (Fig. 5.22 *b* and *d*) are more consistent than at the lower edge of the jet (Fig. 5.22 *a* and *c*). In addition, the lower half of the jet shows more scatter than the upper half in the initial growing range. Kikkert (2006) argued that after normalization by D/Fr, the variation of the upper concentration spread width for different inclinations follows the analytical solution. However, as seen in the plot, it is true for about one D/Fr from the nozzle, which is approximately equal to one L_M. Farther downstream, both the experimental and numerical results are lower than Kikkert's prediction. The numerical results are very close to each other. All turbulence models follow the experimental scatters. However, there is better agreement between the numerical results and experimental data for lower $s/D/Fr$. This is due to stability of the dense flow in the jet-like regime. Farther downstream, where the buoyancy forces grow, more divergent scatters are seen in the numerical and experimental results for both the upper and lower halves of the jet.

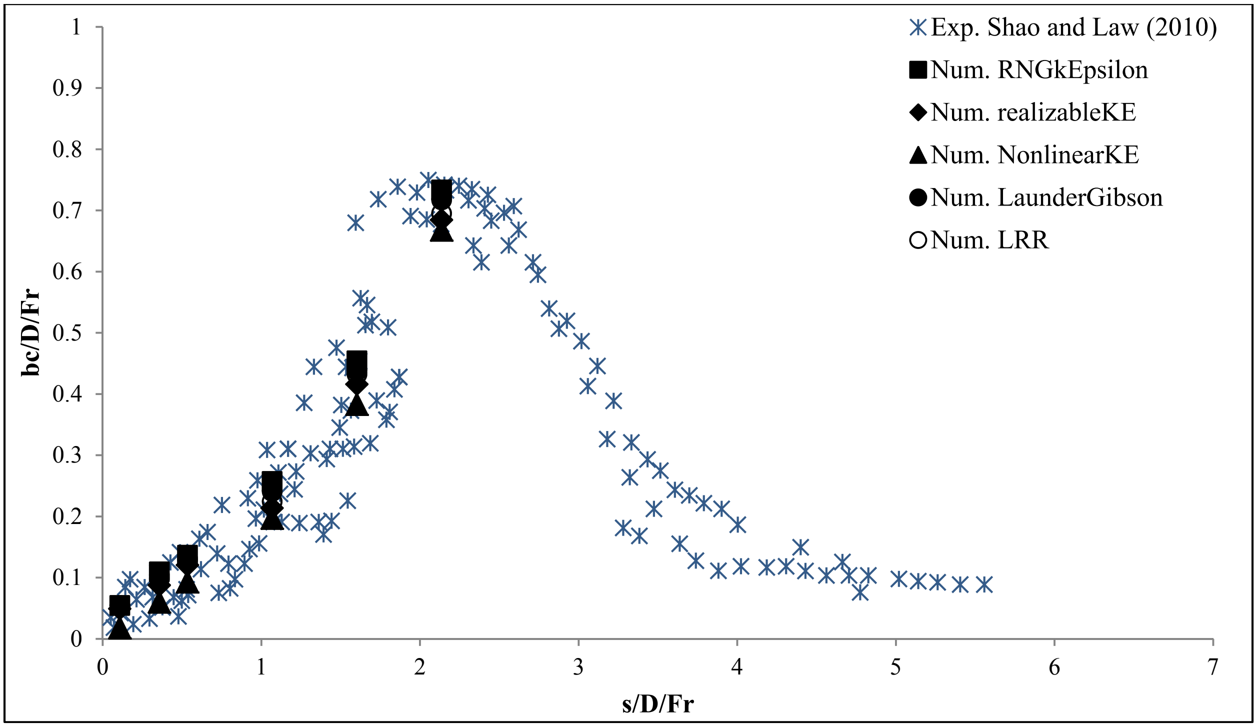
Exp. Shao and Law (2010)
Num. RNGkEpsilon
Num. realizableKE
Num. NonlinearKE
Num. LaunderGibson
Num. LRR
bc/D/Fr
s/D/Fr
0
0.1
0.2
0.3
0.4
0.5
0.6
0.7
0.8
0.9
1
0
1
2
3
4
5
6
7

(a)

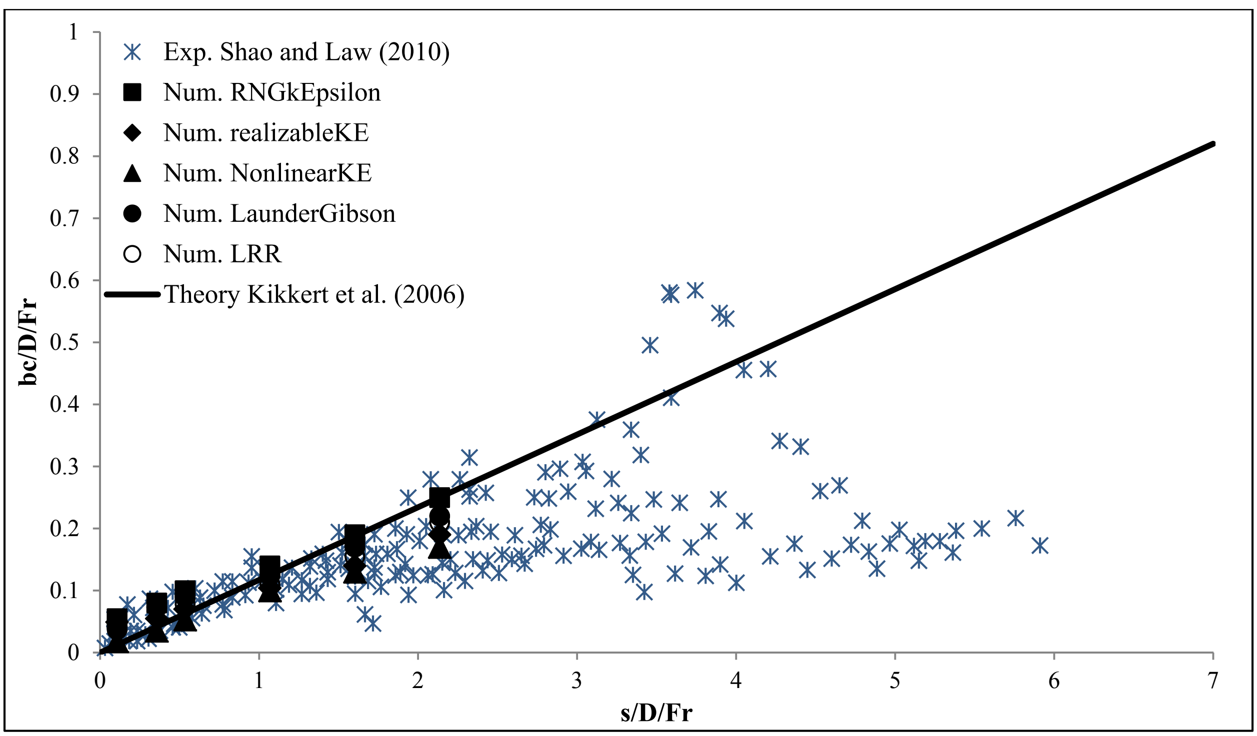
Exp. Shao and Law (2010)
Num. RNGkEpsilon
Num. realizableKE
Num. NonlinearKE
Num. LaunderGibson
Num. LRR
Theory Kikkert et al. (2006)
bc/D/Fr
s/D/Fr
0
0.1
0.2
0.3
0.4
0.5
0.6
0.7
0.8
0.9
1
0
1
2
3
4
5
6
7

(b)

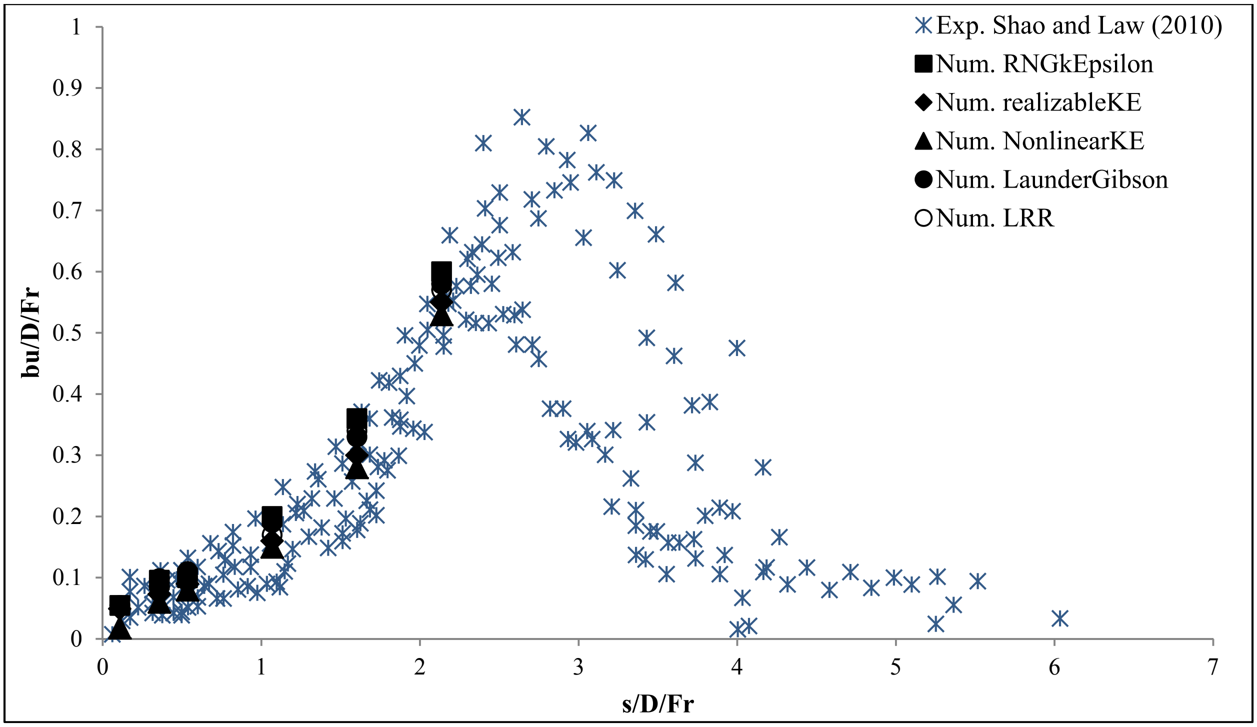

(c)

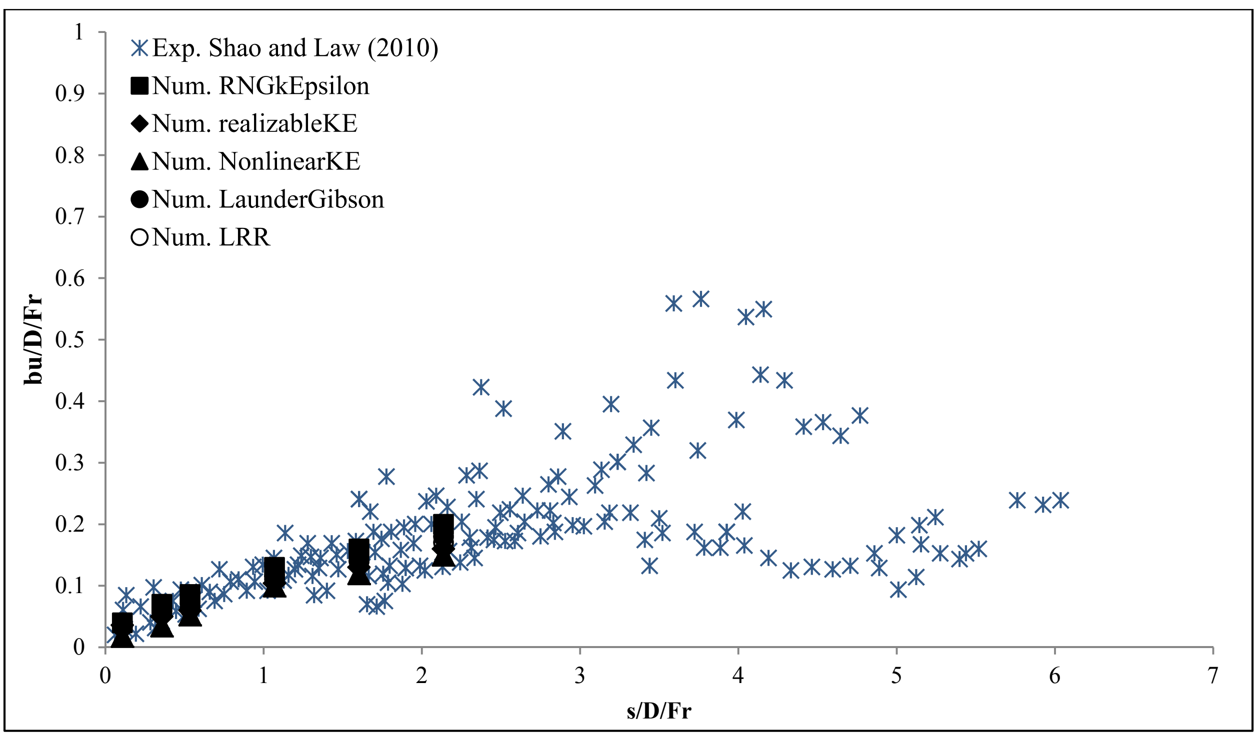

(d)

Fig. 5.22: Comparison of concentration and velocity spread width along the trajectory. a. Lower *bc*, b. Upper *bc*, c. Lower *bu*, d. Upper *bu*

5.5 Concluding Remarks

The main objective of this paper was to numerically study the detailed geometric, concentration, and velocity characteristics of inclined dense jets in stationary ambient water. Many experimental investigations have been done in this field, but more numerical studies need to be conducted. Two inclinations, 30° and 45°, which are very applicable for the brine discharges in shallow coastal waters, were chosen to be modeled using the OpenFOAM CFD toolbox. A range of turbulence models have been applied in order to understand the accuracy of turbulence models in dense jet studies. These models are of the LEVM, NLEVM, and RSM types. The governing equations are solved using finite volume methods on a structured, refined mesh grid system. The numerical results have been compared to comprehensive experimental data as well as results from analytical models proposed by previous studies.

The conclusions of the present study are as follows:

1. The correlations between the terminal rise height, the centerline peak location, the centerline peak dilution, the horizontal location of the return point, and the corresponding dilution with the densimetric Froude number were studied using various turbulence models. The numerical results were in good agreement with various previous experimental data and analytical models. However, the nonlinear k-ε turbulence model showed more discrepancies compared to the experimental data.

2. The dilution, which is one of the key terms in designing ocean outfall systems, is calculated for both the centerline peak and the return point. The return point is chosen in this study due to more generality than the impact point. The numerical models showed a slight underestimation of the dilution values, especially for the RNG k-ε and nonlinear k-ε turbulence models. As seen for the dilution at the return point, there is no large difference between the various inclinations. Therefore, no specific inclination may be considered as the optimum discharge angle. However, previous experimental studies reported 60° as the optimum angle, based on maximum mixing efficiency.

3. Non-dimensionalized centerline maximum velocity decay for 30° and 45° inclinations follows the typical dense jet behavior. The initial flat portion of the results up to about

s/D/Fr < ~ 0.6 shows that there is an initial region corresponding to the potential core. After this point, the maximum velocity at the jet centerline decreases in an almost linear pattern. The numerical results are much closer to each other at the potential core region, where the velocity decay rate is minimal. This initial jet region is also characterized from the prominent momentum forces in this region resulting from the initial jet velocity at the nozzle.

4. The cross-sectional velocity and concentration profiles showed a good axisymmetric Gaussian pattern for the outer half of the jet, which turns into an asymmetric Gaussian pattern with much wider spread in the inner half of the dense jet. There was good agreement between the different turbulence models and the experimental data, especially for the outer half of the jet. Although the results of different turbulence models were slightly lower compared to the experimental data for the inner half, the pattern they followed was similar to that in the experimental data. Moreover, the numerical concentration and velocity profiles are in a better agreement with a standard Gaussian profile closer to the source rather than farther downstream.

5. The jet spread is divided into jet concentration spread and jet velocity spread, since the velocity and concentration centerlines are not exactly coincident with each other. As was expected, the scatters are dispersed more in the inner half of the jet as well as for larger values of *s/D/Fr* due to buoyancy-induced instabilities. The numerical results of different turbulence models are closer to each other for the regions closer to the nozzle, and start to deviate farther downstream.

6. It was found that the realizable k-ε (an LEVM) and LRR (an RSM) turbulence models tend to be more accurate among the five different turbulence models tested herein. However, the computational costs of the different turbulence models have to be considered as well. RSMs are more expensive than both LEVMs and NLEVMs (about 20% more than LEVMs), and thus need more computational resources. The results of the nonlinear k-ε model (an NLEVM) were not as accurate as the other turbulence models, and overestimated the trajectory characteristics of the dense jet.

7. Other inclinations need to be studied numerically for a better understanding of the inclined turbulent dense jets and for evaluating the numerical model's accuracy in this field. The inclined dense jet discharges into flowing ambient water are also required to be studied which are currently being investigated by the authors.

Chapter 6

Conclusions and Suggestions for Future Work

6.1 Conclusions

Two important scenarios of effluent discharges into the ocean waters have been investigated using a mathematical and numerical model in this thesis. Submerged discharges have been selected due to a higher mixing efficiency compared to the surface discharges. Since the nature of the jets discharged into the ambient is turbulent, it is important to examine different turbulence models and evaluate their accuracy in order to suggest the most efficient for engineering applications.

The main contribution of this thesis is the development of an open source code (OpenFOAM) to model the effluent discharges as submerged jets. The aim was to prepare a code suitable for incompressible fluids while the density varies due to salinity and temperature changes. Therefore, the density equations, as well as concentration and temperature equations, have been implemented into this novel code. Among different turbulence models chosen for each scenario, some of them were proven to be more stable. Therefore, the numerical schemes for solving temporal, advection, and diffusion terms had to be carefully chosen and validated. It was found that advection terms in momentum and concentration/temperature equations were more sensitive to higher order schemes compared to diffusion terms. To get a higher convergence rate for iterative solvers, the effective pre-conditioners have been found and applied into the model.

The first case considered the submerged positively buoyant jet discharging into ambient wall as a turbulent wall jet. Four RANS turbulence models have been examined in this case: standard k-ε, RNG k-ε, realizable k-ε, and SST k-ω models. It was found that the numerical results for both velocity and temperature fields were in good agreement with previous experimental and numerical data. The results of k-ε category models were shown to be very close to each other. However, the SST k-ω model was different than those models. This might be due to different governing equations employed, especially for turbulent viscosity. Among the three k-ε turbulence models, RNG k-ε and realizable k-ε models performed more accurately. That was why these two models along with other three models were chosen for the simulation of inclined dense jets.

The numerical results for the offset planes (planes parallel to the symmetrical plane) have been studied for the first time (to the best of the author's knowledge) and it was compared to the available experimental data which showed a good accuracy in flow development even across the width of the tank. Comparison of spanwise velocity confirmed the formation of a secondary vortex, where the flow was directed away from the symmetry plane, and in the area farther from the centerline plane. Moreover, based on the temperature decay profiles and dilution contours of different jets, it was understood that increasing the Froude number may not be the best solution for getting a higher dilution rate. In fact, it is the trajectory that characterizes and significantly influences the dilution rate.

The second case focused on the inclined submerged dense jets discharging into the stationary ambient water. Consideration was given to shallow waters where the mixing and dispersion rate is more critical due to less ambient height for dilution of the jets. Three new turbulence models have been compared to those used in the previous section: nonlinear k-ε, Launder-Gibson, and LRR models. One would expect better results from RSMs as they solve the transport equation for product and dissipation rate simultaneously. These models, however, are more expensive numerically compared to both LEVMs and NLEVMs. Still, the results of RSMs were close to RNG k-ε and realizable k-ε models. The flow field has been modeled well for inclined dense jets and the dilution values were found to be in good agreement with available experimental and analytical data. Nonlinear k-ε turbulence model results were found to be not as good as those of the other models, although the run time for this model is longer than LEVMs.

It is found that for the dilution at the return point, there is no significant difference between the various inclinations of the jet. Therefore, no specific inclination may be considered as the optimum discharge angle. However, based on maximum mixing efficiency, previous experimental studies reported 60° as the optimum angle. For the velocity field, the initial flat portion of the numerical results up to about $s/D/Fr < \sim 0.6$ showed the presence of an initial region corresponding to the potential core. Past this point, the maximum velocity at the jet centerline decreases almost linearly.

The inclined dense jet spread is divided into the jet concentration spread and jet velocity spread, since the velocity and concentration centerlines are not exactly coincident with each other. As expected, the scatters are dispersed more in the inner half of the jet, as well as for larger values of s/D/Fr, due to buoyancy-induced instabilities. The numerical results of the different turbulence models are similar for the regions close to the nozzle, but start deviating farther downstream.

6.2 Suggestions for Future Work

The following recommendations are proposed for numerical modeling of submerged jets in further studies:

- Structured refined mesh systems were used for both cases studied herein. However, OpenFOAM has the capability to apply FVM to unstructured grids. The non-conformal mesh grid is also available in the model and this will be studied by the author in detail during future PhD work.
- A wide range of numerical models have been applied for the cases considered herein. OpenFOAM usually contains the latest version of the turbulence models. However, it is useful if one searches for new changes that may occur at a later date in turbulence modeling and implement those changes to the developed models. This in itself represents a good research line to investigate turbulence models within OpenFOAM.
- A broad range of numerical schemes have been used to solve the advection and diffusion terms. More elaborated numerical schemes can be developed in OpenFOAM to improve their accuracy and stability.
- Stationary and un-stratified ambient is considered here as a first step in numerical modeling. However, cross-flow and stratification may be easily applied to the model.
- More jet inclinations are recommended to be modelled numerically to see the effect of angle. Higher angles can be modeled for the regions with deeper ambient water.

References

1. Abessi O, Saeedi M, Zaker NH, Kheirkhah Gildeh H (2010) Waste field characteristics, ultimate mixing and dilution in surface discharge of dense jets into stagnant water bodies. (in Persian), Journal of Water and Wastewater, Vol. 1, Tehran, Iran

2. Abrahamsson H, Johansson B, Lofdahl L (1997) Turbulence field of a fully develop three dimensional wall jet. Internal report no. 97/1, Department of Thermo and Fluid Dynamics, Chalmers Univ. of Tech., Goteborg, Sweden

3. Anderson JD (1995) Computational Fluid Dynamics, the basic with applications. McGraw-Hill, US

4. ANSYS CFX-5 (2004) User Guide, ANSYS Canada Ltd, Ontario, Canada

5. ANSYS FLUENT (2009), Theory Guide, Version 12.0

6. Anwar HO (1969) Behavior of buoyant jet in calm fluid. J. Hydraul. Division, ASCE HY4, July, 1289-1303

7. Balasubramanian V, Jain SC (1978) Horizontal buoyant jets in quiescent shallow water. J. Environ. Eng. Division, 104(4): 717-730

8. Baldwin B, Lomax H (1978) Thin-layer approximation and algebraic model for separated turbulent flows. AIAA 78-257

9. Bauer W, Haag O, Hennecke DK (2000) Accuracy and robustness of nonlinear eddy viscosity models. J Heat and Fluid Flow, 21:312-319

10. Bigg PH (1983) Density of water in SI units over the range of 0-100 ^{0}C. British Journal of Applied Physics, 18:521-537

11. Bleninger T, Jirka GH (2008) Modeling and environmentally sound management of brine discharges from desalination plants. Desalination 221:585–597

12. Bleninger T, Niepelt A, Jirka GH (2009) Desalination plant discharge calculator. Paper BD 180 for EDS Congress, Baden, Germany

13. Bloomfield LJ, Kerr RC (2002) Inclined turbulent fountains. J Fluid Mech 451:283-294

14. Cebeci T, Smith A (1974) Analysis of turbulent boundary layers. Academic Press

15. Chen CJ, Rodi W (1980) Vertical turbulent buoyant jets: a review of experimental data. NASA STI/Recon Technical Report A 80

16. Chu PCK, Lee JHW, Chu VH (1999) Spreading of a turbulent round jet in coflow. J Hydraul Eng, ASCE 125(2):193-204

17. Cipolina A, Brucato A, Grisafi F et al (2005) Bench-scale investigation of inclined dense jets. J Hydraul Eng, ASCE 131(11):1017-1022

18. Crow SC (1968) Viscoelastic properties of fine-grained incompressible turbulence. J Fluid Mech., 33:1-20

19. Daly BJ, Harlow FH (1970) Transport equations in turbulence. J Phys. Fluids, 13: 2634-2649

20. Davidson L (2011) An introduction to turbulence models. Department of Thermo and Fluid Dynamics, Chalmers University of Technology, Sweden

21. Davis MR, Winarto H (1980) Jet diffusion from a circular nozzle about a solid surface. J. of Fluid Mechanics, 101(1):201-221

22. Einav R, Lokiec F (2003) Environmental aspects of a desalination plant in Ashkelon. Desalination 156:79-85

23. Elhaggag ME, Elgamal MH, Farouk MI (2011) Experimental and numerical investigation of desalination plant outfalls in limited disposal areas, J Environ Protec 2:828-839

24. Ferrari S, Querzoli G (2004) Sea discharge of brine from desalination plants: a laboratory model of negatively buoyant jets. In: MWWD 2004-The 3rd international

conference on marine waste water disposal and marine environment, September 17-October 2, Catania, Italy

25. Ferziger JH, Peric M (2002) Computational methods for fluid dynamics, 3rd revised, Springer-Verlag

26. Fischer HB, List EJ, Koh RCY, Imberger J, Brooks NH (1979) Mixing in inland and coastal waters. Academic Press

27. Foster K, Parker G. Fluids. Wiley-Interscience 1970, New York

28. Fu S, Launder BE, Leschziner MA (1987) Modeling strongly swirling recirculating jet flow with Reynolds-stress transport closure. Six Symposium on Turbulence Shear Flows, Toulouse, France

29. Gibson MM, Launder BE (1978) Ground effects on pressure fluctuations in the atmospheric boundary layer. J Fluid Mech., 86:491-511

30. Global Water Intelligence editorial team (2004) Desalination markets: 2005-2015. Media Analytics Ltd. Oxford, UK

31. Hashim A, Hajjaj M (2005) Impact of desalination plants fluid effluents on the integrity of seawater, with the Arabian Gulf in perspective. Desalination 182: 373-393

32. Huai W, Li Z, Qian Z et al. (2010) Numerical simulation of horizontal buoyant wall jet, J Hydrody 22(1):58-65

33. Issa RI (1985) Solution of the implicitly discretized fluid flow equations by operator-splitting. J Comput. Physics 62:40-65

34. Issa RI, Gosman AD, Watkins AP (1986) The computation of compressible and incompressible recirculating flow by a non-iterative implicit scheme, J Comp Phys 62:66-82

35. Jasak H (1996) Error analysis and estimation for the finite volume method with applications to fluid flows. Ph.D. thesis, Imperial College of Science, Technology and Medicine

36. Jasak H, Weller H, Nordin N (2004) In cylinder CFD simulation using a C++ object-oriented toolkit. SAE Technical Papers

37. Jirka GH (2004) Integral model for turbulent buoyant jets in unbounded stratified flows, Part 1: The single round jet. Environ. Fluid Mech. 4 (2004)1–56

38. Jirka GH (2008) Improved discharge configurations for brine effluents from desalination plants. J Hydraul. Eng., 134:116-120

39. Jirka GH, Abraham G, Harleman DRF (1976) An assessment of techniques for hydrothermal prediction. Department of Civil Engineering, MIT for U.S. Nuclear Regulatory Commission, Cambridge

40. Juretic F (2004) Error analysis in finite volume. Ph.D. thesis, Imperial College of Science, Technology and Medicine

41. Kikkert GA (2006) Buoyant jets with two and three-dimensional trajectories. PhD thesis, University of Canterbury, New Zealand

42. Kikkert GA, Davidson MJ, Nokes RI (2007) Inclined negatively buoyant discharge. J Hydraul Eng, ASCE 133(5):545-554

43. Kim DG, Cho HY (2006) Modeling the buoyant flow of heated water discharged from surface and submerged side outfalls in shallow and keep water with a cross flow, J Environ. Fluid Mech. 6:501-518

44. Kuang CP, Lee JHW (2002) Effect of control on stability and mixing of vertical plane buoyant jet in confined depth. J Hydraul. Research, 39(4): 375-391

45. Lane-Serff GF, Linden PF, Hillel M (1993) Forced, angle plumes. J Hazard Mater 33:75-99

46. Lai CCK, Lee JHW (2012) Mixing of inclined dense jets in stationary ambient. J Hydro-environ Res 6: 9-28

47. Lattemann S, Hoepner T (2008) Environmental impact and impact assessment of seawater desalination. Desalination 220:1-15

48. Launder BE (1989) Second-moment closure and its use in modeling turbulent industrial flows. Int. J for Num. Methods in Fluids, 9:963-985

49. Launder BE (1989) Second-moment closure: Present... and future? Int. J Heat Fluid Flow, 10(4): 282-300

50. Launder BE, Rodi W (1981) The turbulent wall jet. Prog. Aerospace Sci. 19:81-128

51. Launder BE, Reece GJ, Rodi W (1975) Progress in the development of a Reynolds-stress turbulence closure. J Fluid Mech., 68(3):537-566

52. Launder BE, Spalding DB (1972) Lectures in mathematical models of turbulence. Academic Press

53. Law AW, Herlina (2002) An experimental study on turbulent circular wall jets. J Hydral. Eng., 128(2): 161-174

54. Lee JHW, Chu VH (2003) Turbulent jets and plumes: a lagrangian approach. Academic Publishers, The Netherland

55. Maele KV, Merci B (2006) Application of two buoyancy-modified k-ε turbulence models to different types of buoyant plumes. Fire Safety Journal, 41:122-138

56. Madni IK, Ahmed SZ (1989) Prediction of turbulent, axisymmetric, dense jets discharged to quiescent ambients. Math Comput Model 12(3):363-370

57. Malalasekera W, Versteeg HK (1995) Computational Fluid Dynamics. Longman Scientific, England

58. Manceau R (2010) Industrial codes for CFD. A training course for Eng., Univ. of Poitiers

59. Mangani L (2010) Development and validation of an object oriented CFD solver for heat transfer and combustion modeling in turbomachinery applications. Italy

60. Menter FR (1994) Two-equation eddy viscosity turbulence model for engineering applications. AIAA Journal, 32(8):1598-1605

61. Michas SN, Papanicolaou PN (2009) Horizontal round heated jets into calm uniform ambient. Desalination 248:803-815

62. Millero FJ, Poisson A (1981) International one-atmosphere equation of state of sea water, J Deep-Sea Research 28A(6): 625 to 629

63. Moradnia P (2010) CFD of air flow in hydro power generators. Thesis for the degree of licentiate of engineering, Dep. of Appl. Math., Chalmers Univ. of Tech. , Goteborg, Sweden

64. Nemlioglu S, Roberts PJW (2006) Experiments on dense jets using three-dimensional laser-induced fluorescence (3DLIF) MWWD 2006-The 4th international conference on marine waste water disposal and marine environment, November 6-10, Antalya, Turkey

65. Oliveira PJ, Issa RI (2001) An improved PISO algorithm for the computation of buoyancy-driven flows, Num Heat Trans 40:473-493

66. OpenCFD Limited. OpenFOAM - Programmer's Guide, May 2012. Version 2.1.1

67. OpenCFD Limited. OpenFOAM - User Guide, May 2012. Version 2.1.1

68. Orszag SA (1986) Renormalization Group Analysis of Turbulence: Basic Theory. J Scientific Computing 1(1):1-51

69. Papakostantis IG, Christodoulou GC, Papanicolaou PN (2011a) Inclined negatively buoyant jets I: geometrical characteristics. J Hydraul Res 49(1): 3-12

70. Papakostantis IG, Christodoulou GC, Papanicolaou PN (2011b) Inclined negatively buoyant jets II: concentration measurements. J Hydraul Res 49(1): 13-22

71. Padmanabham G, Gowda BHL (1991) Mean and turbulence characteristics of a class of three dimensional wall jets-Part1: Mean flow characteristics. J. Fluids Engineering 113:620-628

72. Patankar SV (1980) Numerical Heat Transfer and Fluid Flow. Taylor & Francis, US

73. Pincince AB, List EJ (1973) Disposal of brine into an estuary. J Water Pollut Control Fed, 45(11):2335-2344

74. Rajaratnam N, Pani BS (1974) Three dimensional turbulent wall jets. J Hydraul. Devision, ASCE 100(1):69-83

75. Roberts PJW, Toms G (1987) Inclined dense jets in flowing current. J Hydraul. Eng. ASCE 113(3):323-341

76. Roberts PJW, Ferrier A, Daviero G (1997) Mixing in inclined dense jets. J Hydraul Eng, ASCE 123(8):693-699

77. Sajwani AA (1998) The desalination plants of Oman: past, present, and future. Desalination 120:53-59

78. Sarkar S, Hussaini MY (1993) Computation of the sound generated by isotropic turbulence. NASA contract report 93-74, NASA Langley Research Center, Hampton, VA

79. Schlichting H (1979) Boundary layer theory. Translated by J. Kestin, McGraw-Hill, New York

80. Sforza PM, Herbst G (1970) A study of three-dimensional incompressible turbulent wall jets. AIAA J 8(2):276-283

81. Shao D (2009) Desalination discharge in shallow coastal waters. PhD thesis, Nanyang Technological University, Singapore

82. Shao D, Law AWK (2010) Mixing and boundary interactions of 30 and 45 inclined dense jets. Env Fluid Mech 10:521-553

83. Sharp JJ (1975) The use of a buoyant wall jet to improve the dilution of a submerged outfall. Proc. Instn. Civ. Eng. (London) Part 2, 59(2): 527-534

84. Sharp JJ, Vyas BD (1977) The buoyant wall jet. Proc. Instn. Civ. Engrs, Part 2, 63: 593-611, London, UK

85. Shih TH, Liou WW, Shabbir A, Yang Z, Zhu J (1994) A new k-ε eddy viscosity model for high Reynolds number turbulent flows- Model development and validation. NASA Lewis research center report # 106721

86. Shih TH, Zhu J, Lumley JL (1995) A new Reynolds stress algebraic equation model. Comput. Methods Appl. Mech. Eng., 125:287-302

87. Sobey RJ, Keane RD, Johnston AJ (1988) Horizontal round buoyant jet in shallow water. J Hydraul. Eng. 114(8): 910-929

88. Speziale CG (1991) Analytical methods for the development of Reynolds-stress closures in turbulence. Annu. Rev. Fluid Mech. 23: 107-157

89. Vafeiadou P (2005) Simulation of denser jets in ambient water bodies. Postgraduate Thesis in Water Resources Science and Technology, National Technical University of Athens, Greece

90. Vafeiadou P, Papakonstantis I, Christodoulou G (2005) Numerical simulation of inclined negatively buoyant jets. The 9th international conference on environmental science and technology, September 1-3, Rhodes island, Greece

91. Verhoff A (1963) The two dimensional turbulent wall jet with and without an external stream. Report no. 626, Princeton Univ., Princeton, N.J

92. Villafruela JM, Castro F, Parra MT (2008) Experimental study of parallel and inclined turbulent wall jets. Experimental Thermal and Fluid Science 33:132-139

93. Wilcox D (1993) Turbulence modeling for CFD. DCW Industries, California, US

94. Xiao J, Travis JR, Breitung W (2009) Non-Boussinesq integral model for horizontal turbulent buoyant round jets. J Scien. and Tech. of Nuclear Installations 862934

95. Zeitoun MA, McHilhenny WF, Reid RO (1970) Conceptual designs of outfall systems for desalination plants. Research and development progress report no. 550. Tech. rep., Office of Saline Water. United States Department of the interior

Appendix A

Submerged Outfall Design Procedure (From Bleninger and Jirka, 2008)

Bleninger and Jirka (2008) applied CorJect model for the different ranges of discharge angles $0^{\circ} \leq \theta_0 \leq 90^{\circ}$ and for the different sea-bed bathymetry $0^{\circ} \leq \theta_B \leq 30^{\circ}$ in order to assess the possible designing options and their efficiency. It can be seen in the Fig. A.1 that the discharge angle $30^{\circ} \leq \theta_0 \leq 45^{\circ}$ provides the longest x_i/L_M. The results lead to this conclusion that the discharge angle $30^{\circ} \leq \theta_0 \leq 45^{\circ}$ seems preferable for negatively buoyant jet discharges located in a near-shore environment, because it produces the highest dilution in the maximum rise and impact point. It also keeps the jet impact point further from offshore. Based on these facts, they recommended the following design procedure for a given discharge rate Q_0 and a discharge density ρ_0:

1. Choose a Froude number design, $F_0 \geq 10$, with the recommended range F_0 = 20 to 25 (Higher values imply larger pumping head losses). With $U_0 = Q_0$ /4πD^2 the required port diameter is computed as:

   $D = [\frac{\left(\frac{4}{\pi}\right)Q_0}{F_0|g'_0|^{0.5}}]^{0.4}$
2. Choose a discharge angle θ_0=45° for weaker bottom slopes (θ_B ≤15°) or θ_0 = 30° for stronger slopes.
3. Evaluate jet geometry using Figs. A.1 and A.2.
4. Select the offshore location for the discharge in terms of a local water depth Ha_0 that guarantees the upper jet boundary $Z_{max} \leq 0.75Ha_0$, in order to prevent dynamic surface interference.
5. Choose a port height h_0 = 0.5 to 1.0 m (In a second iteration, the effect of the port height can be considered as an added slope angle (It will help to get a higher dilution).
6. Evaluate the concentration of key effluent parameters at the impingement point using Fig. A.3 and compare with applicable environmental criteria or regulations. If the dilution effect is insufficient, design iteration is necessary.

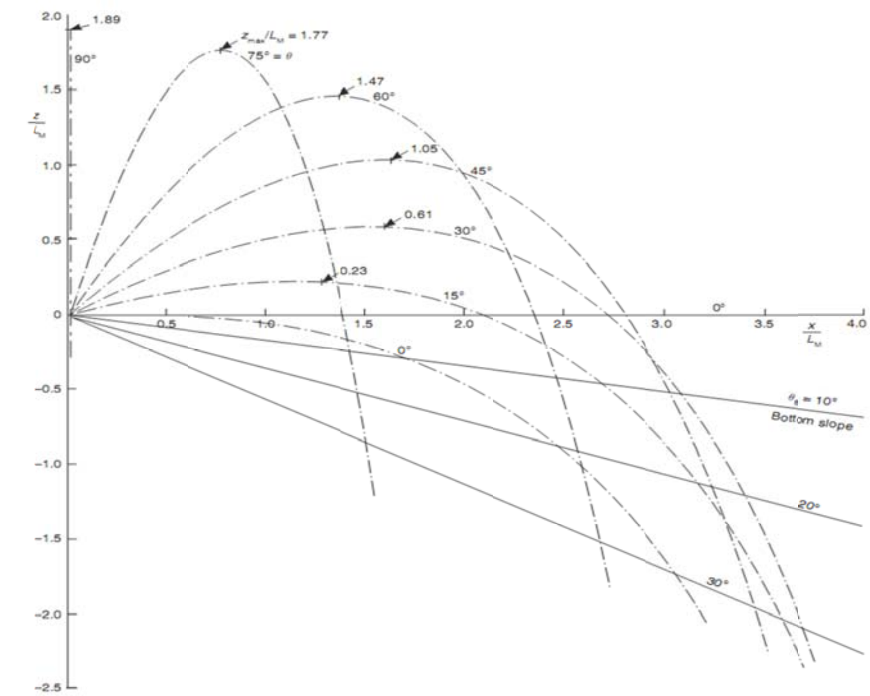

Fig. A.1: Jet trajectories: Negatively buoyant jet behavior for complete range of discharge angles 0°≤ θo ≤ 90° and with variable offshore slopes θ_B from 0° to 30°. A zero discharge height, $h_0 = 0$, is assumed

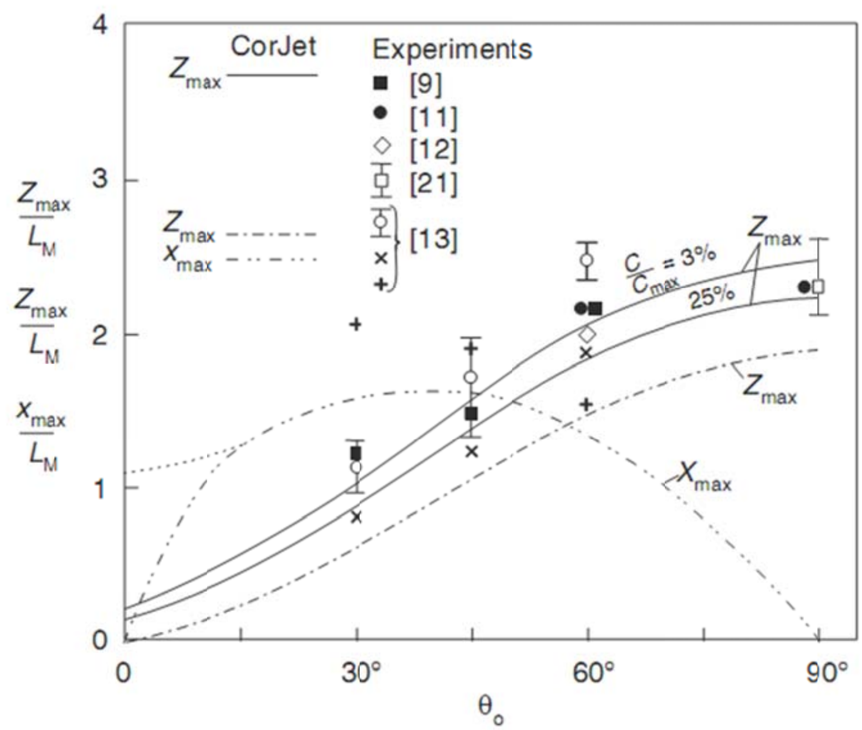

Fig. A.2: Jet properties at maximum level of rise. Comparison of CorJet model with experimental data

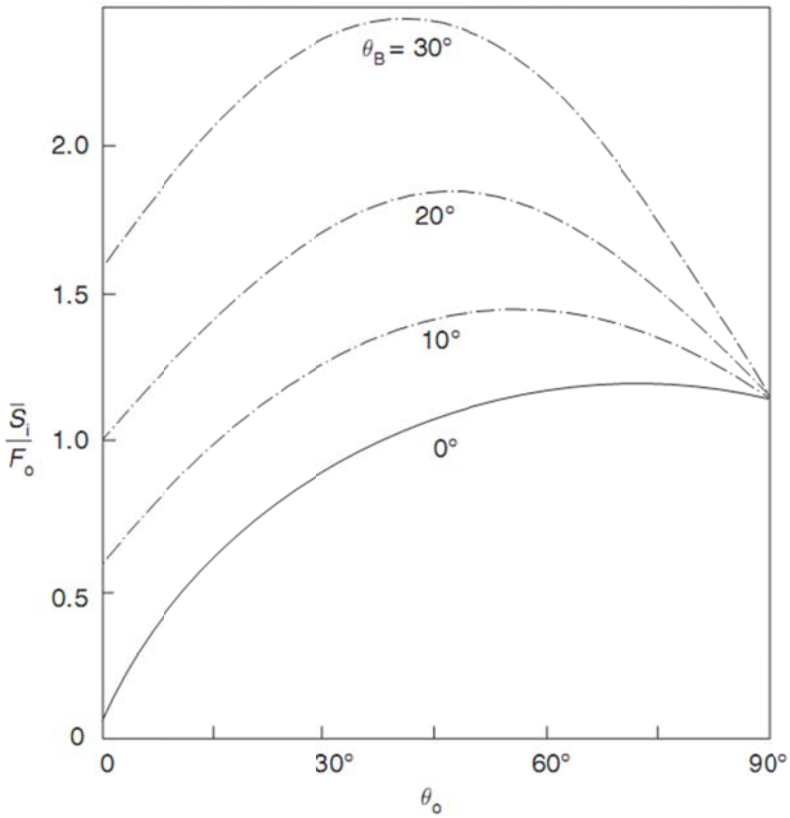

Fig. A.3: Bulk dilutions as a function of discharge angle Θ_0: Negatively buoyant jet behavior for complete range of discharge angles $0° \leq \Theta_0 \leq 90°$ and with variable offshore slopes Θ_B from 0° to 30°. A zero discharge height, $h_0 = 0$, is assumed

Regarding the above statements and design procedure, the following general principals are recommended for a discharge structure:

a) *The discharge location*: It should be in a place that is not a very sensitive coastal region. The locations that are potentially sensitive should not be permitted for building the discharge structures. For instance, coral reefs, lagoons, enclosed bays, within or nearby mangrove regions or similar places and shorelines are the sensitive places that should be avoided as potential places for outfalls. Good transport and flushing characteristics are very important in order to avoid accumulation of effluents and this will increase mixing potential with ambient water.

b) *The discharge design*: According to the above-mentioned notes, therefore, designs should be oriented into the open water body and not against the water surface. In order to get the best results we need to design offshore, submerged diffuser(s). The offshore location provides the necessary distance to sensitive region. Submerged discharges allow for improved mixing before interacting with boundaries. The above goals have to be considered for several siting alternatives in order to find the optimal and cost-efficient solutions.

Appendix B

Available Features within OpenFOAM

OpenFOAM is very rich in term of variety of applications available for users to choose from. The main features are listed below with the options available under each category.

OpenFOAM Solvers:

- Basic CFD
- Incompressible Flows
- Compressible Flows
- Multiphase Flows
- DNS and LES
- Combustion
- Heat Transfer
- Electromagnetics
- Solid Dynamics
- Finance

OpenFOAM Utilities:

- Pre-processing
- The FoamX Case Manager
- Other Pre-processing Utilities
- Post-processing
- The paraFoam Post-processor
- Third-party Post-processing
- Other Post-processing Utilities
- Mesh Processing
- Mesh Generation
- Mesh Converts
- Mesh Manipulation

OpenFOAM Libraries:

- Model Libraries
- Turbulence
- Large-eddy Simulation (LES)
- Transport Models
- Thermophysical Models
- Chemical Kinetics

Other Features:

- Linear System Solvers
- ODE System Solvers
- Parallel Computing
- Mesh Motion
- Numerical Method

Appendix C

OpenFOAM Model Preparation

It was briefly talked in Chapter III about the numerical model implementations, especially for the solver (*mypisoFoam*). In this Chapter, the rest of model preparation procedures are explained.

Compilation of Solver in Linux OS

The PISO algorithm has been explained before extensively (in Chapter III). The PISO loop within the main solver is shown in the following.

```
// --- PISO loop

for (int corr=0; corr<nCorr; corr++)
{
    volScalarField rAU(1.0/UEqn.A());

    U = rAU*UEqn.H();
    phi = (fvc::interpolate(U) & mesh.Sf())
        + fvc::ddtPhiCorr(rAU, U, phi);

    adjustPhi(phi, U, p);

    // Non-orthogonal pressure corrector loop
    for (int nonOrth=0; nonOrth<=nNonOrthCorr; nonOrth++)
    {
        // Pressure corrector

        fvScalarMatrix pEqn
        (
            fvm::laplacian(rAU, p) == fvc::div(phi)
        );

        pEqn.setReference(pRefCell, pRefValue);

        if
        (
            corr == nCorr-1
         && nonOrth == nNonOrthCorr
        )
        {
            pEqn.solve(mesh.solver("pFinal"));
        }
        else
        {
            pEqn.solve();
        }
```

Compilation is an integral part of application development that requires careful management since every piece of code requires its own set instructions to access dependent components of the OpenFOAM library. In *UNIX/Linux* systems these instructions are often organised and delivered to the compiler using the standard *UNIXmake* utility. OpenFOAM, however, is supplied with the *wmake* compilation script that is based on *make* but is considerably more versatile and easier to use; *wmake* can be used on any code, not simply the OpenFOAM library. To understand the compilation process, we first need to explain certain aspects of *C++* and its file structure, shown schematically in Fig. C.1. A class is defined through a set of instructions such as object construction, data storage and class member functions. The file containing the class definition takes *a.C* extension, e.g. a class *nc* would be written in the file *nc.C*. This file can be compiled independently of other code into a binary executable library file known as a shared object library with the *.so* file extension, i.e. *nc.so*. When compiling a piece of code, say *newApp.C* (*mypisoFoam.C* in our real case), that uses the *nc* class, *nc.C* need not be recompiled, rather *newApp.C* calls *nc.so* at runtime. This is known as dynamic linking.

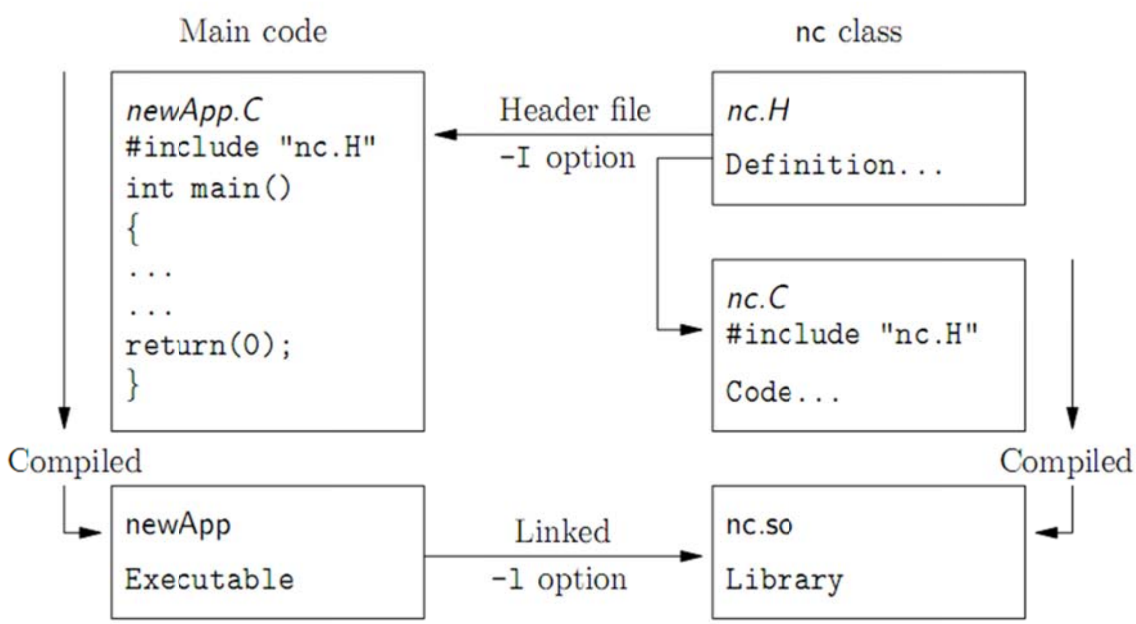

Fig. C.1: Header files, source files, compilation and linking. From OpenFOAM user manual

As a means of checking errors, the piece of code being compiled must know that the classes it uses and the operations they perform actually exist. Therefore each class requires a class declaration, contained in a header file with a *.H* file extension, e.g. *nc.H*, that includes the names of the class and its functions. This file is included at the beginning of any piece of code using the class, including the class declaration code itself. Any piece of *.C* code can resource any number of classes and must begin with all the *.H* files required to declare these classes. The classes in turn can resource other classes and begin with the relevant *.H* files. By searching recursively down the class hierarchy we can produce a complete list of header files for all the classes on which the top level *.C* code ultimately depends; these *.H* files are known as the dependencies. With a dependency list, a compiler can check whether the source files have been updated since their last compilation and selectively compile only those that need to be.

Header files are included in the code using # include statements, e.g. # *include "otherHeader.H";* causes the compiler to suspend reading from the current file to read the file specified. Any self-contained piece of code can be put into a header file and included at the relevant location in the main code in order to improve code readability. For example, in most OpenFOAM applications the code for creating fields and reading field input data is included in a file *createFields.H* which is called at the beginning of the code. In this way, header files are not solely used as class declarations. It is *wmake* that performs the task of maintaining file dependency lists amongst other functions listed below.

- Automatic generation and maintenance of file dependency lists, i.e. lists of files which are included in the source files and hence on which they depend;
- Multi-platform compilation and linkage, handled through appropriate directory structure;
- Multi-language compilation and linkage, e.g. *C*, *C++*, Java;
- Multi-option compilation and linkage, e.g. debug, optimised, parallel and profiling;
- Support for source code generation programs, e.g. *lex*, *yacc*, *IDL*, *MOC*;
- Simple syntax for source file lists;
- Automatic creation of source file lists for new codes;
- Simple handling of multiple shared or static libraries;
- Extensible to new machine types.

OpenFOAM applications are organised using a standard convention that the source code of each application is placed in a directory whose name is that of the application. The top level source file takes the application name with the *.C* extension. For example, the source code for an application called newApp would reside in a directory newApp and the top level file would be newApp.C as shown in Fig. C.2.

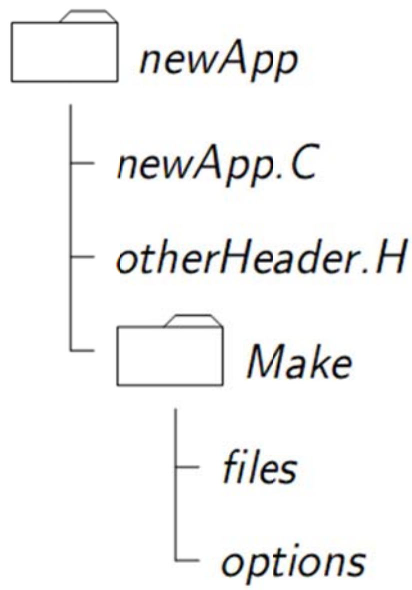

Fig. C.2: Directory structure for an application. From OpenFOAM user manual

The compiler requires a list of *.C* source files that must be compiled. The list must contain the main *.C* file but also any other source files that are created for the specific application but are not included in a class library. For example, we may create a new class or some new functionality to an existing class for a particular application. The full list of *.C* source files must be included in the *Make/files* file. As might be expected, for many applications the list only includes the name of the main *.C* file, e.g. *newApp.C* in the case of our earlier example.

The *Make/files* file also includes a full path and name of the compiled executable, specified by the *EXE* = syntax. Standard convention stipulates the name is that of the application, i.e. *newApp* in our example. The OpenFOAM release offers two useful choices for path: standard release applications are stored in *$FOAM_APPBIN*; applications developed by the user are stored in *$FOAM_USER_APPBIN*.

As explained above, based *pisoFoam* solver includes three dictionaries in its directory: (i) *Make* directory which includes two dictionaries (*files*, and *options*) for calling several header files and to address the compilation folder (ii) *createFields.H* which contains the required fields to be solved such as pressure and velocity fields. It was required to introduce concentration and temperature fields here as seen below.

```
Info<< "Reading field S\n" << endl;
volScalarField S
(
    IOobject
    (
        "S",
        runTime.timeName(),
        mesh,
        IOobject::MUST_READ,
        IOobject::AUTO_WRITE
    ),
    mesh
);

Info<< "Reading field T\n" << endl;
volScalarField T
(
    IOobject
    (
        "T",
        runTime.timeName(),
        mesh,
        IOobject::MUST_READ,
        IOobject::AUTO_WRITE
    ),
    mesh
```

(iii) *pisoFoam.C* which is the main *C++* code for the solver that includes the momentum equation and PISO loop. We need to add concentration and temperature equations here as well. These implementations are shown below.

```
    fvScalarMatrix TEqn
    (
        fvm::ddt(rho,T)
      + fvm::div(rhophi, T)
      - fvm::laplacian(kappaEff, T)
    );

    TEqn.relax();
    TEqn.solve();


    fvScalarMatrix SEqn
    (
        fvm::ddt(rho,S)
      + fvm::div(rhophi, S)
      - fvm::laplacian(kappaEff, S)
    );

    SEqn.relax();
    SEqn.solve();
}
```

Preparation of the Case File

The basic directory structure for an OpenFOAM case, that contains the minimum set of files required to run an application, is shown in Fig. C.3 and described as follows:

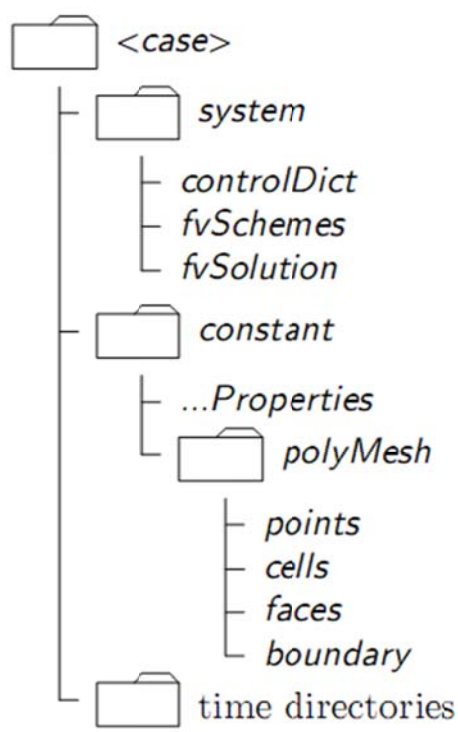

Fig. C.3: Case directory structure. From OpenFOAM user manual

The constant directory

that contains a full description of the case mesh in a sub-directory *polyMesh* and files specifying physical properties for the application concerned, e.g. *transportProperties*.

The system directory

for setting parameters associated with the solution procedure itself. It contains at least the following three files: *controlDict* where run control parameters are set including start/end time, time step and parameters for data output; *fvSchemes* where discretisation schemes used in the solution may be selected at run-time; and, *fvSolution* where the equation solvers, tolerances and other algorithm controls are set for the run.

The 'time' directories

containing individual files of data for particular fields. The data can be: either, initial values and boundary conditions that the user must specify to define the problem; or, results written to file by OpenFOAM. Note that the OpenFOAM fields must always be initialised, even when the solution does not strictly require it, as in steady-state problems. The name of each time directory is based on the simulated time at which the data is written.

The implementations and modifications, which have been done, are summarised as following.

Constant Directory

In this problem, constant directory includes *polyMesh* sub-directory where the mesh is built there using the *blockMeshDict* utility. Boundary conditions are also identified there. The domain is divided into a number of blocks. Each block should have 8 vertices. All the vertices for all the blocks are sorted under vertices dictionary. Each vertex has *x, y* and *z* coordinate value. The vertices are numbered in ordered starting from zero for the first vertex.

These vertices are specified by their number according to their appearance in the vertices dictionary. The line for each block starts with the word *hex* meaning that the mesh will be *hexahedral* followed by the number of the 8 vertices connecting the block. After specifying the vertices connecting one block comes the number of grid points in the three direction *x, y* and *z*.

The patches dictionary specifies the boundary patches in the mesh. Each boundary face should be connected by four vertices. First the type of the boundary condition is specified for a patch and then the name of the patch. If a boundary patch is sharing many blocks, an entry for each piece of the patch in each block should be specified under the patch dictionary. The sample files for *blockMeshDict* and *boundary* are shown below, respectively.

```
    version     2.0;
    format      ascii;
    class       dictionary;
    object      blockMeshDict;
}
// * * * * * * * * * * * * * * * * * * * * * * * * * * * * * * * * * * * * * //

convertToMeters 0.01;

vertices
(
        (0 0 0)//0
        (120 0 0)//1
        (0 0.6405 0)//2
        (120 0.6405 0)//3
        (0 1.5935 0)//4
        (120 1.5935 0)//5
        (0 50 0)//6
        (120 50 0)//7
        (0 0 19.5235)//8
        (120 0 19.5235)//9
        (0 0.6405 19.5235)//10
        (120 0.6405 19.5235)//11
        (0 1.5935 19.5235)//12
        (120 1.5935 19.5235)//13
        (0 50 19.5235)//14
        (120 50 19.5235)//15
        (0 0 20)//16
        (120 0 20)//17
        (0 0.6405 20)//18
        (120 0.6405 20)//19
        (0 1.5935 20)//20
        (120 1.5935 20)//21
        (0 50 20)//22
        (120 50 20)//23
```

```
    version     2.0;
    format      ascii;
    class       polyBoundaryMesh;
    location    "constant/polyMesh";
    object      boundary;
}
// * * * * * * * * * * * * * * * * * * * * * * * * * * * * * * * * * * * * * //

7
(
    inlet
    {
        type            patch;
        nFaces          8;
        startFace       227375;
    }
    leftWall
    {
        type            wall;
        nFaces          1073;
        startFace       227383;
    }
    outlet
    {
        type            patch;
        nFaces          1081;
        startFace       228456;
    }
    lowerWall
    {
        type            wall;
        nFaces          1656;
        startFace       229537;
    }
    atmosphere
```

The *transportProperties* dictionary within *constant* directory, sets the transport model for the fluid to be Newtonian and then gives information about the viscosity and density of that. This is shown as following.

```
|   \\  /    A nd           | Web:      www.OpenFOAM.org                      |
|    \\/     M anipulation  |                                                 |
\*---------------------------------------------------------------------------*/
FoamFile
{
    version     2.0;
    format      ascii;
    class       dictionary;
    location    "constant";
    object      transportProperties;
}
// * * * * * * * * * * * * * * * * * * * * * * * * * * * * * * * * * * * * * //

transportModel  Newtonian;

nu              nu [ 0 2 -1 0 0 0 0 ] 1e-06;
mykappaEff      mykappaEff [ 1 -1 -1 0 0 0 0 ] 1e-03;

CrossPowerLawCoeffs
{
    nu0             nu0 [ 0 2 -1 0 0 0 0 ] 1e-06;
    nuInf           nuInf [ 0 2 -1 0 0 0 0 ] 1e-06;
    m               m [ 0 0 1 0 0 0 0 ] 1;
    n               n [ 0 0 0 0 0 0 0 ] 1;
}

BirdCarreauCoeffs
{
    nu0             nu0 [ 0 2 -1 0 0 0 0 ] 1e-06;
    nuInf           nuInf [ 0 2 -1 0 0 0 0 ] 1e-06;
    k               k [ 0 0 1 0 0 0 0 ] 0;
    n               n [ 0 0 0 0 0 0 0 ] 1;
}

// ************************************************************************* //
```

Moreover, in the *turbulenceProperties* the type of turbulence model is mentioned (RANS or LES) and in the other dictionary, the exact turbulence model should be mentioned regarding the turbulence type. OpenFOAM has lots of different turbulence models which make it a popular and strong application for simulations of turbulent flows. It contains various models for both incompressible and compressible fluids. These turbulence models are divided in two well known categories; RANS (Reynolds Averaged Navier Stokes) and LES (Large Eddy Simulation).

The list of available RANS and LES models in OpenFOAM is presented in Tables C.1 and C.2.

Table C.1: RANS turbulence models for incompressible fluids within OpenFOAM

Model format in OpenFOAM	Model name
laminar	Dummy turbulence model for laminar flow
kEpsilon	Standard high-Re k−ε model
kOmega	Standard high-Re k−ω model
kOmegaSST	k−ω-SST model
RNGkEpsilon	RNG k−ε model
NonlinearKEShih	Non-linear Shih k−ε model
LienCubicKE	Lien cubic k−ε model
qZeta	q−ζ model
LaunderSharmaKE	Launder-Sharma low-Re k−ε model
LamBremhorstKE	Lam-Bremhorst low-Re k−ε model
LienCubicKELowRe	Lien cubic low-Re k−ε model
LienLeschzinerLowRe	Lien-Leschziner low-Re k−ε model
LRR	Launder-Reece-Rodi RSTM
LaunderGibsonRSTM	Launder-Gibson RSTM with wall-reflection terms
realizableKE	Realizable k−ε model
SpalartAllmaras	Spalart-Allmaras one-eqn mixing-length model

Table C.2: LES turbulence models for incompressible fluids within OpenFOAM

Model format in OpenFOAM	Model name
Smagorinsky	Smagorinsky model
Smagorinsky2	Smagorinsky model with 3-D filter
dynSmagorinsky	Dynamic Smagorinsky
homogenousDynSmagorinsky	Homogeneous dynamic Smagorinsky model
dynLagrangian	Lagrangian two equation eddy-viscosity model
scaleSimilarity	Scale similarity model
mixedSmagorinsky	Mixed Smagorinsky/scale similarity model
dynMixedSmagorinsky	Dynamic mixed Smagorinsky/scale similarity model
kOmegaSSTSAS	k−ω-SST scale adaptive simulation (SAS) model
oneEqEddy	k-equation eddy-viscosity model
dynOneEqEddy	Dynamic k-equation eddy-viscosity model
locDynOneEqEddy	Localised dynamic k-equation eddy-viscosity model
spectEddyVisc	Spectral eddy viscosity model
LRDDiffStress	LRR differential stress model
DeardorffDiffStress	Deardorff differential stress model
SpalartAllmaras	Spalart-Allmaras model
SpalartAllmarasDDES	Spalart-Allmaras delayed detached eddy simulation (DDES) model
SpalartAllmarasIDDES	Spalart-Allmaras improved DDES (IDDES) model

System Directory

The *fvSchemes* dictionary in the system directory sets the numerical schemes for terms, such as derivatives in equations, which appear in applications being run. This section describes how to specify the schemes in the *fvSchemes* dictionary.

The terms that must typically be assigned a numerical scheme in *fvSchemes* range from derivatives, e.g. gradient ∇, and interpolations of values from one set of points to another. The aim in OpenFOAM is to offer an unrestricted choice to the user. For example, while linear interpolation is effective in many cases, OpenFOAM offers complete freedom to choose from a wide selection of interpolation schemes for all interpolation terms.

The derivative terms further exemplify this freedom of choice. The user first has a choice of discretization practice where standard Gaussian finite volume integration is the common choice. Gaussian integration is based on summing values on cell faces, which must be interpolated from cell centres. The user again has a completely free choice of interpolation scheme, with certain schemes being specifically designed for particular derivative terms, especially the convection divergence ∇. terms.

The set of terms, for which numerical schemes must be specified, are subdivided within the *fvSchemes* dictionary into the categories listed in Table C.3. Each keyword in Table C.3 is the name of a sub-dictionary which contains terms of a particular type, e.g. *gradSchemes* contains all the gradient derivative terms such as *grad(p)* (which represents ∇p). Further examples can be seen in the extract from an *fvSchemes* dictionary following the Table C.3.

Table C.3: Main keywords used in fvSchemes

Keyword	Category of mathematical terms
interpolationSchemes	Point-to-point interpolations of values
snGradSchemes	Component of gradient normal to a cell face
gradSchemes	Gradient ∇
divSchemes	Divergence $\nabla\cdot$
laplacianSchemes	Laplacian ∇^2
timeScheme	First and second time derivatives $\frac{\partial}{\partial t}, \frac{\partial^2}{\partial t^2}$
fluxRequired	Fields which require the generation of a flux

```
ddtSchemes
{
    default         CrankNicholson 0.5;
}

gradSchemes
{

    default         Gauss linear;
    grad(p)         Gauss linear;
    grad(U)         Gauss linear;

}

divSchemes
{
    default         none;

    div(phi,U)      Gauss cubic corrected;
    div(phi,S)      Gauss cubic corrected;
    div(phi,T)      Gauss cubic corrected;
    div(rhophi,S)      Gauss limitedLinear 1;
    div(rhophi,T)      Gauss limitedLinear 1;
    div(phi,k)      Gauss limitedLinear 1;
    div(phi,epsilon) Gauss limitedLinear 1;
    div(phi,R)      Gauss limitedLinear 1;
    div(R)          Gauss linear;
    div(phi,nuTilda) Gauss limitedLinear 1;
    div((nuEff*dev(T(grad(U))))) Gauss linear;
    div(nonlinearStress) Gauss linear;

}

laplacianSchemes
{
```

The equation solvers, tolerances and algorithms are controlled by the *fvSolution* dictionary in the *system* directory. Below is an example set of entries from the *fvSolution* dictionary required for the *mypisoFoam* solver.

```
solvers
{
    p
    {
        solver          PCG;
        preconditioner  DIC;
        tolerance       1e-06;
        relTol          0.1;
    }

    pFinal
    {
        solver          PCG;
        preconditioner  DIC;
        tolerance       1e-06;
        relTol          0;
    }

    U
    {
        solver          PBiCG;
        preconditioner  DILU;
        tolerance       1e-05;
        relTol          0;
    }
//
    s
    {
        solver          PBiCG;
        preconditioner  DILU;
        tolerance       1e-05;
        relTol          0;
    }
    T
    {
        solver          PBiCG;
```

fvSolution contains a set of sub-dictionaries that are specific to the solver being run. However, there is a small set of standard sub-dictionaries that cover most of those used by the standard solvers. These sub-dictionaries include *solvers*, *relaxationFactors*, *PISO* and *SIMPLE* algorithms (PISO has already been explained).

Linear Solver Control

The first sub-dictionary in our example, and one that appears in all solver applications, is *solver*. It specifies each linear-solver that is used for each discretized equation; it is emphasised that the term linear-solver refers to the method of number-crunching to solve the set of linear equations, as opposed to application solver which describes the set of equations and algorithms to solve a particular problem.

The syntax for each entry within solvers uses a keyword that is the word relating to the variable being solved in the particular equation. For example, *pisoFoam* solves equations for velocity U and pressure P, hence the entries for U and p. The keyword is followed by a dictionary containing the type of solver and the parameters that the solver uses. The solver is selected through the solver keyword from the choice in OpenFOAM, listed in Table C.4. The parameters, including *tolerance*, and *preconditioner* are described in following sections.

Table C.4: Linear solvers

Solver	Keyword
Preconditioned (bi-)conjugate gradient	PCG/PBiCG*
Solver using a smoother	smoothSolver
Generalised geometric-algebraic multi-grid	GAMG
Diagonal solver for explicit systems	diagonal

*PCG for symmetric matrices, PBiCG for asymmetric

In current study, for pressure field, PCG (Preconditioned Conjugate Gradient) is used for each discretized equation. PCG is a linear solver, the same as PBiCG (Preconditioned Bio Conjugate Gradient) which has been used for other remained fields, U, T, C, k, ε, and ω.

Solution Tolerances

The sparse matrix solvers are iterative, i.e. they are based on reducing the equation residual over a succession of solutions. The residual is ostensibly a measure of the error in the solution so that the smaller it is, the more accurate the solution. More precisely, the residual is evaluated by substituting the current solution into the equation and taking the magnitude of the difference between the left and right hand sides; it is also normalised to make it independent of the scale of the problem being analysed.

Before solving an equation for a particular field, the initial residual is evaluated based on the current values of the field. After each solver iteration the residual is re-evaluated. The solver stops if either of the following conditions are reached:

- the residual falls below the solver tolerance, *tolerance*;
- the ratio of current to initial residuals falls below the solver relative tolerance, *relTol*;
- the number of iterations exceeds a maximum number of iterations, *maxIter*.

Preconditioned Conjugate Gradient Solvers

There are a range of options for preconditioning of matrices in the conjugate gradient solvers, represented by the *preconditioner* keyword in the solver dictionary. The preconditioners are listed in Table C.5.

Table C.5: Preconditioner options

Preconditioner	Keyword
Diagonal incomplete-Cholesky (symmetric)	DIC
Faster diagonal incomplete-Cholesky (DIC with caching)	FDIC
Diagonal incomplete-LU (asymmetric)	DILU
Diagonal	diagonal
Geometric-algebraic multi-grid	GAMG
No preconditioning	none

In numerical analysis and linear algebra, a pre-conditioner M of a matrix A is a matrix such that $M^{-1}A$ has a smaller condition number than A. Pre-conditioners are useful in iterative methods to solve linear system $Ax=b$ for x since the rate of convergence for most iterative solvers increases as the condition number of a matrix decreases as a result of preconditioning. In this study, *DIC* (Diagonal Incomplete Cholesky) pre-conditioner is used for pressure field. This is a simplified diagonal based pre-conditioner for the symmetric matrices. However, *DILU* (Diagonal Incomplete LU) pre-conditioner is used for the other fields which mostly include asymmetric matrices to be solved.

Time Control

The OpenFOAM solvers begin all runs by setting up a database. The database controls I/O and, since output of data is usually requested at intervals of time during the run, time is an inextricable part of the database. The *controlDict* dictionary sets input parameters essential for the creation of the database. A sample *controlDict* dictionary is shown in the Following. Only the *time control* and *writeInterval* entries are truly compulsory.

```
{
    version     2.0;
    format      ascii;
    class       dictionary;
    location    "system";
    object      controlDict;
}
// * * * * * * * * * * * * * * * * * * * * * * * * * * * * * * * * * * * * * //

application     pisoFoamIIII;

startFrom       startTime;

startTime       0;

stopAt          endTime;

endTime         90;

deltaT          0.001;

writeControl    adjustableRunTime;

writeInterval   1;

purgeWrite      0;

writeFormat     ascii;

writePrecision  6;

writeCompression off;

timeFormat      general;

timePrecision   6;
```

Appendix D

In this appendix, four turbulence models used in the study are briefly reviewed.

Standard k-ε Turbulence Model

This commonly-used model was proposed by Launder and Spalding (1972). For this model, the transport equation for turbulent kinetic energy (*k*) is derived from momentum equations. However, the transport equation for the turbulent energy dissipation (*ε*) is obtained using physical reasoning and is chosen to be similar to the mathematically derived transport equation of *k*. The turbulent kinetic energy and its rate of dissipation in this model are obtained using the following equations

$$\frac{\partial k}{\partial t}+\frac{\partial k u_i}{\partial x_i}=\frac{\partial}{\partial x_i}(Dk_{eff}\frac{\partial k}{\partial x_i})+G_k-\varepsilon \tag{4.15}$$

$$\frac{\partial \varepsilon}{\partial t}+\frac{\partial \varepsilon u_i}{\partial x_i}=\frac{\partial}{\partial x_i}(D\varepsilon_{eff}\frac{\partial \varepsilon}{\partial x_i})+C_{1\varepsilon}\frac{\varepsilon}{k}G_k-C_{2\varepsilon}\frac{\varepsilon^2}{k} \tag{4.16}$$

where G_k represents the generation of turbulent kinetic energy due to mean velocity gradients and Dk_{eff} and $D\varepsilon_{eff}$ are the effective diffusivity for *k* and *ε*, respectively. Their values are calculated as

$$Dk_{eff}=\nu+\nu_t \tag{4.17}$$

$$D\varepsilon_{eff}=\nu+\frac{\nu_t}{\sigma_\varepsilon} \tag{4.18}$$

The turbulent kinematic viscosity at each point is related to the local values of turbulent kinetic energy and its dissipation rate by

$$\nu_t=C_\mu\frac{k^2}{\varepsilon} \tag{4.19}$$

σ_ε is turbulent Prandtl number for ε. This value has been determined experimentally and is assumed equal to 1.3.

Moreover, $C_{1\varepsilon}$, $C_{2\varepsilon}$ and C_μ are constants that have also been derived experimentally and are chosen to have the following values

$C_{1\varepsilon}=1.44, \quad C_{2\varepsilon}=1.92, \quad C_\mu= 0.09$

The term for the production of turbulent kinetic energy G_k is common in most turbulence models and is defined as

$$G_k = -\overline{u_i^{'} u_j^{'}} \frac{\partial u_j}{\partial x_i} \tag{4.20}$$

This can also be written as

$$G_k = 2\nu_t S_{ij}^{\;2} \tag{4.21}$$

$$S_{ij} = 0.5\left(\frac{\partial u_j}{\partial x_i} + \frac{\partial u_i}{\partial x_j}\right) \tag{4.22}$$

where $u_i^{'}$, $u_j^{'}$ and S_{ij} are the fluctuating parts of velocity and strain-rate tensor respectively.

RNG k-ε Turbulence Model

Similar to the standard k-ε model, the RNG model is derived from the instantaneous Navier Stokes equations, except that it uses a technique called renormalization group theory described by the Yakhot and Orszag (1986). The derivation that they used produces a model with different constants to those used in the standard k-ε model and also added new terms to the transport equations for the turbulent kinetic energy and its dissipation. The effect of swirl is also accounted for in the RNG model enhancing the accuracy of swirling flows. An analytical formula for turbulent Prandtl numbers is provided in this model while the standard model relies on user-specific constant values. Finally, assuming appropriate treatment of the near wall region, the RNG model uses an analytically derived differential formula for the effective turbulent viscosity which accounts for low Reynolds number flows. As a result of these differences, the transport equations are written as

$$\frac{\partial k}{\partial t} + \frac{\partial k u_i}{\partial x_i} = \frac{\partial}{\partial x_i}(Dk_{eff}\frac{\partial k}{\partial x_i}) + G_k - \varepsilon \tag{4.23}$$

$$\frac{\partial \varepsilon}{\partial t} + \frac{\partial \varepsilon u_i}{\partial x_i} = \frac{\partial}{\partial x_i}(D\varepsilon_{eff}\frac{\partial \varepsilon}{\partial x_i}) + (C_{1\varepsilon} - R)\frac{\varepsilon}{k}G_k - \frac{C_{2\varepsilon}\varepsilon^2}{k} \tag{4.24}$$

Some terms are obtained differently from the standard model. Dk_{eff} is calculated as

$$Dk_{eff} = \upsilon + \frac{\upsilon_t}{\sigma_k} \tag{4.25}$$

The renormalization term, R, is formulated as

$$R = \frac{\eta(1 - \frac{\eta}{\eta_0})}{1 + \beta\eta^3} \tag{4.26}$$

$$\eta = S_{ij}\frac{k}{\varepsilon} \tag{4.27}$$

All model constants are defined as

$C_\mu=0.0845,\ C_{1\varepsilon}=1.42,\ C_{2\varepsilon}=1.68,\ \sigma_k=0.71942,\ \sigma_\varepsilon=0.71942,\ \eta_0=4.38,\ \beta=0.012.$

Realizable k-ε Turbulence Model

The realizable model is one of the most recently developed turbulence model in the k-ε category and is developed by Shih (1995). This model exhibits two main differences from standard k-ε model. It uses (i) a new equation for the turbulent viscosity, and (ii) the dissipation rate transport equation has been derived from the equation for the transport of the mean-squared vorticity fluctuation. The form of the eddy viscosity equations is based on the realizability constraints; the positivity of normal Reynolds stresses and Schwarz's inequality for turbulent shear stresses (i.e., certain mathematical constraints on the normal stresses are satisfied). This is not satisfied by either the standard or the RNG k-ε models which makes the realizable model more precise than both models at predicting flows such as separated flows and flows with complex secondary flow features.

In terms of improved changes by Shih (1995), the transport equations become

$$\frac{\partial k}{\partial t} + \frac{\partial k u_i}{\partial x_i} = \frac{\partial}{\partial x_i}(Dk_{eff}\frac{\partial k}{\partial x_i}) + G_k - \varepsilon \tag{4.28}$$

$$\frac{\partial \varepsilon}{\partial t} + \frac{\partial \varepsilon u_i}{\partial x_i} = \frac{\partial}{\partial x_i}(D\varepsilon_{eff}\frac{\partial \varepsilon}{\partial x_i}) + \sqrt{2}C_{1\varepsilon}S_{ij}\varepsilon - C_{2\varepsilon}\frac{\varepsilon^2}{k+\sqrt{\upsilon\varepsilon}} \tag{4.29}$$

Similar to the previous variations of the k-ε models, the turbulent viscosity is determined by

$$\upsilon_t = C_\mu \frac{k^2}{\varepsilon} \tag{4.30}$$

where, C_μ is computed from

$$C_\mu = \frac{1}{A_0 + A_s\frac{kU^*}{\varepsilon}} \tag{4.31}$$

$$U^* = \sqrt{S_{ij}S_{ij} + \tilde{\Omega}_{ij}\tilde{\Omega}_{ij}} \tag{4.32}$$

$$\tilde{\Omega}_{ij} = \overline{\Omega}_{ij} - \varepsilon_{ijk}\omega_k - 2\varepsilon_{ijk}\omega_k \tag{4.33}$$

where $\bar{\Omega}_{ij}$ is the mean rate of rotation tensor viewed in a rotating reference frame with angular velocity ω_k. The constants A_0 and A_s are defined as

$$A_0 = 4,\ \mathrm{A_s} = \sqrt{6}\cos\varphi \tag{4.34}$$

$$\varphi = \frac{1}{3}Arc\cos(\min(\max(\sqrt{6}W,-1),1) \tag{4.35}$$

$$W = \frac{S_{ij}S_{jk}S_{ki}}{\tilde{S}^2} \tag{4.36}$$

It has been shown that C_μ is a function of the mean strain, rotational rates, and the angular velocity of the rotating system. The standard value of $C_\mu=0.09$ is found to be the solution of Eqn. (4.30) for an inertial sub layer in the equilibrium boundary layer. $C_{\varepsilon 1}$ is not constant in this model as well and is calculated as

$$C_{1\varepsilon} = \max\left(\frac{\eta}{5+\eta}, 0.43\right) \tag{4.37}$$

The constants C_2, σ_k and σ_ε have been determined by Shih (1995) and are defined as

$C_2=1.9$, $\sigma_k=1.0$, $\sigma_\varepsilon=1.2$.

SST k-ω Turbulence Model

The shear stress transport k-ω model is another RANS model. This model has been developed by Menter (1994) using the standard k-ω model and a transformed k-ε model. The main difference is the way in which the model calculates the turbulent viscosity to account for the transport of the principal turbulent shear stress. This model also incorporates a cross diffusion term in the ω equation and a blending function to allow proper calculation of the near wall and far field areas. The blending function triggers the standard k-ω model in near wall regions, and the k-ε model in areas away from the surface.

The transport equations for k and ω are given by the following equations

$$\frac{\partial k}{\partial t} + \frac{\partial k u_i}{\partial x_i} = \frac{\partial}{\partial x_i}\left(Dk_{eff}\frac{\partial k}{\partial x_i}\right) + G_k - \beta^* k\omega \tag{4.38}$$

$$\frac{\partial \omega}{\partial t} + \frac{\partial \omega u_i}{\partial x_i} = \frac{\partial}{\partial x_i}\left(D\omega_{eff}\frac{\partial \omega}{\partial x_i}\right) + 2\gamma S_{ij} - \beta\omega^2 + (1-F_1)CD_{k\omega} \tag{4.39}$$

where G_k represents the generation of turbulent kinetic energy due to mean velocity gradients and is calculated as

$$G_k = \min(2\upsilon_t S_{ij}, C_1\beta^*\omega k) \tag{4.40}$$

Dk_{eff}, $D\omega_{eff}$, υ_t, F_1 and F_2 are also formulated as

$$Dk_{eff} = \upsilon + \alpha_k \upsilon_t \tag{4.41}$$

$$D\omega_{eff} = \upsilon + \alpha_\omega \upsilon_t \tag{4.42}$$

$$\upsilon_t = \frac{a_1 k}{\max(a_1\omega, S_{ij}F_2)} \tag{4.43}$$

$$F_1 = \tanh[[\min[\min[\max(\frac{\sqrt{k}}{\beta^*\omega y}, \frac{500\upsilon}{y^2\omega}), \frac{4\alpha_{\omega 2}k}{CD_{k\omega^+}y^2}], 10]]^4] \tag{4.44}$$

$$CD_{k\omega^+} = \max(CD_{k\omega}, 10^{-10}) \tag{4.45}$$

$$CD_{k\omega} = 2\alpha_{\omega 2}\frac{1}{\omega}\frac{\partial k}{\partial x_i}\frac{\partial \omega}{\partial x_i} \tag{4.46}$$

$$F_2 = \tanh[[\max(\frac{2\sqrt{k}}{\beta^*\omega y}, \frac{500\upsilon}{y^2\omega})]^2] \tag{4.47}$$

The constants specific to the SST k-ω model are defined as

$A_1=0.31$, $\alpha_{k1}=0.85034$, $\alpha_{k2}=1$, $\alpha_{\omega 1}=0.5$, $\alpha_{\omega 2}=0.85616$, $\beta_1=0.075$, $\beta_2=0.0828$, $\beta^*=0.09$, $\gamma_1=0.5532$, $\gamma_2=0.4403$.

Appendix E

Non-Linear Eddy Viscosity Models (NLEVMs)

Many turbulent flow calculations are based on using Linear Eddy Viscosity Models (LEVMs) such as the well-known standard and RNG *k-ε* models. However, these models are weak in several cases such as streamwise curvature, predicting of secondary flows, and etc. These linear models are popular due to computational efficiency and robustness. Second moment closures models (or known as Reynolds Stress Models, RSMs) which are explained in the following, are used in order to overcome the limitations of the LEVMs in more complex flows. Nonetheless, since these models (RSMs) require six additional transport equations for the Reynolds stresses to be solved, the computational cost is very expensive compared to LEVMs. Hence, NLEVMs were developed to combine computational robustness and efficiency of LEVMs with improved model accuracy of RSMs (Bauer et al., 2000).

One NLEVM, which is based on *k-ε* model, is used in this study: a quadratic based nonlinear k-ε model named NonlinearKEShih in OpenFOAM (OpenFOAM user and programmer guides, 2011). This model has been proposed by Shih et al. (1995). The NonlinearKEShih model, uses general polynomial approach of a Reynolds stress-strain relationship which is truncated at second power terms.

Mathematical Concepts

The equations required to describe incompressible turbulent flows are those described above as NS equations (Eqns. 5.11-5.14). Turbulence models are necessary to determine the unknown Reynolds stress tensor $\overline{u_i'u_j'}$ appearing in the momentum equation. This can be resolved by deriving a transport equation for $\overline{u_i'u_j'}$ or by determining a relationship between $\overline{u_i'u_j'}$ and known quantities of the mean flow. The first method results in differential turbulence models (i.e. RSMs as will be discussed in the following). The second approach leads to algebraic turbulence models which is also discussed briefly in the following.

All algebraic turbulence models are based on the assumption that the Reynolds stress tensor is a function of mean velocity gradient, turbulent length scale, and turbulent time scale as described below:

$$\overline{u_i^{'}u_j^{'}} = F\left(\frac{\partial \overline{u_i}}{\partial x_j}, \mathrm{l_t}, \mathrm{t_t}\right) \tag{5.21}$$

Turbulent length and time scale may be expressed in terms of the turbulent kinetic energy ($k = 0.5\overline{u_i^{'}u_j^{'}}$) and its dissipation rate *ε*. Eqn. (5.21) thus can be dimensionless using Buckingham theorem (e.g. Shih et al., 1995; Speziale, 1991). Shih et al. (1995) developed a general constitutive relationship for the Reynolds stresses making use of Cayley-Hamilton theorem. Eqn. (5.22) shows this relationship which is truncated at cubic products terms of strain and vorticity tensors.

$$\begin{aligned}\overline{u_i^{'}u_j^{'}} &= \frac{2}{3}k\delta_{ij} - 2C_\mu \frac{k^2}{\varepsilon}S_{ij} + C_1\frac{k^3}{\varepsilon^2}\left(S_{ik}S_{jk} - \frac{1}{3}S_{kl}S_{kl}\delta_{ij}\right) + C_2\frac{k^3}{\varepsilon^2}\left(W_{ik}S_{jk} + W_{jk}S_{ik}\right)\\ &+ C_3\frac{k^3}{\varepsilon^2}\left(W_{ik}W_{jk} - \frac{1}{3}W_{kl}W_{kl}\delta_{ij}\right) + C_4\frac{k^4}{\varepsilon^3}\left(S_{ki}W_{lj} + S_{kj}W_{li}\right)S_{kl}\\ &+ C_5\frac{k^4}{\varepsilon^3}\left(W_{il}W_{lm}S_{mj} + S_{il}W_{lm}W_{mj} - \frac{2}{3}S_{lm}W_{mn}W_{nl}\delta_{ij}\right) + C_6\frac{k^4}{\varepsilon^3}S_{ij}S_{kl}S_{kl} + C_7\frac{k^4}{\varepsilon^3}S_{ij}W_{kl}w_{kl}\end{aligned} \tag{5.22}$$

In Eqn. (5.22), the mean velocity gradient is divided into strain and vorticity tensors which can be written as Eqns. (5.23, 5.24), where Ω_k is the rotation rate of the coordinate system. One should note that this term is not included in the OpenFOAM implementation (Moradnia, 2010).

$$S_{ij} = 0.5\left(\frac{\partial \overline{u_i}}{\partial x_j} + \frac{\partial \overline{u_j}}{\partial x_i}\right) \tag{5.23}$$

$$\omega_{ij} = 0.5\left(\frac{\partial \overline{u_i}}{\partial x_j} - \frac{\partial \overline{u_j}}{\partial x_i}\right) - \varepsilon_{ijk}\Omega_k \tag{5.24}$$

The C_i coefficients in Eqn. (5.22) are as a function of strain and vorticity tensor invariants. Different NLEVMs may be categorized due to the order of products of strain and vorticity tensor terms they include in the Eqn. (5.22). Tables 5.4 and 5.5 show the coefficient values for NonlinearKEShih turbulence model considered in this study. The calibration of coefficient C_μ is very important since the ability of considering the extra rate of strain effects on turbulence is modeled.

Table 5.4. Linear term coefficient (model coefficient C_μ)

Model	C_μ
NonlinearKEShih	$\dfrac{1}{A_0 + A_s\left(\dfrac{k}{\varepsilon}\right)\sqrt{S_2^2 + W_2^2}}$

Table 5.5. Higher order term coefficients (model coefficient C_i)

Model	C_1	C_2	C_3	C_4	C_5
NonlinearKEShih	$\dfrac{\frac{0.75}{C_\mu}}{1000+S_2^3}$	$\dfrac{\frac{3.8}{C_\mu}}{1000+S_2^3}$	$\dfrac{\frac{4.8}{C_\mu}}{1000+S_2^3}$	–	–

Generally the advantages and disadvantages of NLEVMs maybe written as following (Manceau, 2010).

Advantages:

- The constitutive relationships are not very subtle and can potentially reproduce complex flows.
- These models can resolve the effects which LEVMs are unable to resolve: negative production, effects of rotation, secondary flow, and etc.
- These models are as a bridge between LEVMs and RSMs from the computational cost point of view.

Disadvantages:

- NLEVMs are mathematically (numerically) less robust than LEVMs.

- The calibration process is more difficult since there are more coefficients which, due to the nonlinearity, are difficult to isolate considering simple flows. However, the explicit algebraic methodology enables the derivation of nonlinear models from Reynolds stress models, without calibration.
- They have a behavior much less predictable than the standard k-ε model. They might have wrong behaviors for a given flow or region.
- It has been reported that they are not as stable as LEVMs and RSMs numerically.

Reynolds Stress Models (RSMs)

The Reynolds Stress Models (RSMs) or called as Reynolds Stress Turbulence Models (RSTMs) are the most advanced turbulence models which are available within OpenFOAM. RSMs' concept is different from the isotropic eddy-viscosity hypothesis. It closes the Reynolds-Averaged Navier-Stokes (RANS) equations by solving transport equations for the Reynolds stresses as well as an equation for the dissipation rate. Therefore, for a three-dimensional flow, seven additional transport equations are required (i.e. six equations for Reynolds stresses and one for dissipation rate).

Compared to one-equation and two-equation models, RSMs have greater accuracy in prediction of complex flow conditions with complex geometries. They are good models to see the effects of streamline curvature, swirl, rotation, and etc. However, closure assumptions employed to model terms in the exact transport equations for the Reynolds stresses are the limitations of RSMs. The most challenging part of RSMs simulations are modeling of pressure-strain and dissipation-rate terms. The ways these terms are calculated conclude to different RSMs which result to different accuracy of RSMs predictions.

One should note that computational cost of RSMs are more expensive than simpler models and so it might not always yield results that are clearly superior. Some examples of using RSMs may be in cyclone flows, swirling flows, rotating flows, and the stressed-induced secondary flows (ANSYS FLUENT, 2009).

The exact form of the Reynolds stress transport equations is derived by taking moments of the exact momentum equation. After being Reynolds-averaged, several terms in the exact equation are unknown and modeling assumptions are required in order to close the equations.

Reynolds Stress Transport Equations

The exact transport equations for the transport of the Reynolds stresses, $\rho\overline{u_i' u_j'}$, may be written as:

Local Time Derivative + Convection (C_{ij}) = - Turbulent Diffusion ($D_{T,\ ij}$) + Molecular Diffusion ($D_{L,ij}$) - Stress Production (P_{ij}) - Buoyancy Production (G_{ij}) + Pressure strain (ϕ_{ij}) - Dissipation (ε_{ij}) - Production by System Rotation (F_{ij}) + User-Defined Source Term

The mathematical expression is represented as following:

$$\frac{\partial}{\partial t}\left(\rho\overline{u_i' u_j'}\right)+\frac{\partial}{\partial x_k}\left(\rho u_k\overline{u_i' u_j'}\right)=-\frac{\partial}{\partial x_k}\left(\rho\overline{u_i' u_j' u_k'}+\overline{p\left(\delta_{kj}u_i'+\delta_{ik}u_j'\right)}\right)+\frac{\partial}{\partial x_k}\left(\mu\frac{\partial}{\partial x_k}\left(\overline{u_i' u_j'}\right)\right)$$
$$-\rho\left(\overline{u_i' u_k'}\frac{\partial u_j}{\partial x_k}+\overline{u_j' u_k'}\frac{\partial u_i}{\partial x_k}\right)-\rho\beta\left(g_i\overline{u_j'\theta}+g_j\overline{u_i'\theta}\right)+\overline{p\left(\frac{\partial u_i'}{\partial x_j}+\frac{\partial u_j'}{\partial x_i}\right)}-2\mu\overline{\frac{\partial u_i'}{\partial x_k}\frac{\partial u_j'}{\partial x_k}} \tag{5.25}$$
$$-2\rho\Omega_k\left(\overline{u_j' u_m'}\varepsilon_{ikm}+\overline{u_i' u_m'}\varepsilon_{jkm}\right)+Source$$

C_{ij}, $D_{L,ij}$, P_{ij}, and F_{ij} do not need to be modelled. Whereas, $D_{T,ij}$, G_{ij}, ϕ_{ij}, and ε_{ij} require modelling in order to close the equation.

Turbulent Diffusion Transport Equation

$D_{T,ij}$ can be modeled by the generalized gradient-diffusion model of Daly and Harlow (1970) as:

$$D_{T,ij}=C_s\frac{\partial}{\partial x_k}\left(\rho\frac{k\overline{u_k' u_l'}}{\varepsilon}\frac{\partial\overline{u_i' u_j'}}{\partial x_l}\right) \tag{5.26}$$

This is by far the most widely used model. The proposed coefficient by Daly and Harlow is C_s=0.22, but values between 0.20 and 0.25 are used. OpenFOAM uses C_s=0.25.

Pressure-Strain Modeling

Different methods for pressure-strain modeling cause different RSMs. Two of these models which are implemented in OpenFOAM and have been used in this study are the model proposed by Gibson and Launder (1978), and the model proposed by Launder, Reece, and Rodi (1975). These two models are known as LaunderGibsonRSTM and LRR within the OpenFOAM RANS turbulence models. The difference between these two models is explained in the following.

Linear Pressure-Strain Model (LaunderGibsonRSTM Model in OpenFOAM)

The pressure-strained term, ϕ_{ij}, in Eqn. (5.25) is modeled according to the proposals by Gibson and Launder (1978), Fu et al. (1987), and Launder (1980, 1980). This approach to modeling the ϕ_{ij} uses the following decomposition:

$$\phi_{ij} = \phi_{ij,1} + \phi_{ij,2} + \phi_{ij,w} \tag{5.27}$$

where $\phi_{ij,1}$ is the slow pressure-strain term, also known as the return-to-isotropy term, $\phi_{ij,2}$ is called the rapid pressure-strain term, and $\phi_{ij,w}$ is the wall-reflection term.

The slow pressure-strain term, $\phi_{ij,1}$, is modeled as

$$\phi_{ij,1} = -C_1 \rho \frac{\varepsilon}{k}\left(\overline{u_i' u_j'} - \frac{2}{3}\delta_{ij} k\right) \tag{5.28}$$

with $C_1=1.8$.

The rapid pressure-strain term, $\phi_{ij,2}$, is also modeled as

$$\phi_{ij,2} = -C_2\left(\left(P_{ij} + F_{ij} + \frac{5}{6}G_{ij} - C_{ij}\right) - \frac{2}{3}\delta_{ij}\left(P + \frac{5}{6}G - C\right)\right) \tag{5.29}$$

where C_2=0.60, P_{ij}, F_{ij}, G_{ij}, and C_{ij} are defined as in Eqn. (5.25), $P=0.5P_{kk}$, $G=0.5G_{kk}$, and $C=0.5C_{kk}$.

The wall-reflection term, $\phi_{ij,w}$, is responsible for the redistribution of normal stresses near the wall. It is used to damp the normal stress perpendicular to the wall, while enhancing the stresses parallel to the wall. It may be written as

$$\begin{aligned}\phi_{ij,w} &= C_1^{'}\frac{\varepsilon}{k}\left(\overline{u_k^{'}u_m^{'}}n_k n_m\delta_{ij} - \frac{3}{2}\overline{u_i^{'}u_j^{'}}n_j n_k - \frac{3}{2}\overline{u_j^{'}u_k^{'}}n_i n_k\right)\frac{C_l k^{1.5}}{\varepsilon d} \\ &+ C_2^{'}\left(\phi_{km,2}n_k n_m\delta_{ij} - \frac{3}{2}\phi_{ik,2}n_j n_k - \frac{3}{2}\phi_{jk,2}n_i n_k\right)\frac{C_l k^{1.5}}{\varepsilon d}\end{aligned} \tag{5.30}$$

where $C_1^{'}=0.5$, $C_2^{'}=0.3$, n_k is the x_k component of the unit normal to the wall, d is the normal distance to the wall, and $C_l = C_\mu^{3/4}/\kappa$, where $C_\mu=0.09$ and κ is the von Karman constant (=0.4187).

All above-mentioned general coefficients as well as OpenFOAM specified coefficients for LaunderGibsonRSTM model are given in Table 5.6.

Table 5.6. LaunderGibsonRSTM model coefficients

C_μ	κ	C_1	C_2	$C_{\varepsilon 1}$	$C_{\varepsilon 2}$	$C_1^{'}$	$C_2^{'}$	C_s	C_ε	σ_ε	σ_R
0.09	0.41	1.8	0.6	1.44	1.92	0.5	0.3	0.25	0.15	1.3	0.81967

Rotta+IP Model (LRR Model in OpenFOAM)

In a famous paper, Launder, Reece, and Rodi (1975) proposed to associate the following model

$$\phi_{ij}^2 = -C_2\left(P_{ij} - \frac{2}{3}P\delta_{ij}\right) \tag{5.31}$$

to the Rotta model

$$\phi_{ij}^1 = -C_1\varepsilon a_{ij} \tag{5.32}$$

where P_{ij} is the production tensor and $P=0.5P_{kk}$. The model is often simply called LRR model. The model for the rapid-term tends to make the production more isotropic.

In order to satisfy the Crow (1968) constraint, C_2 is chosen as the LaunderGibsonRSTM model. All other coefficients are also similar to previous model (Table 5.6).

Buoyancy Term

The production term due to buoyancy is modeled as

$$G_{ij} = \left(\overline{J_i U_j} + \overline{J_j U_i}\right) = -\beta\left(g_i \overline{u_j \theta} + g_j \overline{U_i \theta}\right) \tag{5.33}$$

$$\overline{U_i \theta} = \frac{\mu_t}{\mathrm{Pr}_t}\left(\frac{\partial T}{\partial X_i}\right) \tag{5.34}$$

where Pr_t is the turbulent Prandtl number for energy with a value of 1.0 for this study.

Turbulent Kinetic Energy

In RSMs, when the turbulent kinetic energy is needed for modeling a specific term, it is obtained of the Reynolds stress tensor:

$$k = \frac{1}{2}\overline{u_i^{'} u_i^{'}} \tag{5.35}$$

Modeling the Dissipation Rate

The dissipation tensor, ε_{ij}, is modeled as

$$\varepsilon_{ij} = \frac{2}{3}\delta_{ij}\left(\rho\varepsilon + Y_M\right) \tag{5.36}$$

where $Y_M=2\rho\varepsilon M_t^2$ is an additional "dilatation dissipation" term according to the model by Sarkar (1993).

However, the scalar dissipation rate, ε, is computed with a model transport equation as following:

$$\frac{\partial\rho\varepsilon}{\partial t}+\frac{\partial}{\partial x_i}\left(\rho\varepsilon u_i\right)=\frac{\partial}{\partial x_j}\left(D\varepsilon_{eff}\frac{\partial\varepsilon}{\partial x_j}\right)+0.5C_{\varepsilon 1}\left(P_{ii}+G_{ii}\right)\frac{\varepsilon}{k}-C_{\varepsilon 2}\rho\frac{\varepsilon^2}{k}+Source \tag{5.37}$$

where σ_ε, $C_{\varepsilon 1}$, and $C_{\varepsilon 2}$ were presented in Table 5.6. It is noteworthy that $D\varepsilon_{eff}$, and turbulent viscosity υ_t are calculated similar to the formulation in the standard k-ε model.

Generally the advantages and disadvantages of RSMs maybe written as following (Manceau, 2010; Davidson, 2011).

Advantages:

- Since the transport equations of Reynolds stresses are solved, the RSMs respond to for instance a sudden change in the mean strain effectively.
- If one increases the modeling order, much is gained in the representation of the physics. In fact, instead of assuming that the Reynolds stresses have a given behavior, their transport equations are solved which contain the main physical mechanisms that derive the evolution of turbulence such as production, redistribution, turbulent transport, viscous diffusion, and dissipation.
- In particular, the production terms, that are sufficient to explain many phenomena, do not require modeling.

Disadvantages:

- RSMs are more complex and difficult to implement.
- They are numerically very sensitive to discretization schemes, specially advection schemes, due to small stabilizing second order derivatives in the momentum equations.
- RSMs are CPU consuming.